CANADIAN THESES

THÈSES CANADIENNES

NOTICE

The quality of this microfiche is heavily dependent upon the quality of the original thesis submitted for microfilming. Every effort has been made to ensure the highest quality of reproduction possible

If pages are missing, contact the university which granted the degree.

Some pages may have indistinct print especially if the original pages were typed with a poor typewriter ribbon or if the university sent us an inferior photocopy.

Previously copyrighted materials (journal articles, published tests, etc.) are not filmed

Reproduction in full or in part of this film is governed by the Canadian Copyright Act, R.S.C 1970, c. C-30

AVIS

La qualité de cette microfiche dépend grandement de la qualité de la thèse soumise au microfilmage Nous avons tout fait pour assurer une qualité supérieure de reproduction

S'il manque des pages, veuillez communiquer avec l'université qui a conféré le grade

La qualité d'impression de certaines pages peut laisser à désirer, surtout si les pages originales ont été dactylographiées à l'aide d'un ruban usé ou si l'université nous a fait parvenir une photocopie de qualité inférieure

Les documents qui font déjà l'objet d'un droit d'auteur (articles de revue, examens publiés, etc) ne sont pas microfilmés

La reproduction, même partielle, de ce microfilm est soumise à la Loi canadienne sur le droit d'auteur, SRC 1970, c. C-30

THIS DISSERTATION HAS BEEN MICROFILMED EXACTLY AS RECEIVED

'LA THÈSE A ÉTÉ MICROFILMÉE TELLE QUE NOUS L'AVONS REÇUE

Characteristics of Some Hydraulic Structures Used for Flow Control and Measurement in Open Channels

Udoyara Sunday Tim

A Thesis
in
The Department
of Civil Engineering

Presented in Partial Fulfillment of the Requirements
for the Degree of Doctor of Philosophy at
Concordia University
Montréal, Québec, Canada

September 1986

ISBN 0-315-35552-2

ABSTRACT

Characteristics Of Some Hydraulic Structures Used For Low Control And Measurement in Open Channels

Udoyara Sunday Tim, Ph.D.
Concordia University, 1986

The efficient management of water to meet the growing needs of people, agriculture and industry has been attracting special interest in recent years. A knowledge of the quantity of water available is important in the areas such as irrigation, flood control, inland navigation and water conservation. A wide variety of hydraulic structures are available for flow control and measurement in an open channel. Lateral weirs, orifices and combinations of these outlets located in the side of the open channels can be utilized to divert and control the flow. Sharp-crested weirs and broad-crested weirs are structures commonly used in open channels to measure the flow. The present study deals with the characteristics of some hydraulic structures that are commonly used for flow control and measurement. The specific flow control structure studied include the trapezoidal lateral weirs, the rectangular lateral orifices and the rectangular lateral weir-orifice units. The specific flow measurement structures studied include the rectangular sharp-crested weirs and the rectangular broad-crested weirs.

For each flow control outlet studied, an existing hydrodynamic model developed for rectangular lateral weirs is adopted to derive theoretical expressions for the mean discharge coefficient of the outlet. Detailed experiments were conducted to provide a verification of the theoretical predictions. Furthermore, the hydraulic design of rectangular lateral weir-orifice units for uniform flow distribution in an open channel is examined.

In the study concerning the characteristics of the rectangular sharp-crested weir, experimental results related to detailed pressure and velocity distributions as well as

surface profiles are used to derive semi-emperical equations for the discharge coefficient. The study on the square-edged and round-nosed rectangular broad-crested weir deals with the hydraulic characteristics for both free-flow and submerged flow conditions. The effect of rounding the upstream corner of the weir on the characteristics of flow is examined for broad-crested weirs.

ACKNOWLEDGEMENT

The author wishes to express his gratitude to Dr. A.S. Ramamurthy for suggesting the topics and for his guidance in the course of the investigation.

Thanks are due to Dr. M.V.J. Rao and Dr. B.L. Carballada for their very helpful discussions.

Thanks are also due to the Chairman and faculty members of the Department of Civil Engineering, Messrs. L. Stankevicius, D. Roy, D. Vo and the staff members of the machine shop for their assistance.

Thanks are also due to Ms. M. Berryman and Ms. C. Egbert for typing the thesis.

TABLE OF CONTENTS

CHAPTER III

HYDRAULIC CHARACTERISTICS OF RECTANGULAR LATERAL ORIFICES IN OPEN CHANNELS

CHAPTER IV

CHARACTERISTICS OF LATERAL WEIR-ORIFICE UNITS FOR UNIFORM FLOW DISTRIBUTION IN OPEN CHANNELS

PART II FLOW MEASUREMENT STRUCTURES

CHAPTER V

DISCHARGE CHARACTERISTICS OF RECTANGULAR SHARP-CRESTED WEIRS

CHAPTER VI

HYDRAULIC CHARACTERISTICS OF THE SQUARE-EDGED AND ROUND-NOSE RECTANGULAR BROAD-CRESTED WEIRS

LIST OF FIGURES

LIST OF TABLES

NOMENCLATURE

A	cross-sectional area lateral weir flow
A^*	area of non-dimensional velocity distributions at section EF of sharp-crested weir
a	height of the rectangular lateral orifice
ABCDEF	control volume for rectangular broad-crested weir (Figure 6.1c)
ABEFJ	control volume for rectangular sharp-crested weir (Figure 5.2)
AF	upstream control section for rectangular broad-crested weir (Figure 6.1c)
AJ	upstream control section for rectangular sharp-crested weir (Figure 5.2b)
AP	flow region within the rectangular lateral orifice (Figure 4.3a)
B	width of two-dimensional approach channel
B_h	width of two-dimensional channel at a depth n below the free surface (Figure 2.1)
b	distance betwen the orifice and weir portions of the lateral weir-roifice unit (Figure 4.1)
b_o	bottom width of trapezoidal channel (Figure 2.3c)
C_c	contraction coefficient
C_d	discharge coefficient of free lateral outlet of two-dimensional channel and local discharge coefficient of lateral weir given in Equation (2.4)
$\bar{C}_d$	mean discharge coefficient of lateral weir
C_{de}	discharge coefficient of rectangular sharp-crested weir
C_{do}	mean discharge coefficient of rectangular lateral orifice

C_{dm}	discharge coefficient of rectangular broad-crested weir under submerged flow condition
C_{dw}	discharge coefficient of rectangular broad-crested weir under free-flow condition
C_D	form drag coefficient of rectangular a surface-mounted body
C_{DC}	form drag coefficient of rectangular surface-mounted bodies corrected for blockage
C_p	pressure coefficient
C_{pb}	pressure coefficient on the rear face of a surface-mounted body
C_{pu}	pressure coefficient on the upstream face of a surface-mounted body
C_o, C_1, C_2, C_3	coefficients for polynominal fit given in Equation (2.5) to Equation (2.8)
D	diameter of the top edge of surface-mounted rectangular body (Figure 7.1)
DE	downstream control section and location of parallel flow on rectangular broad-crested weir crest (Figure 6.1c)
d_3	depth of flow at downstream control section of rectangular broad-crested weir
d_c	critical depth of flow over broad-crsted weir
d_o	brink depth at the downstream end of rectangular broad-crested weir
EF	nappe section of rectangular sharp-crested weir where the bottom profile of nappe reaches its highest elevation (Figure 5.2)

F_1	Froude number of flow upstream of main channel
F_p	pressure force acting on the upstream face of rectangular broad-crested weir
f	drowned flow reduction factor for rectangular broad-crested weirs
f( )	functions of
$f_o(\eta_o, L/B)$	intermediate function for trapezoidal lateral weir given in Equation (2.19)
$f_1(\eta_o, L/B)$	intermediate function for trapezoidal lateral weir given in Equation (2.20)
$f(\eta_{o1}, L/B)$	intermediate function for rectangular lateral orifice given in Equation (3.13)
$f(\eta_{o2}, L/B)$	intermediate function for rectangular lateral orifice given in Equation (3.14)
$f_1(\eta_1, L/B)$	intermediate function for rectangular lateral weir-orifice given in Equation (4.16)
$f_2(\eta_2, L/B)$	intermediate function for rectangular lateral weir-orifice given in Equation (4.17)
$f_3(\eta_3, L/B)$	intermediate function for rectangular lateral weir-orifice given in Equation (4.18)
g	acceleration due to gravity
H	piezometric or measured head over rectangular weir at an upstream location
H_1	upstream total head reckoned above the weir crest

H_2	downstream head over rectangular broad-crested weir under submerged flow condition
H_T	height of the wind-tunnel test section (Figure 7.1)
h	depth of the flow layer below free surface
h_e	depth of flow at the crest section of rectangular sharp-crested weir
h_r	depth of flow at the upstream edge of rectangular broad-crested weir
h_o	depth of flow over sill level of trapezoidal lateral weir
h_{01}	depth of flow over sill level of lateral orifice
h_{02}	depth of flow from the free-surface to top of the lateral orifice
h_1	head over sill level of the orifice portion of lateral weir-orifice unit
h_2	depth of flow from the free surface level to the top of the orifice of rectangular lateral weir-orifice unit
h_3	depth of flow from the free surface to the bottom of the weir of rectangular lateral weir-orifice unit
K	constant (denoting ratio of maximum depth of flow to minimum depth of flow for lateral weir-orifice unit)
K_B	pressure distribution coefficient at section EF (Figure 5.1) of rectangular sharp-crested weir
K_f	pressure distribution coefficient on weir face of rectangular sharp-crested weir

K_p	pressure distribution coefficient on the upstream face of rectangular broad-crested weir
KL	section of the nappe corresponding to a location at the weir plane of rectangular sharp-crested weir (Figure 5.1)
L	longitudinal length of the lateral outlet (lateral weir, lateral orifice and lateral weir-orifice unit)
L_h	length of infinitesimal layer of lateral weir at a depth h below the free surface
L_m	peripheral length of the weir model used for wind-tunnel test
L_s	length of the trapezoidal lateral weir at the sill level
L_w	length of the rectangular broad-crested weir in the direction of flow
L'_w	total length of front face and crest of broad-crested weir model
M_1	momentum rate at the upstream control section of broad-crested weir
M_3	momentum rate at the downstream control section of broad-crested weir
P	height of rectangular broad-crested weir above channel bed and height of hydraulic model used for wind-tunnel test
P_1	pressure force at upstream control section of rectangular broad-crested weir
P_3	pressure force at downstream control section of rectangular broad-crested weir

P_A	pressure force at upstream section (AJ) of a rectangular sharp-crested weir
P_B	pressure force at the nappe section (EF) of a rectangular sharp-crested weir
P_f	pressure force on the upstream face of a rectangular sharp-crested weir
p	pressure intensity
p_b	pressure intensity at any point on the downstream face of a surface-mounted rectangular weir
p_u	pressure intensity at any point on the upstream face of a surface-mounted rectangular weir
p_∞	static pressure intensity of the free-stream taken at an upstream section of a surface mounted rectangular weir
Q	discharge
Q_r	discharge ratio corresponding to maximum flow depth for rectangular lateral weir-orifice units (Equation (4.20))
Q_{ro}	discharge ratio for rectangular lateral weir-orifice unit when the flow depth is at the top of the orifice (Equation (4.22))
Q_w	total discharge over rectangular broad-crested weir under free-flow condition
Q_{wo}	total outflow through rectangular lateral weir-orifice unit defined by Equation (4.15)

Q_o	total discharge through rectangular lateral orifice (Equation (3.12))
Q_1	discharge in the upstream approach channel
Q_2	discharge in the channel downstream of the outlet
Q_m	discharge over rectangular broad-crested weir under submerged flow condition
Q_t	total theoretical discharge through trapezoidal lateral weirs defined by Equation (2.18)
Q_w	actual discharge through the outlets
q	discharge per unit width of main channel
R	radius of upstream nose of rectangular broad-crested weir
R_e	Reynolds number
R_{eD}	Reynolds number based on upstream diameter of upstream corner of surface-mounted rectangular weir
S	sill height of lateral weir and lateral orifice above channel bed
S_h	submergence ratio
T	location of rectangular lateral weir-orifice unit (Figure 4.4)
U_o	reference velocity (taken as $\sqrt{2gH}$)
U_g	gap velocity in wind-tunnel working section
U_y	velocity at any point y above the crest of a rectangular sharp-crested weir (Figure 5.1)

U_∞	mean velocity of free stream for surface-mounted rectangular bodies
$\bar{V}$	velocity vector at a point within the nappe of a rectangular sharp-crested weir
V_1	mean velocity in the approach channel
V_2	mean velocity in the downstream channel
V_3	mean velocity at the downstream section of rectangular broad-crested weir under free-flow condition
V_B	average velocity at the nappe section EF of a rectangular sharp-crested weir
V(h)	horizontal component of the velocity vector at any point h above the weir crest section for a rectangular sharp-crested weir
V_j	resultant velocity of the jet issuing out of a two-dimensional lateral outlet given by Equation (2.2)
$\bar{V}_j$	mean velocity of lateral weir outflow for two-dimensional outlet and area weighted average of the jet velocity V_j over the vertical projection of uncontracted area of lateral weir flow
V_o	mean velocity of flow at the upstream section AJ for rectangular sharp-crested weir
V(y)	horizontal component of the velocity vector V at any point y above the lower nappe at section EF of a rectangular sharp-crsted weir
W	height of the rectangular sharp-crested weir above the channel bed

We	Webber number
X	horizontal distance measured from the lower edge of the front face of a surface mounted rectangular body located in a wind tunnel wall
X_w	distance from the beginning of a rectangular broad-crested weir
X'_w	distance along the perimeter of a rectangular broad-crested weir
Y	depth of flow, vertical distance
Y_1	depth of flow in the upstream channel
Y_u	maximum depth of flow upstream of rectangular lateral weir-orifice unit (Figure 4.2)
y	vertical distance
Y_o	depth of flow at section EF for the flow over a rectangular sharp-crested weir
Z_1	side slope of trapezoidal channel
Z	side slope of trapezoidal lateral weir projection on the vertical plane (cotangent of slope angle)
z	vertical elevation
η_{01}	velocity parameter for rectangular lateral orifice defined by Equation (3.9)
η_{02}	velocity parameter for rectangular lateral orifice defined by Equation (3.10)
η_1	velocity parameter for rectangular lateral weir-orifice defined by Equation (4.12)

η_2	velocity parameter of rectangular lateral weir-orifice unit given by Equation (4.13)
η_3	velocity parameter of rectangular lateral weir-orifice unit defined by Equation (4.14)
$\phi( )$	a function of
ϕ	angle of inclination of streamlines at section EF rectangular sharp-crested plate weirs
ΔQ_r	deviation in the discharge ratio Q_r
α	kinetic energy coefficient
β	momentum coefficient
μ	dynamic viscosity of water
υ	kinematic viscosity of water
σ	surface tension of water
ρ	density of water
γ	specific weight of water

CHAPTER I

CHARACTERISTICS OF SOME HYDRAULIC STRUCTURES USED FOR FLOW CONTROL AND MEASUREMENT IN OPEN CHANNELS

1.1 INTRODUCTORY REMARKS

A hydraulic structure may be defined as any structure which is designed to handle a flowing fluid (for example, water) in any way. This may include retention, conveyance, control and measurement. Such structures are required in many fields of civil engineering, the principal ones being water and wastewater treatment, water conservation, hydroelectric power, irrigation, drainage, inland navigation and flood control.

The need to control and measure the flow in rivers and canals arises from the value of water to the community. As population expands and industry develops, the availability of water becomes increasingly important. Economical design of environmental and irrigation projects requires the size of structures to be optimized. This is possible only if the system is well regulated.

Flow control and measurement in open channels can be realized with the use of weirs and orifices besides other structures. A weir is a hydraulic structure built across a canal or channel to raise the level of water and to divert it. An orifice is an opening with a closed perimeter located in an open channel through which water flows. A weir formed in the side of an open channel is termed a lateral weir, while a weir placed across the channel is termed a normal weir. Normal weirs are usually classified into two distinct groups depending on the crest length in the direction of flow. Other control structures may also be used for discharge measurement.

1.2 SCOPE AND OBJECTIVE OF THE PRESENT STUDY

The primary objective of the present study is to investigate the discharge characteristics of some common weirs and orifices, generally grouped as hydraulic structures for control and measurement of open channel flow. For each structure considered, the basic geometric and hydrodynamic variables influencing the characteristics of flow are identified. A natural consequence of the investigation is the development of equations which can be used to obtain the discharge coefficient of each structure for a wide range of geometric forms and flow variables. The two part study consists of investigating analytically and experimentally the hydraulic characteristics of some flow control and measurement structures. The first part of the study deals with the hydraulic characteristics of flow control structures such as trapezoidal lateral weirs, rectangular lateral orifices and rectangular lateral weir-orifice units. The second part of the study deals with the characteristics of flow measurement structures such as rectangular sharp-crested weirs and rectangular broad-crested weirs.

CHAPTER II

CHARACTERISTICS OF FLOW THROUGH TRAPEZOIDAL LATERAL WEIRS

2.1 INTRODUCTION

A lateral weir is an overflow weir located in the side of a channel that allows lateral flow of water when the surface of water in the channel rises above the weir crest. The flow through a lateral weir is spatially varied and the discharge through the weir is affected significantly by the depth and velocity of flow in the main channel.

Lateral weirs are used extensively in irrigation, land drainage, flood alleviation and urban drainage works. In urban drainage works, lateral weirs are used for decanting excess flow in sewerage networks. Lateral weirs are also used in water and wastewater treatment plants to bypass excess wet-weather flow and for side-line equalization.

The characteristics of flow through a rectangular lateral weir has been studied by a number of investigators [1, 11, 14]. The first rational approach to study the characteristics of rectangular lateral weirs was made by De Marchi [18] in 1934. He presented an explicit solution to the problem of flow through a rectangular lateral weir based on the assumption that the energy loss is negligible in the main channel section that spans the lateral weir. Various versions of the De Marchi equation have been proposed by several investigators [15, 22, 69]. In particular, Collinge [15], Frazer [22] and Subramany [69] studied the effect of main channel velocity on the weir discharge coefficient. A brief summary of previous studies related to lateral weirs is provided in Table 2.1.

For the outflow through a trapezoidal lateral weir, limited information is available in literature. Allen [3] and Uyumaz [72] presented experimental results for the lateral outflow through rectangular lateral weirs located in the side of circular channels. El-Khashab and

Smith [20] used the momentum and energy relationships to predict the nature of flow through a rectangular lateral weir located in a trapezoidal channel. Recently, a hydrodynamic model [11] was developed for the outflow through a rectangular lateral weir located in the side of a rectangular channel on the basis of the existing two-dimensional conduit outlet model proposed by McNown [42]. For the flow through the rectangular lateral weir, the mean discharge coefficient of the weir was expressed in terms of the hydrodynamic and geometric variables.

The study presented in this chapter deals with the theoretical and experimental investigations of the characteristics of flow through trapezoidal lateral weirs. The two-dimensional lateral outlet model (hydrodynamic model) developed for the flow through a rectangular lateral weir [11] is adopted in this chapter to derive a general expression for the mean discharge coefficient C_d of the weir. The results of the experiments conducted are presented to validate the proposed expressions for the mean discharge coefficient.

2.2 TWO-DIMENSIONAL LATERAL OUTLET MODEL

The characteristics of flow through an outlet located in the side of a two-dimensional channel have been studied by a number of investigators [27, 42, 44]. For the outflow through a lateral outlet of width L_h located in the side of a two-dimensional channel of width B_h (Figure 2.1), the local discharge coefficient C_d is defined as

$$C_d = \frac{\text{jet flow per unit depth}}{LV_j} \tag{2.1}$$

in which V_j is the resultant velocity of the outflow jet given by Equation (2.2).

$$V_j = \sqrt{V_1^2 + 2gh} \tag{2.2}$$

In the above expression, h is the pressure head differential across the face of the outlet and V_1 is the velocity of flow in the main channel. Furthermore, in Equation (2.1), C_d is a function of the geometric parameter L_h/B_h and the velocity parameter η defined as,

$$\eta = \frac{V_1}{V_j} = \frac{V_1}{\sqrt{V_1^2 + 2gh}} \qquad (2.3)$$

The theoretical expression relating the local discharge coefficient C_d, the geometric parameter L_h/B_h and the main channel velocity ratio V_2/V_1 is known [27, 42]. This relationship together with the continuity condition directly gives the dependence of C_d on L/B and η as shown in Figure 2.2. V_2 is the mean velocity in the downstream channel. For $0<L/B\leq 1.0$ and $0<\eta\leq 1.0$, the relationship between C_d and η can be approximated by the following polynominal [11]

$$C_d = C_0 + C_1\eta^2 + C_2\eta^4 + C_3\eta^6 \qquad (2.4)$$

in which

$$C_0 = 0.611 \qquad (2.5)$$

$$C_1 = -0.538 + 0.254\left(\frac{L}{B}\right) \qquad (2.6)$$

$$C_2 = 0.058 + 0.234\left(\frac{L}{B}\right) \qquad (2.7)$$

and

$$C_3 = -0.129 - 0.489\left(\frac{L}{B}\right) \qquad (2.8)$$

In the following sections, the two-dimensional lateral outlet model presented above is used to obtain an expression for the mean discharge coefficient of a trapezoidal lateral weir.

2.3 TRAPEZOIDAL LATERAL WEIR IN A TRAPEZOIDAL CHANNEL

2.3.1 Theoretical Considerations

In order to derive a general expression for the mean discharge coefficient of a sharp-edged trapezoidal lateral weir located in the side of a trapezoidal channel, the following assumptions are made:

1. The flow in the appraoch channel is subcritical.
2. The bed of the main channel is horizontal.
3. The lateral weir and the main channel have the same trapezoidal cross-section.
4. For a specific weir, the width L_h (Figure 2.3) at a depth h below the free surface bears a constant ratio with the channel width B_h (Figure 2.3) at the same depth h below the free surface ($L_h/B_h = L/B = \text{constant}$).
5. For the jet issuing from the outlet of any infinitesimal layer of thickness dh at a depth h below the free surface (Figure 2.3a), the velocity component normal to the channel axis is $\sqrt{2gh}$.
6. The velocity in the approach channel is not a function of depth and the parameters L/B and η are within the limits imposed on Equation (2.4).

The total weir outflow is obtained by adding the flows through the outlets of a large number of infinitesimal layers [Figure 2.3(b)] that constitute the emerging jet. For all the emerging jets, the approach velocity V_1 provides the velocity component parallel to the channel axis. The velocity components V_1 and $\sqrt{2gh}$ can be added vectorially [74] to obtain the

jet velocity V_j.

In general, for the weir outflow through an infinitesimal layer of width L_h and thickness dh [Figure 2.3(b)], the local weir discharge coefficient C_d is a function of η and L_h/B_h is constant for all layers. Thus, the local discharge coefficient C_d for all the layers that contribute to the weir outflow varies only with the velocity parameter η.

Noting that the vertical projection of the contracted area of the layer is $C_d L_h\, dh$, an expression for the total theoretical discharge Q_t through the weir can be written as,

$$Q_t = \int_0^{h_o} C_d\ L_h\, V_j\ dh \qquad (2.9)$$

in which,

$$h_o = Y_1 - S \qquad (2.10)$$

and

$$L_h = L_s + 2Z(h_o - h) \qquad (2.11)$$

where, S is the weir sill height and Y_1 is the depth of flow upstream of the weir (Figure 2.3). Furthermore, L_s denotes the width of the weir at the sill level and Z is the slope of the projection of the sides of the weir on the vertical plane (co-tangent of the slope angle).

Replacing V_j and L_h in Equation (2.9) using Equation (2.3) and (2.11) respectively, Q_t can be rewritten as

$$Q_t = \int_0^{h_o} C_d\left(\frac{V_1}{\eta}\right)[L_s + 2Z\ h_o]\ dh - \int_0^{h_o} C_d\left(\frac{V_1}{\eta}\right)2Z\,h\ dh \qquad (2.12)$$

An expression for η can be written using Equation (2.3) as

$$h = \frac{V_1^2}{2g}\left(\frac{1}{\eta^2} - 1\right) \qquad (2.13)$$

Differentiating Equation (2.13) with respect to η yields an expression for dh.

$$dh = -\frac{V_1^2}{g}\left(\frac{1}{\eta^3}\right)d\eta \qquad (2.14)$$

Substituting for C_d and dh in Equation (2.12) using Equation (2.4) and Equation (2.14) respectively, and rearranging the resulting expression yields Equation (2.15)

$$Q_t = \frac{V_1^3}{g}\left[L_s + 2Z\, h_o\right]\int_{\eta_o}^{1}\left(\frac{C_0}{\eta^4} + \frac{C_1}{\eta^2} + C_2 + C_3\eta^2\right)d\eta$$

$$- \frac{V_1^5}{g^2}\, Z \int_{\eta_o}^{1}\left(\frac{C_0}{\eta^4} + \frac{C_1}{\eta^2} + C_2 + C_3\eta^2\right)\left(\frac{1}{\eta^2} - 1\right)d\eta \qquad (2.15)$$

in which, η_o is the value of the velocity ratio η at the sill level of the weir and is defined by Equation (2.16).

$$\eta_o = \left(\frac{V_1^2}{(V_1^2 + 2gh_o)}\right)^{1/2} = \left(\frac{1}{\left(1 + \frac{2}{F_o^2}\right)}\right)^{1/2} \qquad (2.16)$$

where

$$F_o^2 = \left(\frac{V_1^2}{gh_o}\right) \qquad (2.17)$$

Integrating Equation (2.15) yields an expression for the total theoretical outflow through the weir. Thus,

$$Q_t = \frac{V_1^3}{g}\,[L_s + 2Z\,h_o]\,f_o\left(\eta_o, \frac{L}{B}\right) - \frac{V_1^5}{g^2}\,Z\left[f_1\left(\eta_o, \frac{L}{B}\right) - f_o\left(\eta_o, \frac{L}{B}\right)\right] \qquad (2.18)$$

in which,

$$f_o\left(\eta_o, \frac{L}{B}\right) = \left(1 - \eta_o^3\right)\left(\frac{C_3}{3} + \frac{C_0}{3\eta_o^3}\right) + \left(1 - \eta_o\right)\left(C_2 + \frac{C_1}{\eta_o}\right) \qquad (2.19)$$

and

$$f_1\left(\eta_o, \frac{L}{B}\right) = \left(1 - \eta_o\right)\left(C_3 + \frac{C_2}{\eta_o}\right) + \frac{C_1}{3}\left(\frac{1}{\eta_o^3} - 1\right) + \frac{C_0}{5}\left(\frac{1}{\eta_o^5} - 1\right) \qquad (2.20)$$

To obtain the mean discharge coefficient C_d, of the trapezoidal lateral weir, an alternate expression for the total outflow Q_t can be written as

$$Q_t = C_d A \overline{V}_j \qquad (2.21)$$

in which

$$A = [L_s + Zh_o]h_o \qquad (2.22)$$

and

$$\bar{V}_j = \frac{1}{A} \int_A V_j \, dA = \frac{1}{A} \int_0^{h_o} \sqrt{V_1^2 + 2gh} \; L_h \, dh \qquad (2.23)$$

Substituting for L_h in Equation (2.23) using Equation (2.11) one gets,

$$\bar{V}_j = \frac{1}{A} \int_0^{h_o} \sqrt{V_1^2 + 2gh} \left(L_s + 2Z(h_o - h) \right) dh \qquad (2.24)$$

Using Equation (2.13) and Equation (2.14), Equation (2.24) can be expressed in terms of the velocity ratio η. The resulting expression can be integrated to yield V_j. Thus,

$$\bar{V}_j = \frac{V_1^3}{3gA} \left(\left\{ (L_s + 2Zh_o) \left[\left(1 + \frac{2}{F_o^2} \right)^{3/2} - 1 \right] \right\} - \frac{V_1^2}{g} Z \left\{ \frac{3}{5} \left[\left(1 + \frac{2}{F_o^2} \right)^{5/2} - 1 \right] - \left[\left(1 + \frac{2}{F_o^2} \right)^{3/2} - 1 \right] \right\} \right) \qquad (2.25)$$

in which,

$$F_o = \sqrt{\left(\frac{2\eta_o^2}{(1 - \eta_o^2)} \right)} \qquad (2.26)$$

Using Equations (2.22) and (2.25), Equation (2.21) can be rewritten as

$$Q_t = \bar{C}_d \frac{V_1^3}{3g} \left(\left\{ [L_s + 2Z h_o] \left[\left(1 + \frac{2}{F_o^2} \right)^{3/2} - 1 \right] \right\} - Z F_o^2 h_o \left\{ \frac{3}{5} \left[\left(1 + \frac{2}{F_o^2} \right)^{5/2} - 1 \right] - \left[\left(1 + \frac{2}{F_o^2} \right)^{3/2} - 1 \right] \right\} \right) \qquad (2.27)$$

The mean discharge coefficient of the trapezoidal lateral weir can be written using Equation (2.18) and Equation (2.27) as

$$\bar{C}_d = 3\left(\frac{[L_s + 2Z\,h_0]f_0\left(\eta_0, \frac{L}{B}\right) - ZF_0^2\,h_0\left[f_1\left(\eta_0, \frac{L}{B}\right) - f_0\left(\eta_0, \frac{L}{B}\right)\right]}{\left\{(L_s + 2Zh_0)\left[\left(1 + \frac{2}{F_0^2}\right)^{3/2} - 1\right]\right\} - ZF_0^2\,h_0\left\{\frac{3}{5}\left[\left(1 + \frac{2}{F_0^2}\right)^{5/2} - 1\right] - \left[\left(1 + \frac{2}{F_0^2}\right)^{3/2} - 1\right]\right\}}\right) \tag{2.28}$$

2.3.2. Experimental Set-up for Trapezoidal Lateral Weir

Experiments were performed in a horizontal trapezoidal mild steel channel 6.0m long (Figure 2.4). The bottom width b_o of the main channel was fixed at 101.6mm and the side slope Z_1 of the main channel was 1.5. The surfaces of the test channel were painted to render it smooth. Plexiglass sheets were used to form sharp-edged weirs which were located in the side of the main channel. Table 2.2 gives the range of geometric variables covered in the tests.

The incoming flow from the supply line enters the inlet section of the test channel and is then tranquilized by a system of baffles and screens (Figure 2.4) before entering the main channel. As the water enters the weir location, some of it spills over the weir and the remainder continues towards the downstream end of the channel. At the downstream end, an adjustable gate was used to control the water level in the test channel. Standard V-notches were used to measure the lateral outflow through the weir and the downstream discharge. Point gages capable of reading to the nearest 0.1mm were used to measure the water levels in the channel and in the V-notches. The upstream flow depth in the main channel was realized at the center line of the channel at a location where the effect of curvature was negligible. In all the test series (Table 2.2), the free-falling nappes were fully ventilated.

2.3.3 Analysis of Results for Trapezoidal Lateral Weirs

In the derivation of the expression for the mean weir discharge coefficient of the weir, the velocity distribution was assumed to be uniform (assumption #6) in the main channel. However in the experiments, the top layers of the approach flow have a higher velocity than the mean velocity V_1. This generally reduces the outflow through the weir especially when the sill height is large compared to the depth of flow. To partly account for this effect and for a better presentation of the data, a flow reduction factor equal to 0.95 is proposed for the weir outflow [54]. Using this factor, the modified expressions for the theoretical discharge Q_t and the mean discharge coefficient $\bar{C}_d$ can be written as

$$Q_t = 0.95 \frac{V_1^3}{g} \left\{ (L_s + 2Zh_0) f_0\left(\eta_0, \frac{L}{B}\right) - \frac{V_1^2}{g} Z\left(f_1\left(\eta_0, \frac{L}{B}\right) - f_0\left(\eta_0, \frac{L}{B}\right)\right) \right\} \qquad (2.29)$$

and

$$\bar{C}_d = 2.85 \left(\frac{(L_s + 2Zh_0) f_0\left(\eta_\sigma, \frac{L}{B}\right) - ZF_0^2 h_0 \left\{ f_1\left(\eta_\sigma, \frac{L}{B}\right) - f_0\left(\eta_\sigma, \frac{L}{B}\right) \right\}}{(L_s + 2Zh_0)\left[\left(1 + \frac{2}{F_0^2}\right)^{3/2} - 1\right] - ZF_0^2 h_0 \left\{ \frac{3}{5}\left[\left(1 + \frac{2}{F_0^2}\right)^{5/2} - 1\right] - \left[\left(1 + \frac{2}{F_0^2}\right)^{3/2} - 1\right] \right\}} \right) \qquad (2.30)$$

The results of the series of tests conducted to verify the theoretical predictions for the flow through the trapezoidal lateral weir located in the side of a trapezoidal channel are shown in

Figures 2.5 to 2.10. For all these series, Table 2.2 provides the geometric details of the test weirs.

Figures 2.5, 2.6 and 2.7 show the variations of the mean discharge coefficient $\bar{C}_d$ of the weir with the weir parameter η_o for the three values of L/B considered. From Figures 2.5 to 2.7, the agreement between the experimental data and the predicted trends of $\bar{C}_d$ with η_o is reasonable for all L/B values.

Figures 2.8, 2.9 and 2.10 show the correlation between the actual and predicted discharge for all the test series conducted. It can be seen that the agreement between the actual and predicted weir discharge appears to be fair.

2.3.4 Conclusions

In the foregoing sections, expressions for the discharge and mean discharge coefficient were obtained using the two-dimensional lateral outlet model. Based on the results of the theoretical and experimental study, the following conclusions can be drawn:

1. For subcritical flow in the approach channel, the mean discharge coefficient of the weir $\bar{C}_d$ is dependent on the jet velocity ratio η_o. The geometric parameter L/B emerges as a significant parameter and $\bar{C}_d$ appears to depend also on L/B.
2. The sill level of the weir is an important parameter for the flow through trapezoidal lateral weirs since it determines the ratio of surface flow to the bed-flow that is deflected through the weir. In addition, the mean discharge coefficient $\bar{C}_d$ is drastically reduced at higher weir sill ratios due to the

increase in n_o.

3. The experimental data appears to validate the proposed relationships (which includes a factor of 0.95 applied to account for the velocity distribution in the main channel). The results obtained applies to trapezoidal lateral weirs that can be as wide as the main channel.

CHAPTER III

HYDRAULIC CHARACTERISTICS OF RECTANGULAR LATERAL ORIFICES IN OPEN CHANNELS

3.1 INTRODUCTION

In the design and planning of water and wastewater treatment plants, hydraulic control devices such as lateral orifices are used extensively to distribute incoming flows to parallel process units such as flocculation basins, aeration tanks and clarification basins. Various types of devices can also be employed in an open channel to achieve the desired flow distributions. The most commonly used control devices are free-discharging lateral weirs and submerged orifices. The control device serves to counterbalance the variation of the hydraulic energy so that the incoming flow can be evenly distributed to the process units.

Hydraulic analyses of closed pressure dispersion conduits consisting of small circular orifices have been well developed. Interest in this type of device results from its application to the design of ocean outfall diffusers. Camp and Garber [10] studied the characteristics of dispersion conduits used as thermal discharge diffusers. They presented functional hydraulic interpretations for a number of flow phenomena. French [23] has provided a critical analysis of the internal hydraulics of diffusers fitted with small circular orifices. Vigander [74] studied the mechanics of flow through small orifices located in conduits. For the design of open channel flow distribution and control systems involving relatively large (height of orifice compared to the depth of flow) lateral orifices, very limited information is available in literature. In particular, the effect of the ratio of the orifice length to the main channel width on the discharge characteristic of the orifice has not been studied in the past.

This chapter, therefore, is devoted to the study of the characteristics of rectangular lateral and free-discharging orifices located in open channels. Expressions are developed for the outflow through the orifice and the mean discharge coeficient using the two-dimensional

lateral outlet model (hydrodynamic model) presented in Chapter II. Experiments conducted to provide a verification of the predicted expressions are also presented.

3.2 THEORETICAL CONSIDERATIONS

The development of the theoretical expressions describing the flow through a sharp-crested rectangular lateral orifice (Figure 3.1a) is very similar to the development of the expression for the flow through rectangular lateral weirs reported earlier [54].

Assuming that the main channel is horizontal, and that the outflow through the orifice is obtained by adding the flows through a large number of infinitesimal layers that constitute the emerging jet, the two-dimensional lateral outlet model [54] is adopted to develop expressions for the outflow and the mean discharge coefficient of the rectangular lateral orifice in the following section.

3.2.1 Theoretical Outflow Through Lateral Orifice

For the lateral orifice shown in Figure 3.1a, noting that the local discharge coefficient C_d varies from layer to layer and also that the contracted area of any infinitesimal layer contributing to the outflow is $C_d L dh$, the total discharge Q_o can be written as

$$Q_o = \int_{h_{02}}^{h_{01}} C_d V_j L\, dh = \int_0^{h_{01}} C_d V_j L\, dh - \int_0^{h_{02}} C_d V_j L\, dh \qquad (3.1)$$

in which

$$h_{01} = Y_1 - S \qquad (3.2)$$

and

$$h_{02} = Y_1 - S - a \qquad (3.3)$$

Here, Y_1 = depth of the flow upstream of the orifice; S = Sill height of the orifice above the channel bed; and a = height of the orifice (Figure 3.1a). Furthermore, expressions for C_d and V_j were given earlier in Chapter II as

$$C_d = C_o + C_1\eta^2 + C_2\eta^4 + C_3\eta^6 \qquad (3.4)$$

and

$$V_j = \frac{V_1}{\eta} = \sqrt{V_1^2 + 2gh} \qquad (3.5)$$

In Equation (3.4), the constants C_0, C_1, C_2 and C_3 were expressed earlier [Equations (2.5 to (2.8)] as a function of L/B. Substituting for C_d and V_j in Equation (3.1) using Equations (3.4) and (3.5) respectively, yields

$$Q_0 = \frac{V_1 L}{g}\left\{ \int_0^{h_{01}} \left(C_0 + C_1\eta^2 + C_2\eta^4 + C_3\eta^6\right)\frac{1}{\eta}\,dh - \int_0^{h_{02}} \left(C_0 + C_1\eta^2 + C_2\eta^4 + C_3\eta^6\right)\frac{1}{\eta}\,dh \right\} \qquad (3.6)$$

Expressing h in terms of η in Equation (3.5), and differentiating the resulting expression yields,

$$dh = -\frac{V_1^2}{g}\left(\frac{1}{\eta^3}\right)d\eta \qquad (3.7)$$

in which g is the acceleration due to gravity and V_1 is the mean velocity in the main channel.

Substituting for dh in Equation (3.6) using Equation (3.7) yields

$$Q_0 = \frac{V_1^3}{g} L \left\{ \int_{\eta_{01}}^{1} \left(C_0 + C_1 \eta^2 + C_2 \eta^4 + C_3 \eta^6 \right) \frac{1}{\eta^4} \, d\eta \right.$$

$$\left. - \int_{\eta_{02}}^{1} \left(C_0 + C_1 \eta^2 + C_2 \eta^4 + C_3 \eta^6 \right) \frac{1}{\eta^4} \, d\eta \right\} \qquad (3.8)$$

in which

$$\eta_{01} = \left(\frac{V_1^2}{V_1^2 + 2g(h_{01})} \right)^{1/2} = \left(\frac{1}{1 + \frac{2}{F_{01}^2}} \right)^{1/2} \qquad (3.9)$$

and

$$\eta_{02} = \left(\frac{V_1^2}{V_1^2 + 2g(h_{02})} \right)^{1/2} = \left(\frac{1}{1 + \frac{2}{F_{01}^2} \left(1 - \frac{a}{h_{01}} \right)} \right)^{1/2} \qquad (3.10)$$

In Equation (3.10), F_{01} is an orifice parameter defined by Equation (3.11).

$$F_{01} = \frac{V_1}{\sqrt{g h_{01}}} = \frac{V_1}{\sqrt{g(Y_1 - S)}} = \frac{F_1}{\sqrt{1 - \left(\frac{S}{Y_1} \right)}} \qquad (3.11)$$

in which F_1 is the Froude number of flow in the upstream channel. Integrating Equation (3.8) yields the following expression for the theoretical outflow Q_0. Thus

$$Q_0 = \frac{V_1^3}{g} L \left\{ f\left(\eta_{01}, \frac{L_r}{B}\right) - f\left(\eta_{02}, \frac{L}{B}\right) \right\} \qquad (3.12)$$

in which

$$f\left(\eta_{01}, \frac{L}{B}\right) = \left(1 - \eta_{01}^3\right)\left(\frac{C_3}{3} + \frac{C_0}{3\eta_{01}^3}\right) + \left(1 - \eta_{01}\right)\left(C_2 + \frac{C_1}{\eta_{01}}\right) \qquad (3.13)$$

and

$$f\left(\eta_{02}, \frac{L}{B}\right) = \left(1 - \eta_{02}^3\right)\left(\frac{C_3}{3} + \frac{C_0}{3\eta_{02}^3}\right) + \left(1 - \eta_{02}\right)\left(C_2 + \frac{C_1}{\eta_{02}}\right) \qquad (3.14)$$

3.2.2 Mean Discharge Coefficient of the Orifice

To obtain the mean discharge coefficient of the lateral orifice, an alternate expression can be written for the total outflow through the orifice as

$$Q_o = C_{do} \bar{V}_j L \left(h_{01} - h_{02}\right) \qquad (3.15)$$

in which C_{do} is the mean discharge coefficient of the orifice and $\bar{V}_j$ is defined by Equation (3.16).

$$\bar{V}_j = \frac{1}{A} \int_A V_j \, dA = \frac{1}{L(h_{01} - h_{02})} \int_{h_{02}}^{h_{01}} V_j \, L \, dh \qquad (3.16)$$

Replacing V_j in Equation (3.15) using Equation (3.16) gives

$$Q_0 = \bar{C}_{do} L\left(\int_{h_{02}}^{h_{01}} V_j \, L \, dh\right) \tag{3.17}$$

Substituting for V_j and dh in Equation (3.17) using Equations (3.5) and (3.7) respectively yields Equation (3.18). Thus,

$$Q_0 = \bar{C}_{do} \frac{V_1^3}{g} L\left\{\int_{\eta_{02}}^{\eta_{01}} \left(\frac{1}{\eta^4}\right) d\eta\right\} \tag{3.18}$$

Integrating Equation (3.18) yields an expression for the outflow through the orifice.

$$Q_0 = \bar{C}_{do} \frac{V_1^3}{3g} \left\{ L\left(\frac{1}{\eta_{01}^3} - \frac{1}{\eta_{02}^3}\right)\right\} \tag{3:19}$$

Thus, the expression for the mean discharge coefficient of the orifice $\bar{C}_{do}$, can be obtained using Equations (3.12) and (3:19).

$$\bar{C}_{do} = \frac{2.85\left(f\left(\eta_{01}, \frac{L}{B}\right) - f\left(\eta_{02}, \frac{L}{B}\right)\right)}{\left(\frac{1}{\eta_{01}^3} - \frac{1}{\eta_{02}^3}\right)} \tag{3.20}$$

In Equation (3:20), a flow reduction factor of 0.95 is also used as in Equation (2.30).

3.3 EXPERIMENTAL SET-UP

A series of experiments were conducted in a rectangular steel flume 25.4cm wide, 1.2m high and 6.0m long. The orifice models were located on the side of the flume at a Section T (Figure 3.2) which was 360 cm from the entrance to the channel. At the entrance, a system of baffles and screens were used to quell the turbulence and to ensure a uniform flow in the channel. The depth of flow upstream of the orifice was measured at the center-line of the flume at Section R (Figure 3.2).

Plexiglass sheets were used to form sharp-edged orifices 25.4cm in length. The sill height S and the height of the orifice a were the main geometric variables considered (Table 3.1).

Standard V-notches were used to measure the discharge from the channel and the lateral orifice. The point gages used to measure the water levels in the flume and the respective V-notches could be read to the nearest 0.1mm. The error in the measured discharge was estimated at 3%. The experiments conducted on all the models pertain to fully ventilated nappes.

3.4 ANALYSIS OF RESULTS

Figures 3.3 and 3.4 show the results of the experiments conducted to verify the theoretical expressions given by Equation (3.12) and (3.20) for L/B = 1.0. For these figures, Table 3.1 provides the detail of the geometry of the lateral orifice models used in the tests.

Figure 3.3 shows the variation of the mean discharge coefficient of the orifice $\bar{C}_{do}$, with the velocity parameter η_{o1}. The velocity parameter η_{o1} was chosen as a main parameter since η_{o1} and η_{o2} are related for a given orifice height a. The sill height S

of the orifice above the channel bed is an important parameter in the design of lateral orifices used in water and wastewater treatment plants since it determines the quantity of flow that is deflected through the orifice.

From Figure 3.3 it can be seen that there is a fair agreement between the theoretical and experimental values of the mean discharge coefficient.

Figure 3.4 shows the plot of the predicted and actual values of the total outflow through the orifice for the models tested. The correlation appears to be fairly reasonable.

3.5 CONCLUSIONS

Based on the theoretical and experimental investigations, the following conclusions are drawn:

1. The mean discharge coefficient of the orifice is a function of the geometric parameter L/B (which denotes the ratio of the length of the orifice to the width of the main channel) and the velocity parameter η_{01} (which denotes the velocity ratio V_1/V_j at the sill level of the orifice).
2. The sill height S and the orifice height a are important geometric parameters in the design of lateral orifices since they jointly determine the ratio of flow to be diverted through the orifice.
3. The experimental data provides a fair verification of the proposed expressions for the discharge and the mean discharge coefficient of the lateral orifice. Based on the experimental results, one can conclude that the proposed expressions for $\bar{C}_{do}$ and Q_o are applicable to rectangular lateral orifices that can be as wide as the main channel.

CHAPTER IV

CHARACTERISTICS OF LATERAL WEIR-ORIFICE UNITS FOR UNIFORM FLOW DISTRIBUTION IN OPEN CHANNELS

4.1 INTRODUCTION

Hydraulic control devices and dispersion conduits such as flumes and manifolds are widely used for achieving uniform flow distribution among parallel process units in chemical, water and wastewater treatment plants. In water and waste-water treatment plants, open channel type devices rather than manifolds are often used to distribute incoming flow to parallel process units such as sedimentation tanks and aeration basins. A reliable flow distribution and equalization among the process units are essential to the operation efficiency of a process plant. For example, a relatively uniform distribution of mixed liquor flows among secondary sedimentation basins is critical to the operation of the activated sludge system and to high effluent quality.

In open channels, to obtain a uniform distribution of incoming flow to process basins, simple geometric modifications to the side and bed of the main channel have been suggested [53]. Modification to the sill levels of rectangular lateral weirs was suggested by Jain [35] as a possible means of distributing the flow uniformly among parallel basins. Chao [12], Benefield [7] and Yoa [79] investigated the characteristic of flow distribution devices or structures such as submerged orifices and side weirs. In Chapter III of this thesis, a theoretical and experimental investigation of the characteristics of rectangular lateral orifices was presented. The characteristics of uniformly discharging rectangular lateral weirs was studied by Carballada [11].

In this chapter, the study related to the characteristics of uniformly discharging lateral weir-orifice units is presented. A method to analyse the flow through lateral

weir-orifice units in a flow distribution channel is also presented. The design procedure for proportioning the flow through the weir-orifice unit for a given inflow is discussed. The pertinent structural and flow parameters influencing the flow and operation efficiency of the unit are also examined. It is shown that the lateral weir-orifice unit can be properly designed to ensure an outflow which is a prescribed percentage of the channel inflow over a range of upstream flow depths. The experimental data obtained in a test flume are presented to provide a verification of the theoretical relationship between the geometric and hydrodynamic parameters of the lateral weir-orifice flow.

4.2 THEORETICAL CONSIDERATIONS

4.2.1 Functional Relationships

For purposes of analysis, a single rectangular lateral weir-orifice unit (Figure 4.1) located in the side of a rectangular channel is considered. Let Q_1 be the discharge in the main channel at a velocity V_1 and depth Y_1. Also, let Q_{wo} be the total discharge through the weir-orifice unit. In order to predict the characteristics of the lateral weir-orifice unit which will give the desired uniform flow distribution, a functional relationship between the total outflow Q_{wo} and the geometric and flow variables need to be developed. For the lateral weir-orifice unit (Figure 4.1a), the total discharge Q_{wo} can be expressed in terms of the pertinent geometric and hydrodynamic variables as follows:

$$Q_{wo} = \phi_1 (L, B, S, a, b, h_3, V_1, g, Y) \qquad (4.1)$$

in which L = length of the lateral weir-orifice unit; B = width of the main channels; S = sill

height of the orifice portion above the channel bed (Figure 4.1(b)); a = height of the orifice (Figure 4.1(b)); b = distance between the top of the orifice and the bottom of the weir; h_3 = depth of flow above the bottom of the weir sill; V_1 = mean velocity in the main channel; g = acceleration due to gravity; and Y = depth of flow upstream of the lateral weir-orifice unit.

Normalising the variables in Equation (4.1) yields

$$\frac{Q_{wo}}{Q_1} = Q_r = \phi_2 \left(\frac{L}{B} \, , \, \frac{S}{a} \, , \, \frac{b}{a} \, , \, \frac{h_3}{a} \, , \, F_1 \right) \qquad (4.2)$$

in which, $F_1 = V_1/\sqrt{gY}$ = Froude number of flow in the main channel upstream of the lateral weir-orifice unit when the depth of flow $Y = Y_U$. Here, Y_U is the maximum depth of flow upstream of the unit.

In the analysis of the flow through the unit, three distinct cases of operation can be considered. In the first case, both the weir and orifice are effective in diverting the flow and the flow depth Y is at a level h_3 above the bottom of the weir ($Y = Y_U$). In the second case, the orifice alone is effective and the flow depth in the channel is at the bottom sill level of the weir ($Y = S + a + b$), (Figure 4.2). In the last case, the flow depth Y coincides with the top of the orifice ($Y = S + a$).

Equation (4.2) denotes the functional relationship between the discharge ratio Q_r and the weir-orifice parameters for the first case when the flow depth Y is at a level h_3 above the bottom of the weir portion of the unit.

When the depth of flow is at the bottom of the weir, for which $Y = s + a + b$,

Equation (4.2) can be rewritten as

$$\frac{Q_o}{Q} = Q_{ro} = \phi_3\left(\frac{L}{B} \cdot \frac{S}{a} \cdot \frac{b}{a} \cdot F_1\right) \qquad (4.3)$$

in which Q_o = discharge through the orifice; Q_1 = discharge in the main channel at a depth $Y = S + a + b$; and F_1 = Froude number of flow in the main channel when the depth of flow $Y = S + a + b$.

Similarly, when the depth of flow is at the top of the orifice portion of the unit, for which $Y = S + a$ (Figure 4.2), Equation (4.2) becomes

$$\frac{Q_o}{Q} = Q_{ro} = \phi_4\left(\frac{L}{B} \cdot \frac{S}{a} \cdot F_1\right) \qquad (4.4)$$

in which, Q_o = discharge through the orifice; Q_1 = discharge in the main channel at a depth $Y = S + a$; and F_1 = Froude number of flow in the main chanel when the depth of flow $Y = S + a$ (Figure 4.2). The functional relationships given in Equations (4.2), (4.3) and (4.4) are formulated to denote the dependence of the discharge ratio the geometric (structural) and flow (hydrodynamic) parameters for flow depth at some level h_3 above the bottom of the weir portion, at the bottom of the weir portion and at the top of the orifice portion of the unit respectively.

4.2.2 Lateral Weir-Orifice Units in Open Channels

The lateral outflow through a free outlet located in a two-dimensional channel has been

analysed by a number of investigators [27, 42]. The discharge characteristics of rectangular lateral weirs [11] and trapezoidal lateral weirs [Section 2.3] have been studied using the two-dimensional lateral outlet model [Section 2.2] as the basis of analysis. In Chapter III, a general expression for the total outflow through a rectangular lateral orifice was obtained on the basis of the two-dimensional lateral outlet model.

In the following section, the two-dimensional lateral outlet model discussed briefly in Section 2.2 is again adopted to develop a general expression for the total outflow through a lateral weir-orifice unit located in the side of an open channel. For the weir-orifice unit (Figure 4.1), the discharge through the weir or the orifice is obtained by adding the flow through the infinitesimal flow layers. In so doing, the local coefficient of discharge C_d for the layers of both weir or orifice depends only on the depth h of the layer below the free surface and the mean velocity V_1 in the main channel.

In developing an expression for the flow through a rectangular lateral weir-orifice unit, the following assumptions are made:

1. The bed of the main channel is horizontal.
2. The flow in the main channel upstream of the unit is subcritical.
3. The length L of the unit in the direction of flow is limited to the width B of the main channel ($L/B \leq 1$).
4. For flow through a sharp-edged weir-orifice unit the flow in the approach channel is uniform.
5. The normal velocity component of the jet through any flow layer is equal to $\sqrt{2gh}$, in which h is the depth of the layer below the free surface.

Based on the above assumptions, and noting that for each layer the effective flow area is

C_d L dh, the expression for the total theoretical discharge Q_{wo} through the weir-orifice unit can be written as

$$Q_{wo} = \int_{h_2}^{h_1} (C_d V_j L\, dh) + \int_0^{h_3} (C_d V_j L\, dh) \qquad (4.5)$$

in which,

$$h_1 = Y_u - S \qquad \text{(Figure 4.1)} \qquad (4.6)$$

$$h_2 = Y_u - (S+a) \qquad \text{(Figure 4.1)} \qquad (4.7)$$

and

$$h_3 = Y_u - (S+a+b) \qquad \text{(Figure 4.1)} \qquad (4.8)$$

In Equation (4.5), V_j is the velocity of the outflow jet and C_d is the local discharge coefficient of the infinitesimal layers of flow: In section 2.2, V_j and C_d were defined respectively as

$$V_j = \frac{V_1}{\eta} = \sqrt{V_1^2 + 2gh} \qquad (4.9)$$

and

$$C_d = C_0 + C_1\eta^2 + C_2\eta^4 + C_3\eta^6 \qquad (4.10)$$

in which η is the jet velocity ratio and C_0, C_1, C_2, and C_3 are constants given in Equations (2.5) to (2.8).

Expressing h in terms of η using Equation (4.9) and substituting for C_d in Equation (4.5) using Equation (4.10), the expression for Q_{wo} can be rewritten as

$$Q_{wo} = \frac{V_1^3}{g} L \left\{ \int_{\eta_2}^{\eta_1} \left(C_0 + C_1 \eta^2 + C_2 \eta^4 + C_3 \eta^6 \right) \frac{1}{\eta^4} \, d\eta + \int_{\eta_3}^{1} \left(C_0 + C_1 \eta^2 + C_2 \eta^4 + C_3 \eta^6 \right) \frac{1}{\eta^4} \, d\eta \right\} \quad (4.11)$$

in which

$$\eta_1 = \left(\frac{V_1^2}{V_1^2 + 2g(Y_u - S)} \right)^{1/2} = \left(\frac{1}{1 + \frac{2}{F_1^2}\left(1 - \frac{S}{Y_u} \right)} \right)^{1/2} \quad (4.12)$$

$$\eta_2 = \left(\frac{V_1^2}{V_1^2 + 2g[Y_1 - (S + a)]} \right)^{1/2} = \left(\frac{1}{1 + \frac{2}{F_1^2}\left(1 - \frac{(S + a)}{Y_u} \right)} \right)^{1/2} \quad (4.13)$$

and

$$\eta_3 = \left(\frac{V_1^2}{V_1^2 + 2g[Y_u - (S + a + b)]} \right)^{1/2} = \left(\frac{1}{1 + \frac{2}{F_1^2}\left(1 - \left(\frac{(S + a + b)}{Y_u} \right) \right)} \right)^{1/2} \quad (4.14)$$

Integrating Equation (4.11) yields

$$Q_{wo} = \frac{V_1^3 L}{g} \left\{ f\left(\eta_1 \cdot \frac{L}{B} \right) - f\left(\eta_2 \cdot \frac{L}{B} \right) + f\left(\eta_3 \cdot \frac{L}{B} \right) \right\} \quad (4.15)$$

in which

$$f\left(\eta_1 , \frac{L}{B}\right) = \left(1 - \eta_1^3\right)\left(\frac{C_3}{3} + \frac{C_0}{3\eta_1^3}\right) + \left(1 - \eta_1\right)\left(\frac{C_1}{\eta_1} + C_2\right) \quad (4.16)$$

$$f\left(\eta_2 , \frac{L}{B}\right) = \left(1 - \eta_2^3\right)\left(\frac{C_3}{3} + \frac{C_0}{3\eta_2^3}\right) + \left(1 - \eta_2\right)\left(\frac{C_1}{\eta_2} + C_2\right) \quad (4.17)$$

and

$$f\left(\eta_3 , \frac{L}{B}\right) = \left(1 - \eta_3^3\right)\left(\frac{C_3}{3} + \frac{C_0}{3\eta_3^3}\right) + \left(1 - \eta_3\right)\left(\frac{C_1}{\eta_3} + C_2\right) \quad (4.18)$$

The discharge in the main channel upstream of the weir-orifice unit at a depth $Y = Y_u$ is given by Equation (4.19) as

$$Q_1 = B\, Y_u V_1 \quad (4.19)$$

in which, V_1 is the mean velocity in the approach channel at a depth $Y = Y_u$.

Using Equations (4.25) and (4.19), the discharge ratio Q_r for the weir-orifice unit can be written as

$$\frac{Q_{wo}}{Q_1} = Q_r = F_1^2 \frac{L}{B}\left| f\left(\eta_1 , \frac{L}{B}\right) - f\left(\eta_2 , \frac{L}{B}\right) + f\left(\eta_3 , \frac{L}{B}\right)\right| \quad (4.20)$$

in which,

$$F_1^2 = \frac{V_1^2}{g Y_u} \quad (4.21)$$

From Equation (4.20), the desired flow distribution ratio Q_r can be obtained by a proper choice of the geometric parameters S, a, and b and the hydrodynamic parameter such as F_1.

4.2.3 Simulated Variation of Discharge Ratio Q_r with Depth Y

Figure 4.3(a) shows a rectangular lateral weir-orifice unit. For such a unit, Figure 4.3(b) shows the simulated variation of the discharge ratio Q_r with the depth as the flow depth Y increases from a minimum value of $Y = S + a$ to a maximum value of $Y = Y_U = S + a + b + h_3$. In the region AP [Figure 4.3(a)], the discharge ratio increases as the depth of flow increases from $Y = S$ to $Y = S + a$. At this level of flow depth, Equation (4.4) gives the functional dependence of the discharge ratio with the pertinent parameters. For values of $Y > S + a$, the discharge ratio Q_r increases further, reaches a peak value of $Q_r = Q_{ro} + \Delta Q_r$ at an arbitrary point say G [Figure 4.3(a)] and then decreases for higher values of Y until $Y = S + a + b$. In Figure 4.3(b), ΔQ_r denotes the maximum deviation between the discharge ratio at the arbitrary point G and the design value of $Q_r = Q_{ro}$. At the flow depth $Y = S + a + b$, Equation (4.3) denotes the functional relationship between the discharge ratio and the main parameters. When the value of Q_r reaches the design value of Q_{ro} at an arbitrary point D' [Figure 4.3(a)], a weir may be provided to augment the outflow from the orifice portion of the unit such that $Q_r = Q_{ro} + \Delta Q_r$. As shown in Figures 4.3(a) and 4.3(b), at point F, $Q_r = Q_{ro} + \Delta Q_r$ when the flow depth is at

a level $Y = Y_U = S + a + b + h_3$. The total discharge through the unit is the summation of the discharge through the orifice and the weir portions of the unit. For $Y = S + a + b + h_3$, Equation (4.2) gives the functional dependence of the discharge ratio with the relevant geometric and flow parameters.

4.3 EXPERIMENTAL SET-UP

Experiments were conducted using three lateral weir-orifice models to verify the expressions developed for the discharge ratio. The sill height S, the orifice height a and the distance b (between the orifice and the weir) were the main geometric variables (Table 4.1). Figure 4.4 shows the schematic layout of the experimental set-up. The main channel was 6.0m long and was made of steel plates. The sides of the channel were painted to render it smooth. Plexiglass sheets were used to form sharp-edged weir-orifice units. The model was located at section T (Figure 4.4) which was 360cm from the inlet to the channel. A system of baffles and screens were used in the stilling basin to reduce the large-scale turbulence at the inlet section and to ensure a uniform distribution of velocity across the inlet section. Standard V-notches were used to measure the flow rate from the channel and the lateral weir-orifice unit. Water surface elevations and flow depths at three locations in the flume were measured with a point gage whose least count was 0.1mm. In all the experiments conducted, the nappes were fully ventilated.

4.4 ANALYSIS OF RESULTS

The results of the series of experiments conducted to verify the expressions developed for the discharge ratio Q_r are shown in Figures 4.5 to 4.8. For all the series, Table 4.1 provides the details of the geometry of the lateral weir-orifice unit. Figure 4.5 shows the

variation of the discharge ratio Q_{ro} with the Froude number F_1 when the flow depth is at the top of the orifice. For this case, the theoretical discharge ratio can be obtained using Equation (4.22).

$$Q_{ro} = \frac{Q_o}{Q_1} = F_1^2 \frac{L}{B} \left| f\left(\eta_1 \, , \frac{L}{B}\right) \right| \qquad (4.22)$$

Here, F_1 and S/a are respectively the main hydrodynamic and geometric parameters.

Figure 4.6 shows the variation of the maximum deviation ΔQ_r in the discharge ratio with the Froude number F_1. For this situation, the geometric parameters S/a, and b/a and the flow (hydrodynamic) parameter F_1 are the important variables. The plots of the variation of Q_r and h_3/a with the Froude number F_1 are shown in Figures 4.7 and 4.8 respectively. The theoretical values of Q_r were obtained using Equation (4.20).

In all the figures presented, the experimental results obtained (within the practical range of Froude numbers) appears to validate the predicted relationships within acceptable deviations.

Finally, for the discharge through the lateral weir-orifice unit, Figure 4.9 shows the correlation between the predicted discharge and the actual discharge [Equation (4.15)] for the three models tested. The correlation appears to be fairly reasonable.

4.5 SUMMARY AND CONCLUSION

In the operation of water and wastewater treatment plants, some of the more fundamental problems are short term variations in hydraulic loading caused by the variable

inflow rates. Quite often , plants designed for a specified design flow are forced to handle the much greater flow rates at some period of the day. This practice can be inefficient in many ways. For example, the flow distributed to individual process basins may be more than the designed ratio at some period and less at other periods. It is therefore desirable to use a flow distribution device which is able to maintain a good performance within the anticipated range of discharge ratios. To this end, a lateral weir-orifice unit can be used effectively to distribute the flow evenly to the process basins over a range of incoming discharges when the ratio of outflow to inflow is expected to stay within a prescribed range of Q_r to $Q_{ro} + \Delta Q_r$.

The ratio Q_r between the outflow through a lateral orifice-weir unit and the inflow in the main channel can be expressed as a function of the geometric parameters L/B, S/a, b/a, h_3/a and the Froude number F_1 of the approach flow. Experimental data obtained over a range of Froude numbers appear to validate the proposed relationships such as Equation (4.20) within acceptable deviations.

CHAPTER V

DISCHARGE CHARACTERISTICS OF RECTANGULAR SHARP-CRESTED WEIRS

5.1 INTRODUCTION

The rectangular sharp-crested weir is of fundamental importance in the laboratory and in the field because it seves as a simple and accurate device for flow measurement in open channels. Although this is the primary purpose of the weir, the fact that it serves as a control section in an open channel cannot be overlooked. Furthermore, the lower surface profile of the nappe if adequately ventilated forms the basis for designing the spillways of hydraulic structures.

For many years the problem of flow over rectangular sharp-crested weirs has been subject to several investigations (Table 5.1). Among the many problems about the rectangular sharp-crested weir are those related to the discharge coefficient and the upper and lower surface profiles of the nappe. Investigations on these two aspects have been made for relatively high weirs, leading to the establishment of the relationship between the discharge coefficient C_{de} and H/W (Table 5.1), where H is the upstream head causing flow over a weir of height W. For studies related to the curvature of the streamlines, the pressure and velocity distributions within the nappe region of the weir, limited experimental results are available in literature.

Kandaswamy and Rouse [37] investigated the discharge characteristics of rectangular sharp-crested weirs located at the end of an open channel. On the basis of their experimental results, they identified two distinct ranges for the flow over rectangular sharp-crested weirs in terms of H/W: The range of H/W between 0 and 10 was

arbitrarily designated as the weir range while the range of H/W between 10 and ∞ was arbitrarily designated as the sill range. Kindsvater and Carter [38] presented a comprehensive solution for the weir discharge characteristics based on the experimental results of other investigators and dimensional analysis. For potential flow over rectangular sharp-crested weirs, several theoretical solutions have been proposed [16, 30, 43, 67]. McNown [43] obtained some numerical results for the flow over a relatively high sharp-crested weir through relaxation techniques. Strelkoff [67] solved the problem of two-dimensional irrotational flow over a sharp-crested weir by conformal transformations. He presented some numerical results which yielded the discharge coefficient for some values of H/W. Han and Chow [30] investigated the characteristics of relatively high sharp-crested weirs through hodograph transformation. They presented some results for the pressure distribution on the upstream face of the weir and within the nappe region. Rajaratnam and Muralidhar [50] provided detailed pressure and velocity profiles within the nappe region and at the weir crest of rectangular sharp-crested weirs. For the range of H/W covered in their tests ($0.19<H/W<8.57$), their results showed that pressure and velocity distribution at a location in the nappe region can be described by a single curve. Sarginson [63] reported the scale effects which can be attributed to surface tension and viscosity for flow over a rectangular sharp-crested weir.

For flow over a rectangular free-overall ($H/W = \infty$), several investigations have been made [28, 49, 61]. Hager [28] theoretically obtained the relation for the brink depth ratio using the momentum and energy principles. Rajaratnam and Muralidhar [49] used the momentum theory to study the characteristics of flow over a rectangular free-overfall for three conditions of the channel slopes.

As stated earlier, existing expressions relating the discharge coefficient C_{de} with H/W for the flow over rectangular sharp-crested weirs rely either on experimental results

only or on the theory of ideal flows. In the present study, the characteristics of rectangular sharp-crested weirs used widely as a hydraulic structure for flow measurement in open channels is presented. A simple theory based on the experimental data related to the surface profile, pressure distribution and velocity distribution in the nappe region of the weir and generalized momentum relationship is proposed to predict the relationship between the discharge coefficient C_{de} and H/W. An alternate analytical method based on the velocity distributions within the nappe section is also presented. The predicted results based on the two approaches are compared with the present result and some existing experimental results.

5.2 THEORETICAL ANALYSIS

5.2.1 Functional Relationship

For the flow over a rectangular sharp-crested weir shown in Figure 5.1, the functional relationship between the discharge Q and the main parameters can be written as

$$Q = \phi_5 \left(B, W, H, g, \rho, \mu, \sigma \right) \qquad (5.1)$$

in which B = width of the main channel; W = weir height above channel bed; H = upstream head causing flow; g = acceleration due to gravity; ρ = density of water; μ = dynamic viscosity of water; and σ = surface tension of water.

Applying the theory of dimensions to Equation (5.1) and re-arranging of the parameter yields Equation (5.2).

$$\frac{Q}{BH\sqrt{gH}} = \phi_6 \left(\frac{H}{W}, \frac{H\sqrt{gH}}{\mu/\rho}, \frac{H\sqrt{g}}{\sqrt{\sigma/\rho}} \right) \qquad (5.2)$$

The discharge over a rectangular sharp-crested weir can be written as

$$Q = C_{de}\, H B \sqrt{gH} \qquad (5.3)$$

where C_{de} denotes the discharge coefficient of the weir. Using Equation (5.3) and recognising that the second and third terms in Equation (5.2) represent the Reynolds number and Webber number respectively, Equation (5.2) can be rewritten as

$$\frac{Q}{BH\sqrt{gH}} = C_{de} = \phi_7\left(\frac{H}{W},\ R_e,\ W_e\right) \qquad (5.4)$$

Assuming that the effects of the two relevant fluid properties represented by R_e and W_e are negligible especially at high flow heads [63], Equation (5.4) can be rewritten in terms of H/W only. Thus,

$$\frac{Q}{BH\sqrt{gH}} = C_{de} = \phi_8\left(\frac{H}{W}\right) \qquad (5.5)$$

An alternate expression for the discharge coefficient can also be written in terms of the area ratio H/(H+W) as

$$\frac{Q}{BH\sqrt{gH}} = C_{de} = \phi_9\left(\frac{H}{H+W}\right) \qquad (5.6)$$

The functional relationships given in Equations (5.5) and (5.6) are developed to show the dependence of the discharge coefficient C_{de} on the parameters H/W and H/(H + W).

5.2.2 Traditional Equation for Weir Discharge Coefficient

For the flow over a rectangular sharp-crested weir shown in Figure 5.1, one of the earliest theoretical approaches to determine the discharge was put forward by Weisbach [75] in 1855. Reasoning that, as the nappe was ventilated above and below, atmospheric pressure must exist at all points within the nappe, Weisbach [75] suggested that the velocity U_y at a point y above the weir crest (Figure 5.1) would be given by Equation (5.7) as

$$U_y = \sqrt{2g\,(H_1 - y)} \qquad (5.7)$$

in which, H_1 is the total head above the weir crest. The discharge per unit width q passing through the weir is

$$q = \int_0^H U_y\, dy = \int_0^H \sqrt{2g(H_1 - y)}\, dy \qquad (5.8)$$

Integrating Equation (5.8) yields

$$q = \frac{2}{3}\sqrt{2g}\left[(H_1)^{3/2} - (H_1 - H)^{3/2} \right] \qquad (5.9)$$

Implicit in the development of Equation (5.9) is a further incorrect assumption that the velocity vector U_y is horizontal at all points within the nappe. Once again, if one ignores the drawdown of the water surface as the flow approaches the weir crest, the assumption could be made that

$$H_1 = \left(H + \frac{U_o^2}{2g}\right) \tag{5.10}$$

where U_o is the mean velocity in the approach channel. Using Equation (5.10), the discharge per unit width q given by Equation (5.9) can be rewritten as

$$q = \frac{2}{3}\sqrt{2g}\left[\left(H + \frac{U_o^2}{2g}\right)^{3/2} - \left(\frac{U_o^2}{2g}\right)^{3/2}\right] \tag{5.11}$$

To obtain the discharge coefficient C_{de} of the weir, an alternate expression for q can be written as

$$q = \frac{2}{3}\sqrt{2g}\, C_{de}\, H^{3/2} \tag{5.12}$$

in which,

$$C_{de} = \left[\left(1 + \frac{U_o^2}{2gH}\right)^{3/2} - \left(\frac{U_o^2}{2gH}\right)^{3/2}\right] \tag{5.13}$$

Equation (5.13), traditionally used by various experimenters, involves a time consuming trial and error solution for C_{de}. Furthermore, as shown in Figure 5.1 the flow pattern, pressure distribution, and velocity distribution within the nappe and its approach clearly shows that the assumptions implied in Equation (5.13) are incorrect.

In the following section, an approach based on the momentum relationship and the experimental data related to the water surface profile, pressure distribution, and velocity distribution within the nappe region is used to obtain an expression for the discharge coefficient C_{de} of the weir.

5.2.3 Determination of C_{de} using the Momentum Relationship

Figure 5.2(a) shows a rectangular sharp-crested weir located at the downstream end of a smooth, horizontal, rectangular channel. The upper and lower surfaces of the nappe are fully ventilated. As shown in Figure 5.2(a), as the flow approaches the weir, the meanvelocity of flow increases considerably leading to a strong vertical curvature of the flow profile. Consequently, the pressure distribution within the regions of the nappe will be non-hydrostatic. In the interior of the nappe region at Section EF [Figure 5.2(a)], denoting the maximum location of the lower nappe profile, the pressure is not atmospheric.

Considering the control volume ABEFJ [Figure 5.2(b)] bounded by the upstream control surface AJ and the downstream control surface EF, the following assumptions are made in applying the momentum relationship to the weir flow:

1. The pressure distribution at the upstream control section AJ [Figure 5.2(b)] is hydrostatic.
2. The momentum and kinetic energy coefficients at section AJ have the value of unity.
3. The boundary shear forces along the solid surface AB [Figure 5.2(b)] are not significant.

For the control volume ABEFJ, the momentum relationsbips in a direction parallel to the channel bed can be written as

$$P_A - P_B - P_f = \frac{\gamma}{g}\left(q\,(\beta V_B - V_0)\right) \qquad (5.14)$$

in which P_A = pressure force at the upstream section AJ; P_B = pressure force at the downstream section EF; P_f = pressure force on the face of the weir of height W; γ = specific weight of water; g = acceleration due to gravity; q = discharge per unit width of weir; β = momentum coefficient at section EF (obtained experimentally); V_B = velocity at the downstream section EF; and V_0 = mean velocity at the upstream section AJ. The left hand side of Equation (5.14) can be written as

$$P_A - P_B - P_f = \left(\frac{\gamma}{2}(H+W)^2\right) - K_B\left(\frac{\gamma}{2}(Y_0)^2\right) - K_f\left(\frac{\gamma}{2}(H+W)^2\right) \qquad (5.15)$$

in which K_B = pressure coefficient at section EF; and K_f = pressure coefficient at the weir face. Both coefficients denote the deviation of the pressure from the hydrostatic distribution. Using Equation (5.15), Equation (5.14) can be rewritten as

$$\left(\frac{\gamma}{2}(H+W)^2\right) - K_B\left(\frac{\gamma}{2}(Y_0)^2\right) - K_f\left(\frac{\gamma}{2}(H+W)^2\right) = \frac{\gamma}{g}\left(q\,(\beta V_B - V_0)\right) \qquad (5.16)$$

The continuity relationship between the two control sections AJ and EF can be written as

$$q = V_0(H+W) = V_B(Y_0) \qquad (5.17)$$

in which Y_o is the depth of flow at section EF [Figure 5.2(b)]. Using Equation (5.17), the momentum relationships given by Equation (5.16) can be rewritten as

$$(1 - K_f)\left((H+W)^2\right) - K_B\left(Y_o^2\right) = \frac{2q^2}{g}\left(\frac{\beta}{Y_o} - \frac{1}{H+W}\right) \qquad (5.18)$$

Substituting for q in Equation (5.18) using Equation (5.12) and simplifying the resulting expression yields

$$(1 - K_f)\left(\frac{H+W}{H}\right)^2 - K_B\left(\frac{Y_o}{H}\right)^2 = \frac{16}{9} C_{de}^2\left(\frac{\beta H}{Y_o} - \frac{H}{H+W}\right) \qquad (5.19)$$

Equation (5.19) can be further simplified to yield

$$C_{de} = \frac{3}{4}\left(\frac{\left(\frac{1+\frac{H}{W}}{\frac{H}{W}}\right)^2\left(1 - K_f\right) - K_B\left(\frac{Y_o}{H}\right)^2}{\left(\frac{\beta}{\frac{Y_o}{H}}\right) - \left(\frac{\frac{H}{W}}{\left(1+\frac{H}{W}\right)}\right)}\right)^{1/2} \qquad (5.20)$$

In Equation (5.20), the discharge coefficient C_{de} of the weir is expressed in terms of the parameter H/W. The values of Y_o/H, K_B and K_f are obtained from the experimental results and their dependence on H/W will be discussed in a subsequent section.

An alternate method of determining the discharge coefficient C_{de} of the weir based on direct integration of the velocity distribution at section EF [Figure 5.2(a)] is presented

below.

5.2.4 Determination of C_{de} Using the Velocity Distribution

In Figure 5.2(c), let V(y) represent the horizontal component of the velocity vector V at a point y above point E [Figure 5.2(c)]. Also let ϕ represent the angle of inclination of the streamline at elevation y at section EF with the horizontal. The discharge per unit width q over the weir can be written as

$$q = \int_0^{Y_o} \vec{V} \cos\phi \, dy = \int_0^{Y_o} \alpha V(y) \, dy = Y_o \alpha \int_0^1 V(y) \, d\left(\frac{y}{Y_o}\right) \qquad (5.21)$$

in which Y_o = depth of flow at section EF; and dy = thickness of an infinitesimal flow element at section EF [Figure 5.2(c)]. Let U_o be the reference velocity at an upstream section of the weir and is defined by Equation (5.22)

$$U_o = \sqrt{2gH} \qquad (5.22)$$

Then, dividing both sides of Equation (5.21) using Equation (5.22) one gets

$$\frac{q}{\sqrt{2gH}} = Y_o \left(\int_0^1 \alpha \left(\frac{V(y)}{U_o}\right) d\left(\frac{y}{Y_o}\right) \right) \qquad (5.23)$$

Replacing q in Equation (5.22) using Equation (5.12) yields

$$\frac{2}{3} C_{de} \left(\frac{H\sqrt{2gH}}{\sqrt{2gH}}\right) = Y_o \left(\int_0^1 \alpha \left(\frac{V \cos\phi}{U_o}\right) d\left(\frac{y}{Y_o}\right) \right) = Y_o \left(\int_0^1 \alpha \left(\frac{V(y)}{U_o}\right) d\left(\frac{y}{Y_o}\right) \right) \qquad (5.24)$$

Equation (5.24) can be further simplified to yield an expression for the discharge coefficient C_{de} of the weir as

$$C_{de} = \frac{3}{2}\frac{Y_o}{H}\left(\int_0^1 \alpha\left(\frac{V(y)}{U_o}\right)\, d\left(\frac{y}{Y_o}\right)\right) \qquad (5.25)$$

Defining

$$A^* = \left(\int_0^1 \left(\frac{V(y)}{U_o}\right)\, d\left(\frac{y}{Y_o}\right)\right) \qquad (5.26)$$

in which, A^* is an integrand denoting the area under the non-dimensional velocity distribution curve at section EF and α' is the velocity distribution coefficient. Thus, Equation (5.26) can be rewritten as

$$C_{de} = \frac{3}{2}\alpha'\left(\left(\frac{Y_o}{H}\right)A^*\right) \qquad (5.27)$$

To calculate the discharge coefficient C_{de} for a given H/W, the values of Y_o/H, α' and A^* have to be obtained from experiments. The variation of Y_o/H with H/W and the values of α' and A^* for the ranges of H/W considered will be discussed later.

5.3 EXPERIMENTAL SET-UP

Experiments were conducted in a rectangular, horizontal mild steel flume 60cm wide, 61cm deep and 6.0m long whose sides were painted to obtain a smooth finish. The layout of

the apparatus is shown in Figure 5.3. The sharp-crested weir models were made of plexiglass plates 6.4mm thick with a bevelled edge. Table 5.2 indicates the range of variables considered.

The weir models were fixed at the downstream end of the flume. Proper stilling devices consisting of baffles, perforated screens, and floats were used at the inlet section to ensure a smooth flow in the channel free from large-scale turbulence.

A five-hole pitot sphere (pitch probe) of diameter 9.5mm was used to measure the total head at section EF and section KL. The horizontal limb of the pitot sphere [48] was tilted through a vertical angle to register equal pressures in the piezometers connected to the two holes at the top and bottom of the central hole. In this position, the central hole of the pitot sphere records the maximum total head reading. For each location y along the vertical plane at section EF, the value of the angle ϕ corresponding to the maximum total head reading was recorded. It may be added that the maximum total head measured by the pitot-sphere was found to be identical to the total head recorded by a 3.0mm diameter five-hole directional probe (United Sensors - DC-125-12-CD). The static pressure distribution in the curvilinear region of the nappe was measured using a screw-driver shaped static probe of 3mm external diameter [50, 58]. This probe, when oriented along the direction of flow, was found to be insensitive to the curvature of the flow in the vertical plane. The difference between the static head and the total head readings yielded the velocity head. The pressure and velocity distributions were measured at section EF and KF [Figure 5.2]. Static pressure tappings along the centerline of the channel bed and on the weir face were connected to a manometer board to record the pressure variations along the channel floor and on the weir face. The water manometers registered the pressure to the nearest mm. Near the top of the weir, the static holes of diameter 0.8mm were spaced at 3.2mm centers. For the weir heights of 3.2mm and 6.4mm respectively, the spacing was

reduced to 1.6mm and the hole size was 0.4mm in diameter. Where the pressure differences were very small, an inclined manometer with an inclination of 1 in 6 was used to record the pressure head. The water surface levels were taken along the centerline of the channel with a precision point gage which could be read to the nearest 0.1mm. The discharge over the weir was measured using a Standard V-notch. The head over the V-notch was always in excess of 50mm and the maximum error in the discharge measurement is estimated to be 3%.

5.4 ANALYSIS OF RESULTS

5.4.1 Water Surface Data

Figure 5.4 shows the composite plot of water surface profile of the upper and lower nappes of the weir for the arbitrary designation of the weir range ($0<H/W<10$). A similar plot of the water surface profiles for some values of H/W within the sill range ($10\leq H/W<\infty$) is shown in Figure 5.5. As has long been realized, the head H over the weir must be measured at a considerable distance upstream of the weir crest where the drawdown effects are negligible. For the experimental results obtained in the present study, a distance of about 2H is recommended for values of H/W within the weir range. Similarly, for the sill range, a value of 3H is recommended. Figures 5.6 and 5.7 show the variation of the depth ratio h_e/H and Y_o/H with H/W. Here, h_e is the depth of flow at the weir crest section KL [Figure 5.2(c)]. It can be seen that the maximum values of h_e/H and Y_o/H appear to occur at $H/W \equiv 10$. An earlier study by Kandaswamy and Rouse [37] indicated also that the elevation of the water surface of the upper and lower nappes attain maximum values at H/W close to 10. In Figure 5.7, the end depth ratio corresponding to the rectangular free-overfall ($H/W = \infty$) is found to be 0.723.

5.4.2 Pressure Distribution Data

For analysing the pressure distribution at section KL [Figure 5.2(c)], if p is the pressure level at a normal distance y above the weir crest, the variation of $p/\gamma h_e$ with y/h_e for the weir and sill ranges of flow are shown in Figures 5.8 and 5.9 respectively. It can be seen that the pressure distribution increases continuously towards the hydrostatic line as H/W increases up to 2.0 and then for any further increase in H/W in the weir range, it decreases towards the free-overfall curve ($H/W = \infty$). For values of H/W within the sill range, Figure 5.9 shows the variation of the non-dimensional pressure $p/\gamma h_e$ with y/h_e. It can be seen that the pressure distribution at the weir crest for values of H/W with the sill range ($10 \leq H/W < \infty$) continuously moves towards the distribution corresponding to the free-overfall.

Figures 5.10 and 5.11 show the non-dimensional pressure distribution at section EF [Figure 5.2(c)]. The pressure level p at a point y has been made dimensionless by the overall depth of flow Y_o at section EF. Figure 5.10 shows the variation of $p/\gamma Y_o$ with y/Y_o at section EF for values of H/W within the weir range ($0 \leq H/W < 8.57$). It can be seen that the non-dimensional pressure distribution at section EF is a unique function of y/Y_o. Based on the non-dimensional pressure distributions at section EF shown in Figures 5.10 and 5.11, the values of the pressure coefficient K_B for the weir and sill ranges of flow are found to be 0.445 and 0.279 respectively.

Figures 5.12 to 5.17 show the non-dimensional pressure distribution on the face of the weir for some typical values of H/W within the weir and sill ranges of flow. For some values of H/W within the sill range ($10 < H/W < \infty$) the sum of H and W is close to 0.667

H_1. Here, the sum of H and W can be replaced by the critical depth d_c. The values of the pressure coefficient K_f on the front face of the sharp-crested weir were obtained with the help of Figures 5.12 to 5.17. The variation of the computed values of K_f with H/W is shown in Figure 5.18.

5.4.3 Velocity Distribution Data

Figures 5.19 to 5.22 show the plots of the variation of the non-dimensional velocity distribution at sections KL and EF for the weir and sill ranges of flow. The velocity distribution is made dimensionless by the reference velocity U_o ($=\sqrt{2gH}$). At section KL or EF, the depth at any point y in the vertical plane is rendered dimensionless by the overall depth of flow at that section.

At section KL, for the values of H/W within the weir and sill ranges, Figures 5.19 and 5.20 indicate the variation of the non-dimensional horizontal component of the velocity vector with y/h_e. Here, h_e is the depth of flow at section KL. It can be seen that the velocity distribution moves towards the free overfall curve as H/W is increased.

Similarly, at section EF, for values of H/W within the weir and sill ranges of flow, Figures 5.21 and 5.22 show the variation of the non-dimensional horizontal component of the velocity vector with y/Y_o. It can be seen from Figure 5.21 that a single curve describes the velocity distribution at section EF for all H/W values with in the weir range. A similar observation can also be made for the values of H/W within the sill range (Figure 5.22). Based on the non-dimensional velocity distributions at section EF shown in Figures 5.21 and 5.22, the values of A^* [Equation (5.26)] for the weir and sill ranges of flow were

obtained as 0.730 and 0.773 respectively. Furthermore, the values of the momentum coefficient β at section EF were obtained as 1.024 and 1.043 for the weir and sill ranges of flow respectively. Also the values of α' were obtained as 1.19 and 1.25 for the weir and sill ranges of flow respectively.

Finally, if ϕ is the angle of inclination of the velocity vector V with the horizontal plane at section EF, Figure 5.23 shows the variation of ϕ with y/Y_o for values of H/W within the weir and sill ranges of flow.

5.4.4 Discharge Coefficient of the Weir C_{de}

For any given value of H/W, the pressure distributions were compared with the hydrostatic distribution to compute the values of K_f and K_B. Using these values together with the values of α', β, A^* and Y_o/H in Equations (5.20) and (5.27), the discharge coefficient C_{de} of the weir was obtained for the entire range of H/W. Figures 5.24 and 5.25 show the plot of the variation of C_{de} with H/W based on Equation (5.20) and Equation (5.27) respectively. The experimental data obtained in the present study, the existing experimental study of Kandaswamy and Rouse [37] and the theoretical results of Strelkoff [68] are also plotted in figures 5.24 and 5.25 for qualitative comparison. From Figure 5.24 and Figure 5.25, it can be seen that the maximum value of C_{de} occurs at H/W ≈10. Furthermore, for the range 8.0<H/W<15, a smooth curve describes the predicted values of C_{de}. A comparison of the values of C_{de} obtained using the two analytical methods show a maximum deviation of about 10%.

5.5 CONCLUSIONS

Through the combination of detailed experimental measurements and a simplified theoretical approach, information is at hand for the coefficient of discharge of a sharp-crested weir as the weir parameter H/W varies from zero to infinity. Based on the results obtained, it can be concluded that the discharge coefficient C_{de} for flow over a rectangular sharp-crested weir in the weir range ($0<H/W<10$) and in the sill range ($10<H/W<\infty$) can be related to the weir parameter H/W. The proposed dependence of C_{de} on H/W based on the two expressions presented and the experimentally derived quantities is in close agreement with the present experimental results and other published results [37, 67].

CHAPTER VI

HYDRAULIC CHARACTERICTICS OF THE SQUARE-EDGED AND ROUND-NOSED RECTANGULAR BROAD-CRESTED WEIR

6.1 INTRODUCTION

The necessity for gaging structures to measure flows more accurately and economically has increased signficantly with recent developments in water resource planning. The on-site determination of the flow rate is often the key to the operation efficiency of a water resources project. This is particularly true of irrigation and hydro-power developments which require that the flow rate be measured accurately. However, measurement of flowing water is also important in other areas such as water supply projects, river engineering and hydrologic studies on water-sheds.

Hydraulic structures such as rectangular broad-crested weirs with square-edged or round-nosed upstream corner are widely used in field and laboratory channels for open channel flow measurement. The weir has an advantage over other flow metering structures such as the rectangular sharp-crested weir because of its good range of discharge and high modular limit. Rounding the upstream corner of the square-edged rectangular broad-crested weir increases the discharge coefficient and renders the weir to be less sensitive to silt deposition at the upstream face. In addition, rounding the upstream corner prevents or eliminates the separation pocket at the upstream corner of a square-edged weir which is a primary source of energy loss.

In recent years, the characteristics of flow over rectangular broad-crested weirs has been the subject of many investigations [6, 19, 24, 31, 46, 65] aimed at evolving emperical expressions for the discharge coefficient of the weir. Woodburn [78] carried out a comprehensive experimental study of the characteristics of rectangular broad-crested

weirs under free-flow and submerged flow conditions. On the basis of boundary layer theory, Hall [29] derived an expression for the free-flow characteristics of a square-edged rectangular broad-crested weir. He verified his expressions using the experimental data of Bazin [6]. For the flow over a rectangular broad-crested weir with an inclined upstream face Bos [9], Clemmens [13] and Replogle [59] provided simplified design procedures based on rating tables covering a wide range of flow variables. For the flow over a broad-crested weir with a round-nosed upstream corner, Harrison [31] derived an equation for the discharge coefficient based on critical flow theory including an allowance for the boundary layer development on the weir crest. Singer [65] showed conclusively that the weir length and weir height has a noticeable effect on the discharge coefficient of square-edged rectangular broad-crested weirs. Doeringsfeld and Baker [19] developed a theoretical expression for the discharge over a square-edged rectangular broad-crested weir based on the momentum relationship. They assumed a hydrostatic distribution of pressure on the upstream face of the weir thereby neglecting the effects of the approach velocity. Based on earlier studies, Tracy [71] presented a comprehensive review of the characteristics of flow over rectangular broad-crested weirs with square-edged, round-nosed and inclined upstream corners.

In the study presented in this chapter, the hydraulic characteristics of the square-edged weir is obtained considering the non-hydrostatic distribution of pressure on the front face of the weir. For the round-nosed rectangular broad-crested weir, the effect of rounding the upstream corner of the weir on the flow characteristics is examined. An expression for the weir discharge coefficient is obtained based on the momentum principle. Experimental results obtained within the broad-crested weir range ($0.25<H/P<1.20$) are presented to validate the relationships proposed.

6.2 THEORETICAL CONSIDERATIONS

6.2.1 Functional Relationships

For the free-flow over a smooth broad-crested weir with a square-edged or round-nosed upstream corner (Figure 6.1) a functional relationship linking the main flow variables may be expressed as follows

$$\phi_{10}(q, H, L_w, P, R, g, \upsilon) = 0 \qquad (6.1)$$

in which q = discharge over the weir per unit width; H = upstream measured head; L_w = length of the weir; P = height of the weir; R = radius of the upstream corner of the weir [Figure 6.1(b)]; g = acceleration due to gravity and υ = kinematic viscosity of the liquid. Dimensional analysis followed by a regrouping of the pertinent parameters leads to the familiar form of Equation (6.2).

$$C_{dw} = \frac{q}{\frac{2}{3} H \sqrt{\frac{2}{3} gH}} = \phi_{11}\left(\frac{P}{L_w}, \frac{H}{P}, \frac{R}{P}, \frac{H\sqrt{gH}}{\upsilon}\right) \qquad (6.2)$$

In Equations (6.1) and (6.2), ϕ_{10} and ϕ_{11} are unknown functions and C_{dw} is the dimensionless weir discharge coefficient. Noting that the fourth term on the right-hand side of Equation (6.2) represents the Reynolds number (R_e) which incorporates the scale effects, Equation (6.2) can also be rewritten in a slightly different form as

$$C_{dw} = \phi_{12}\left(\frac{P}{L_w}, \frac{H}{P}, \frac{R}{P}, R_e\right) \qquad (6.3)$$

In Equation (6.3), coefficient of discharge of the weir is shown as a function of the Reynolds

number $R_e = (H\sqrt{gH})/\upsilon$ and a number of independent length ratios involving the head and the physical dimensions of the weir. The main objective of the test is to determine the effects of rounding the upstream top corner on C_{dw}. Equation (6.3) indicates that one can study the effect of H/P and R/P on C_{dw} by conducting tests on weir models for which P/L_w is held constant since R_e will have very large values and hence will not affect C_{dw} very much.

In the following section, an expression for the discharge coefficient C_{dw} of the weir is presented.

6.2.2 Theoretical Weir Discharge Coefficient

Based on the momentum relationships, a general expression for the weir discharge coefficient can be developed. For the free-flow over the broad-crested weir, the following assumptions are made:

1. The channel bed and the weir crest are both horizontal.
2. The effects of boundary shear among the control surfaces AB and CD [Figure 6.1(c)] are negligible.
3. For the control volume ABCDEF [Figure 6.1(c)] the pressure distribution is hydrostatic at the upstream section (AF) and the downstream section (DE) where the flow is parallel for $0.083 \leq H/L_w \leq 0.40$ (or $0.25 < H/P < 1.20$).
4. The velocity coefficient at the control sections (AF and DE) is unity.

For the control volume, applying the momentum equation in a direction parallel to the channel bed yields

$$P_1 + M_1 = F_p + P_3 + M_3 \qquad (6.4)$$

in which, P_1 = external pressure force acting at the upstream section AF; M_1 = momentum rate at the upstream section; F_p = external pressure force acting on the downstream section DE; and M_3 = momentum rate at the down stream section (DE). At section DE, the flow lines are nearly parallel for the range of H/P considered. At the upstream and downstream sections AF and DE respectively.

$$P_1 = \frac{\gamma}{2}\left(H + P\right)^2 B \qquad (6.5)$$

and

$$P_3 = \frac{\gamma}{2}\left(d_3\right)^2 B \qquad (6.6)$$

In which, B = width of the main channel; d_3 = depth of flow at section DE and γ = specific weight of fluid. The external force on the weir face F_p can be written as

$$F_p = K_p \frac{\gamma}{2}\left(P\left(2H + P\right)\right)B \qquad (6.7)$$

For the weir face, K_p is a coefficient which accounts for the deviation of pressure from hydrostatic distribution.

The momentum rates at the two control sections AF and DE are respectively,

$$M_1 = \frac{\gamma}{g}(Q_w\ V_1) \qquad (6.8)$$

and

$$M_3 = \frac{\gamma}{g}(Q_w\ V_3) \qquad (6.9)$$

in which, V_1 and V_3 are the mean velocities at the control sections AF and DE respectively and Q_w is the discharge over the weir. Using Equations (6.5) to (6.9), Equation (6.4) can be rewritten as

$$\frac{\gamma}{2}(H+P)^2\ B + \frac{\gamma}{g}(Q_w\ V_1) = K_p\frac{\gamma}{2}\left(P(2H+P)\right)B + \frac{\gamma}{2}(d_3)^2B + \frac{\gamma}{g}(Q_w\ V_3) \qquad (6.10)$$

The equation of continuity for the two control sections considered can be written as

$$V_1(H+P)\,B = V_3 d_3\,B = Q_w \qquad (6.11)$$

Using Equation (6.11) in Equation (6.10) and further simplification yields

$$(H+P)^2 - d_3^2 - K_p P(2H+P) = \frac{2Q_w^2}{gB^2}\left(\frac{1}{d_3} - \frac{1}{(H+P)}\right) \qquad (6.12)$$

For a rectangular broad-crested weir, assuming critical flow on the weir crest with no boundary layer development, the expression for the discharge can be written as

$$Q_w = C_{dw} \frac{2}{3} HB\sqrt{\frac{2}{3} gH} \qquad (6.13)$$

in which Q_w is the discharge over the weir and C_{dw} is the coefficient of discharge. Using Equation (6.13) in Equation (6.12), and further manipulation of the resulting expression yields Equation (6.14) as

$$C_{dw} = \left(\frac{27}{16} \left(\frac{\left(\frac{H+P}{H}\right)^2 - \left(\frac{d_3}{H}\right)^2 \cdot K_p \left(\frac{2H+P}{H}\right) \frac{P}{H}}{\left(\frac{H}{d_3}\right) \cdot \left(\frac{H}{H+P}\right)} \right) \right)^{1/2} \qquad (6.14)$$

The values of K_p and d_3/H can be determined experimentally for a given weir geometry (P/L_w = constant) to obtain the discharge coefficient C_{dw}.

6.3 EXPERIMENTAL SET-UP

In order to check the validity of the proposed relationships, experiments were carried out in a horizontal glass-walled tilting flume (Figure 6.2) 6.0m long, 25.4cm wide and 51 cm high. The floor of the flume consisted of polished stainless steel plates. The broad-crested weir models (Table 6.2) were made of plexiglass. The weir models were fixed at a distance of 300cm from the inlet section. At this section, stilling arrangements were provided to ensure uniform flow in the channel with very low turbulence. Pressure taps 0.8mm in diameter were fixed normal to the weir surface along the center-line of the model at intervals of 2.54cm. These pressure taps were more closely spaced near the corners of the model. Surface pressures were recorded on a bank of water manometers. The surface pressures were meassured to the nearest mm. The water surface levels were recorded along the center-line of the flume

for each test run and the discharge over the weir was measured with a standard V-notch. The water surface levels and the head over the V-notch were measured with precision point gages whose least count was 0.3mm. The upstream flow head was measured at a location 4H from the upstream face of the weir. Here, H is the maximum upstream head for each series of tests. In all the tests conducted under free-flow conditions, the nappes at the down stream end of the weir were fully ventilated.

For submerged flow tests, the tailwater level was adjusted to obtain the necessary submergence ratio S_h. Furthermore, for each weir and test run, the submergence limit was also noted.

6.4 ANALYSIS OF RESULTS

6.4.1 Water Surface Profiles

Figures 6.3 to 6.9 show the non-dimensional water surface profiles for the broad-crested weir models tested. The upstream head H (Figure 6.1) causing flow is used to render the depth of flow Y' reckoned above the weir crest and the distance X_w measured from the upstream end of the weir (inset Figure 6.3) dimensionless. From these profiles, it can be seen that the approximate limit where the surface profile is horizontal is at a location 3H from the upstream face of the weir. This is the nearest location where a gage well should be located to measure the upstream head correctly. For the range of H/L_w covered in the test ($0.083<H/L_w\leq 0.400$, Table 6.2), the water surface profile for each weir model (represented by R/P) decreases from the upstream face of the weir and reaches a constant value at the downstream end. Furthermore, in the range $0.25\leq H/P\leq 1.20$ tested, a region of nearly parallel flow existed over the weir crest. The depth

corresponding to parallel flow and the depth at the brink are denoted as d_3 and d_o respectively. Similarly, the depth corresponding to the critical flow at a point on the weir crest is denoted as d_c (computed based on the assumption of parallel flow on the weir). Figures 6.10(a), 6.10(b) and 6.10(c) show the plots of the variation of d_3/H, d_o/H and d_c/H respectively with R/P. These ratios increase with an increase in R/P. These trends are consistent with the decrease in the energy losses associated with increased rounding of the upstream corner of the models. Additional details on the effects of rounding the upstream corner of a square-edged broad-crested weir are discussed in a subsequent section.

6.4.2 Pressure Profiles

Figures 6.11 to 6.15 show the distribution of the static pressure heads along the front and top surfaces of the weir models. For models with round-nosed upstream corner, the radial static pressure heads registered normal to the curved surface are resolved into its two components (inset Figure 6.12) and plotted. In all the pressure head profiles presented (Figures 6.11 to 6.15), it can be seen that the pressure head deviates from a hydrostatic distribution towards the upstream top corner of the weir. Furthermore, it can also be seen that on the top upstream edge of the weir crest the pressure head levels decrease sharply. This may be attributed to the downward acceleration of the flow in the proximity of the upstream crest region.

For all the models tested, the horizontal force on the front vertical portion of the model was added to the horizontal component of the radial force on the curved surface to determine the total horizontal force F_p in Equation (6.7). This in turn yielded the pressure coefficient

K_p given in Equation (6.14).

6.4.3 Weir Discharge Coefficient: Free-flow

For free-flow conditions over the broad-crested weir [Figures 6.1(a) and 6.1(b)], tests made to determine the coefficient of discharge C_{dw} involved the measurement of the upstream head H and the discharge Q_w. The experimental and predicted values of the discharge coefficient C_{dw} for a given head were obtained using Equations (6.13) and (6.14) respectively. Figures 6.16 to 6.21 show the variation of C_{dw} with H/P for the models tested. In general, it can be observed that the agreement between the predicted value of the discharge coefficient [Equation (6.14)] and the actual value (based on the measured discharge) is fairly reasonable.

6.4.4 Discharge Reduction with Submergence

For the flow over a rectangular broad-crested weir, the discharge Q_m under submerged flow conditions can be obtained by the introduction of the drowned flow reduction factor $f\ (= Q_m/Q_w)$ which is the ratio of the discharge Q_m under submerged conditions to the dischrage Q_w that would have passed over the weir under a head equal to the upstream head H. Accordingly,

$$f = \frac{Q_m}{Q_w} = \frac{Q_m}{\frac{2}{3} H\sqrt{\frac{2}{3} gH}\, C_{dw}} \qquad (6.26)$$

Figures 6.22 to 6.25 show the variation of f with the submergence ratio H_2/H for some of the weir models tested.

6.4.5 Effects of Rounding the Upstream Corner

The radius R of the upstream corner of a round-nosed rectangular broad-crested weir influences the flow characteristics in two ways as outlined by Harrison [31]: first, if it is too sharp ($R/P \rightarrow 0$), separation of flow can occur at upstream corner of the crest; second, the depth of flow at the upstream end of the weir is influenced by the radius.

The effect of rounding the upstream corner of the square-edged broad-crested weir is to increase the coefficient of discharge by eliminating or reducing flow separation at the crest which is a primary source of energy loss. For the flow over a broad-crested weir with rounded upstream corner, it has been suggested [31, 78] that the discharge coefficient C_{dw} increases due to the reduction of flow separation as R/H_{max} is increased up to 0.11. Here, H_{max} is the maximum value of the upstream total head H_1 for which the flow over the weir crest is parallel. It was also stated that C_{dw} did not increase significantly when R/H_{max} was increased beyond 0.11. To further analyse the results of the present investigation and to show the effects of rounding the upstream corner of the weir on the flow characteristics, the following classifications based on the degree of rounding of the upstream corner are considered:

1. The weir is 'slightly rounded' ($0 \leq R/P \leq 0.094$), if the rounding of the upstream corner is very small and it does not affect the flow characteristics such as water surface profile, pressure profile and weir discharge coefficient.

2. The weir is 'moderately rounded' ($0.094 \leq R/P < 0.250$), if the rounding of the upstream corner is considerable and it reduced flow separation and is also effective in increasing the discharge coefficient.
3. The weir is 'well-rounded' ($0.250 \leq R/P \leq 1.0$), if flow separation is essentially eliminated and the discharge coefficient has attained the highest value. Further rounding beyond $R/P = 0.250$ does not alter the flow characteristics.

On the basis of the above classifications of the weir in terms of R/P, the data obtained in the present study are replotted and shown in Figures 6.26 to 6.29. Figure 6.26 shows the non-dimensional water surface profiles for the three groups of R/P mentioned above. Figure 6.27 shows the static pressure profiles along the periphery of the model for a typical value of H/P. The static pressures is non-dimensionalised by the variable (H_1+P), while the distance X' measured from A' to G'(inset, Figure 6.27) is non-dimensionalised by the total peripheral length of the model from A' to G . The variation of the discharge coefficient C_{dw} with H/P for the three groups of R/P is shown in Figure 6.28. Furthermore, Figure 6.29 shows the variation of the flow reduction factor f with the submergence ratio H_2/H. In general, it can be seen that the three classifications of the weir in terms of the parameter R/P which represents the degree of rounding of the upstream corner of the weir holds good for both free-flow and submerged flow conditions.

6.5 SUMMARY AND CONCLUSIONS

The characteristics of flow over a square-edged and round-nosed rectangular broad-crested weir is shown to depend on the parameters H/P and R/P. An expression for the discharge coefficient is obtained based on the momentum principle. Based on the relative effects of R/P on the flow characteristics, three classifications are identified to denote the

degree of rounding the upstream corner of the weir. The following conclusions can be drawn on the basis of results obtained :

1. The water surface and static pressure profiles are determined principally by the radius R of the upstream corner, the crest length L_w, and the weir height P. The discharge coefficient C_{dw} depends on H/P and R/P.
2. Rounding the upstream corner with $0.000 < R/P \leq 0.094$ seems to have no effect on the nature of weir flow. Rounding in this range of R/P tends to behave as a minor perturbation to the weir geometry. The weir discharge coefficient C_{dw} increases gradually as R/P increases from 0.094 to 0.250.
3. The upstream gaging position for both square-edge and round-nose broad-crested weir should be located at a distance 2H upstream from the front face of the weir.
4. Submerged flow over the weir can be obtained by the introduction of the drowned flow reduction factor f in the broad-crested weir range ($0.25 \leq H/P \leq 1.20$) as shown in Figure 6.29.

CHAPTER VII

AERODYNAMIC FORM DRAG COEFFICIENT OF SQUARE-EDGED AND ROUND-NOSED RECTANGULAR BROAD-CRESTED WEIRS

7.1 INTRODUCTION

The flow of an incompressible fluid past a rectangular prismatic body attached to a plane boundary is of great importance for such diverse application as wind loads on man-made structures, the estimation of head loss due to obstructions in air ducts, the resistance of isolated roughness elements, and the hydraulic resistance of rectangular weirs. In most of these applications, rounding of the upstream corner of the body improves the flow characteristics significantly. For example, in Chapter VI of this thesis, it was observed that rounding the upstream corner of a square-edged rectangular broad-crested weir increases the discharge coefficient significantly.

Several researchers have conducted experiments using a two-dimensional rectangular bodylocated in midstream of finite or infinite extent. As a result, a considerable amount of useful information has been gathered with regards to the form drag coefficient of the body. The flow characteristics past surface-mounted rectangular bodies cannot be directly inferred from existing data related to centrally-mounted bodies as the oscillations of the flow in the near wake of surface-mounted bodies are not present.

Delany [17], Lindsey [41] and Rhosko [60] have studied the form drag characteristics of various centrally-mounted rectangular bodies. Vickery [73] investigated the fluctuating lift and drag forces acting on surface-mounted rectangular prisms in turbulent flow. Bergelles [8], Good [25] and Laneville [39] performed detailed experimental studies of the flow past various two-dimensional surface-mounted objects. Lee [40], and Ramamurthy [52]

provided experimental data on the drag coefficient of rectangular and triangular prisms at various blockage ratios. The effects of rounding the edges of several centrally-mounted rectangular bodies on the form drag coefficient has been reported by Hoerner [33].

In the present study, an experimental investigation of the aerodynamic drag coefficient of surface-mounted rectangular broad-crested weirs was carried out. Experimental data was collected to study the effect of rounding the upstream corner of a square-edged rectangular broad-crested weir on the form drag coefficient.

7.2 NEED FOR AERODYNAMIC STUDIES OF RECTANGULAR BROAD-CRESTED WEIR

The phenomenon of flow over a rectangular broad-crested weir is greatly influenced by both the non-linear conditions at the free surface and by gravity. These conditions include the presence of surface waves and a longitudinal pressure gradient. Under field conditions, the associated Reynolds number is relatively high and does not significantly influence the flow characteristics. Consequently, in the simulation of free surface flow models only the Froude criterion is considered. However, dimensional analysis of the flow over a broad-crested weir shows that the discharge over the weir is a function of not only the geometric parameters and Froude number but also the Reynolds number (section 6.2). Nevertheless, in laboratory or model studies of the flow over rectangular broad-crested weirs the role of Reynolds number is often under estimated or omitted in the analysis. For flow over a rectangular broad-crested with a free-surface, the improvement of the discharge coefficient may be due to the significant reduction in the form drag experienced by the weir as a result of rounding the upstream corner. Thus, one may conclude that the form drag and hence the Reynolds number are also important parameters in the analysis of flow over the weir. It can be deduced from flow modelling criteria that either the scale ratio of the model has to be unity or the kinematic viscosity of the modelling fluid has to be changed

suitably if both Froude number and Reynolds number are to be satisfied simultaneously. However, it is difficult to adopt either of these conditions in the laboratory. A possible alternative is to design and conduct the experiments deliberately eliminating the effects of one of the parameters (e.g. Froude number). In the wind tunnel, the free-surface effects are neglected and the flow is governed entirely by the Reynolds criterion. Thus, the wind tunnel test may provide the necessary data on the role played by the viscous forces.

7.3 EXPERIMENTAL APPARATUS AND PROCEDURE

The experiments were carried out in a low speed, open circuit wind tunnel (Figure 7.1) with a test section 25.4cm wide and 50.8cm long. The height H_T of the test section was 35.6cm. The air speed in the test section could be varied from 6 m/sec to 36 m/sec. Turbulence reducing screens were installed upstream of a contraction cone which preceeded the test section. The basic models chosen for the study were rectangular broad-crested weirs whose height P was 10.16cm. The surface-mounted models spanned the width of the test section and were 30.5cm long (Figure 7.2). The models were made of plexiglass sheets. Ten models with upstream corner radii ranging from 0.00 to 10.16cm were tested (Table 7.1). Pressure taps 0.8mm in diameter were provided to measure the distribution of surface pressure along the centerline of the model. The taps were generally spaced at 12.7mm centers along the upstream face and the spacing was reduced to 3.2mm near the corners. The models created a blockage of 28.6%. The pressure level along the model was recorded with the help of an inclined airflow manometer which read pressures to the nearest 0.1mm of water. The velocity at the entrance to the test section was obtained with the help of a pitot tube-micro-manometer combination. This in turn was correlated to the mean undisturbed velocity U_∞ at the test section. The free stream turbulence level in the test

section was close to 1% and the boundary layer thickness δ in the test section was very thin ($\delta/P \approx 0.03$). The maximum value of δ in the test section was estimated as 3mm. During each test run, the air temperature and barometric pressure were recorded. The air temperature recorded was accurate to the nearest 0.25°C. Graphical integration of the pressure distributions on the front and rear faces of the models yielded the value of the form drag coefficient C_D.

7.4 ANALYSIS OF RESULTS

7.4.1 Pressure Distribution Data

Figures 7.3, 7.4 and 7.5 show the effect of the radius of the upstream corner of the weir model on the surface pressure distribution. The pressure distribution coefficient C_p is defined by Equation (7.1).

$$C_p = \frac{p - p_\infty}{\frac{1}{2}\left(\rho \ U_\infty^2\right)} \qquad (7.1)$$

in which p = surface pressure at any point on the model; p_∞ = stagnation pressure recorded at an upstream section from the model; ρ = density of air; and U_∞ = velocity of main stream. In Figures 7.3, 7.4 and 7.5, the distance X is measured from the lower edge of the front face of the model and is rendered dimensionless by the overall peripheral length L_m of the model. Figure 7.3 represents a composite plot of the surface pressure distributions for the models with $R/P \leq 0.008$. The degree of rounding for these models is considered to be slight. A perusal of Figure 7.3 shows that the pressure distribution on the surface of the

model is unaffected by the rounding of the top corner when $R/P \leq 0.008$. The Reynolds number R_{eD} (based on the diameter of the upstream corner) does not seem to have any effect on the surface pressure distribution in the range $750 \leq R_{eD} \leq 3400$. Clearly, for each model, flow separates at the upstream top edge and the corresponding velocity of the separating streamline $U_s = 1.41\ U_\infty$. The pressure distributions on the top surface of these models (Figure 7.3) does not clearly indicate the existence of a reattachment point as there is no distinct location where a significant pressure rise occurs. Figure 7.4 shows the non-dimensional surface pressure distributions around models with medium degree of rounding of the upstream corner. These models ($0.047 \leq R/P \leq 0.250$) register a lower form drag coefficient C_D compared to the rectangular model ($R/P = 0$) and the models with very small upstream corner radii (Figure 7.3). This is due to the severe increase in the negative pressures on portions of the front face and only a slight decrease in the pressures on the rear face. Hence, rounding the upstream corner of the model is effective for $R/P \geq 0.047$.

Figure 7.5 shows the non-dimensional surface pressure distributions for models with large R/P values. For these models, the flow accelerates as it moves towards the junction of the upstream face and the top surface and gives rise to negative pressures on the front face. When the rounding of the upstream corner is large ($R/P > 0.25$), the negative pressures on portions of the front face decrease while the corresponding pressures on the rear face increase slightly resulting in a constant value of the form drag coefficient C_D.

Figure 7.6 shows a composite plot of the non-dimensional pressure coefficients on the front and rear faces of the models. The vertical distance y along the front and rear faces of the model is normalised by the overall height P of the model. For some of the models

tested, Figures 7.7 to 7.11 show the individual plot of the pressure distribution of the front face and rear face of the model based on the data given in Table 7.2. In general, on the front face of the model, a maximum value of the pressure coefficient (Cpu) is attained at a height between 0.4P and 0.60P from the tunnel wall. This location is close to the point of reattachment of the streamline separating from the tunnel wall upstream of the model. A value between 0.45P and 0.65P is reported by Good [25] for the height of reattachment of the separating streamline for surface-mounted normal plates. In Figure 7.6, it can be seen that the rear pressure coefficient C_{pb} is uniform along the height of the models tested. The value of C_{pb} increases from -1.80 to -1.00 as R/P increases from 0.00 to 1.00. The variation of C_{pu} (+ve and -ve) with R_{eD} and the corresponding variation of $-C_{pb}$ with R_{eD} are shown in Figures 7.12a, 7.12b and Figure 7.13 respectively.

7.4.2 Form Drag Coefficient C_D & C_{DC}

The pressure distributions on the front and rear faces of the models tested were graphically integrated to obtain the form drag coefficient C_D. The value of C_D for each test run is given in Table 7.2. For the models tested (Table 7.1), Figure 7.14 shows the variation of the average form drag coefficient C_D with R/P. In Figure 7.14, the variation of C_{DC} with R/P for centrally-mounted rectangular bodies with rounded upstream corners reported by Delany [17] are also shown. However, a comparison with the data obtained in the present study should be made on a qualitative basis as the effects of blockage and surface-mounting were absent in his tests. Figure 7.15 shows the variation of C_D with Reynolds number R_{eD}. The diameter D of the upstream corner of the model was considered

to be the appropriate dimension to form the Reynolds number for studying the variation of C_D with R_{eD}.

An attempt was made to apply a correction for blockage for the present test data. For the slightly rounded models ($R/P \leq 0.008$), the drag coefficient C_{DC} corrected for blockage can be obtained using the method suggested by Awbi [4]. According to Awbi [4] .

$$C_{DC} = C_D\left(1 - 1.76\,\frac{P}{H_T}\right) \qquad (7.2)$$

in which P = height of the model; and H_T = height of the wind tunnel test section. For the present case,

$$C_{DC} = 0.503\,C_D \qquad (7.3)$$

For round-nosed rectangular models for which the upstream corner radii were large ($0.344 \leq R/P \leq 1.0$) one should expect the flow velocity in the gap betwen the model and the tunnel wall to be $(H_T/(H_T-P))\,U_\infty = 1.4U_\infty$ which corresponds to a value of about $C_p = -1.0$ (Figure 7.5) in the top rear portion of the models. Using the gap velocity U_g as the characteristic velocity for blockage correction, one gets

$$C_{DC} = C_D\left(\frac{U_g}{U_\infty}\right)^2 = C_D\left(\frac{(H_T - P)}{H_T}\right) = 0.510\;C_D \qquad (7.4)$$

The procedure outlined above was used earlier [40, 52] to provide blockage corrections for centrally-mounted cylinders.

For models with intermediate radii, a linear interpolation was used to estimate C_{DC}. Thus for $0.047 \leq R/P \leq 0.250$,

$$C_{DC} = 0.507\, C_D \qquad (7.5)$$

Figure 7.16 shows the variation of C_{DC} with R_{eD} along with the curves related to centrally mounted circular and rectangular cylinders reported by Delany [17]. It can be seen from Figure 7.16 that the characteristic dip in C_{DC}, near $R_{eD} = 1.5 \times 10^5$, is qualitatively similar to the dips in the form drag coefficient near $R_{eD} = 1 \times 10^6$ and 3×10^5 respectively for the centrally-mounted circular cylinders and rectangular cylinders [17].

Finally, Figure 7.17 shows the plot of the variation of the discharge coefficient C_{dw} of a rectangular broad-crested weir (investigated in Chapter VI) with the parameter R/P.

A comparison of the variation of C_{dw} with R/P to the variation of C_{DC} with R/P supports an earlier classification of the broad-crested weir based on R/P.

7.5 SUMMARY AND CONCLUSIONS

The study presented in this chapter dealt with the aerodynamic form drag coefficient of two-dimensional surface-mounted rectangular (square-edged, and round-nosed rectangular broad-crested weirs). Measurement of the surface pressures were carried out in order to clarify the effect of rounding the upstream corner of the broad-crested weir on the form

drag coefficient. Based on the experimental results obtained over a practical range of Reynolds numbers, the following conclusions can be drawn:

1. The effect of rounding the upstream corner of a rectangular broad-crested weir was not found to be effective in reducing the form drag coefficient C_{DC} for $R/P \leq 0.008$. For $0.047 < R/P < 0.250$, a significant reduction in C_{DC} is achieved. Furthermore, for the range $0.344 < R/P \leq 1.000$, no significant decrease in C_{DC} was registered.
2. A noticeable difference exists between the variation of the form drag coefficient C_{DC} with R/P for surface-mounted and centrally-mounted rectangular bodies. Hence, the flow characteristics of surface-mounted rectangular bodies (such as weirs) cannot be directly inferred from existing data related to similar centrally-mounted bodies.
3. The dependence of C_{DC} on the Reynolds number R_{eD} for surface-mounted rectangular bodies is qualitatively similar to the dependence of C_{DC} on R_{eD} for centrally-mounted rectangular bodies.
4. The increase in the discharge coefficient C_{dw} of rectangular braod-crested weirs as a result of rounding the upstream corner is strikingly similar to the decrease in the form drag coefficient C_{DC}.

CHAPTER VIII

SUMMARY AND CONCLUSIONS

8.1 SUMMARY AND CONCLUSIONS

This study is concerned with the characteristics of some hydraulic structures commonly used for the control and measurement of flows in open channels. Hydraulic control structures investigated include the trapezoidal lateral weir, the rectangular lateral orifices and the rectangular lateral weir-orifice unit. Flow measurement structures considered include the rectangular sharp-crested weirs and the rectangular broad-crested weirs.

In Chapter II, the hydraulic characteristics of trapezoidal lateral weirs is presented. For the weir, an expression for the mean discharge coefficient is developed based on an existing two-dimensional lateral outlet model (hydrodynamic model). From the theoretical and experimental results obtained, it is shown that the mean discharge coefficient is highly dependent on the geometric parameter L/B and the hydrodynamic parameter related to the Froude number in the approach channel. It is also shown that the mean discharge coefficient decreases when the parameter L/B is decreased.

Chapter III deals with the hydraulic characteristics of relatively large rectangular lateral orifices. Again, the two-dimensional lateral outlet model is adopted to develop a general expression for the discharge coefficient of the orifice. The discharge coefficient of the orifice is found to be influenced by various geometric and hydrodynamic variables: namely, the sill height S of the orifice, the height a of the orifice, and the Froude number of flow in the main channel. It was also found that the width ratio L/B emerges as an important parameter and the discharge coefficient of the orifice depends on L/B.

In Chapter IV, the characteritics of flow through a rectangular lateral weir-orifice unit is studied. The formulation of the basic equation for the discharge through the outlet is essentially similar to that of Chapter III but with a lateral weir located above the orifice being the additional outlet. The effects of the geometric and flow variables on the total outflow through the unit (weir-orifice) are investigated. It is shown that by an optimal choice of the structural and flow parameters, the lateral weir-orifice unit can be properly designed to ensure an outflow which is a prescribed percentage of the inflow. The practical application of the weir-orifice unit as an efficient device for flow equalization and control in an open channel is also examined.

Chapter V is devoted to the study of the flow over a rectangular sharp-crested weir. A generalized expression for the discharge coefficient of the weir is developed based on the experimental data related to the water surface profiles, the pressure distributions, and the velocity distributions at a section within the nappe region. It is found that the discharge coefficient of the weir depends primarily upon the parameter H/W. It has also been found that the curve describing the variation of the discharge coefficient C_{de} with the parameter H/W attains a peak value when $H/W \cong 10$. The curves describing the variation of the ratios h_e/H and Y_o/H with H/W are also presented. These curves attain peak values at $H/W \cong 10$ as does the curve for coefficient of discharge.

Chapter VI deals with the characteristics of a rectangular broad-crested weir as a simple and efficient device for the measurement of open channel flow. It is found that the discharge coefficient of the weir depends on the ratio parameters H/P and R/P. The parameter R/P denotes the ratio between the radius R of the upstream corner and the weir height P. Based on the ratio R/P, it is found that rounding the upstream corner with $0.00 \leq R/P \leq 0.094$ seems to have no effect on the flow characteristics. Hence, rounding in this range tends to behave as a minor perturbation to the weir geometry. The weir

discharge coefficient C_{dw} in-creases gradually as the parameter R/P is increased beyond 0.094.

It is found that the water surface and static pressure profiles for the free-flow over the weir are determined by the radius R of the upstream corner. It is also observed that for accurate measurement of the upstream head, the stilling or gage well should be located at a distance 3H to 4H form the upstream face of the weir.

A study on the submergence limit of the broad-crested weir reveals some important findings. The submergence limit is found to depend on the degree of rounding of the upstream corner. The discharge over the weir under submerged conditions can be obtained by the introduction of the drowned flow reduction factor f into the equations developed for the free-flowing weir.

In Chapter VII the study on the characteristics of rectangular broad-crested weir is extended to include the effect of rounding the upstream corner of the weir on the form drag coefficient C_D. Based on the experimental results obtained, it is found that rounding the upstream corner of the square-edged rectangular broad-crested weir for $R/P \leq 0.008$ does not significantly reduce the drag coefficient. It has also been found that for the range $0.047 < R/P \leq 0.250$, a significant reduction in the form drag coefficient was realized. The variation of the form drag coefficient C_D on the Reynolds number R_{eD} is qualitatively similar to the variation of C_D with R_{eD} for rectangular cylinders.

A comparison of the results obtained in the two closely related but independent investigations presented in Chapters VI and VII reveals some interesting findings. The increase in the discharge coefficient C_{dw} of the rectangular broad-crested weir with increased rounding of the upstream corner is qualitatively similar (and may be attributed) to the decrease in the form drag coefficient C_D of a similar weir. The pressure distribution

data obtained from the wind tunnel test provides an indication of the range of negative pressures that might develop in a broad-crested weir under submerged flow conditions.

8.2 RECOMMENDATIONS FOR FUTURE STUDY

Research on an optimal design of hydraulic structures to control and measure the flow in an open channel is at present a growing field of activity. Improved understanding of the relationship between the channel regime and the control and measurement structure is vital and requires additional research. However, as a direct extension to the work of this thesis, the following additional studies could be performed:

1. Work on the flow through rectangular lateral orifices can be expanded to examine the performance of multiple lateral orifices located in the side of rectangular channel with varying bottom widths.
2. An in-depth study on the nature and effects of boundary layer on the characteristics of rectangular broad-crested weirs may supplement the present study.

REFERENCES

[1] Ackers, P., "A Theoretical Consideration of Side Weirs as Storm Water Overflows". Proceedings of the Institution of Civil Engineers, London, England, Vol, 6, 1957, pp. 250-269.

[2] Ackers, P., White, W.R., Perkins, J.A., and Harrison, A.J.M., Weirs and Flumes for Flow Measurement, John Wiley & Sons, New York, 1978.

[3] Allen, J.W., "The Discharge of Water over Side Weirs in Circular Pipes", Proceedings of the Institution of Civil Engineers, London, England, Vol. 6, 1957, pp. 270-287.

[4] Awbi, H.B., "Wind-Tunnel-Wall Constraint on Two-Dimensional Rectangular- Section Prisms," Journal of Industrial Aerodynamics, Vol. 3, 1978, pp. 285- 306.

[5] Bazin, H., "Experiences Nouvelles sur L'ecoulement en Deversoir", Annales des Pont et Chaussees, October, 1888, pp. 393.

[6] Bazin, H., "Experiences Nouvelles sur L'ecoulement en Deversoir," Annales des Pont et Chaussees, Vol. 7, Series 7, 1896, pp. 249-357.

[7] Benefield, L.D., Treatment Plant Hydraulics for Environmental Engineers, Prentice-Hall, Englewood Cliffs, New Jersey, 1984.

[8] Bergeless, G., and Athanassiadis, N., "The Flow Past a Surface-Mounted Obstacle," Journal of Fluid Engineering, ASME, Vol. 105, pp. 461-463.

[9] Bos, M.G., Replogle, J.A., and Clemmens, A.J., Flow Measuring Flumes for Open Channel Systems, John Wiley & Sons, Inc., New York, 1984.

[10] Camp, T.R., and Garber, S.D., "Dispersion Conduits," Journal of the Sanitary Engineering Division, ASCE, Vol. 94, No. SAI, Feb., 1968, pp. 31-39.

[11] Carballada, B.L., "Some Characteristics of Lateral Flow," Thesis presented to Concordia University, Montreal, Canada, in 1978, in partial fulfillment of the requirements for the degree of Docotor of Philosophy.

[12] Chao, J.L., and Trussell, R.R., "Hydraulic Design of Flow Distribution Channels," Journal of the Environmental Engineering Division, ASCE, Vol. 106, No. EE2, April, 1980, pp. 321-335.

[13] Clemmens, A.J., Replogle, J.A., and Bos, M.G., "Rectangular Measuring Flumes for Lines and Earthen Channels", Journal of Irrigation and Drainage Engineering, ASCE, Vol. 110, No. 2, June, 1984, p. 121-137.

[14] Coleman, G.S., and Smith, D., "The Discharging Capacity of Side Weirs," Selected Engineering Paper, No. 6, Institute of Civil Engineers, London, England, 1923.

[15] Collinge, V.K., "The Discharge Capacity of Side Weirs," Proceedings of the Institution of Civil Engineers, London, England, Vol. 6, 1957, pp. 288-304.

[16] Das-Daniel, A.J., and Ramadurgaiah, D., "Flow over Sharp-crested Rectangular Weirs," Irrigation and Power, Jan., 1966, pp. 55-61.

[17] Delany, N.K., and Sorensen, N.E., "Low Speed Drag on Cylinders of Various Shapes," Technical Note 3038, National Advisory Committee for Aeronaautics (NACA), Nov., 1953.

[18] De Marchi, G., "Essay on the Performance of Lateral Weirs," L'energia Elettrica, Milano, Italy, Vol. 11, Nov., 1934, pp. 849.

[19] Doeringsfeld, H.A., and Baker, C,L., "Pressure-Momentum Theory applied to the Broad-crested Weir," Transactions, ASCE, Vol. 106, 1941, pp. 934-969.

[20] El-Khashab, A., and Smith, K.V.H., "Experimental Investigation of Flow Over Side Weirs," Journal of the Hydraulics Division, ASCE, Vol. 102, No. HY9, Sept., 1976, pp. 1255-1268.

[21] Francis, J.B., Lowell Hydraulics Experiments, Little, Brown & Co., Lowell, Massachusetts, 1955.

[22] Frazer, W., "The Behaviour of Side Weirs in Prismatic Rectangular Channels," Proceedings of the Institution of Civil Engineers, London, England, Vol. 6, Feb., 1957, pp. 305-328.

[23] French, J.A., "Internal Hydraulics of Multiport Diffusers," Journal of Water Pollution Federation, Vol. 44, No. 5, May, 1972, pp. 782-795.

[24] Fteley, A., and Stearns, F.P., "Experiments on the Flow of Water over Weirs with Wide Crests", Transactions, ASCE, Vol. 12, 1983, pp. 86-95.

[25] Good, M.C., and Joubert, P.N., "The Form Drag of Two-Dimensional Bluff Plates Immersed in Turbulent Boundary Layers," Journal of Fluid Mechanics, Vol. 31, Part 3, 1065, pp. 547-582.

[26] Greve, F.W., "Flow of Water Through Circular, Parabolic and Triangular Vertical Notch-Weirs", Research Bulletin No. 40, Engineering Experimental Station, Purdue University, Lafayette, Indiana, March 1932.

[27] Gurevitch, M.I., The Theory of Jets in an Ideal Fluid, 1st Edition, Vol. 1, Pergamon Press, New York, 1966.

[28] Hager, W.H., "Hydraulics of Plane Free Overfall," Journal of Hydraulic Engineering, ASCE, Vol. 109, No. HY12, Dec., 1983, pp. 1683-1697.

[29] Hall, G.W., "Discharge Characteristics of Broad-Crested Weirs using Boundary Layer Theory," Proceedings of the Institution of Civil Engineers, London, England, Vol. 22, 1962, pp. 177-190.

[30] Han, T.Y., and Chow, W.L., "The Study of Sluice Gates and Sharp-Crested Weirs Through Hodograph Transformations," Journal of Applied Mechanics, ASME, Vol. 48, June 1981, pp. 229-234.

[31] Harrison, A.J.M., "The Streamlined Broad-Crested Weir," Proceedings of the Institution of Civil Engineers, London, England, Vol. 38, 1967, pp. 657-678.

[32] Henderson, F.M., Open Channel Flow, McMillan & Co., New York, 1966.

[33] Hoerner, S., Fluid Dynamic Drag, Published by the author, 1958

[34] Ippen, A.T., "Channel Transitions and Controls, Engineering Hydraulics", Chapter VIII, Rouse, H., Editor, John Wiley & Sons, Inc., New York, 1950, pp. 525-528.

[35] Jain, S.C., and Fischer, E.E., "Uniform Flow Over Skewed Side Weir," Journal of the Irrigation and Drainage Division, ASCE, Vol. 108, No. IR2, June, 1982, pp. 163-166.

[36] Kandaswamy, P.K., "Discharge Characteristics of Low Weirs and Sills," Thesis presented to the State University of Iowa, Iowa, 1957, in partial fulfillment of the degree of Master of Science.

[37] Kandaswamy, P.R., and Rouse, H., "Characteristics of Flow Over Terminal Weirs and Sills," Journal of the Hydraulic Division, ASCE, Vol. 83, No. HY4, August, 1957, pp. 1-13.

[38] Kindsvater, C.E., and Carter, R.W., "Discharge Characteristics of Rectangular Thin-Plate Weirs," Journal of the Hydraulic Division, ASCE, Vol. 83, No. HY6, Dec., 1957, pp. 1-36.

[39] Laneville, A., and Young, L., "Mean Flow Patterns around Two-Dimensional Rectangular Cylinders and their Interpretation," Journal of Wind Engineering and Industrial Aerodynamics, Vol. 14, 1983, pp. 387-398.

[40] Lee, P.M., "Boundary Layer Effects on Flow Past Bluff Bodies," Thesis presented to Concordia University, Montreal, Canada, 1973, in partial fulfillment of the requirements for the degree of Doctor of Engineering.

[41] Lindsey, W.F., "Drag of Cylinders of Simple Shapes," Technical Report No. 619, National Advisory Committee for Aeronautics (NACA), 1938.

[42] McNown, J.S., and Hsu, E.Y., "Application of Confirmal Mapping to Divided Flow," Proceedings of the Midwestern Conference on Fluid Dynamics, State University of Iowa, Reprints in Engineering, No. 96, 1951, pp. 143-154.

[43] McNown, J.S., Hsu, E.Y., and Yih, C.S., "Applications of the Relaxation Technique in Fluid Mechanics", Transactions, ASCE, Vol. 120, 1955.

[44] Mitchell, J.M., "On the Theory of Free Streamlines," Philosophical Transactions of the Royal Society, London, England, Vol. A181, 1890, pp. 389-431.

[45] Moore, W.L., and Morgan, C.W., "Hydraulic Jump at an Abrupt Drop," Transactions, ASCE, Vol. 124, 1959, pp. 507-524.

[46] Moss, W.D., "Flow Separation at the Upstream Edge of a Square-edged Broad-crested Weir," Journal of Fluid Mechanics, Vol. 52, Part 2, 1972, pp. 307-320.

[47] Nimo, W.H.R., "Side Spillways for Regulating Diversion Channels," Transactions, ASCE, Vol. 92, 1928, pp. 1561.

[48] Pope, A., and Rae, W.H., Wind Tunnel Testing, 2nd Edition, John Wiley & Sons, New York, 1984.

[49] Rajaratnam, N., and Muralidhar, D., "Characteristics of the Rectangular Free Overfall," Journal of Hydraulic Research, IAHR, Vol. 6, No. 3, 1968, pp. 233-258.

[50] Rajaratnam, N., and Muralidhar, D., "Pressure and Velocity Distributions for Sharp-crested Weirs," Journal of Hydraulic Research, IAHR, Vol. 9, No. 2, 1971, pp. 241-248.

[51] Ranga Raju, K.G., and Garde, R.J., "Resistance of an Inclined Plate Placed on a Plane Boundary in Two-Dimensional Flow," Journal of Basic Engineering, ASME, March, 1970, pp. 21-31.

[52] Ramamurthy, A.S., and Ng, C.P., "Effect of Blockage of Steady Force Coefficients," Journal of the Engineering Mechanics Division, ASCE, Vol. 99, 1973, pp. 755-760.

[53] Ramamurthy, A.S., and Carballada, B.L., "Uniformly Discharging Lateral Weirs," Journal of the Irrigation and Drainage Division, ASCE, Vol. 104, No. IR4, Dec. 1978, pp. 399-412.

[54] Ramamurthy, A.S., and Carballada, B.L., "Lateral Weir Flow Model," Journal of the Irrigation and Drainage Division, ASCE, Vol. 106, No. 1R1, March 1980, pp. 9-25.

[55] Rao, N.S.L., and Rao, M.V.J., "Characteristics of Hydrofoil Weirs," Journal of the Hydraulics Division, ASCE, Vol. 99, No. HY2, Feb., 1973, pp. 259-281.

[56] Rawn, A.M., Bowerman, F.R., and Brooks, N.H., "Diffusers for Disposal of Sewage in Seawater," Journal of the Sanitary Engineering Division, ASCE, Vol. 86, No. SA2, March 1960, pp. 65-105.

[57] Rehbock, T., discussion of "Precise Weir Measurements," by Schoder, E.W., and Turner, K.B., Transactions, ASCE, Vol. 93, 1929, pp. 1143-1162.

[58] Replogle, J.A., discussion of "The End Depth at a Drop in Trapezoidal Channels," by Diskin, M.H., Journal of the Hydraulics Division, ASCE, Vol. 88 No. HY2, March, 1962, pp. 162-165.

[59] Replogle, J.A., "Flumes and Broad-crested Weirs: Mathematical Modelling and Laboratory Ratings," Flow Measurement of Fluids, Dijstelberger, H.H., and Spencer, E.E., editors, North-Holland Publishing Co., Amsterdam, the Netherlands, 1978, pp. 321-328.

[60] Rhosko, A., "On the Drag and Shedding Frequency of Two-Dimensional Bluff Bodies," Technical Note 3169, National Avisory Committee for Aeronautics (NACA), July 1954, pp. 1-29.

[61] Rouse, H., "Discharge Characteristics of the Rectangular Free Overfall," Civil Engineering, ASCE, Vol. 6, No. 4, April, 1936, pp. 257-260.

[62] Rouse, H., and Arie, M., "Experiments on Two-Dimensional Flow over a Normal Wall," Journal of Fluid Mechanics, Vol. 1, 1956, pp. 129-141.

[63] Sarginson, E.J., "The Influence of Surface Tension on Weir Flow," Journal of Hydraulic Research, IAHR, Vol. 10, No. 4, 1972, pp. 431-466.

[64] Seitz, E., Die, S.I.A., "Normen fur Wassermessungen bie Durchfuhrung Von Abnahmererersuchen an Wasserkraft Maschinen," Schweiz, Bauz, Vol. 88, No. 1, 1926, pp. 17-18.

[65] Singer, J., "Square-edged Broad-crested Weir as a Flow Measurement Device," Water and Water Engineering, Vol. 28, No. 820, June, 1964, pp. 229-235.

[66] Smith, C.D., "Open Channel Water Measurement with the Broad-crested Weir," Annual Bulletin, International Commission on Irrigation and Drainage, 1958, pp. 46-51.

[67] Strelkoff, T., "Irrotational Flow Over Sharp-crested Weirs," thesis presented to the State University of Iowa, Iowa, 1962, in partial fulfillment of the requirements for the degree of Doctor of Philosophy.

[68] Strelkoff, T., "Solution of Highly Curvilinear Gravity Flows," Journal of the Engineering Mechanics Division, ASCE, Vol. 90, No. EM3, June, 1964, pp. 195-221.

[69] Subramanya, K., and Awasthy, S.C., "Spatially Varied Flow Over Side Weirs," Journal of the Hydraulics Division, ASCE, Vol. 98, No. HY1, Jan., 1972, pp. 1-9.

[70] Surya Rao, S., and Shukla, M.K., "Characteristics of flow Over Weirs of Finite Crest Width," Journal of the Hydraulics Division, ASCE, Vol. 97, No. HY11, Nov., 1971, pp. 1807-1815.

[71] Tracy, H.J., "Discharge Characteristics of Broad-crested Weirs," Circular 397, Geological Survey, United States Department of the Interior, Washington, 1957.

[72] Uyumaz, A., and Muslu, Y., "Flow Over Side Weirs in Circular Channels," Journal of Hydraulic Engineering, ASCE, Vol. III, No. 1, Jan., 1985, pp. 144-160.

[73] Vickery, B.J., "Fluctuating Lift and Drag on a Long Cylinder of Square Cross-Section in a Smooth and Turbulent Stream," Journal of Fluid Mechanics, Vol. 25, Part 3, 1966, pp. 481-494.

[74] Vigander, S., Elder, R.A., and Brooks, N.H., "Internal Hydraulics of Thermal Discharge Diffusers," Journal of the Hydraulics Division ASCE, Vol. 96, No. HY2, Feb., 1970, pp. 509-527.

[75] Weisbach, J., Die Experimental-Hydrauhk, Engelhardt, Freiber, Saxony, 1855.

[76] White, W.R., "Field Calibration of Flow Measuring Structures," Proceedings of the Institution of Civil Engineers, London, England, Vol. 59, Part 2, Sept., 1975, pp. 429-447.

[77] White, W.R., "Thin-Plate Weirs: An Investigation into Performance Characteristics," Report, INT, 152, Hydraulics Research Station, Wallington, U.K., 1975.

[78] Woodburn, J.G., "Tests on Broad-crested Weirs," Transactions, ASCE, Vol. 96, 1932, pp. 387-408.

[79] Yao, K.M., "Hydraulic Control for Flow Distribution," Journal of the Sanitary Engineering Division, ASCE, Vol. 98, No. SA2, April, 1972, pp. 275-285.

APPENDIX A

ACCURACY OF MEASUREMENTS

APPENDIX A

A1 ACCURACY OF MEASUREMENTS

1. Head Measurement

Head measurements were taken using a precision point gage whose least count was 0.30mm. Flow conditions for all the tests performed were steady enough to obtain consistent readings over a certain time domain.

2. Length Measurements

The crest length and width were measured in several positions above the crest of the weir and also along the width of the channel to an accuracy of ± 0.3mm.

3. Volumetric Flow Measurements

Flows were measured using standard (ASME) V-notch. Measurements of head over the V-notches were made when the flow was steady. The accuracy of the measured flow was ± 3.0%.

4. Measurement of Pressure Head

Pressure gage and manometers used for the tests had a least count of ± 0.50mm.

5. Overall Accuracy in the Measurement of Flow

The overall accuracy in the measurement of flow is dependent upon the constituent errors (Table A1) and the form of the discharge equation, this latter factor affecting the relative importance of the separate errors. The method of assessing the overall error

in discharge is best illustrated by an example and for this purpose a rectangular broad-crested weir is considered. For the weir, a general equation for the discharge equation is

$$Q_w = \frac{2}{3}\sqrt{\frac{2}{3}g}\; C_{dw}\; B\; H^{3/2} \qquad (A1)$$

The error in Q_w can be written as

$$\left(\partial Q_w\right)^2 = \left(\left(\frac{\partial Q_w}{\partial C_{dw}}\;\delta C_{dw}\right)^2 + \left(\frac{\partial Q_w}{\partial B}\;\delta B\right)^2 + \frac{3}{2}\left(\frac{\partial Q_w}{\partial H}\;\delta H\right)^2\right) \qquad (A2)$$

The overall accuracy can be represented as

$$X_Q = \pm\sqrt{\left(X_{C_{dw}}\right)^2 + \left(X_B\right)^2 + 1.5\left(X_H\right)^2} \qquad (A3)$$

in which X_Q, $X_{C_{dw}}$, X_B and X_H denote the percentage errors in discharge, discharge coefficient, width of the weir and head measurement respectively. To illustrate the application of Equation (A3) to the braod-crested weir, a typical example based on the present study is presented below. Weir Details:

Discharge, Q = 0.056 m^3/sec

Gaged Head, H = 0.12 m

Weir Height P = 0.10 m

Weir Length P = 0.30 m

Weir Radius R = 0.10 m

Channel Width B = 0.254 m

Error Details (Table A1)

Error in discharge coefficient (related to error in discharge) = 3%

Error in gaged head = ±0.25%

Error in weir width = ±0.12%

From Equation (A3).

$$X_Q = \pm \sqrt{(3)^2 + (0.12)^2 + (1.5 \times 0.25)^2} = \pm 3.03\%$$

The true value of the discharge $Q_W = 0.058\ m^3/sec$

TABLE A1

TABLE A1 ACCURACY OF MEASUREMENTS

Variables	Accuracy of Measurements
Length	±0.30 mm
Depth gage	±0.30 mm
Discharge	±3.0%
Pressure gage	±0.50 mm

APPENDIX B

SAMPLE COMPUTATIONS AND COMPUTER PROGRAMS

Sample Computations No.1

Sample Computations for Lateral Weirs in Trapezoidal Channels (Chapter II)

(Computations for Run Number 5, Table 2.3)

b_o = 10.2 cm; Z_1 = 1.5, Z = 0.83, L_s = 10.2 cm, L/B = 1.0, S = 0.0

Depth of flow = Y_1 = 5.2 cm = 0.052 m

Discharge in Channel = Q_1 = 3.76 l/sec = 0.00376 m^3/sec

Weir discharge (actual or experimental) = Q'_w = 2.83 l/sec = 0.00283 m^3/sec

Sill distance = S' = 0.0

Sill height (vertical) = 0.0/1.803 = 0.00

Average Velocity = V_1 = Q/A = 0.402 m/sec

Weir parameter

$$\eta_0 = \frac{V_1}{\sqrt{V_1^2 + 2g\,(Y_1 - S)}} = 0.370$$

Actual mean discharge coefficient $\bar{C}_d$ (Equation 2.27):

$$Q'_w = \bar{C}_d \frac{V_1^3}{3g}\left(\left\{ (L_s + 2Zh_o) \left(\left(1 + \frac{2}{F_0^2} \right)^{1.5} - 1 \right) \right\} - Zh_o F_0^2 \left\{ \left(\left(1 + \frac{2}{F_0^2} \right)^{2.5} - 1 \right) - \left(\left(1 + \frac{2}{F_0^2} \right)^{1.5} - 1 \right) \right\} \right) \qquad (2.27)$$

For η_0 = 0.370,

$$F_o = \sqrt{\frac{2\eta_0^2}{1 - \eta_0^2}} = 0.563$$

$h_o = Y_1 - S$ = 0.052 m , Q_w = 0.00283 m^3/sec

Solving Equation (2.27) gives $\bar{C}_d$ = 0.491 (See Table 2 column 7).

Sample Computations No. 2

Sample Computations for Rectangular Lateral Orifice (Chapter III)

(Computations for Run Number 5, Table 3.2)

B = 25.4 cm, L = 25.4 cm, L/B = 1.0, S = 10.16cm, a = 2.54 cm, S/a = 4.0

Depth of flow = Y_1 = 18.6 cm = 0.186 m

Discharge in Channel = Q_1 = 26.20 l/sec = 0.0262 m^3/sec

Actual Orifice discharge = Q_o = 4.40 l/sec = 0.0044 m^3/sec

Average Velocity = V_1 = Q/A = 0.5546 m/sec

Flow depths $h_{01} = Y_1 - S$ = 8.4 cm = 0.084 m

$h_{02} = Y_1 - S - a$ = 5.9 cm = 0.059 m

Orifice parameters:

$$\eta_{01} = \frac{V_1}{\sqrt{V_1^2 + 2gh_{01}}} = 0.397$$

$$\eta_{02} = \frac{V_1}{\sqrt{V_1^2 + 2gh_{02}}} = 0.458$$

Actual discharge coefficient of orifice:

$$Q_o = \bar{C}_{do} \frac{V_1^3}{3g} L \left(\frac{1}{\eta_{01}^3} - \frac{1}{\eta_{02}^3} \right) \qquad (3.19)$$

$(9.806 \times 3 \times 0.0044) = \bar{C}_{do} [0.254 \times (0.5546)^3 \times 5.634]$

C_{do} = 0.530

The actual coefficient of discharge of orifice is $\bar{C}_{do}$ = 0.530
(Table 3.2, column 7)

Sample Computations No. 3

Sample Computations for Lateral Weir-Orifice Unit (Chapter IV)

B = 254 mm, L = 254 mm, S = 101.6 mm, a = 127.0 mm, b = 127.0 mm

(Computations for Run number 5, Table 4.3)

Flow depth in channel = $Y_u = KY_1$ = 452.6 mm = 0.4526 m

Discharge in Channel = Q_1 = 98.1 l/sec = 0.0981 m^3/sec

Actual weir-orifice discharge = 61.6 l/sec = 0.0616 m^3/sec

Flow depth above weir portion = h_3 = 97.0 mm = 0.097 m

Parameters S/a = 0.80, b/a = 1.00, and h_3/a = 0.764

Froude number $$F_1 = \frac{V_1}{\sqrt{g\,Y_u}} = \frac{Q_1}{A\sqrt{g\,Y_u}} = 0.405$$

Parameters $$\eta_1 = \frac{1}{\sqrt{\left\{1 + \frac{2}{F_1^2}\left(1 - \frac{S}{Y_u}\right)\right\}}} = 0.309$$

$$\eta_2 = \frac{1}{\sqrt{\left\{1 + \frac{2}{F_1^2}\left(1 - \frac{(S+a)}{Y_u}\right)\right\}}} = 0.377$$

and $$\eta_3 = \frac{1}{\sqrt{\left\{1 + \frac{2}{F_1^2}\left(1 - \frac{(S+a+b)}{Y_u}\right)\right\}}} = 0.526$$

Using Equation (4.20), the discharge ratio Q_r ($=Q_{wo}/Q_1$) is obtained as Q_r = 0.632

The actual discharge ratio is

$$Q_r = \frac{Q_{wo}}{Q_1} = \frac{61.6}{98.1} = 0.628$$

The percentage deviation in Q_r is

$$\frac{0.632 - 0.628}{0.628} \times 100 = +0.6\%$$

Sample Computations No. 4

Sample Computations for Rectangular Sharp Crested Weir (Chapter V)

(Computations for Run number 04, Table 5.3 using the momentum approach)

Measured Head over weir = H = 5.0 cm = 0.05 m
Discharge = Q_1 = 15.7 l/sec=0.0157 m^3/sec
Depth of flow at section EF = Y_o = 3.10 cm
channel width = B = 60.3 cm = 0.603 m
Height of weir = W = 2.50 cm
Parameter H/W = 5/2.5 = 2.00
Parameter Y_o/H = 3.1/5.0 = 0.62
Pressure coeficient on weir face = K_f = 0.446
Pressure coefficient at section EF = K_B = 0.445
Momentum coefficient at section EF = β = 1.024

(a) Predicted Coefficient of Discharge:

$$C_{de} = \frac{3}{4}\left\{\frac{\left(\frac{1+H/W}{H/W}\right)^2\left[1-K_f\right] - K_B\left(\frac{Y_o}{H}\right)^2}{\left(\frac{\beta}{Y_o/H}\right) - \left(\frac{H/W}{1+H/W}\right)}\right\}^{1/2}$$

$$= 0.780$$

(b) Actual Coefficient of Discharge:

$$Q = \frac{2}{3}\sqrt{2g}\, C_{de}\, BH^{1.5} = C_{de}\, 1.78\, H^{1.5}$$

$$C_{de} = \frac{0.0157}{1.78(.050)^{1.5}} = 0.790$$

Based on the momentum theory, the predicted coefficient of discharge is 0.780 (Table 5-3, Column 11) and the actual coefficient of discharge is 0.790.
% deviation in C_{de} is -1.3%.

Sample Computations No. 5

Sample Computations for Rectangular Broad-Crested Weir (Chapter VI)

(Computations for Run number 2, Table 6.3, using the momentum theory)

B = 25.4 cm, L_w = 30.5 cm, P = 10.16 cm, R = 0.0 cm, R/P = 0.0

Measured Head over weir = H = 3.10 cm = 0.031 m
Discharge over Weir = Q = 2.00 l/sec = 0.002 m^3/sec
Depth of flow at point of parallel streamlines = d_3 = 1.35 cm = 0.0135 m
Pressure coeficient on weir upstream face = K_p = 0.996
Parameters:

H/P = 0.30
and $d_3/H = 0.435$

(a) Predicted Discharge coefficient C_{dw}:

$$\left(\frac{H+P}{H}\right)^2 - \left(\frac{d_3}{H}\right)^2 - K_p\left(\frac{2H+P}{H}\right)\frac{P}{H} = \frac{16}{27} C_{dw}^2 \left(\frac{H}{d_3} - \frac{H}{H+P}\right)$$

Solving the above equation for C_{dw} gives

C_{dw} = 0.848 (Table 6.3, Column 7)

(b) Actual discharge coefficient C_{dw}:

$$Q = \frac{2}{3}\sqrt{\frac{2}{3}g}\, B\, C_{dw}\, H^{1.5} = 0.433\, C_{dw} H^{1.5}$$

$$\text{Hence, } C_{dw} = \frac{0.002}{0.433 \times (0.031)^{1.5}} = 0.846$$

The predicted and actual discharge coefficients are respectively 0.848 and 0.846.
% deviation in C_{dw} is +0.2%.

COMPUTER PROGRAM 1a

Computer Program for Trapezoidal Lateral Weir with L/B=1·00

This program predicts the discharge and discharge coefficient of the Lateral weir using the 2-d Lateral channel outlet model.

```
      PROGRAM TW5(INPUT,OUTPUT,TAPE 8)
      DIMENSION Y1(60),QW(60),Q2(60),Q1(60)
      B=0.102
      G=9.806
      Z1=1 5
      Z2=0.83
      READ(8,*)(Y1(I),Q1(I),QW(I),I=1,60)
      DO 70 I=1,60
      IF(I LE.20)THEN
      S=0.0
      XL=0 102
      BL=0.1020
      ELSE,
      IF(I.LE.40)THEN
      S=0.028
      XL=0 186
      BL=0 186
      ELSE
      S=0.056
      XL=0.271
      BL=0.271
      ENDIF
      ENDIF
      Y11=Y1(I)/100
      Q2(I)=Q1(I)/1000
      V1=Q2(I)/((B+1 5*Y11)*Y11)
      C1=0.254*1.0-0.538
      C2=0.058+0.234
      C3=-0.129-0.489
      RS=2*G*(Y11-S)
      ETS=V1/SQRT((V1*V1)+RS)
      FR=V1/SQRT(G*Y11)
      FO=V1/SQRT(0.5*RS)
      AH=(1-(ETS**3))*((C3/3)+(0 203/(ETS**3)))+(1-ETS)*
     1(C2+(C1/ETS))
      BH=(1-ETS)*(C3+(C2/ETS))+(C1/3)*(1/(ETS**3)-1)+(
     20.122)*(1/(ETS**5)-1)
      PD=((1+(2/(FO*FO)))**1.5-1)
      PD2=((1+(2/(FO*FO)))**2.5-1)
      PD3=Z2*FO*FO*(Y11-S)*(0.6*PD2-PD)
```

COMPUTER PROGRAM 1a (CONTINUED)

Computer Program for Trapezoidal Lateral Weir with L/B=1.00.

This program predicts the discharge and discharge coefficient of the Lateral weir using the 2-d Lateral channel outlet model.

```
      VMJ=V1*FO*FO*(PD/3)
      QT=(((XL+2*0.83*(Y11-S))*(V1*V1*V1)*AH)/G)-(((V1**5)
     3*0.83*(BH-AH))/(G*G))
      CDT=2.85*(((XL+2*0.83*(Y11-S))*AH-0.83*FO*FO*(Y11-S)*
     4(BH-AH))/((XL+1.66*(Y11-S))*PD-(PD3)))
      CDW=(29.418*QW(I))/((V1**3)*((((XL+1.66*(Y11-S))*PD
     1     )-PD3)*1000)
      S1=S*1.803*100
      PRINT 40,Y1(I),V1,Q1(I),QW(I),QT,E1S,CDT,CDW,
     5S1,I
   70 CONTINUE
   40 FORMAT(4(2X,F5.2),2X,F6.3,2X,4(2X,F5.2),3X,I3/)
      STOP
      END
```

COMPUTER PROGRAM 1b

Computer Program for Trapezoidal Lateral Weir with L/B=0.75

This program predicts the discharge and discharge coefficient of the Lateral weir using the 2-d Lateral channel outlet model.

```
PROGRAM TW5(INPUT,OUTPUT,TAPE 9)
DIMENSION Y1(60),QW(60),Q2(60),Q1(60)
B=0 102
G=9 806
Z1=1 5
Z2=0 62
READ(9,*)(Y1(I),Q1(I),QW(I),I=1,60)
DO 70 I=1,60
IF(I.LE 20)THEN
S=0.0
XL=0.076
BL=0.1010
ELSE
IF(I.LE.40)THEN
S=0 028
XL=0.142
BL=0.186
ELSE
S=0.056
XL=0.203
BL=0.271
ENDIF
ENDIF
Y11=Y1(I)/100
Q2(I)=Q1(I)/1000
V1=Q2(I)/((B+1.5*Y11)*Y11)
C1=0.254*0.75-0.538
C2=0.058+0.234*0.75
C3=-0.129-0.489*0.75
RS=2*G*(Y11-S)
ETS=V1/SQRT((V1*V1)+RS)
FR=V1/SQRT(G*Y11)
FO=V1/SQRT(0.5*RS)
AH=(1-(ETS**3))*((C3/3)+(0.203/(ETS**3)))+(1-ETS)*
1(C2+(C1/ETS))
BH=(1-ETS)*(C3+(C2/ETS))+(C1/3)*(1/(ETS**3)-1)+(
20.122)*(1/(ETS**5)-1)
PD=((1+(2/(FO*FO)))**1.5-1)
PD2=((1+(2/(FO*FO)))**2.5-1)
PD3=Z2*FO*FO*(Y11-S)*(0.6*PD2-PD)
```

COMPUTER PROGRAM 1b (CONTINUED)

Computer Program for Trapezoidal Lateral Weir with L/B=0.75.

This program predicts the discharge and discharge coefficient of the Lateral weir using the 2-d Lateral channel outlet model.

```
      VMJ=V1*FO*FO*(PD/3)
      QT=(((XL+2*0.62*(Y11-S))*(V1*V1*V1)*AH)/G)-(((V1**5)
     3*0.62*(BH-AH))/(G*G))
      CDT=2.85*(((XL+2*0.62*(Y11-S))*AH-0.62*FO*FO*(Y11-S)*
     4(BH-AH))/((XL+1.24*(Y11-S))*PD-(PD3)))
      CDW=(29.418*QW(I))/((V1**3)*(((XL+1.24*(Y11-S))*PD
     1     )-PD3)*1000)
      S1=S*1.803*100
      PRINT 40,Y1(I),V1,Q1(I),QW(I),QT,ETS,CDT,CDW,
     5S1,I
   70 CONTINUE
   40 FORMAT(4(2X,F5.2),2X,F6.3,2X,4(2X,F5.2),3X,I3/)
      STOP
      END
```

COMPUTER PROGRAM 1C

Computer Program for Trapezoidal Lateral Weir with L/B=0.50

This program predicts the discharge and discharge coefficient of the Lateral weir using the 2-d Lateral channel outlet model.

```
PROGRAM TW5(INPUT,OUTPUT,TAPE 7)
DIMENSION Y1(60),QW(60),Q2(60),Q1(60)
B=0.102
G=9 806
Z1=1.5
Z2=0.43
READ(7,*)(Y1(I),Q1(I),QW(I),I=1,60)
DO 70 I=1,60
IF(I.LE.20)THEN
S=0.0
XL=0 051
BL=0 1010
ELSE
IF(I.LE.40)THEN
S=0.028
XL=0.093
BL=0.186
ELSE
S=0.056
XL=0.135
BL=0.271
ENDIF
ENDIF
Y11=Y1(I)/100
Q2(I)=Q1(I)/1000
V1=Q2(I)/((B+1.5*Y11)*Y11)
C1=0.254*0.5-0.538
C2=0.058+0.234*0.5
C3=-0.129-0.489*0.5
RS=2*G*(Y11-S)
ETS=V1/SQRT((V1*V1)+RS)
FR=V1/SQRT(G*Y11)
FO=V1/SQRT(0.5*RS)
AH=(1-(ETS**3))*((C3/3)+(0.203/(ETS**3)))+(1-ETS)*
1(C2+(C1/ETS))
BH=(1-ETS)*(C3+(C2/ETS))+(C1/3)*(1/(ETS**3)+1)+(
20.122)*(1/(ETS**5)-1)
PD=((1+(2/(FO*FO)))**1.5-1)
PD2=((1+(2/(FO*FO)))**2.5-1)
PD3=Z2*FO*FO*(Y11-S)*(0.6*PD2-PD)
```

COMPUTER PROGRAM1C (CONTINUED)

Computer Program for Trapezoidal Lateral Weir with L/B=0.50

This program predicts the discharge and discharge coefficient of the Lateral weir using the 2-d Lateral channel outlet model.

```
      VMJ=V1*FO*FO*(PD/3)
      QT=(((XL+2*0.43*(Y11-S))*(V1*V1*V1)*AH)/G)-(((V1**5)
     3*0.43*(BH-AH))/(G*G))
      CDT=2.85*(((XL+2*0.43*(Y11-S))*AH-0.43*FO*FO*(Y11-S)*
     4(BH-AH))/((XL+0.86*(Y11-S))*PD-(PD3)))
      CDW=(29.418*QW(I))/((V1**3)*(((XL+0.86*(Y11-S))*PD
     1     )-PD3)*1000)
      S1=S*1.803*100
      PRINT 40,Y1(I),V1,Q1(I),QW(I),QT,ETS,CDT,CDW,
     5S1,I
   70 CONTINUE
   40 FORMAT(4(2X,F5.2),2X,F6.3,2X,4(2X,F5.2),3X,I3/)
      STOP
      END
```

COMPUTER PROGRAM 2

Computer program for Rectangular Lateral Orifice with L/B=100 .

```
      PROGRAM ORIF(INPUT,OUTPUT,TAPE10)
C     THIS PROGRAM COMPUTES THE DISCHARGE AND DISCHARGE COEFFICIENT
C     FOR THE FLOW THROUGH A LATERAL ORIFICE FOR L/B= 100
      DIMENSION Y(56),Q1(56),AO(56),V1(56),RNO1(56),RNO2(56),
     *Z01(56),Z02(56),CDO(56),ACO(56),P1(56),P2(56),D3(56),S(56),A(56),
     *HO2(56),ACO1(56),Q1(56)
     1   ,P3(56)
      RL=25.4
      READ(10,*)(Y(I),Q1(I),AO(I),I=1,56)
      G=980.6
      B=25.4
      C1=+0.284
      C2=0.292
      C3=-0.620
      DO 5 I=1,8
      S(I)=10.2
      A(I)=2.5
5     CONTINUE
      DO 6 I=9,18
      S(I)=5.0
      A(I)=2.5
6     CONTINUE
      DO 7 I=19,28
      S(I)=10.2
      A(I)=7.6
7     CONTINUE
      DO 8 I=29,43
      S(I)=10.2
      A(I)=12.7
8     CONTINUE
      DO 9 I=44,56
      S(I)=5.0
      A(I)=12.7
9     CONTINUE
      DO 50 I=1,56
      V1(I)=Q1(I)*1000.0/(B*Y(I))
      RRN=V1(I)**2.0+2.0*G*(Y(I)-S(I))
      RNO1(I)=(V1(I)**2.0/RRN)**0.5
      HO2(I)=Y(I)-S(I)-A(I)
      IF(HO2(I).LE.0.0)GO TO 13
      RNO2(I)=(V1(I)**2.0)/(V1(I)**2.0+2.0*G*HO2(I)))**0.5
      GO TO 14
13    RNO2(I)=1.0
14    P1(I)=1.0/RNO1(I)**3.0
      P2(I)=1.0/RNO2(I)**3.0
      P3(I)=P1(I)-P2(I)
```

COMPUTER PROGRAM 2 (CONTINUED)

Computer program for Rectangular Lateral Orifice with L/B=100 .

```
      D3(I)=1.0/RNO1(I)
      ZO1(I)=(1-RNO1(I)**3.0)*(C3+0.333+0.203*P1(I))+
     *(1-RNO1(I))*(C2+C1*D3(I))
      ZO2(I)=(1-RNO2(I)**3.0)*(C3+0.333+0.203*P2(I))+
     *(1-RNO2(I))*(C2+C1/RNO2(I))
      CDO(I)=3.0*0.95*(ZO1(I)-ZO2(I))/(P1(I)-P2(I))
      ACD(I)=(AO(I)*3000.0*G)/((RL*V1(I)**3.0)*(P3(I)))
      QT(I)=0.95*((RL*V1(I)**3.0)*(ZO1(I)-ZO2(I)))/(1000.0*G)
50    CONTINUE
      PRINT 30
30    FORMAT(5X,"RESULTS OF LATERAL ORIFICE TESTS")
      PRINT 40
40    FORMAT(//7X,"Y1",7X,"Q1",5X,"QO",5X,"QT",5X,"S",5X,"A",5X,"NO1",
     *5X,"CDO",5X,"ACD",5X,"I",/)
      DO 70 I=1,56
      PRINT 60,V1(I),ZO1(I),ZO2(I),P3(I),S(I),A(I),RNO1(I),
     *CDO(I),ACD(I),I
60    FORMAT(5X,4E10.4,5X,5F7.3,6X,I3,/)
70    CONTINUE
      STOP
      END
```

COMPUTER PROGRAM 3

Computer program for Rectangular Sharp-crested Weir based on the Momentum principle.

This program predicts the discharge coefficient of the weir.

```
      PROGRAM TIM1(INPUT,OUTPUT,TAPE 15)
      REAL A(17),BA(17),C(17),D(17),H(17),W(17),KF(17),YO(17),Q(17),B,KB
     1   ,E(17),CDE(17),CDT(17),HW(17),YOH(17)
      PRINT 100
      PRINT 150
      READ(15,*)(KF(I),YO(I),Q(I),H(I),W(I),I=1,17)
      DO 10 I=1,17
      A(I)=(1+H(I)/W(I))/(H(I)/W(I))
      IF (I.LE.10)THEN
      KB=0.445
      B=1.024
      ELSE
      KB=0.279
      B=1.046
      ENDIF
      BA(I)=KB*((YO(I)/H(I))**2)
      C(I)=B/(YO(I)/H(I))
      D(I)=1/A(I)
      E(I)=(A(I)**2)*(1-KF(I))
      CDE(I)=0.75*(((E(I)-BA(I))/(C(I)-D(I)))**0.5)
      CDT(I)=Q(I)/(1.78*H(I)**1.5)
      HW(I)=H(I)/W(I)
      YOH(I)=YO(I)/H(I)
      PRINT 200,I,H(I),W(I),Q(I),HW(I),YOH(I),CDT(I),CDE(I)
200   FORMAT(2X,I2,5X,F4.2,5X,F5.2,5X,F5.2,5X,F5.2,5X,F5.2,5X,F5.2
     1,5X,F5.2/)
 10   CONTINUE
100   FORMAT(2X,'I',6X,'H(I)',6X,'W(I)',6X,'Q(I)',6X,'HW(I)',
     25X,'YOH(I)',3X,'CDT(I)',5X,'CDE(I)')
150   FORMAT('**********************************************************
     1**********',//)
      STOP
      END
```

COMPUTER PROGRAM 4

Computer program for Rectangular Broad-crested Weir based on the Momentum principle.

This program predicts the discharge coefficient of the weir.

```
      PROGRAM TIM2(INPUT,OUTPUT,TAPE 11)
      REAL H(48),KP(48),Q(48),CDE(48),CDW(48),A(48),B(48),C(48),D(48),
     1    RHS(48),CD(48),D3(48),A2(48)
      READ (11,*)(H(I),D3(I),KP(I),Q(I),I=1,48)
      P=10.2
      DO 10 I=1,48
      A(I)=1+(P/H(I))
      A2(I)=2+(P/H(I))
      B(I)=(D3(I)/H(I))**2
      C(I)=KP(I)*A2(I)*(P/H(I))
      D(I)=(H(I)/D3(I))-(H(I)/(H(I)+P))
      RHS(I)=(A(I)**2)-B(I)-C(I)
      CD(I)=((27/16)*RHS(I))/D(I)
      CDW(I)=SQRT(CD(I))
      CDE(I)=Q(I)/(0.433*H(I)**1.5)
      PRINT 20,I,H(I),D3(I),KP(I),Q(I),CDW(I),CDE(I)
20    FORMAT(2X,I2,5X,F6.3,5X,F6.3,5X,F6.3,5X,F6.3,5X,F6.3,5X,F6.3)
10    CONTINUE
      STOP
      END
```

FIGURES

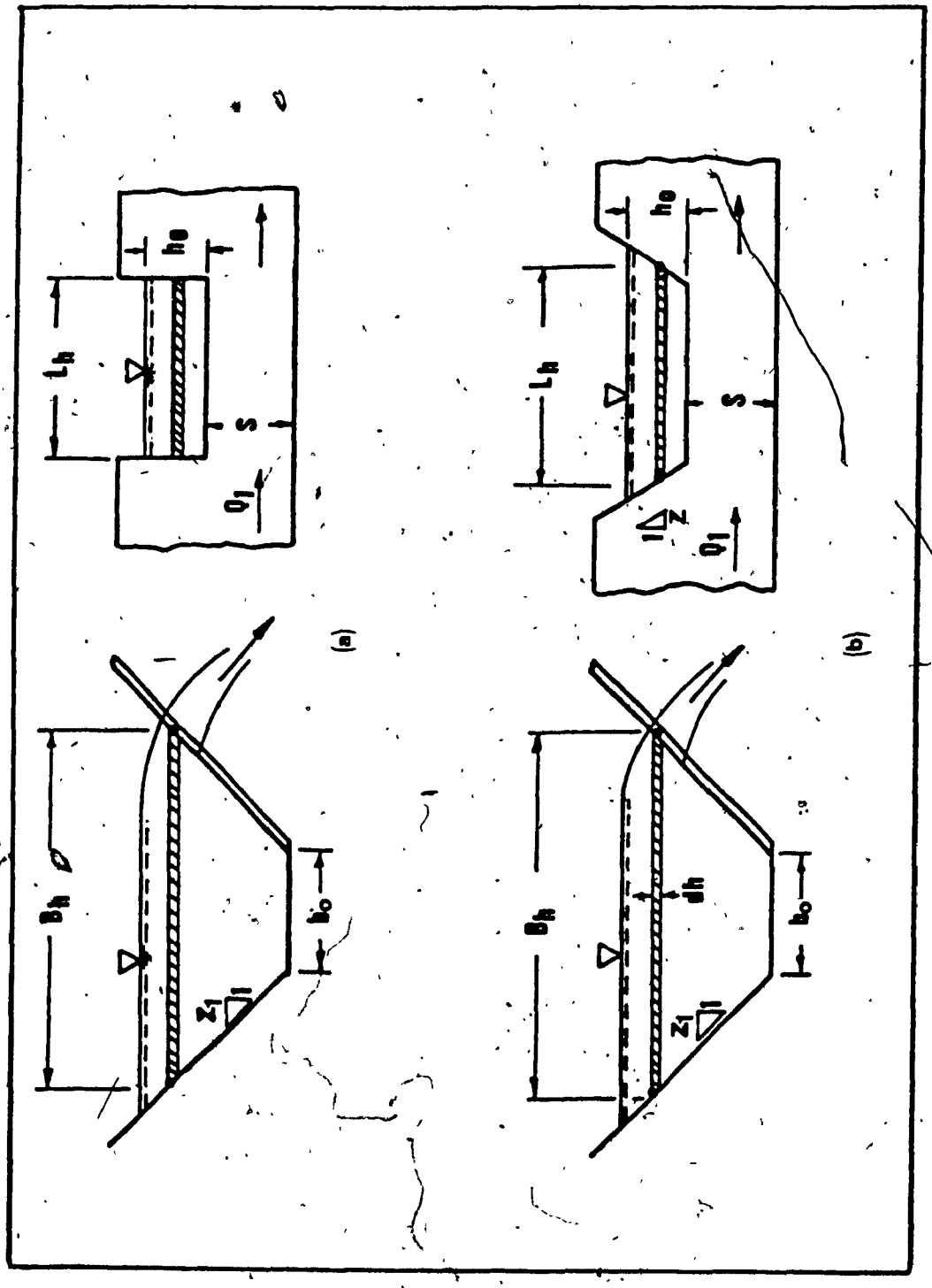

Figure 2.1 Lateral Weir Flow Model:

(a) Variable L_h/B_h.

(b) Constant L_h/B_h.

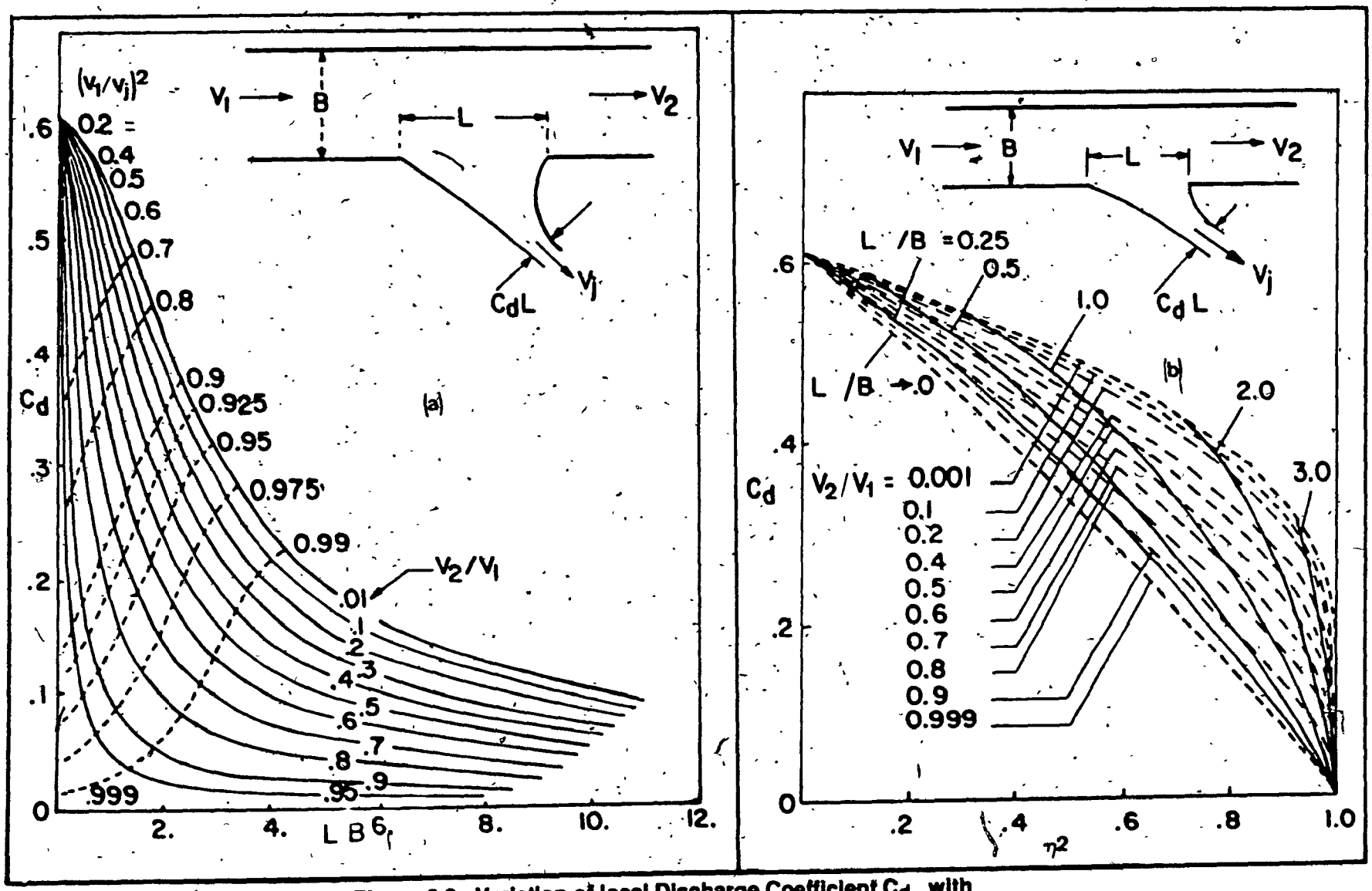

Figure 2.2 Variation of local Discharge Coefficient C_d with

(a) Width Ratio L/B; (b) Velocity Ratio η^2

[REF. 54]

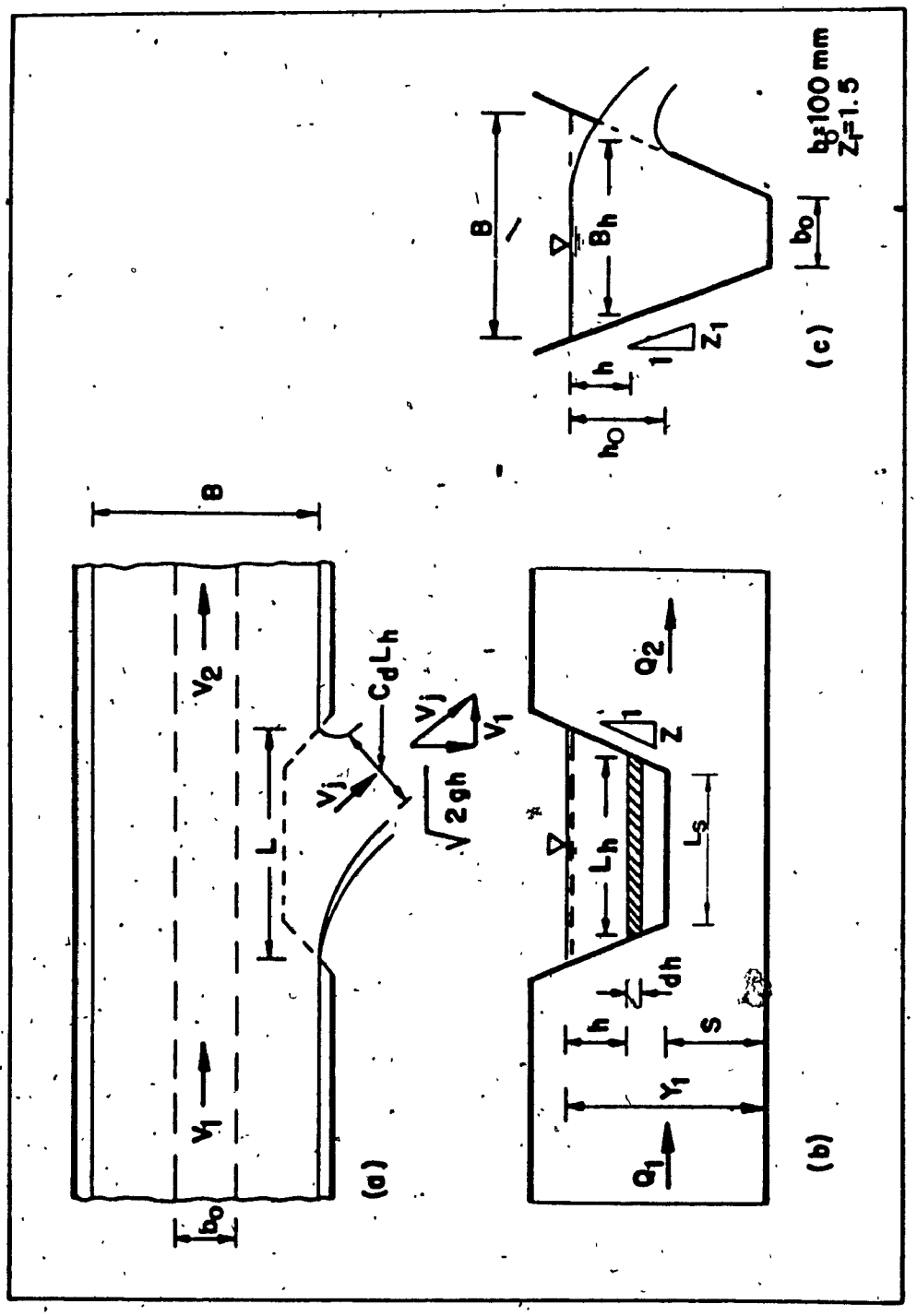

Figure 2.3 Definition Sketch : Trapezoidal Lateral Weir

(a) Plan View; (b) Side View; (c) Sectional View

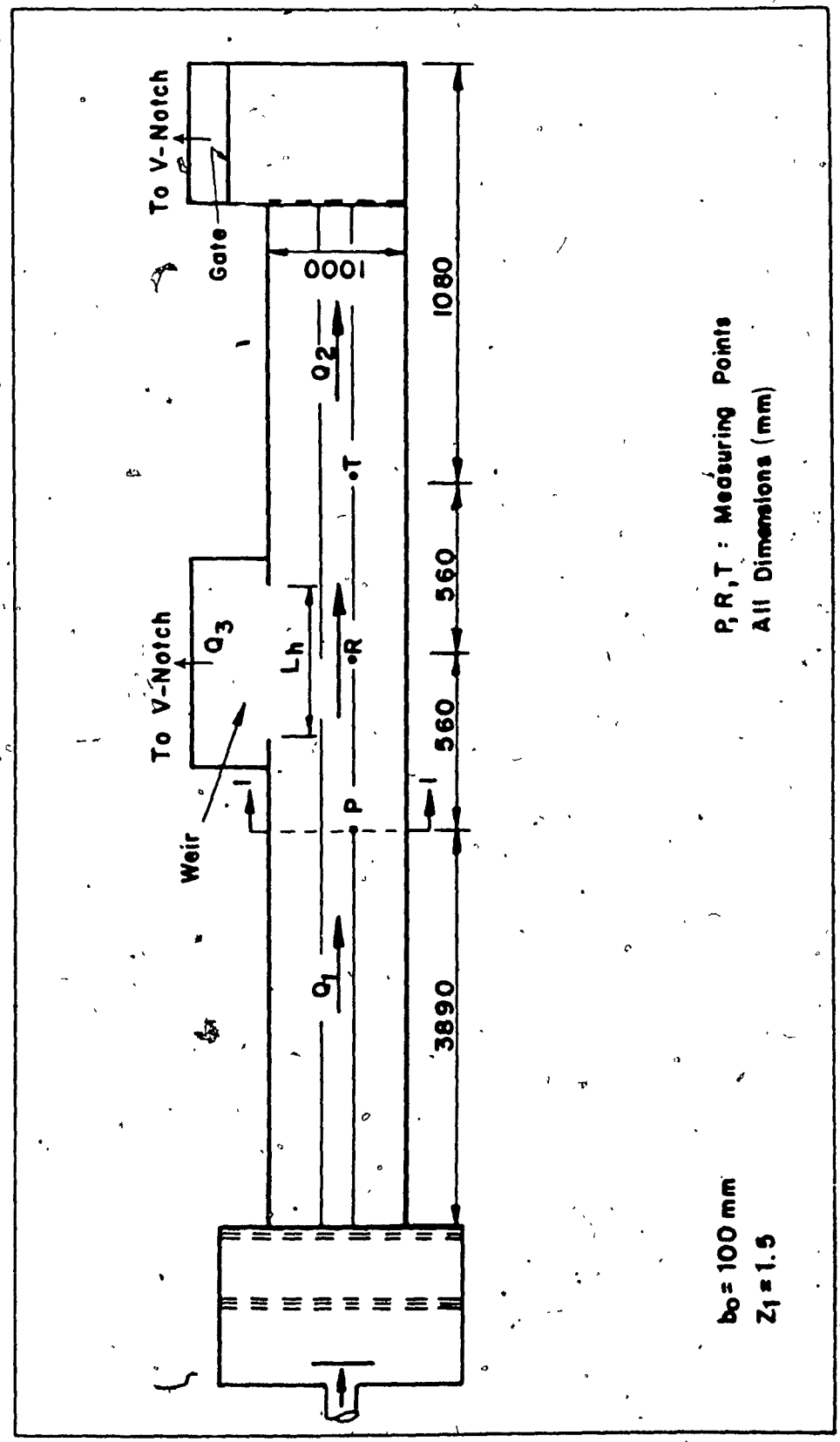

Figure 2.4 Experimental Set-up for Trapezoidal Lateral Weir Study

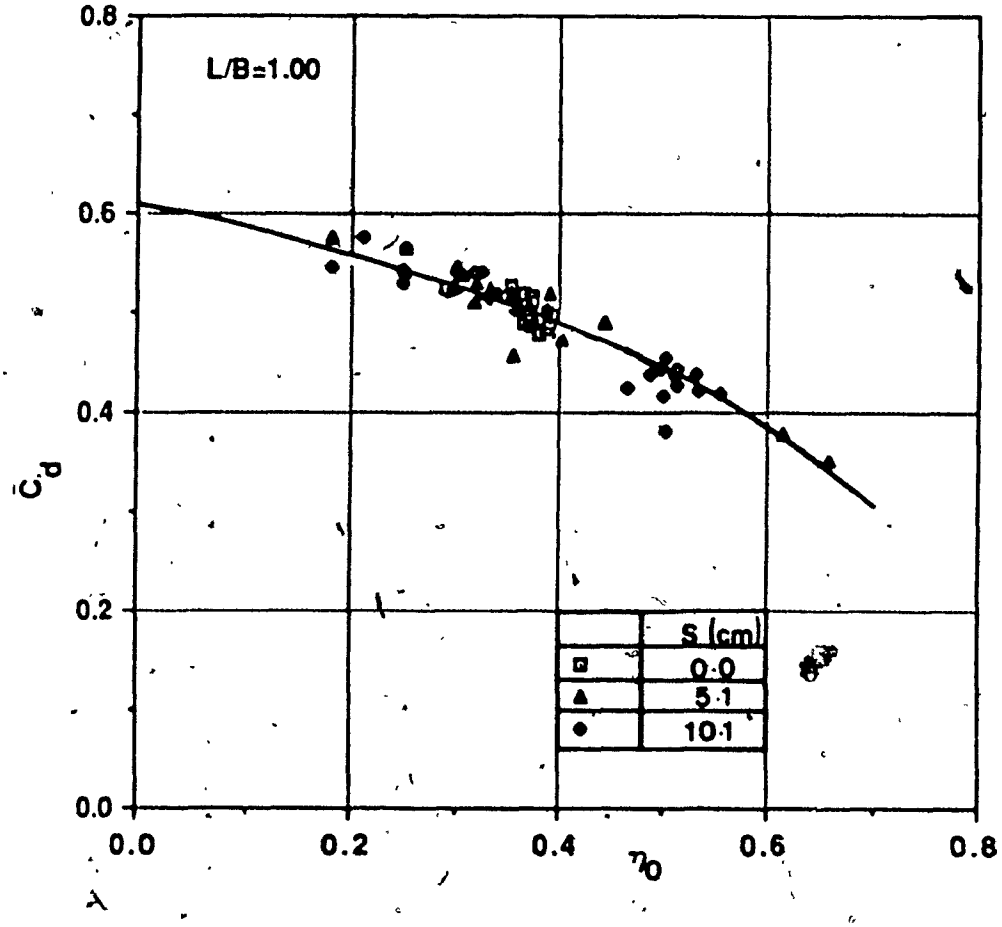

Figure 2.5 Variation of mean Discharge Coefficient $\bar{C}_d$ of Trapezoidal weir with the Velocity Parameter η_0 for L/B=1.00

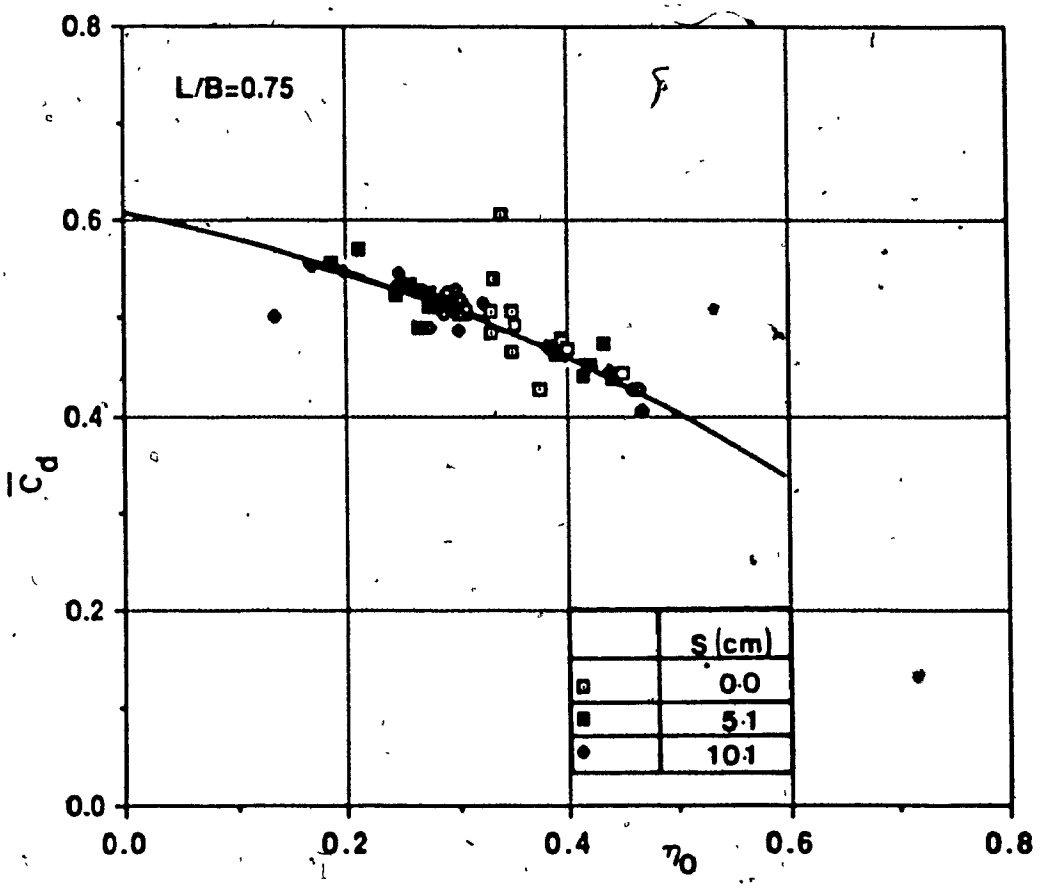

Figure 2.6 Variation of mean Discharge Coefficient $\bar{C}_d$ of Trapezoidal weir, with the Velocity Parameter η_0 for L/B=0.75

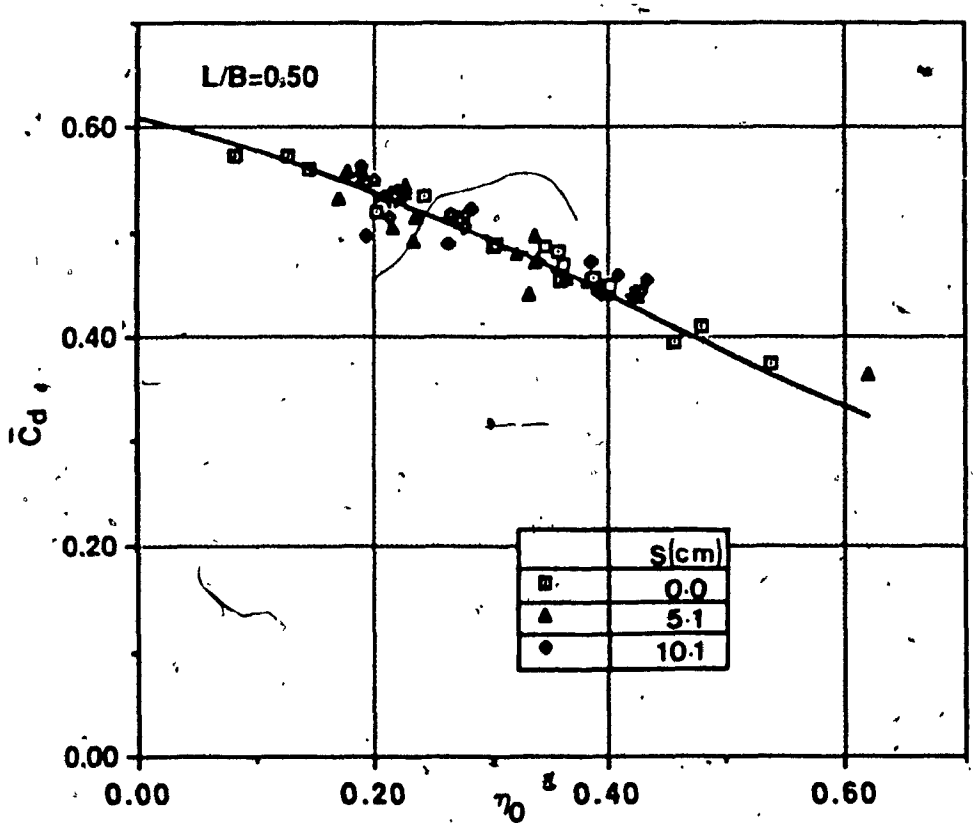

Figure 2.7 Variation of mean Discharge Coefficient $\bar{C}_d$ of Trapezoidal weir with the Velocity Parameter η_0 for L/B=0.50

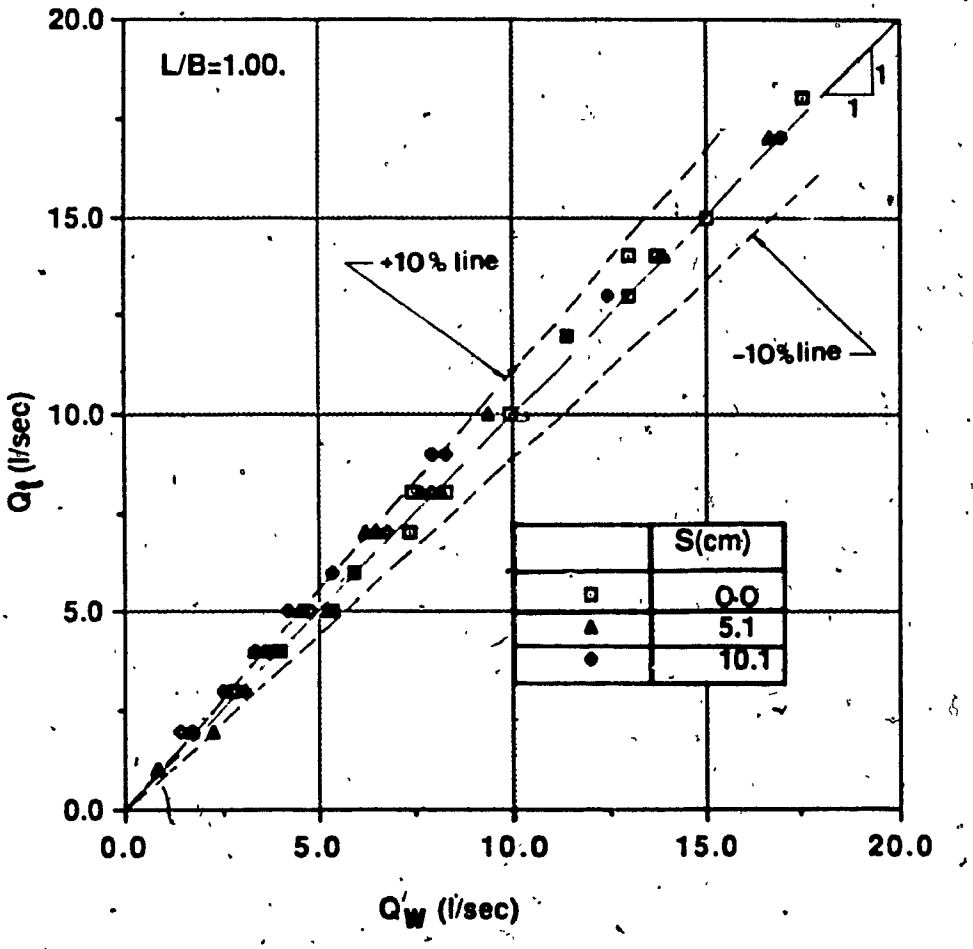

Figure 2.8 Correlation between Predicted Discharge and Measured Discharge through Trapezoidal lateral weir for L/B=1.00

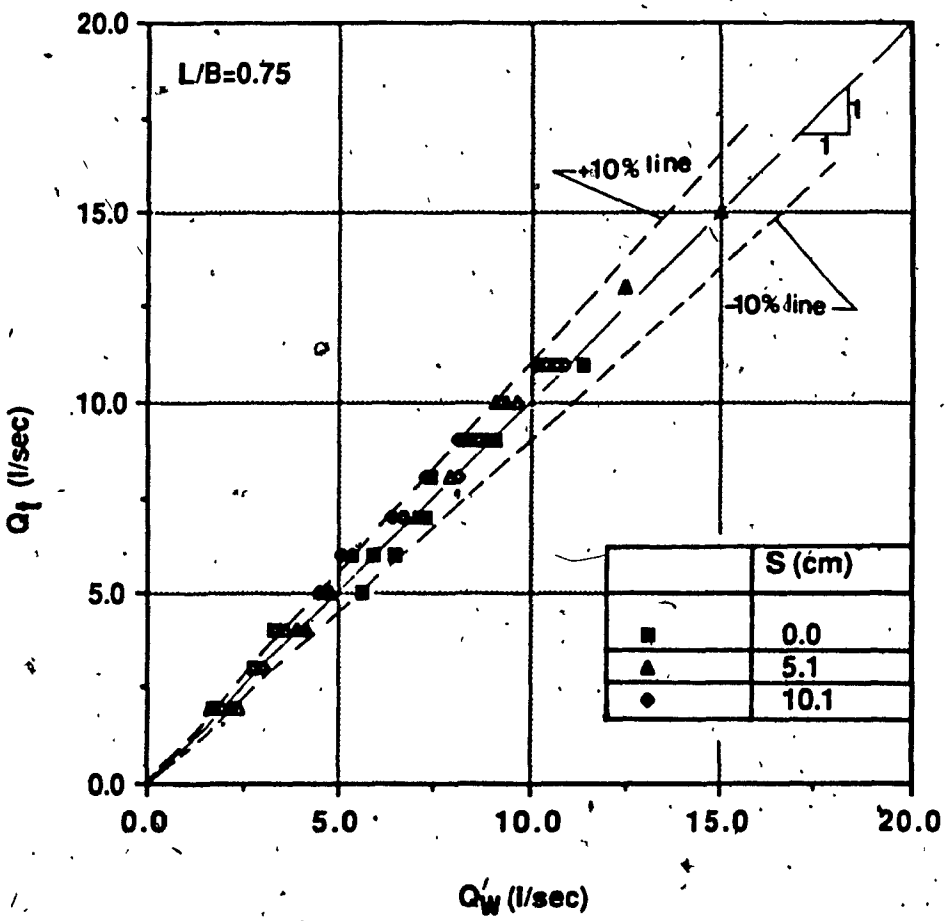

Figure 2.9 Correlation between Predicted Discharge and Measured Discharge through Trapezoidal lateral weir for L/B=0.75

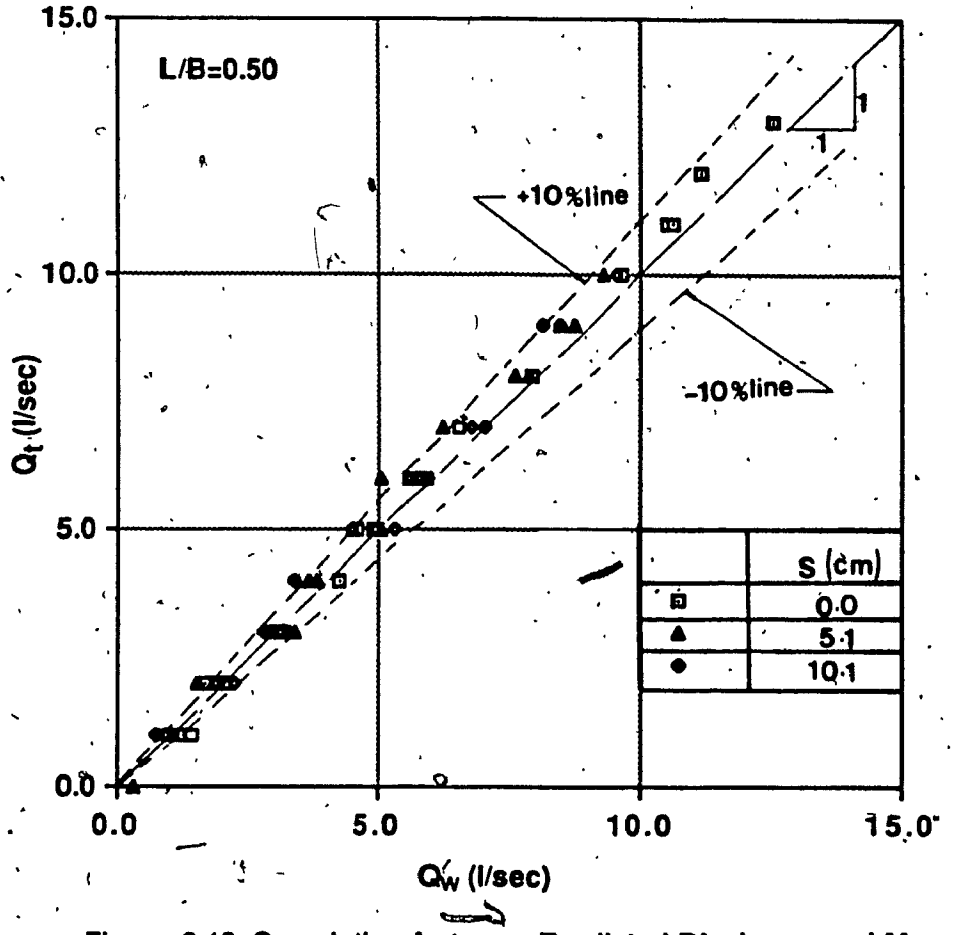

Figure 2.10 Correlation between Predicted Discharge and Measured Discharge through Trapezoidal lateral weir for L/B=0.50

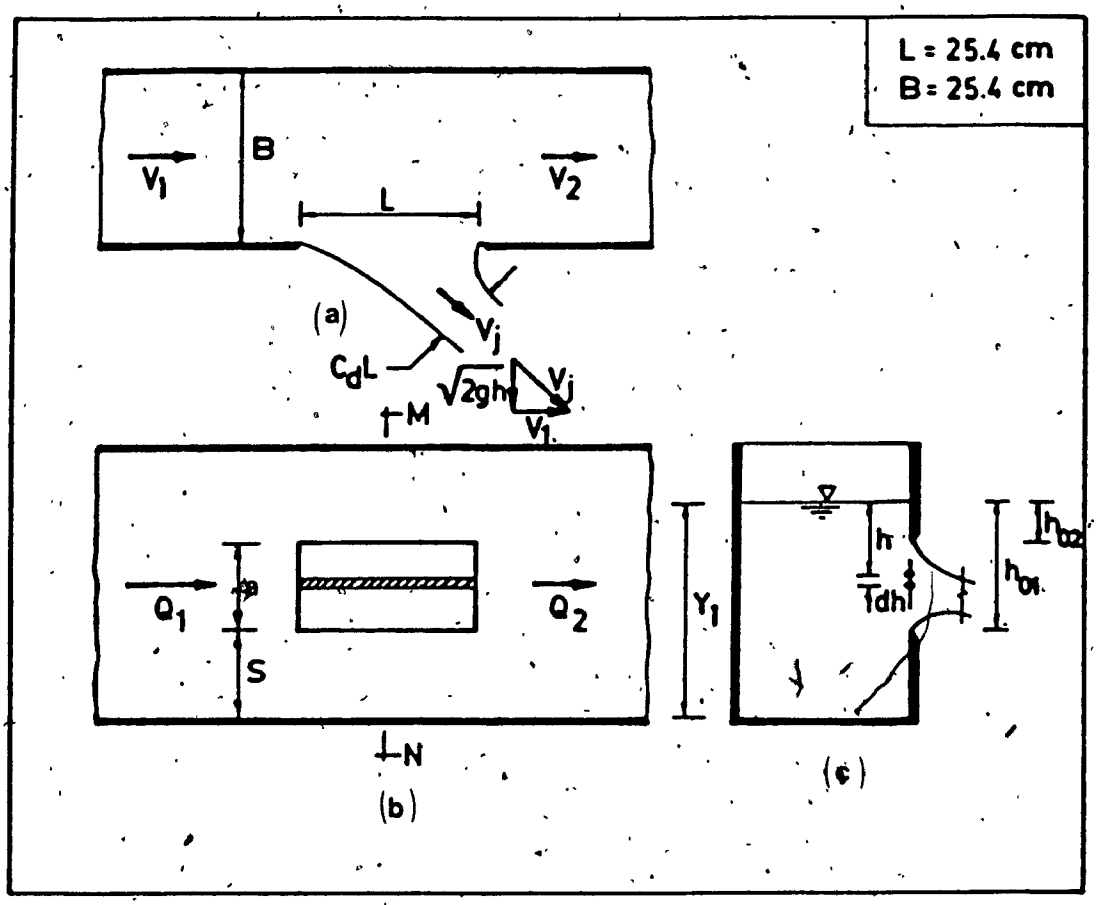

Figure 3.1 Definition Sketch : Rectangular Lateral Orifice

(a) Plan View; (b) Side View; (c) Sectional View

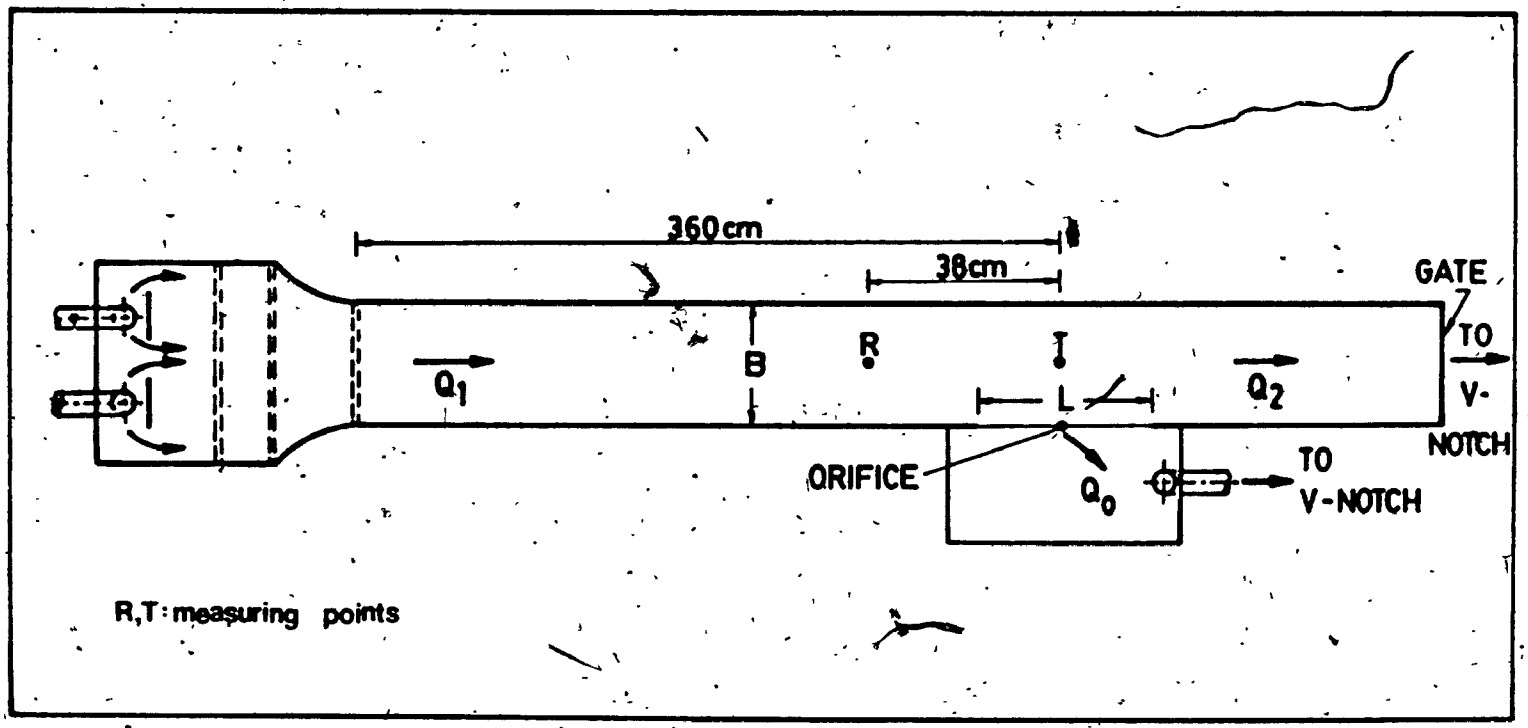

Figure 3.2 Experimental Set-up for Rectangular Lateral Orifice Study

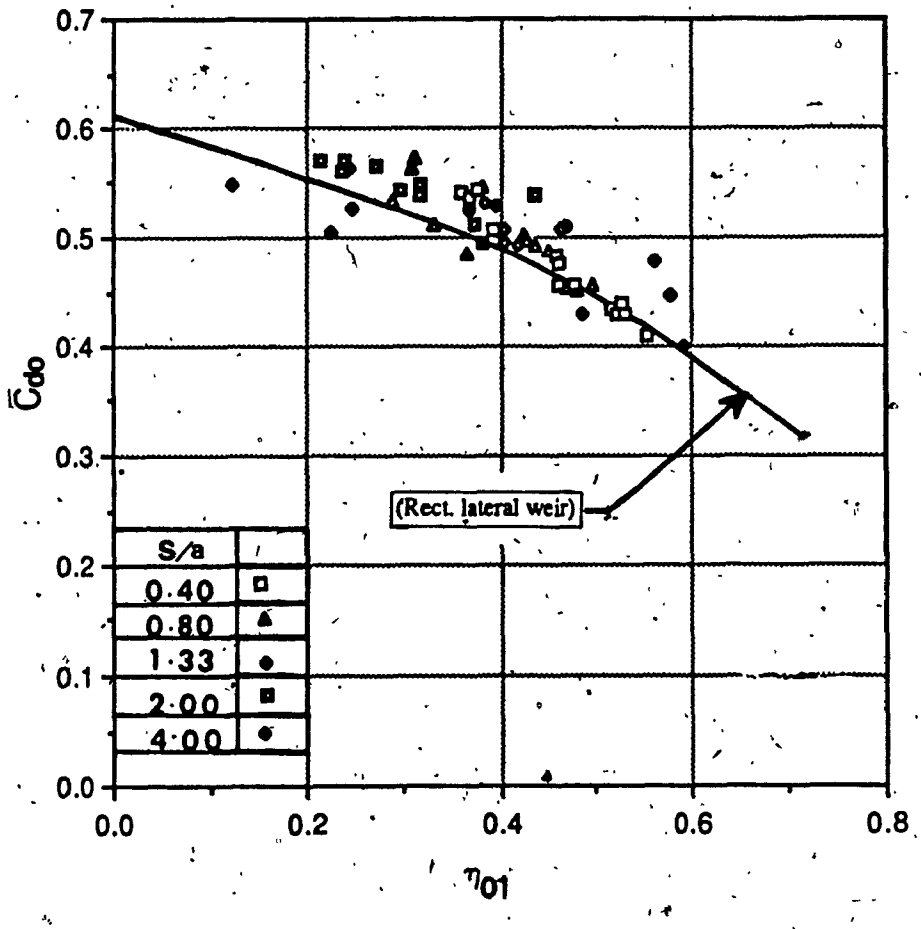

Figure 3.3 Variation of Mean Discharge Coefficient

of Lateral Orifice with Velocity Parameter

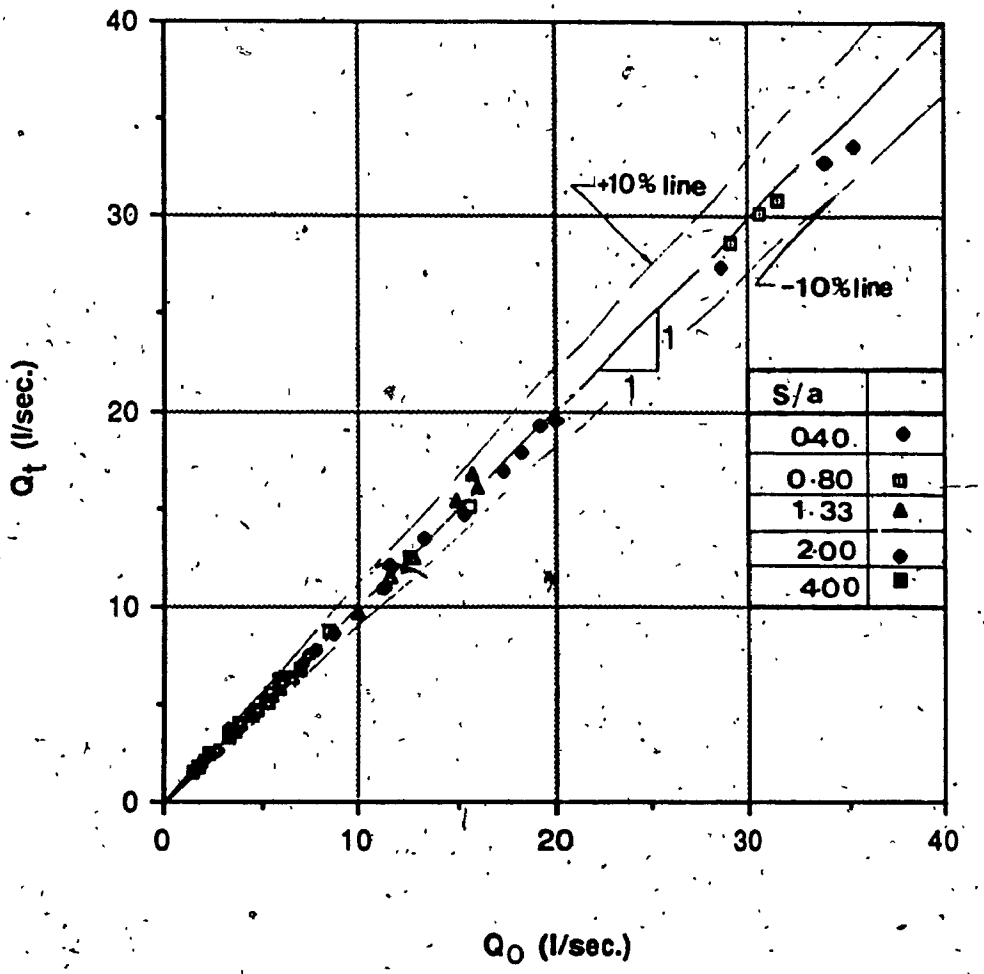

Figure 3.4 Correlation Between Predicted Discharge and Measured Discharge through Orifice

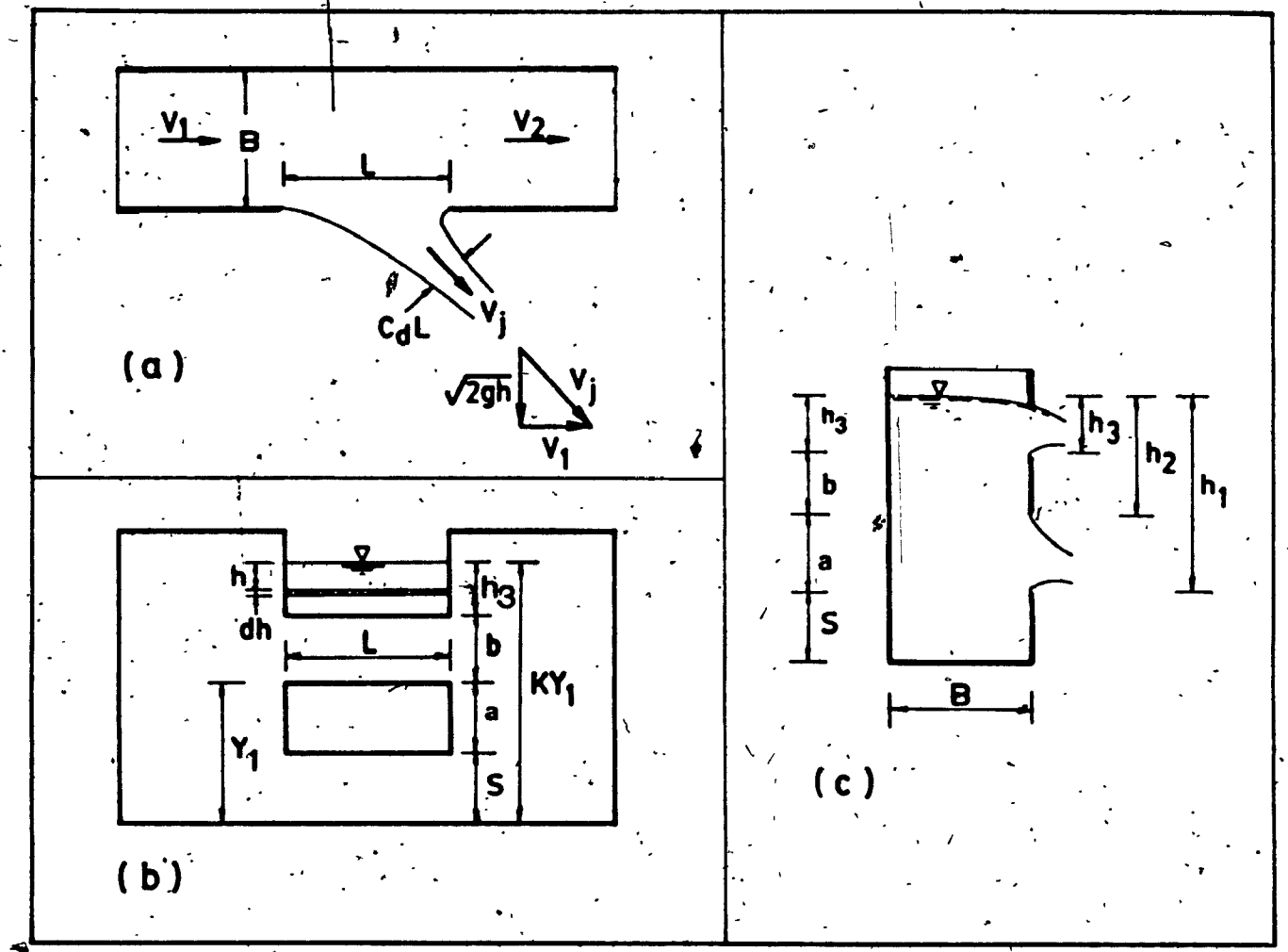

Figure 4.1 Definition Sketch : Rectangular Weir-Orifice Unit

(a) Plan View; (b) Side View ; (c) Sectional View

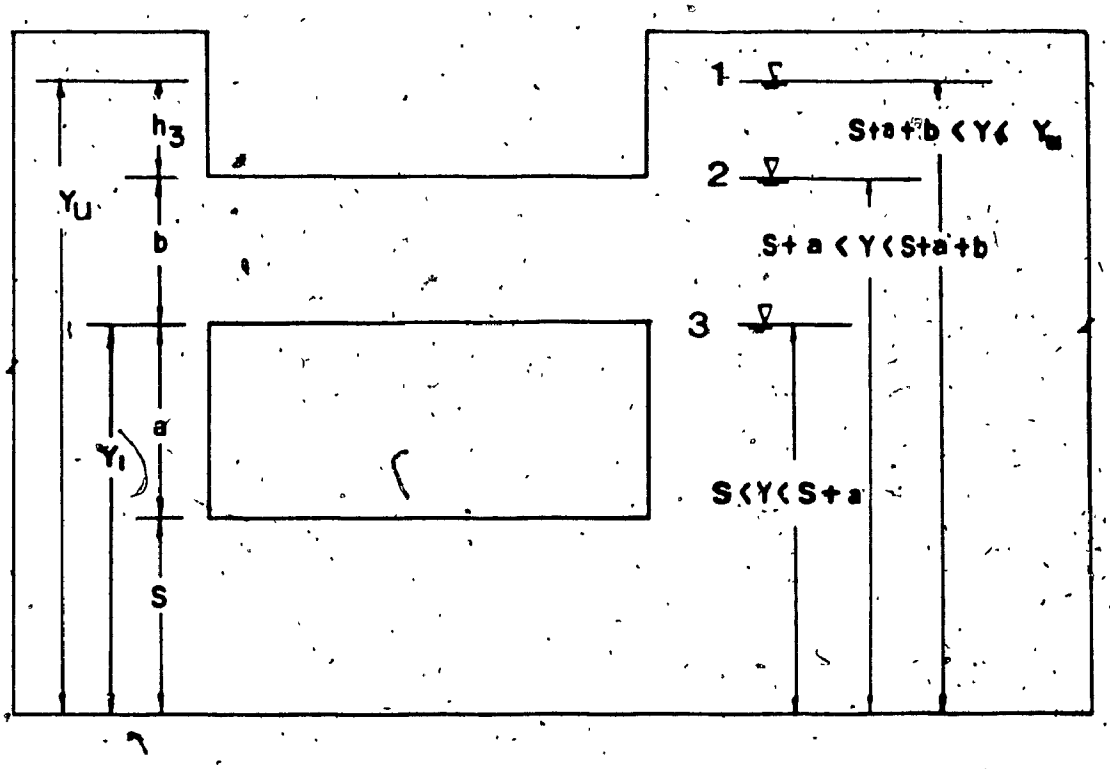

Figure 4.2 Weir-Orifice Unit: Sketch showing the three flow cases

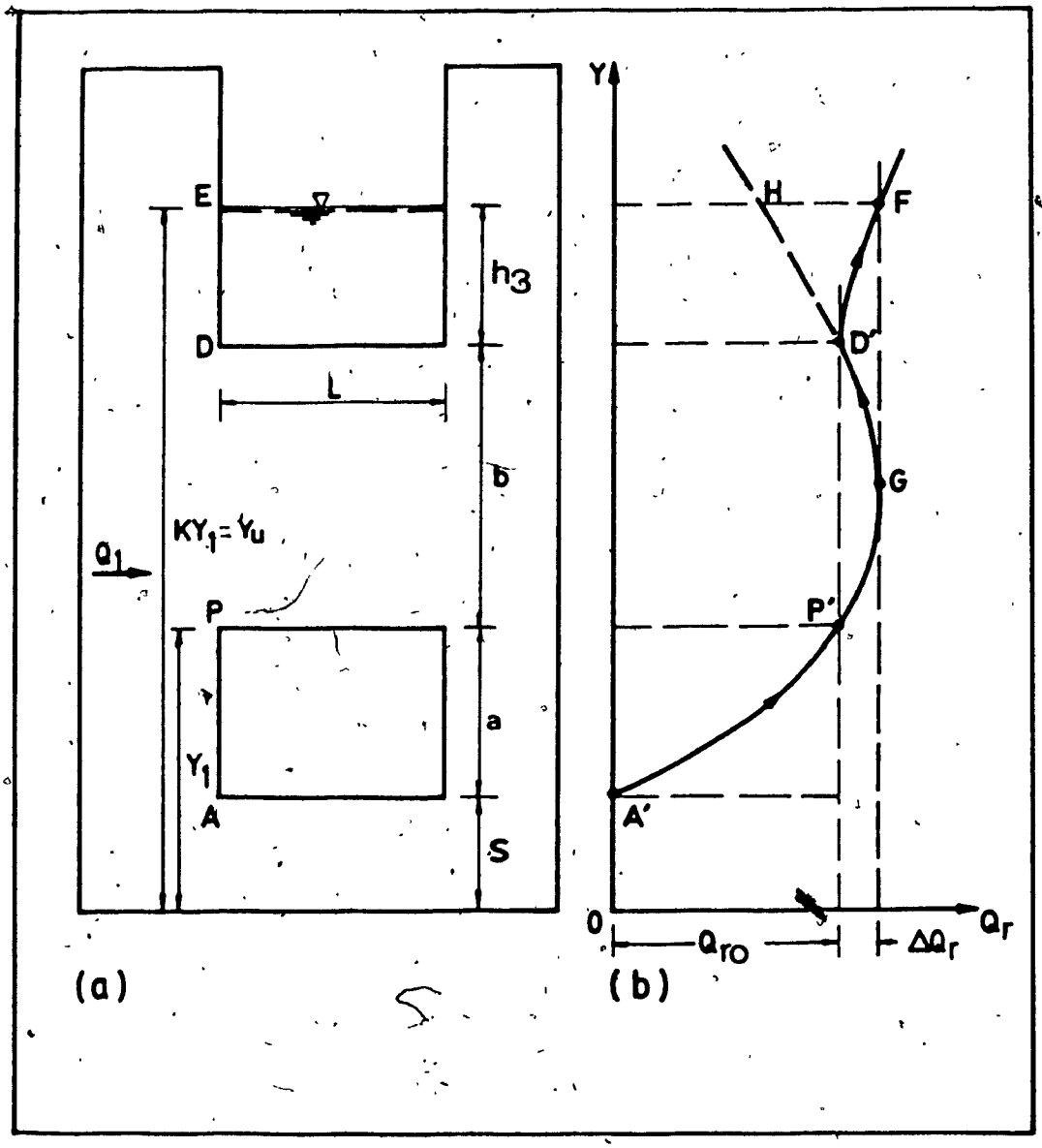

Figure 4.3 Typical Discharge Distribution Characteristics of Weir-Orifice Unit

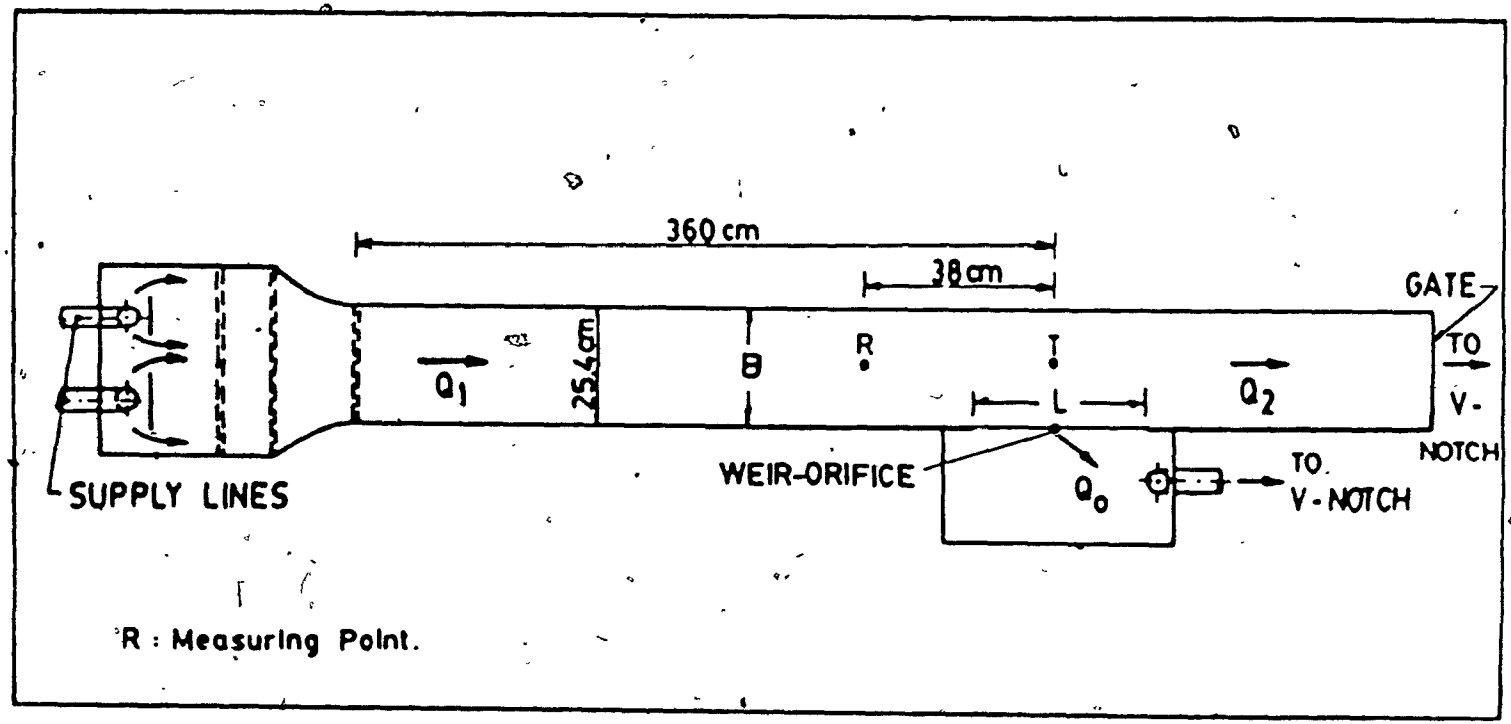

Figure 4.4 Experimental Set-up for Lateral Weir-Orifice Study.

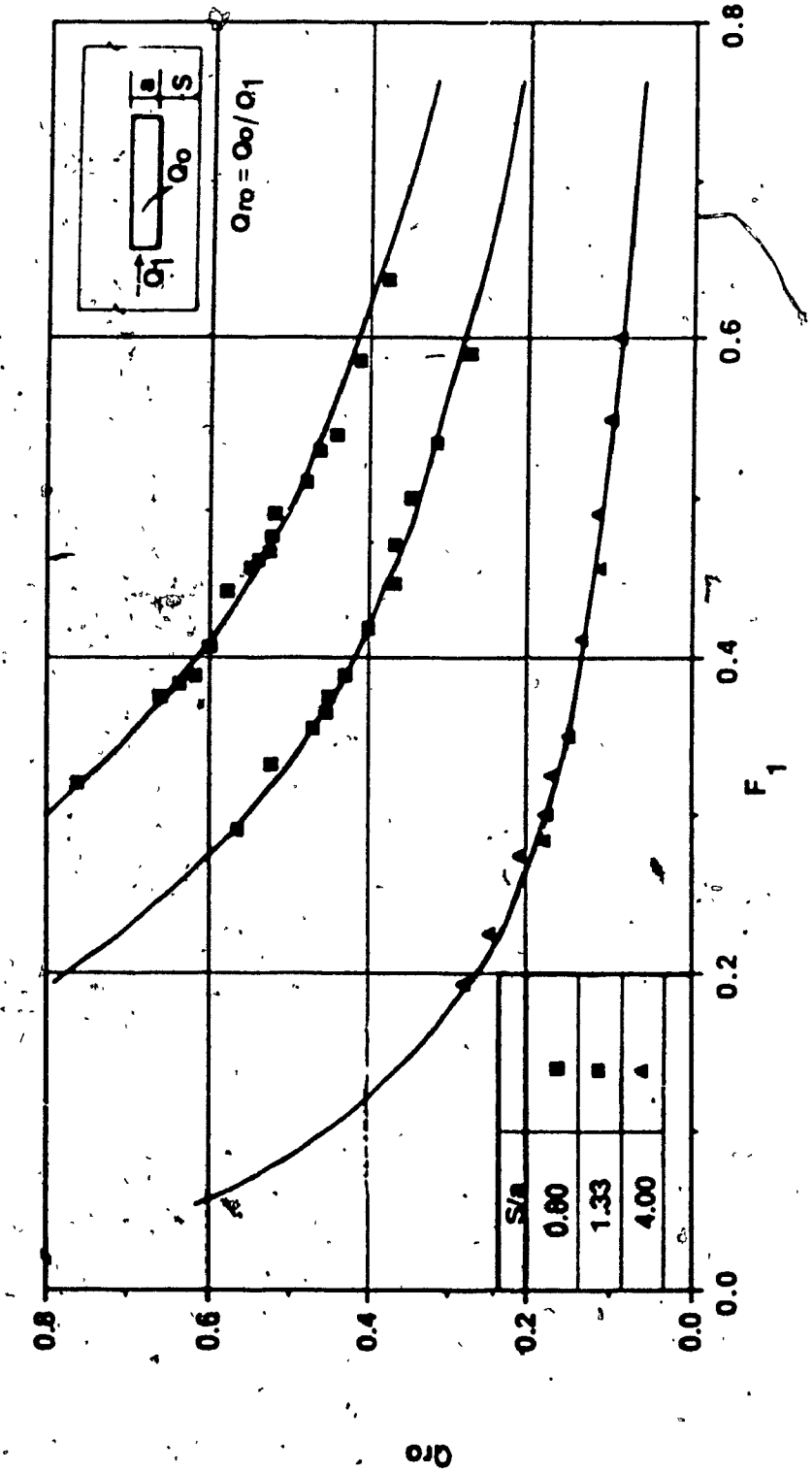

Figure 4.5 Variation of Qro with the Froude Number F_1

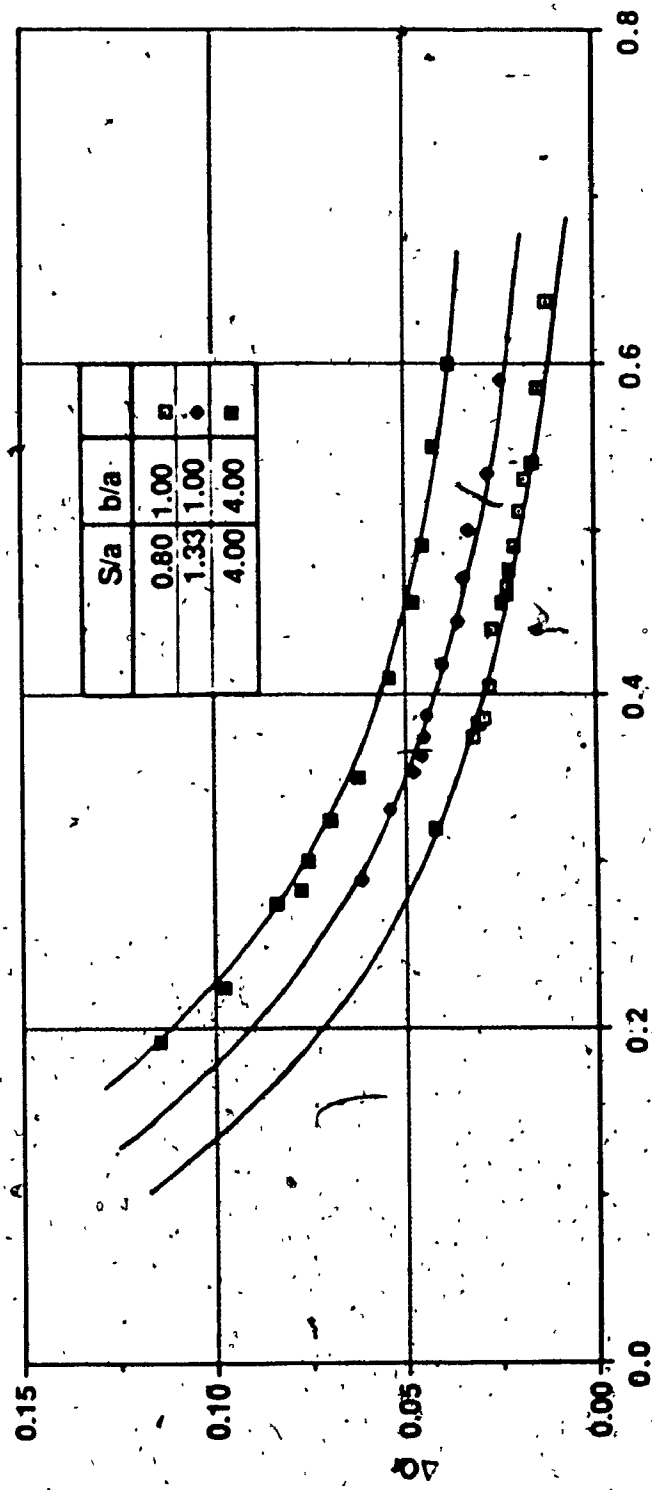

Figure 4.6 Variation of ΔQr with Froude Number F_1

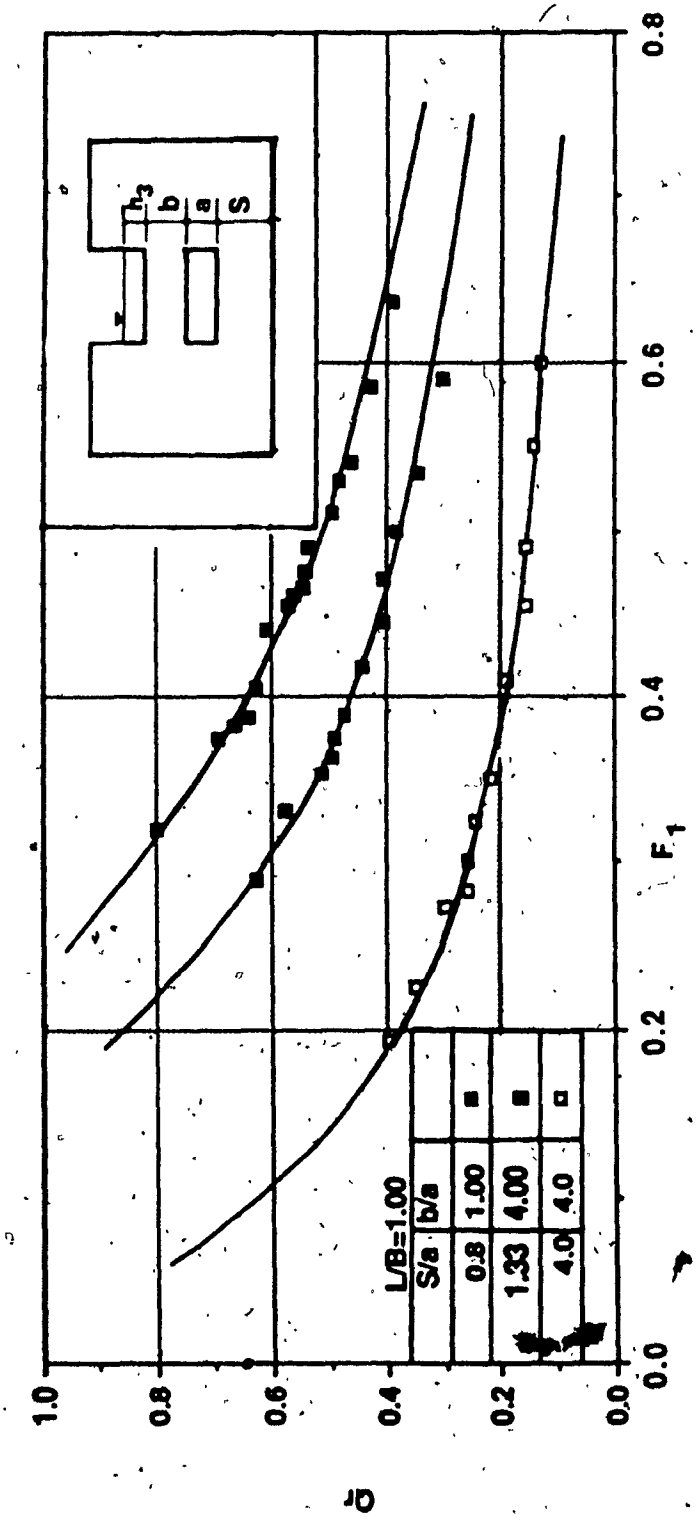

Figure 4.7 Variation of Qr with Froude Number F_1

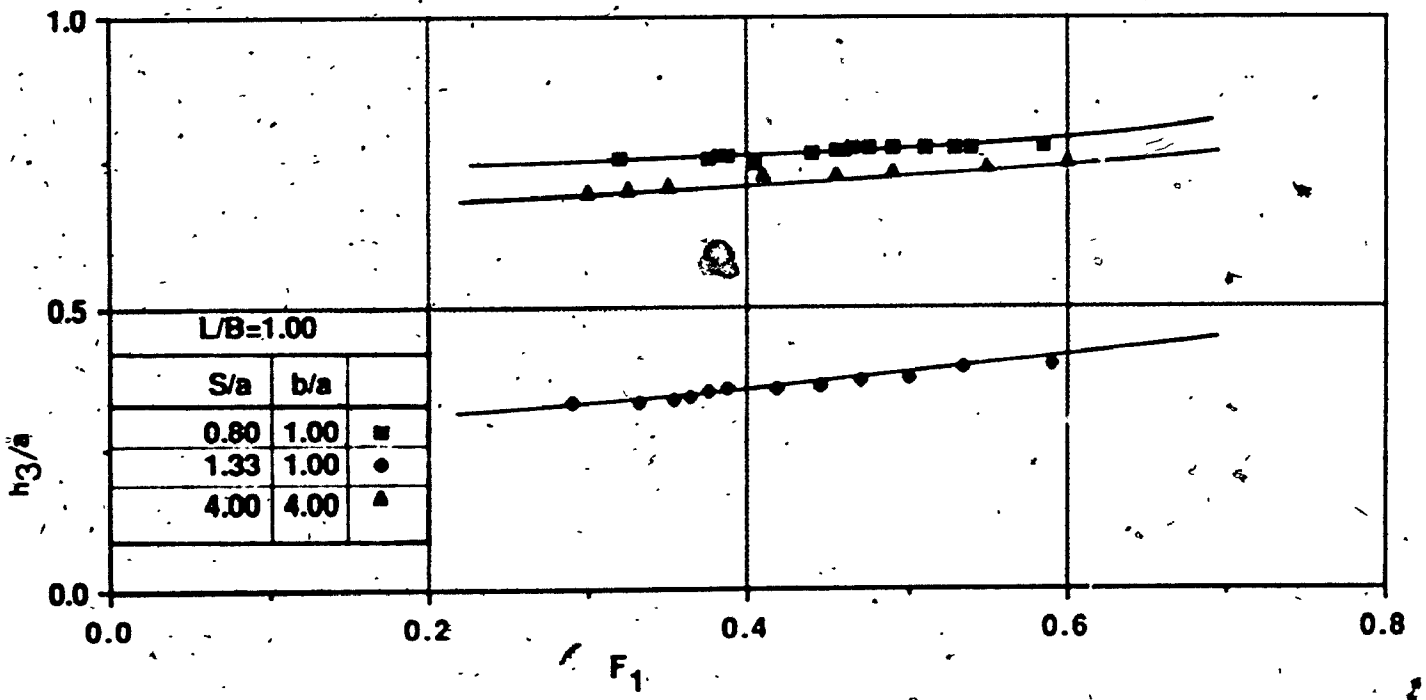

Figure 4.8 Variation of h_3 /a with Froude Number F_1

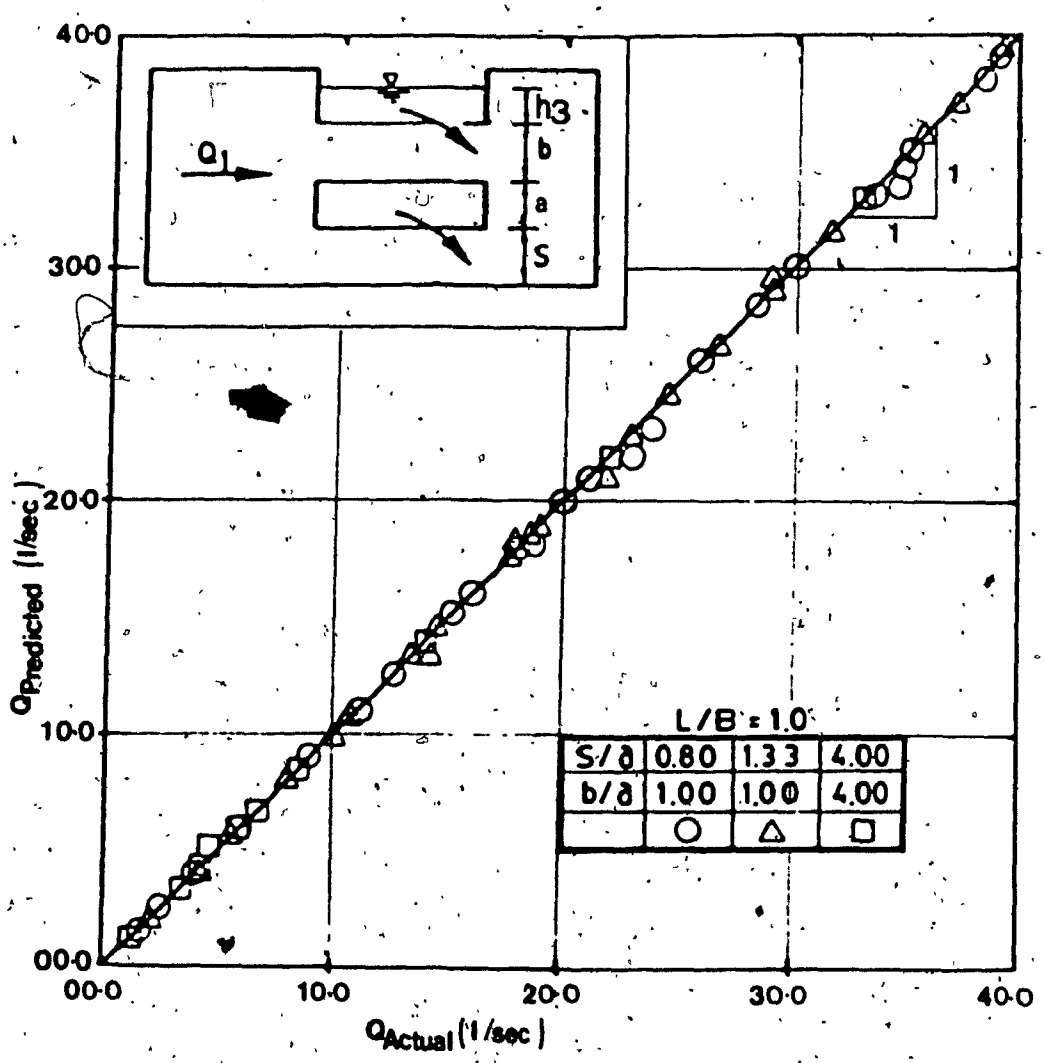

Figure 4.9 Correlation between Predicted Discharge and Measured Discharge through Weir-Orifice Unit

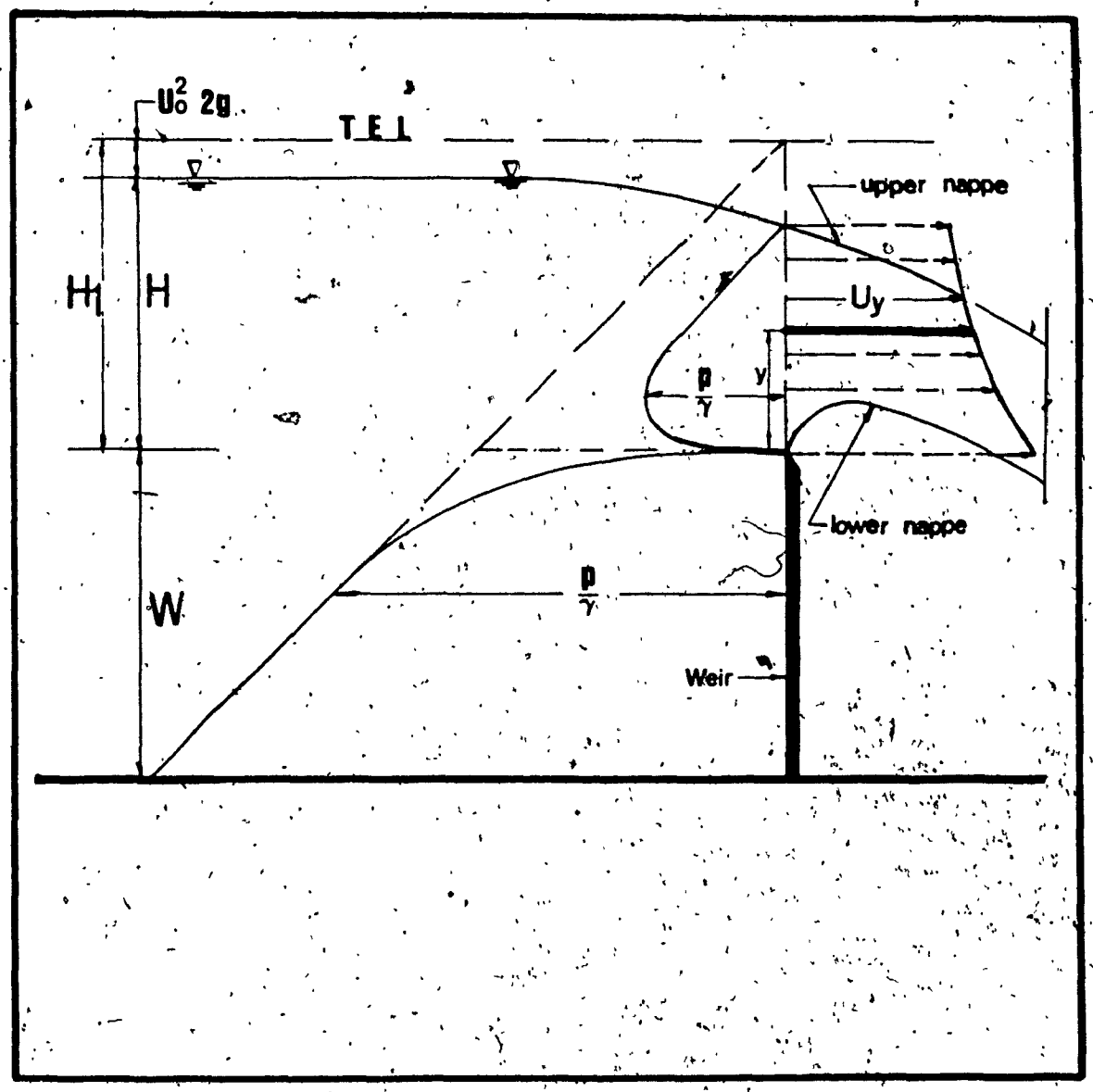

Figure 5.1 Definition Sketch: Rectangular Sharp-crested Weir

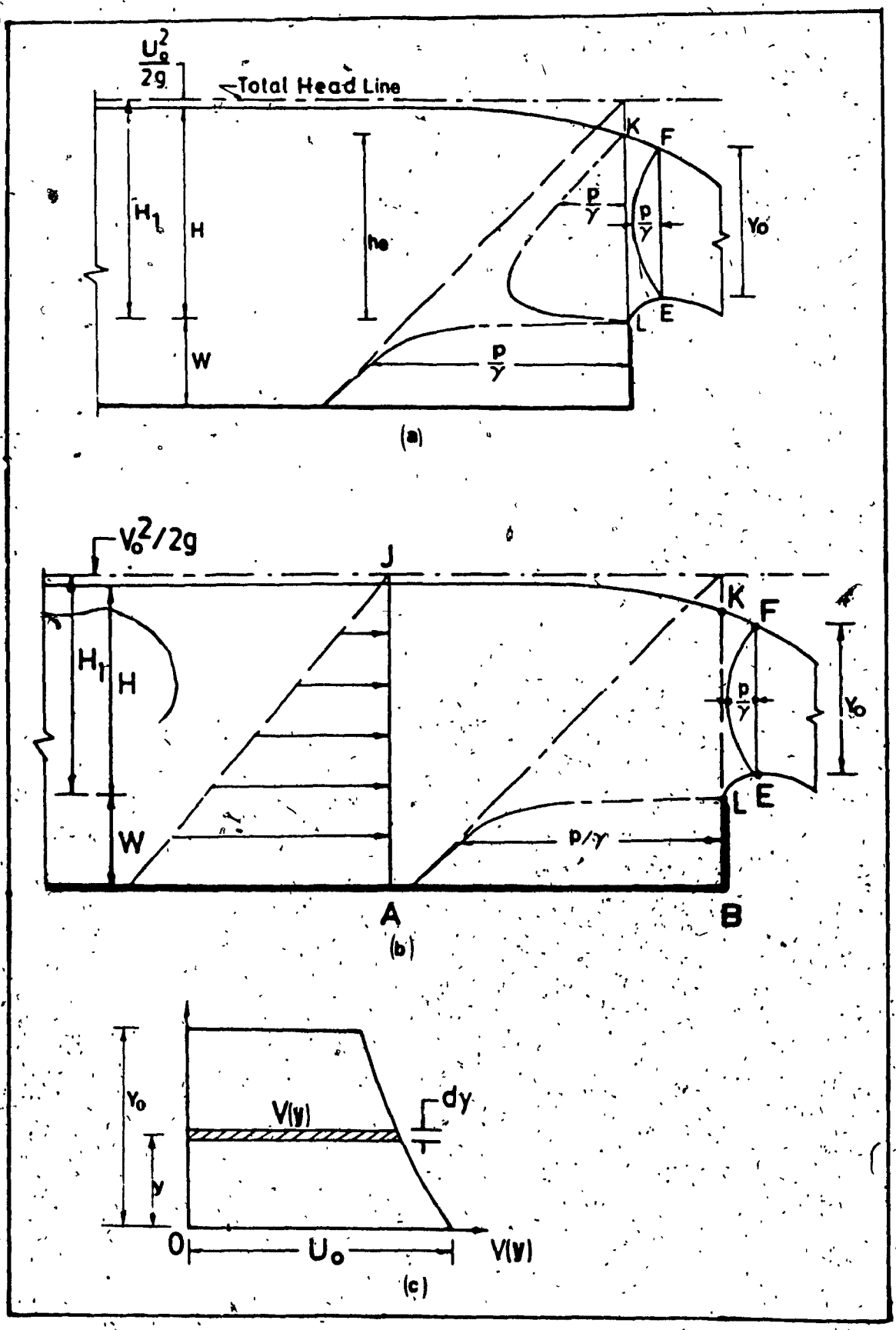

Figure 5.2 Flow Pattern over Rectangular Sharp-crested Weir

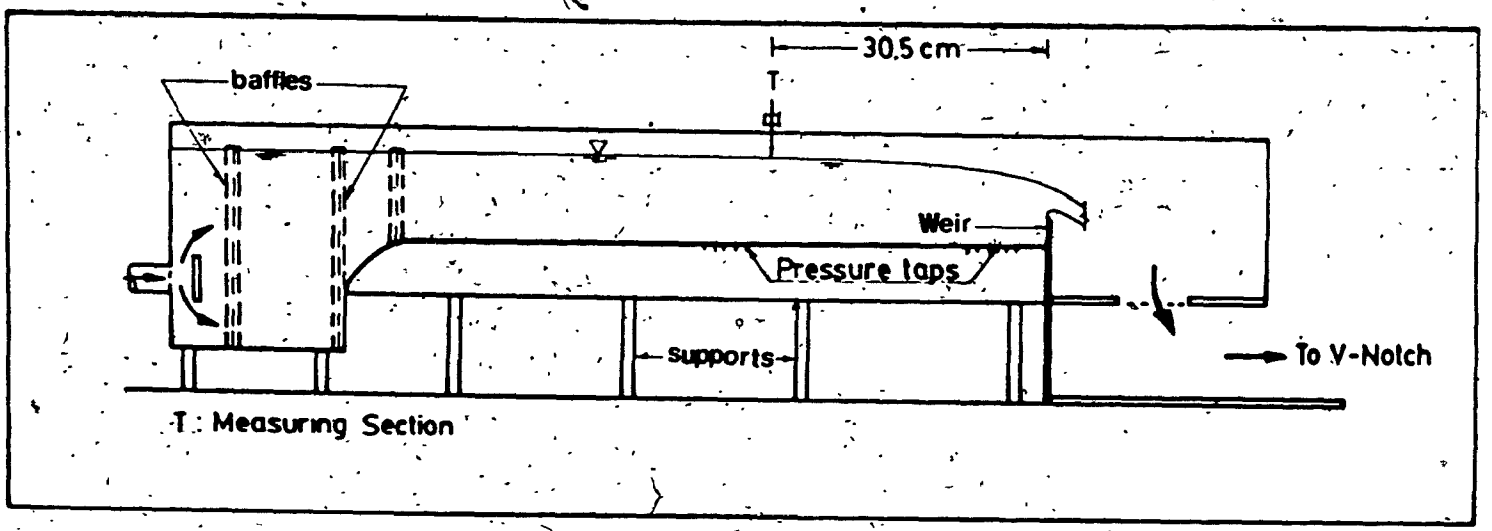

Figure 5.3 Experimental Set-up for Sharp-crested Weir Study

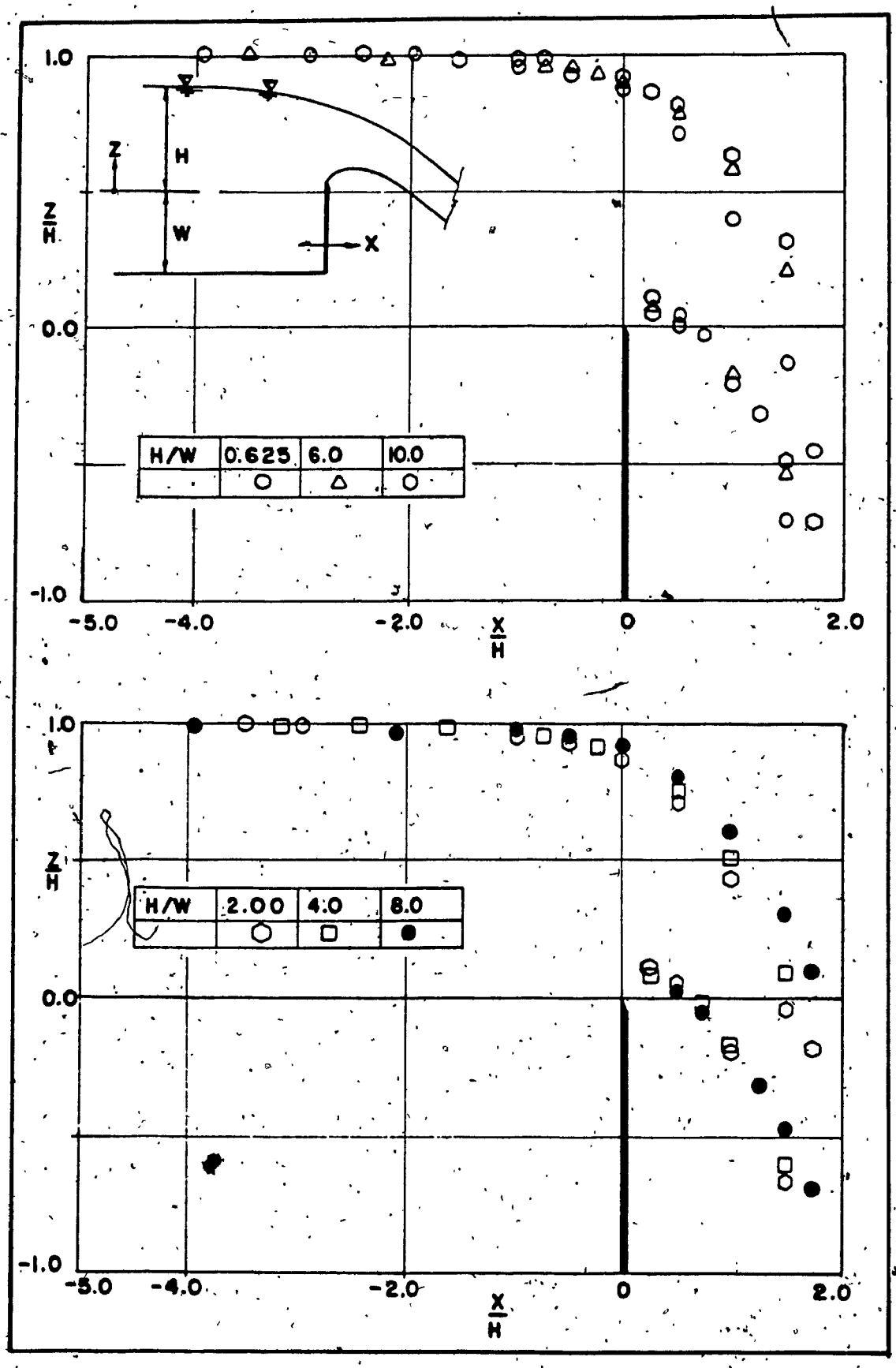

Figure 5.4 Composite Plot of Non-dimensional Water Surface Profile for values of H/W in the Weir Range(0.0 < H/W < 8.57)

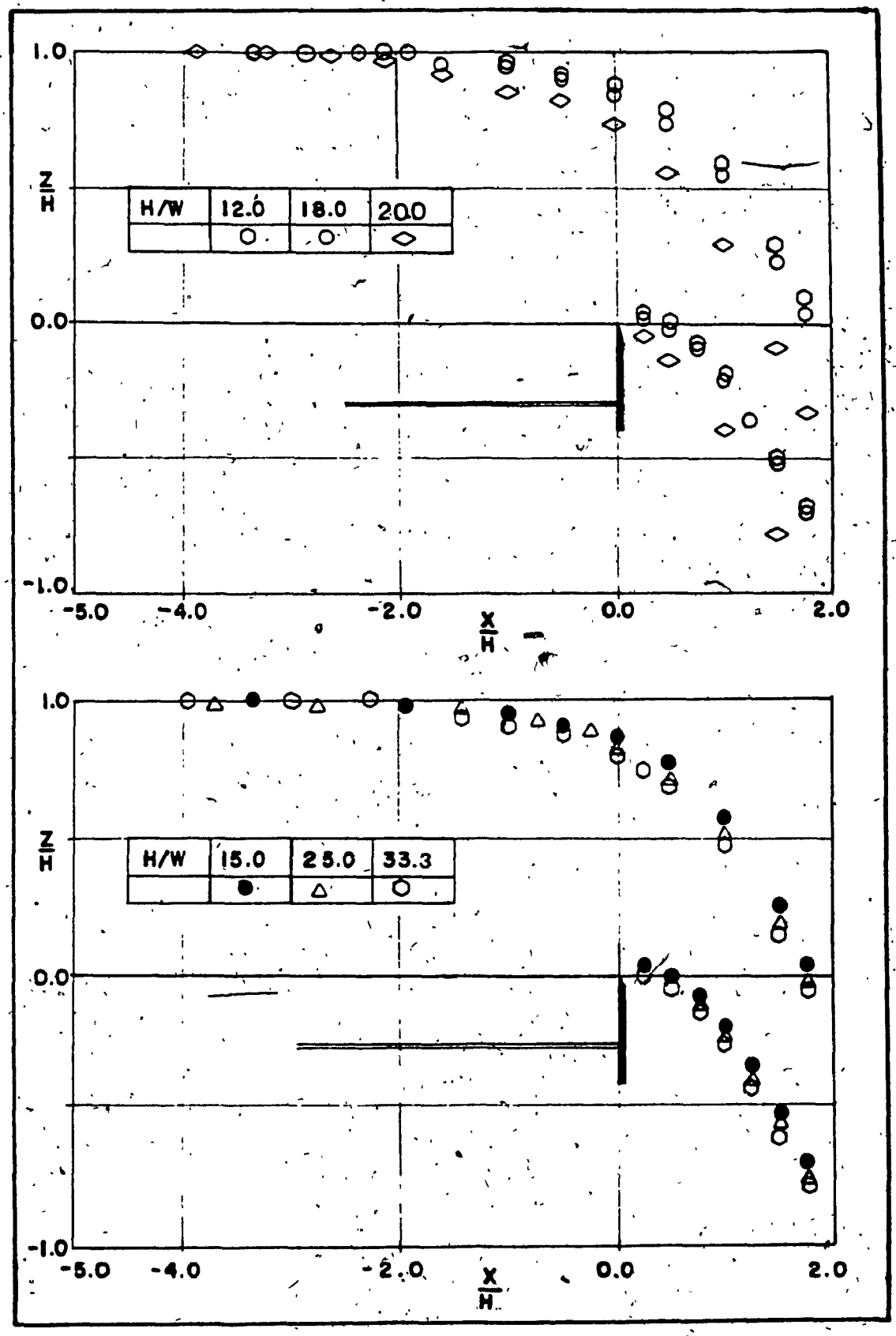

Figure 5.5 Composite Plot of Non-dimensional Water Surface Profile for values of H/W in the Sill Range(10.0 < H/W <➡)

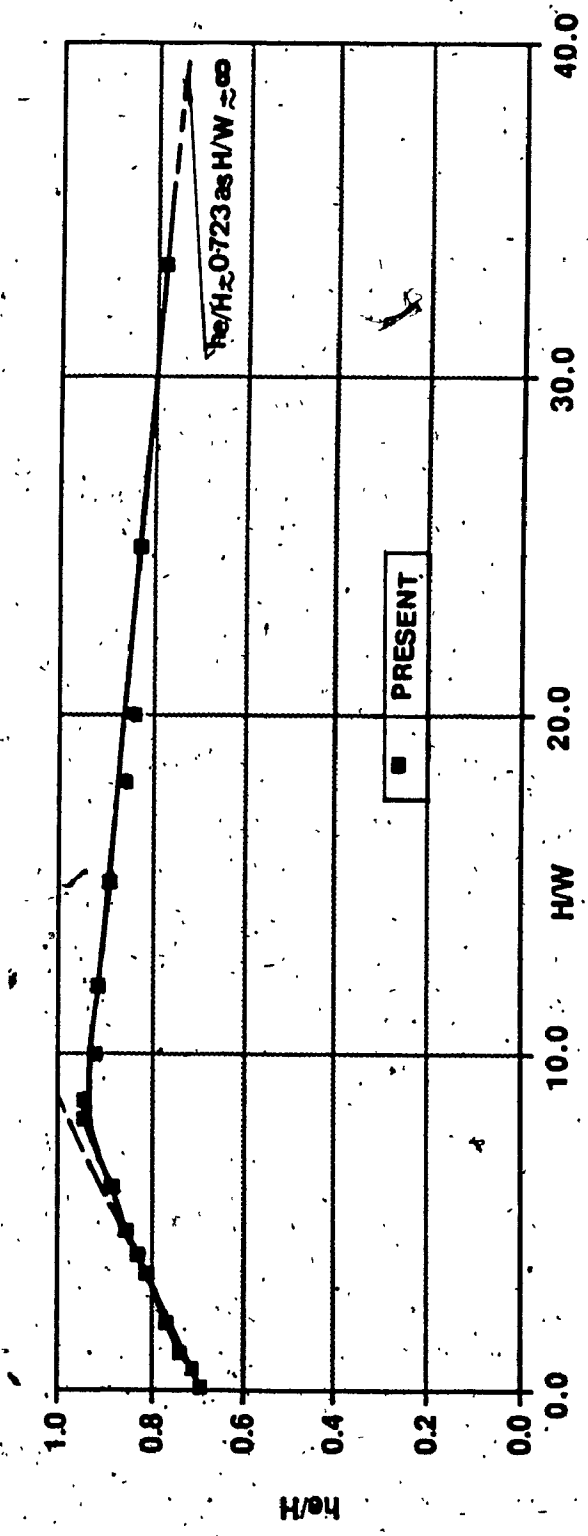

Figure 5.6 Variation of Depth Ratio he/H with H/W

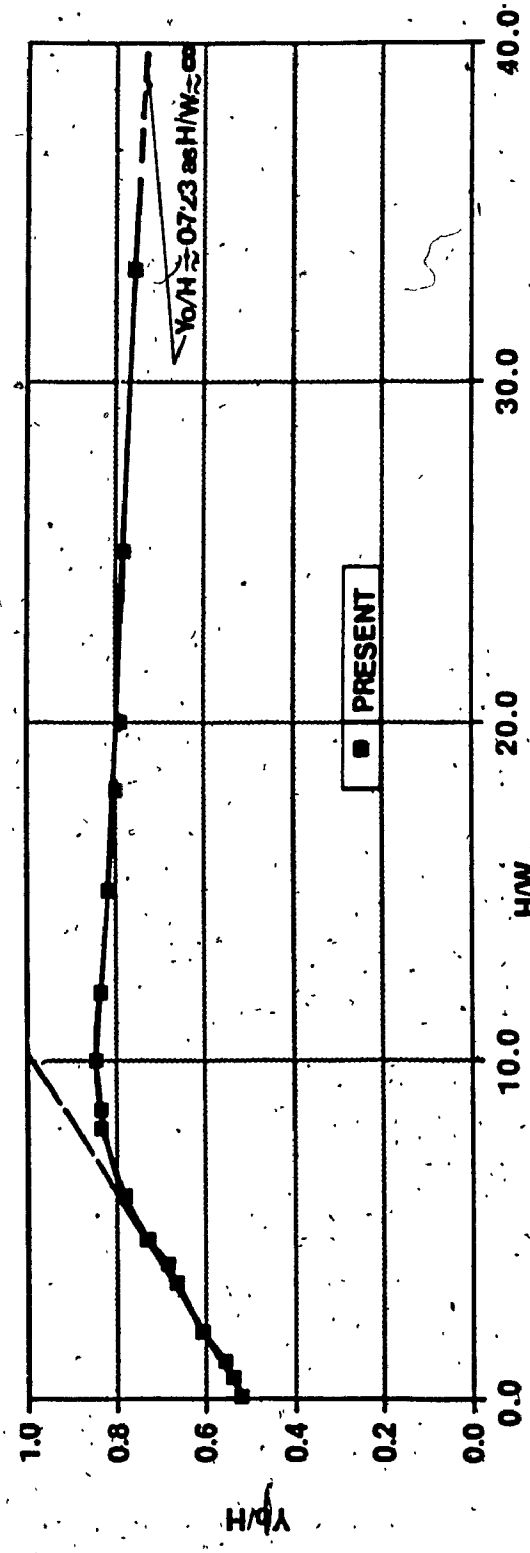

Figure 5.7 Variation of Depth Ratio Yo/H with H/W

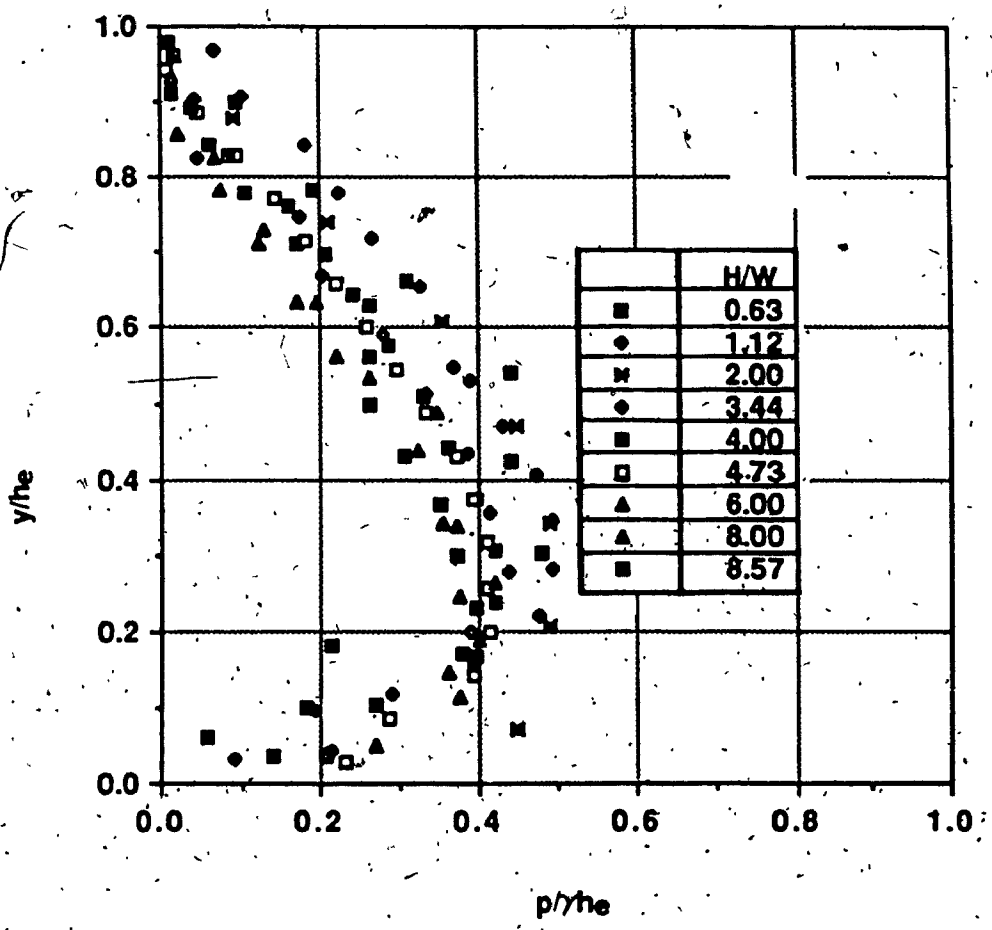

Figure 5.8 Variation of Non-dimensional Pressure $p/\gamma h_e$ with y/h_e at section KL for values of H/W in the Weir Range (0.0<H/W<8.57)

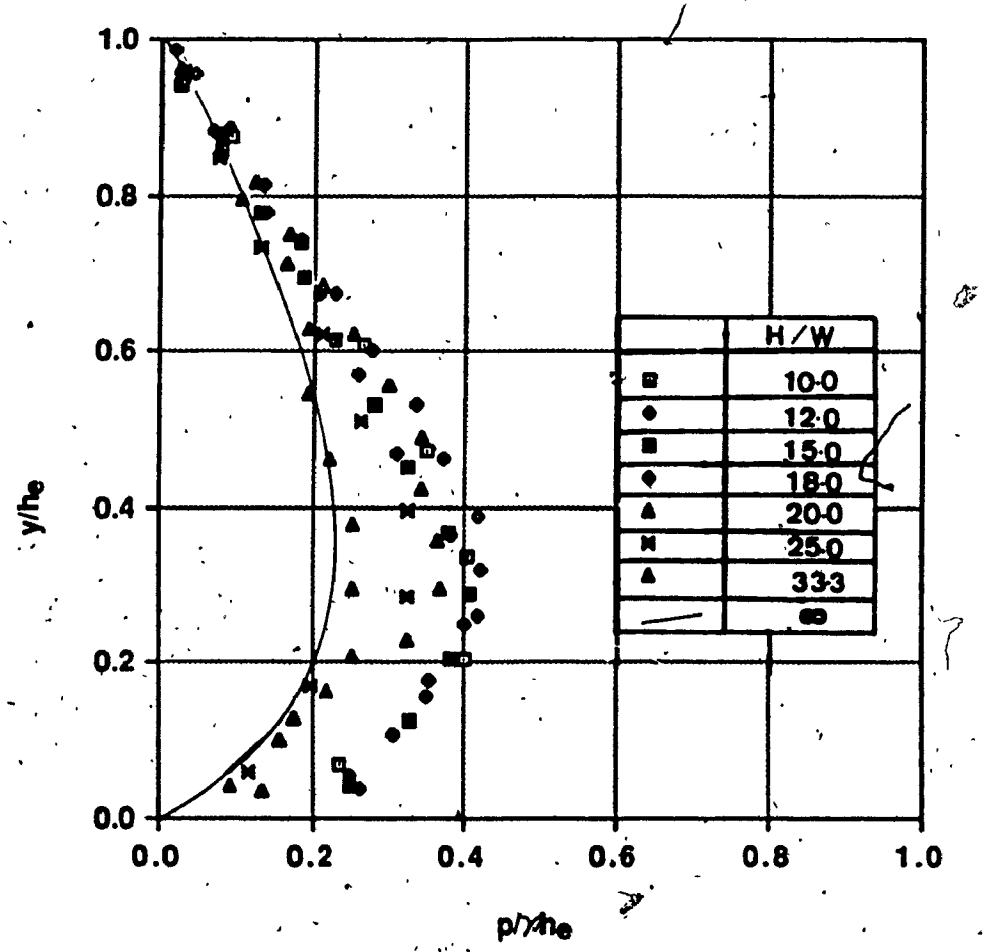

Figure 5.9 Variation of Non-dimensional Pressure $p/\gamma h_e$ with y/h_e at section KL for values of H/W in the SIII Range ($10.0 < H/W < \infty$)

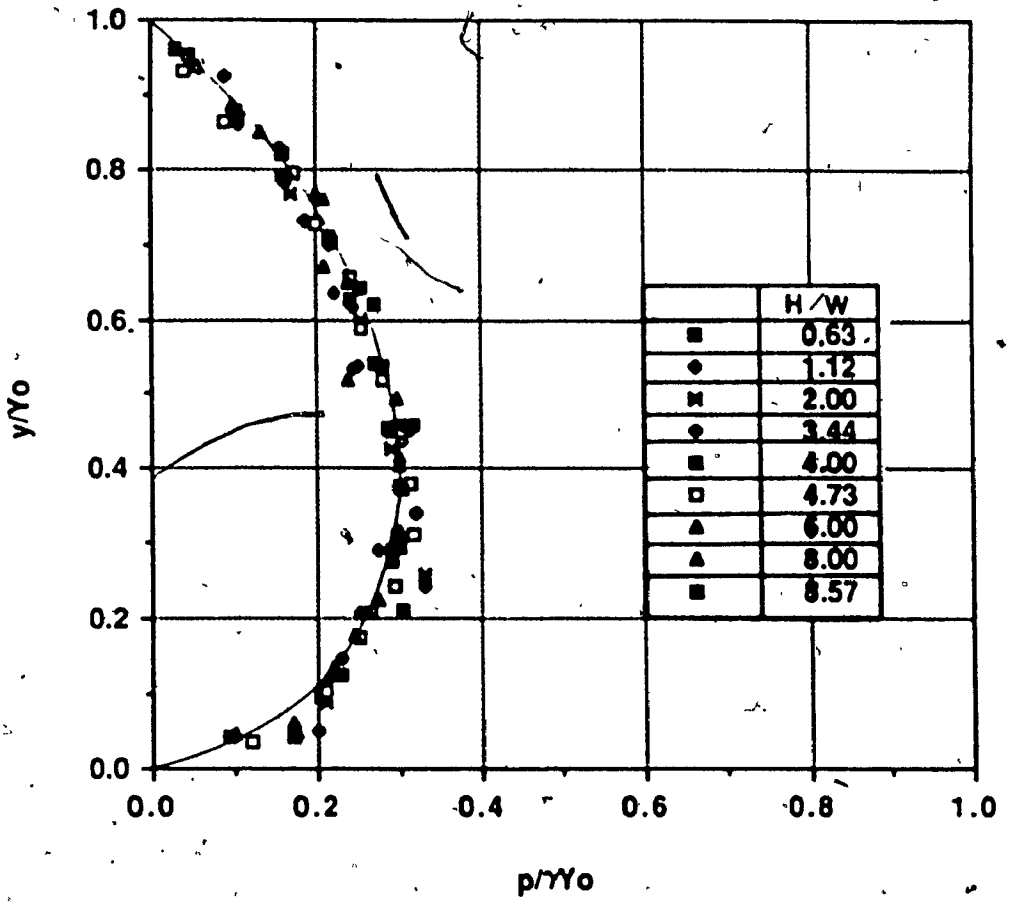

Figure 5.10 Variation of Non-dimensional Pressure p/γYo with y/Yo at section EF for values of H/W in the Weir Range (0.0<H/W<8.57)

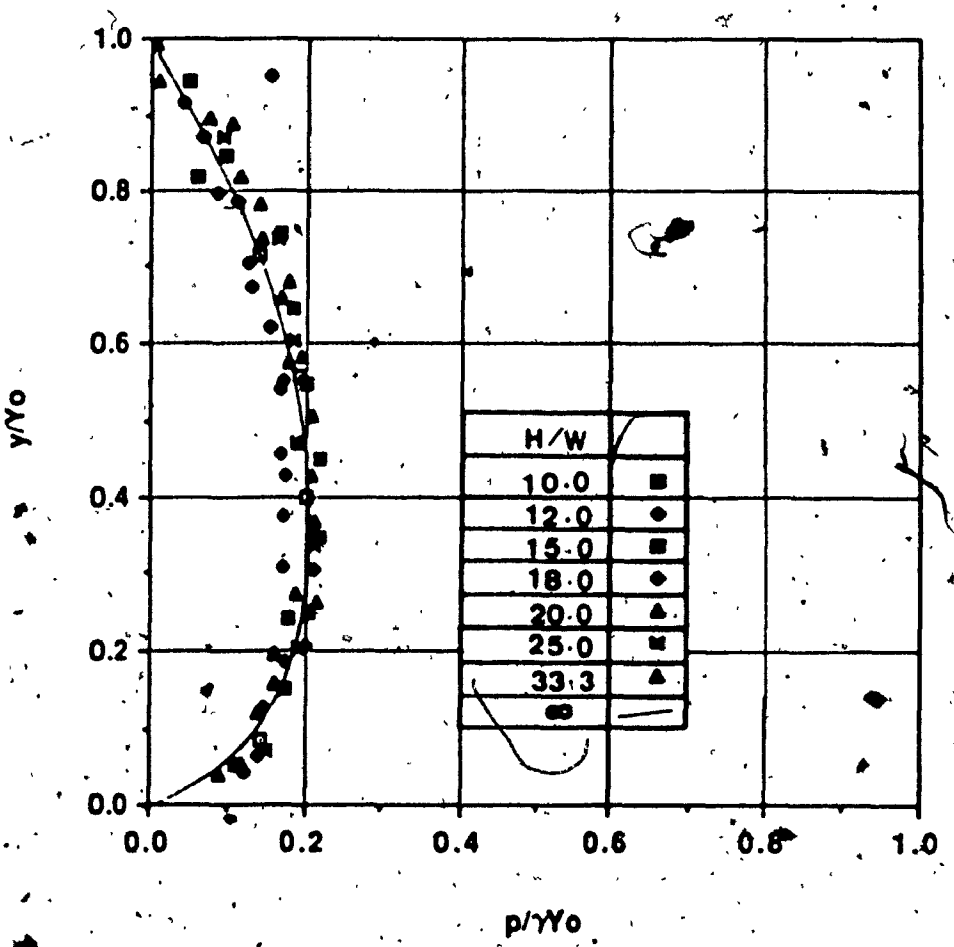

Figure 5.11 Variation of Non-dimensional Pressure p/γYo with y/Yo at section EF for values of H/W in the SIII Range (10.0≤H/W≤∞)

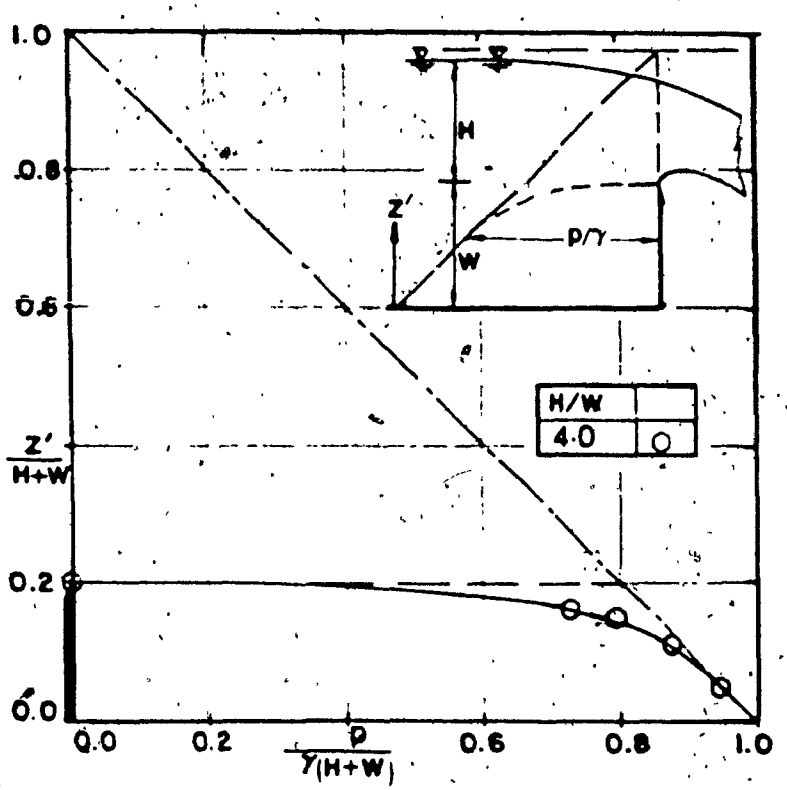

Figure 5.12 Pressure Distribution on the Weir Face for H/W = 4.00

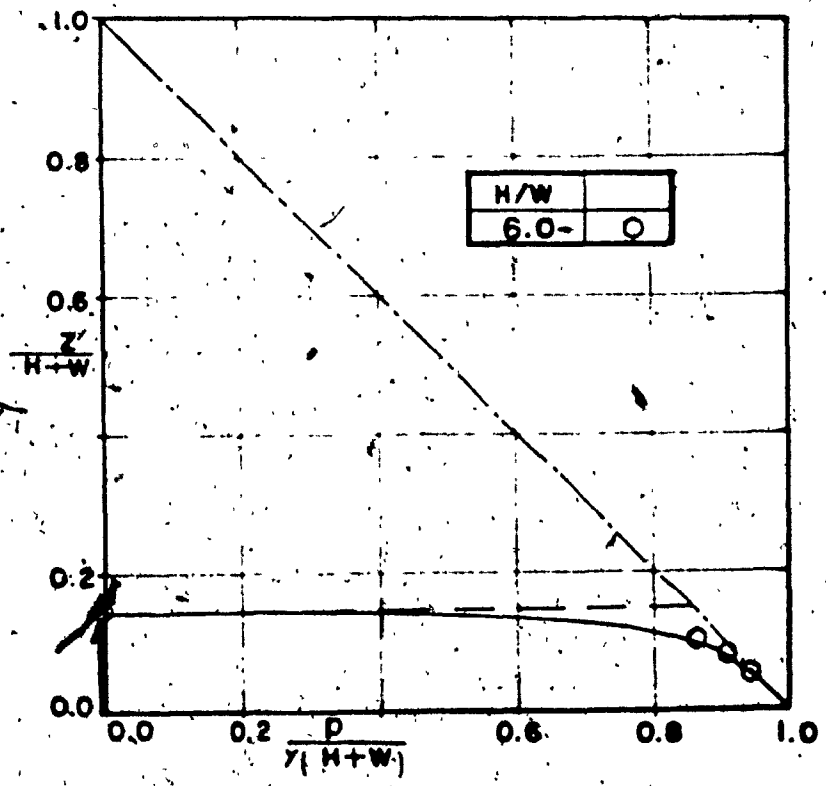

Figure 5.13 Pressure Distribution on the Weir Face for H/W = 6.00

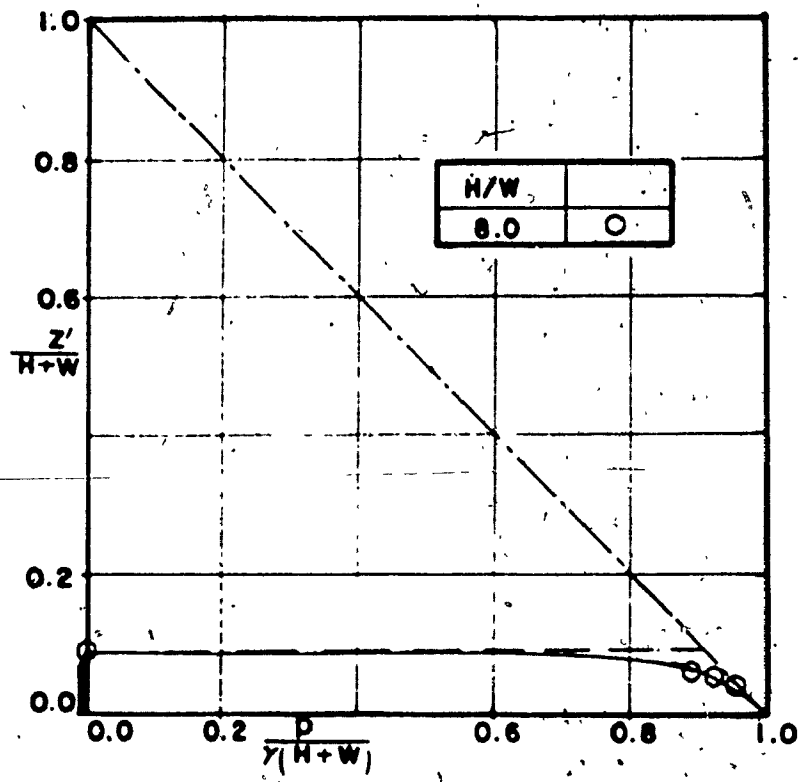

Figure 5.14 Pressure Distribution on the Weir Face for H/W = 8.0

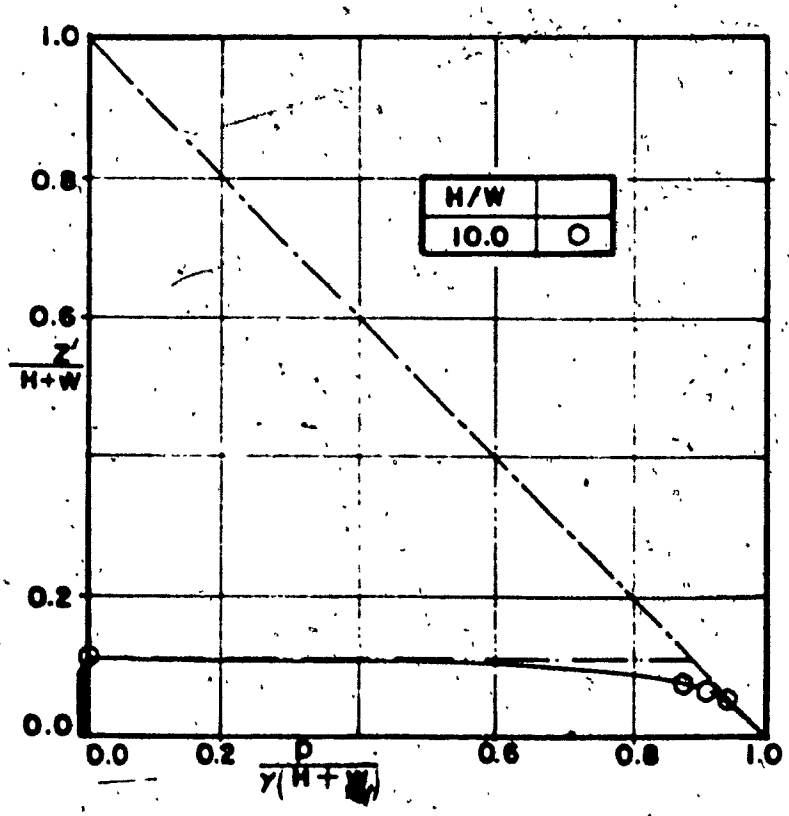

Figure 5.15 Pressure Distribution on the Weir Face for H/W = 10.0

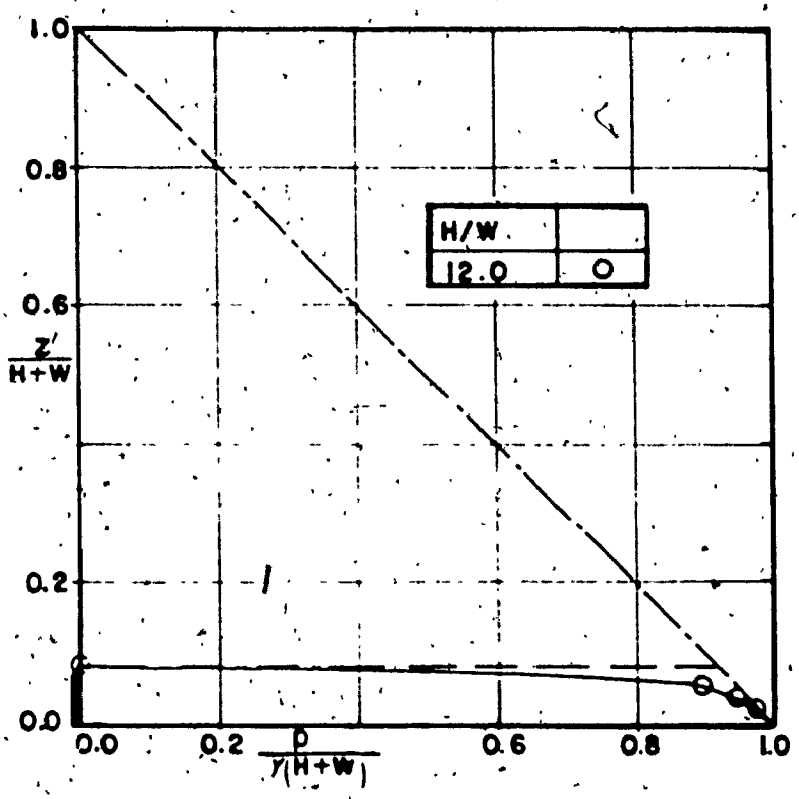

Figure 5.16 Pressure Distribution on the Weir Face for H/W = 12.0

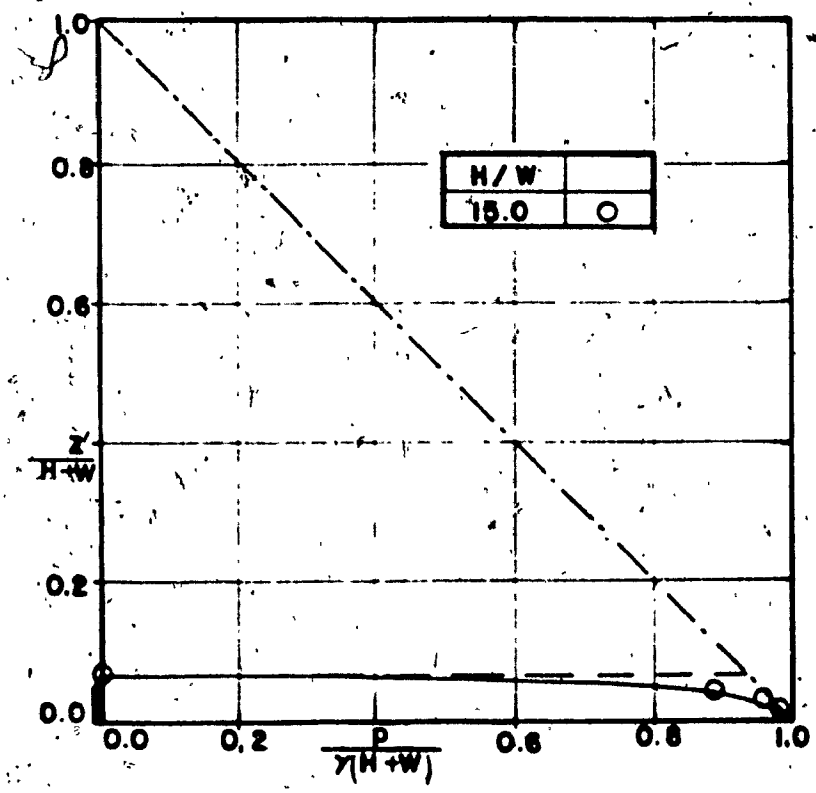

Figure 5.17 Pressure Distribution on the Weir Face for H/W = 15.0

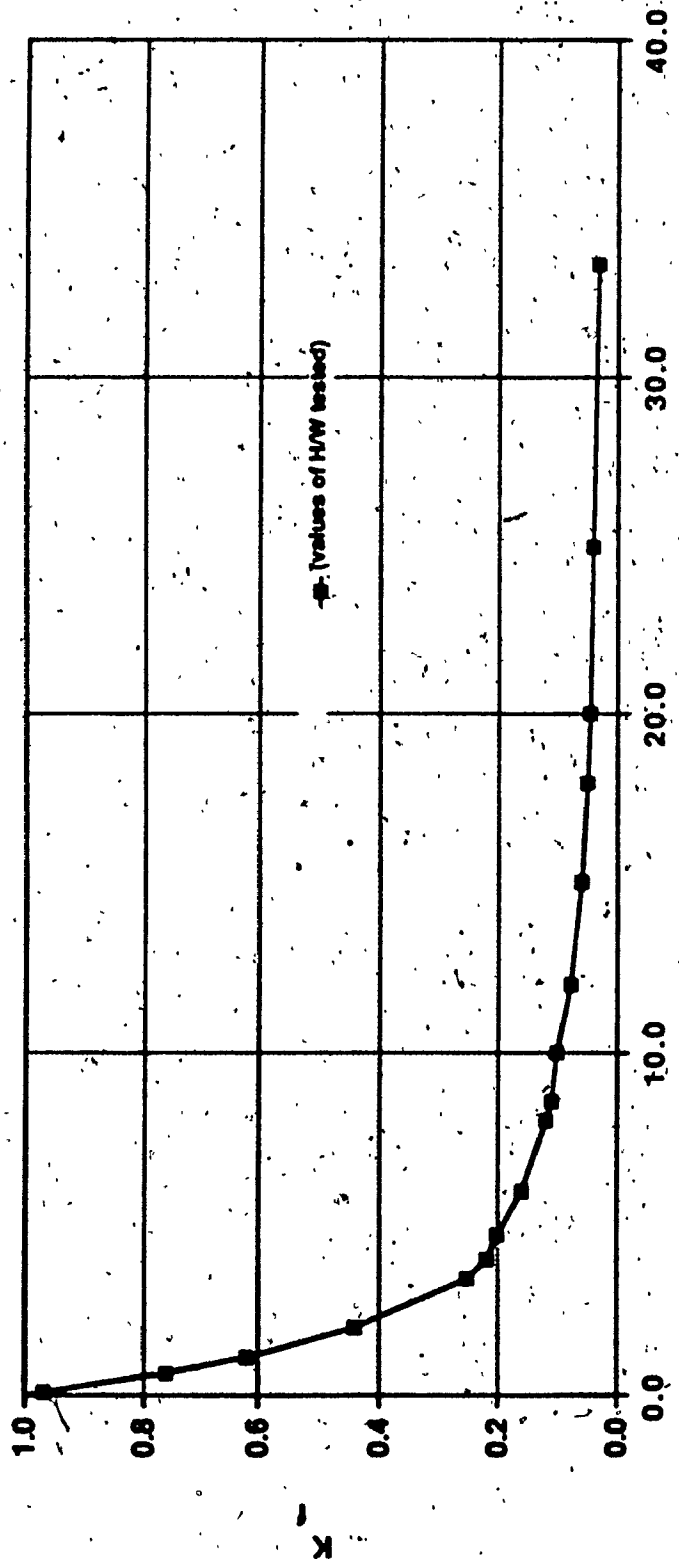

Figure 5.18 Variation of Pressure Coefficient with H/W

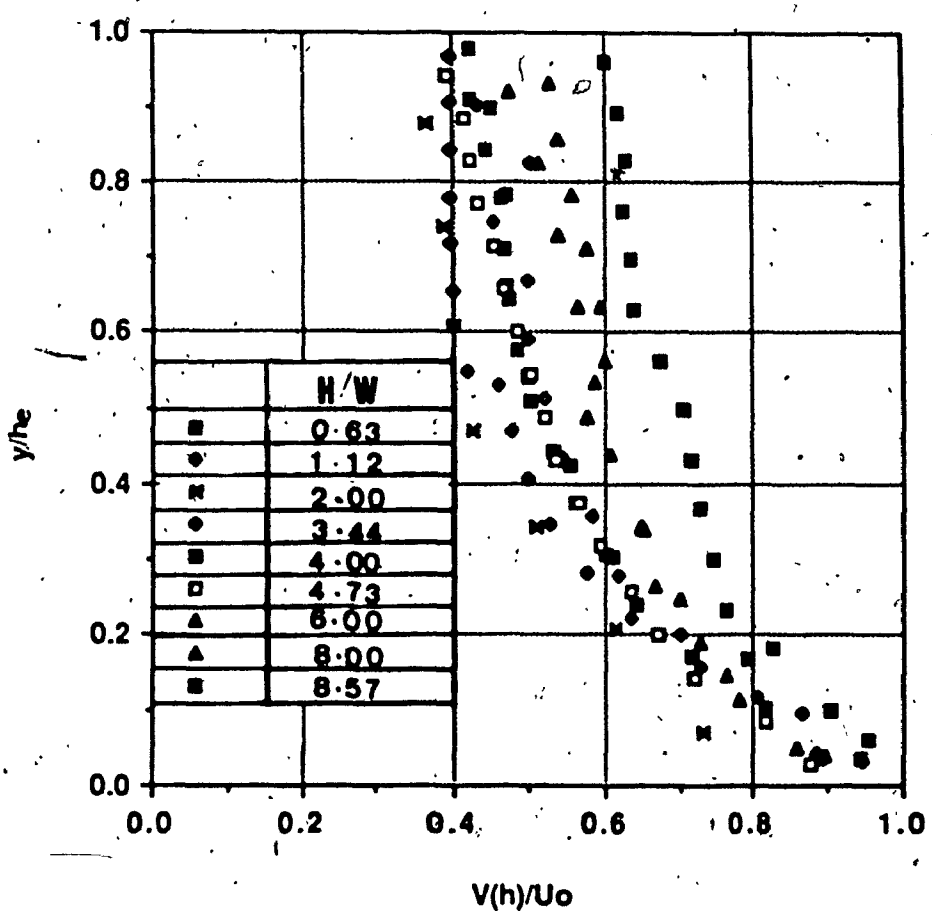

Figure 5.19 Variation of Non-dimensional Velocity V(h)/Uo with y/h_e at section KL for values of H/W in the Weir Range (0.0<H/W<8.57)

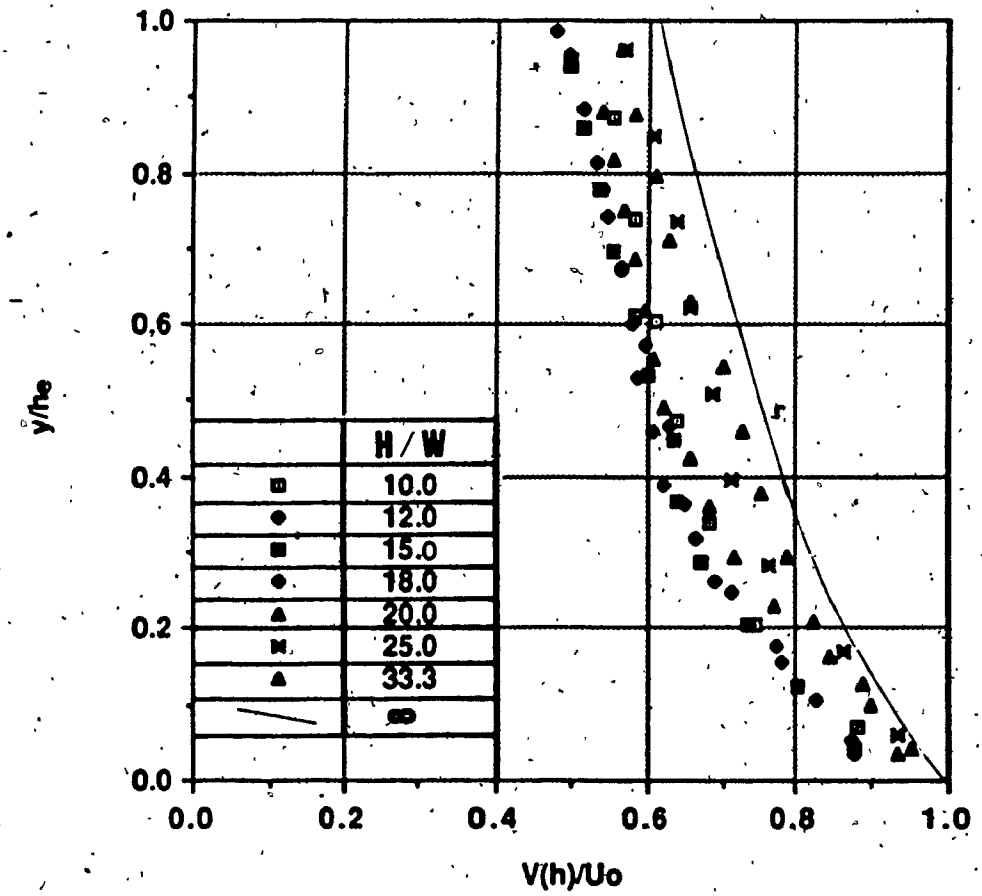

Figure 5.20 Variation of Non-dimensional Velocity V(h)/Uo with y/h_e at section KL for values of H/W in the Sill Range ($10.0 \leq H/W \leq \infty$)

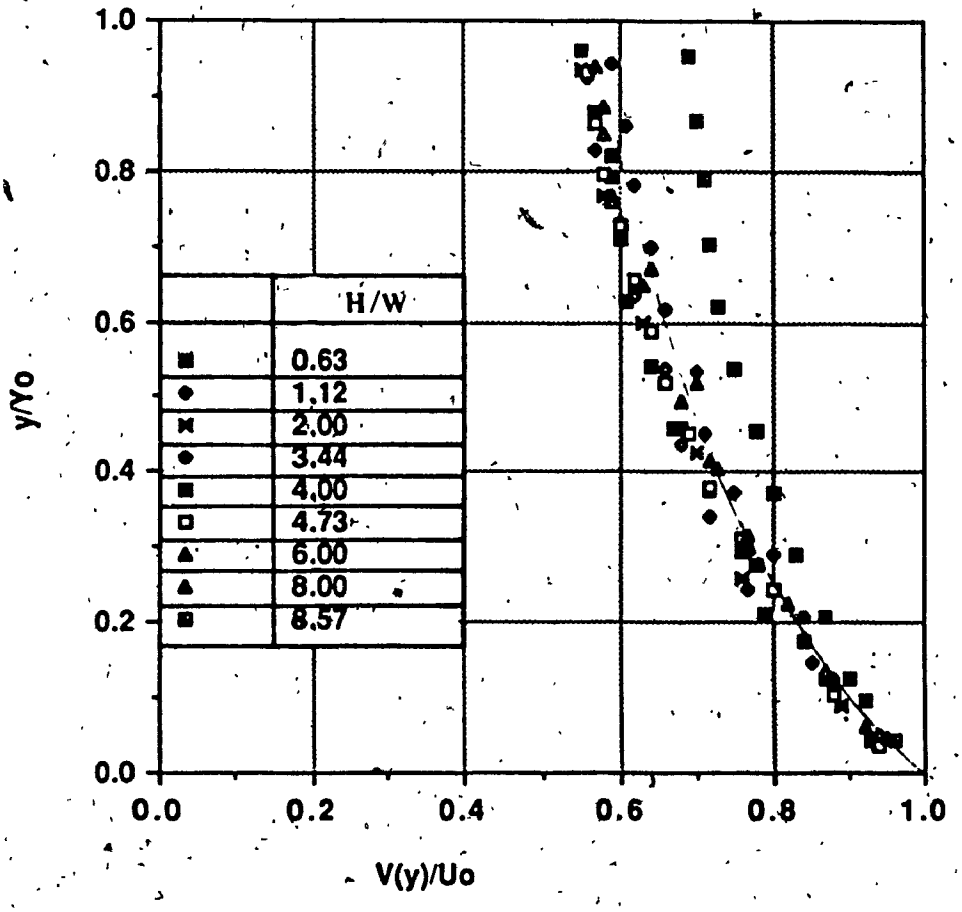

Figure 5.21 Variation of Non-dimensional Velocity V(y)/Uo with y/Yo at section EF for values of H/W in the Weir Range (0.0< H/W < 8.57)

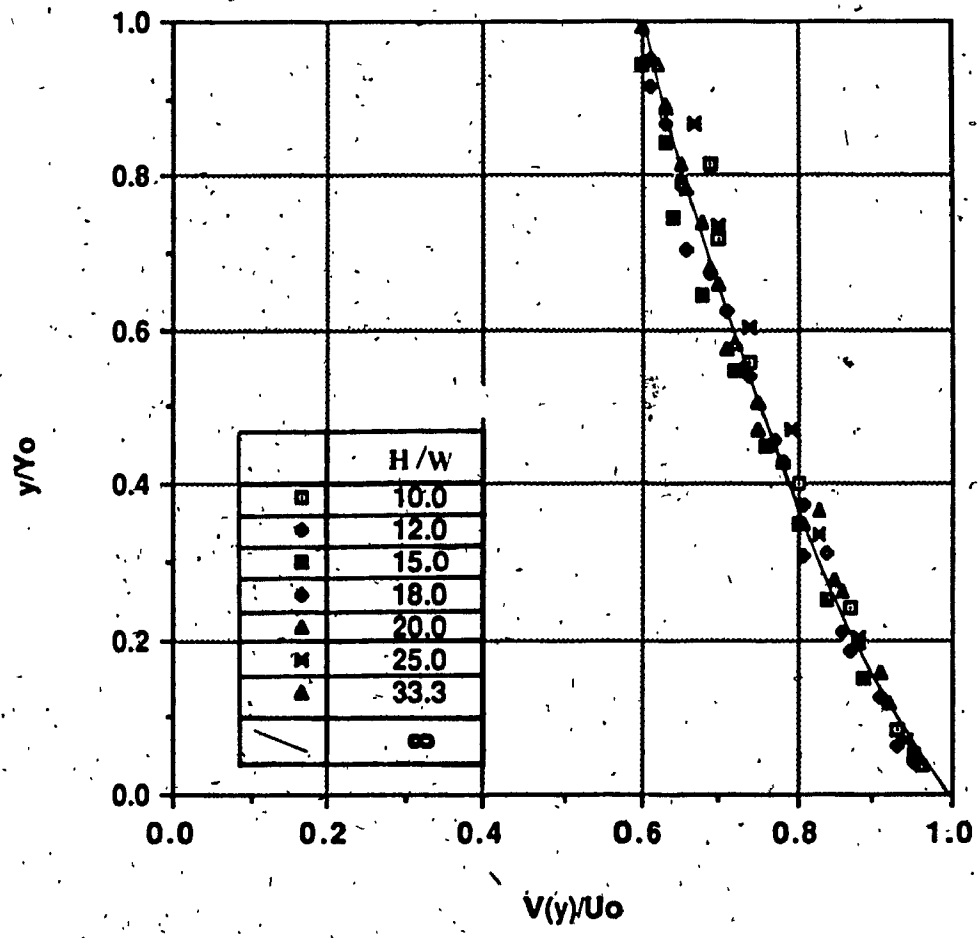

Figure 5.22 Variation of Non-dimensional Velocity V(y)/Uo with y/Yo at section EF for values of H/W in the Sill Range ($10.0 \leq H/W < \infty$)

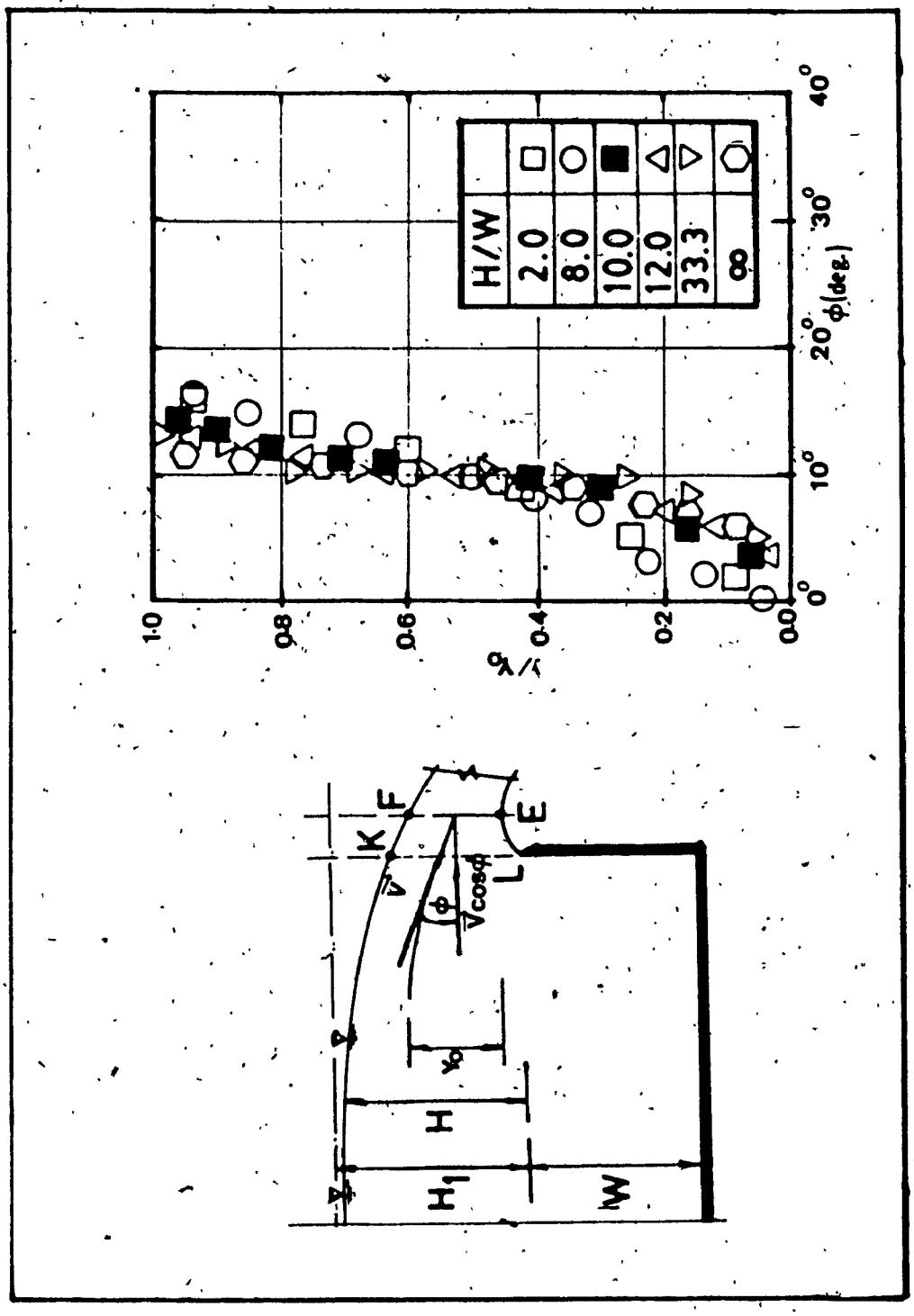

Figure 5.23 Variation of Angle of Inclination ϕ' at section EF with y/Yo

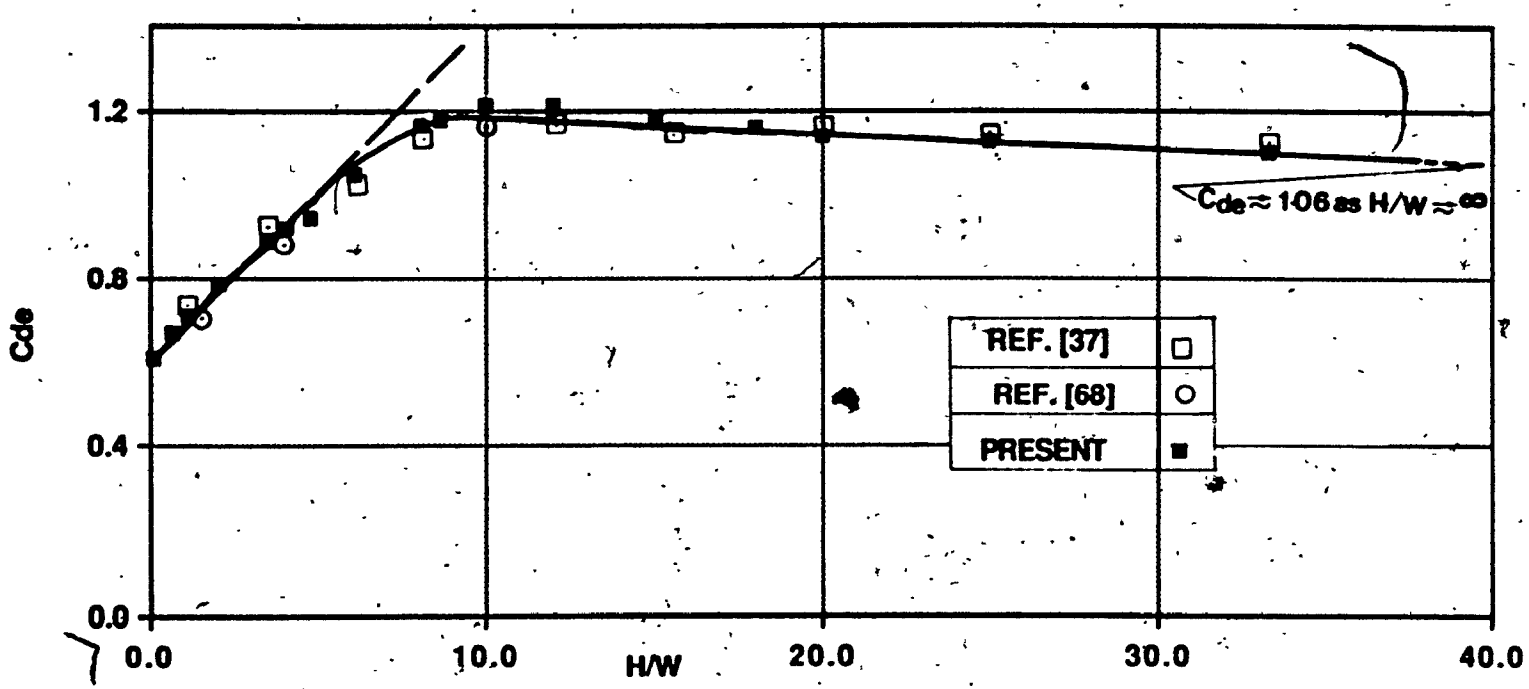

Figure 5.24 Variation of Discharge Coefficient Cde with H/W based on Momentum Relationship

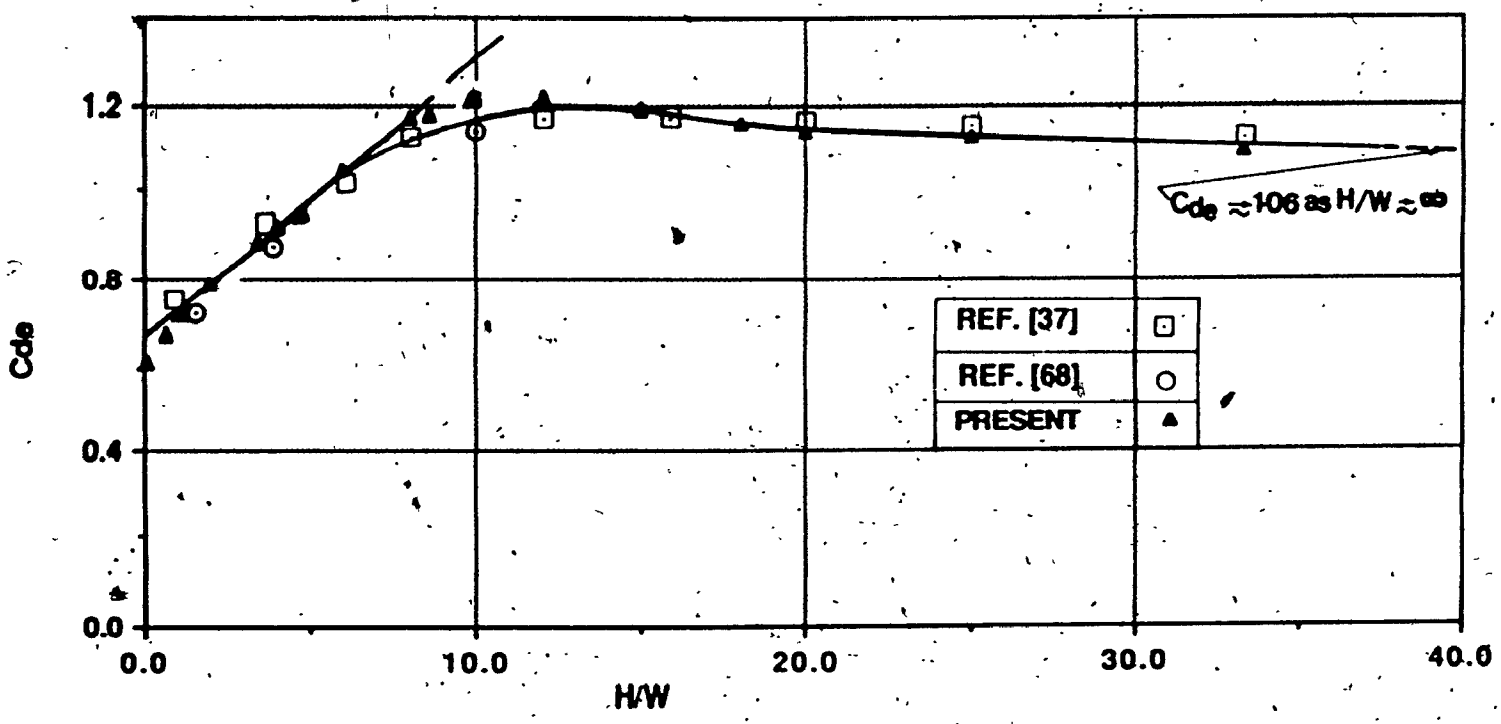

Figure 5.25 Variation of Discharge coefficient Cde with H/W

based on Velocity distribution at Section EF

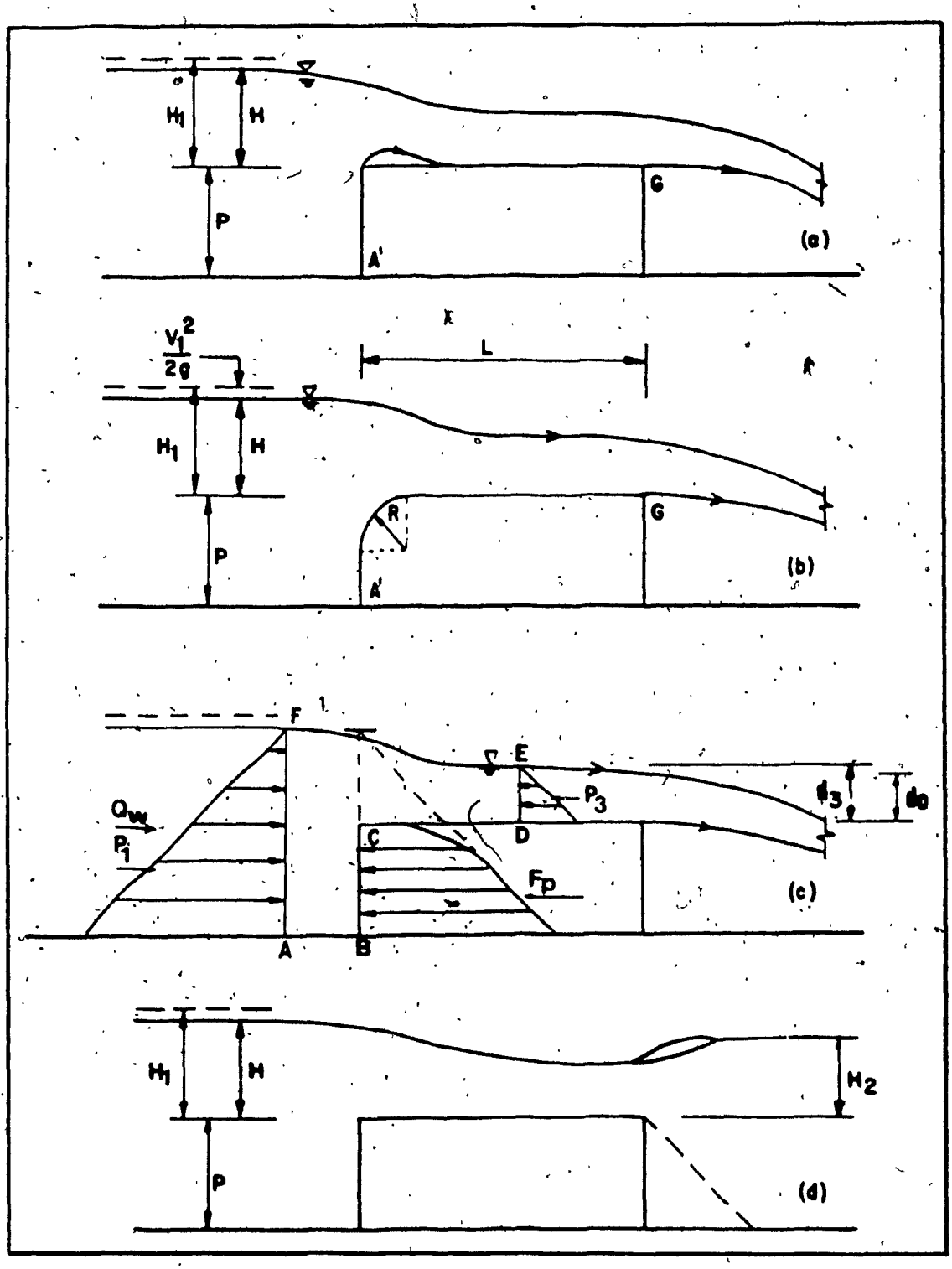

Figure 6.1 Definition Sketch: Rectangular Broad-crested Weir
(a) Free-flow Over Square-Edged Weir;
(b) Free-flow Over Round-nosed Weir;
(c) Control Volume for Momentum Relationship;
(d) Submerged Flow Over the Weir

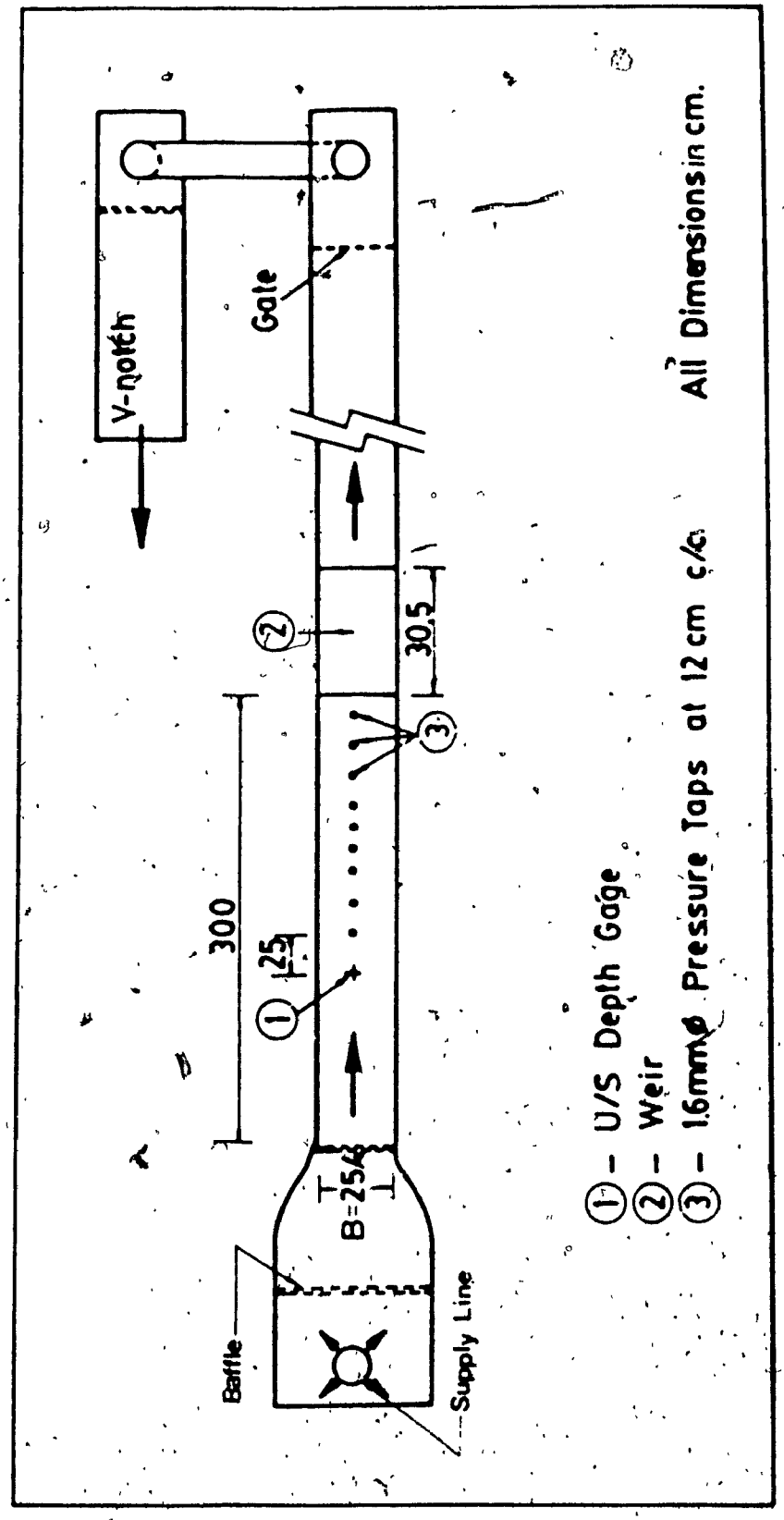

Figure 6.2 Experimental Set-up for Broad-crested Weir Study

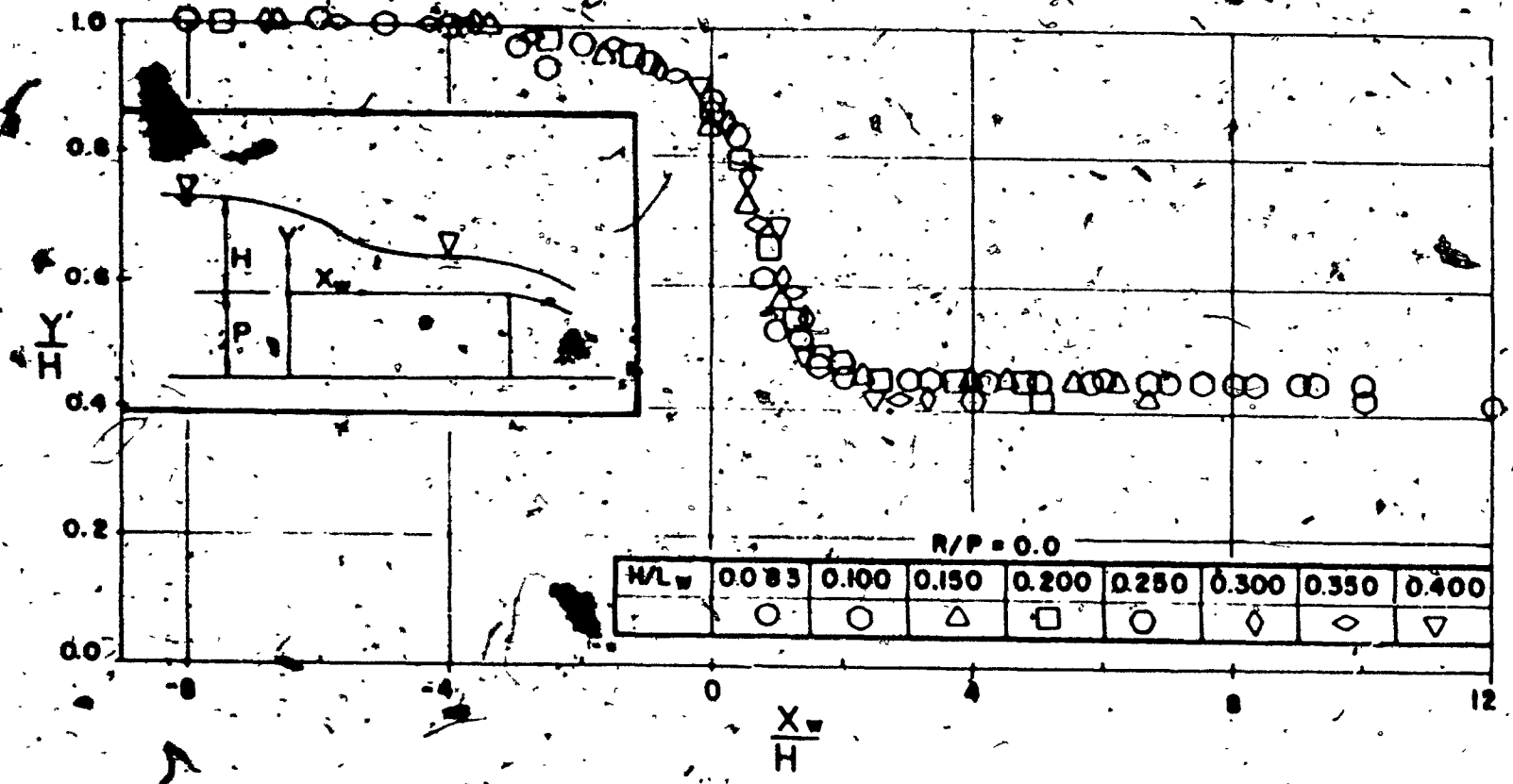

Figure 6.3 Non-dimensional Water Surface Profile for Broad-crested Weir with R/P=0.0

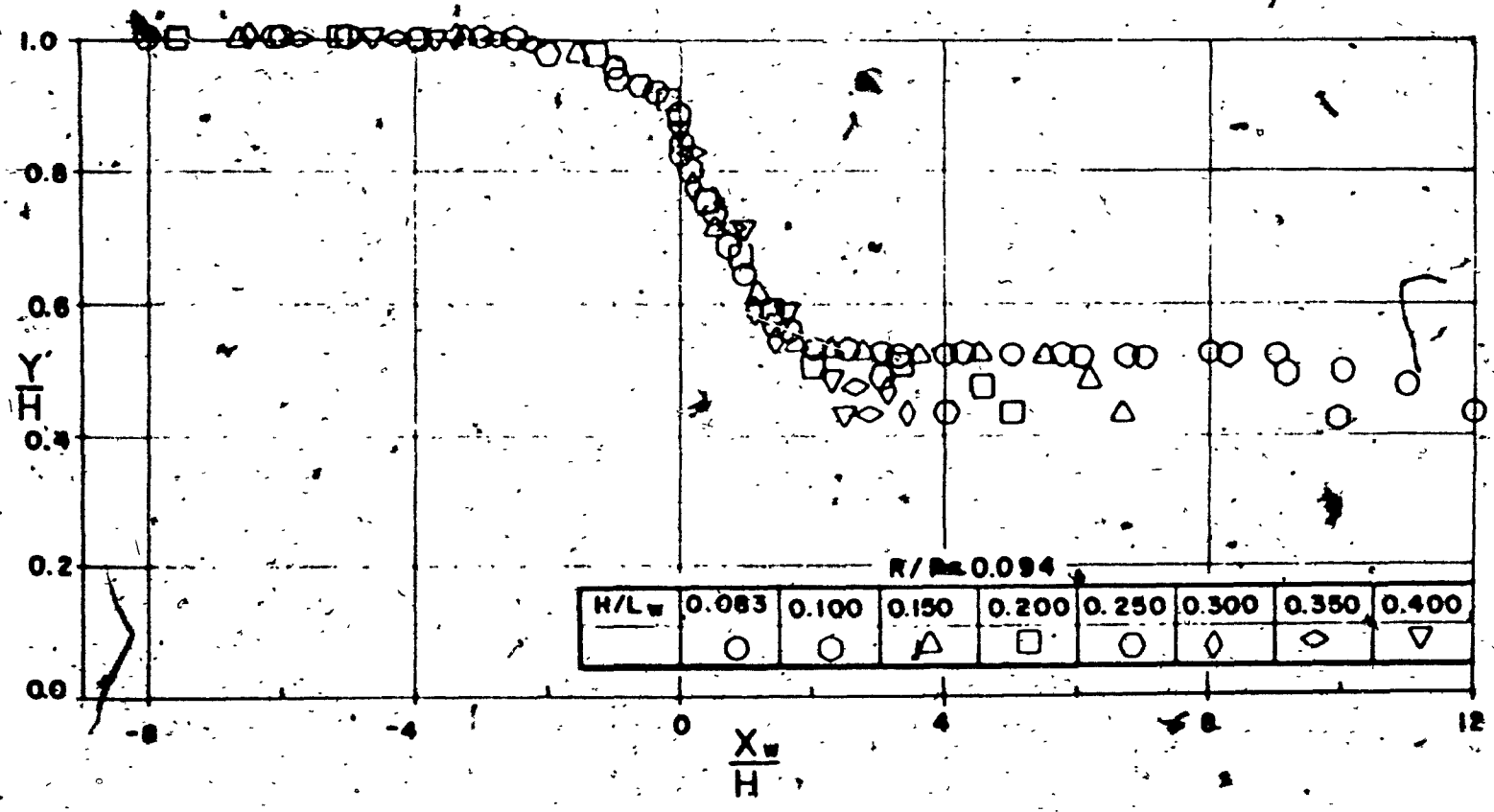

Figure 6.4 Non-dimensional Water Surface Profile for Broad-crested Weir with R/P=0.094

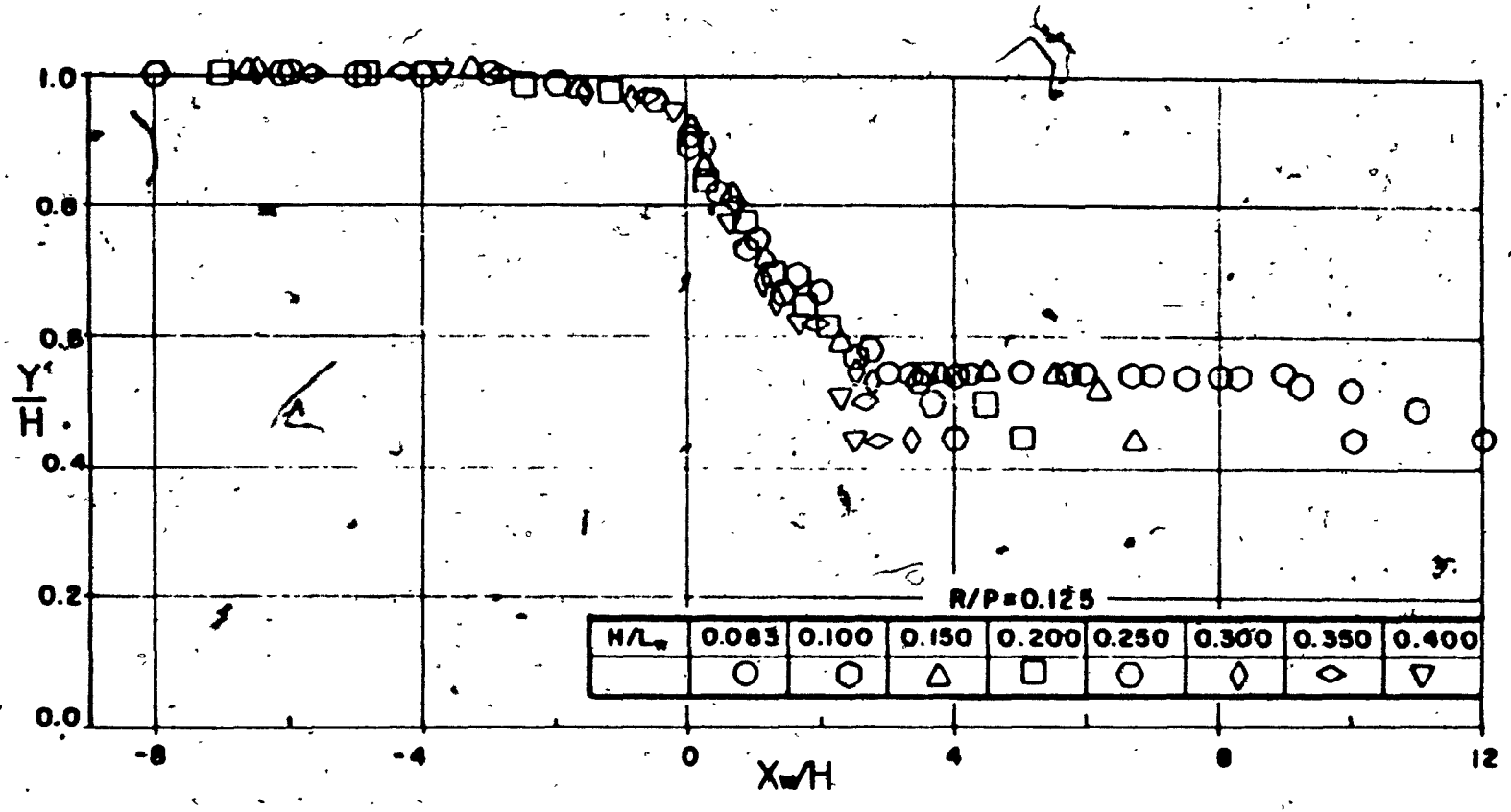

Figure 6.5 Non-dimensional Water Surface Profile for Broad-crested Weir with R/P=0.125

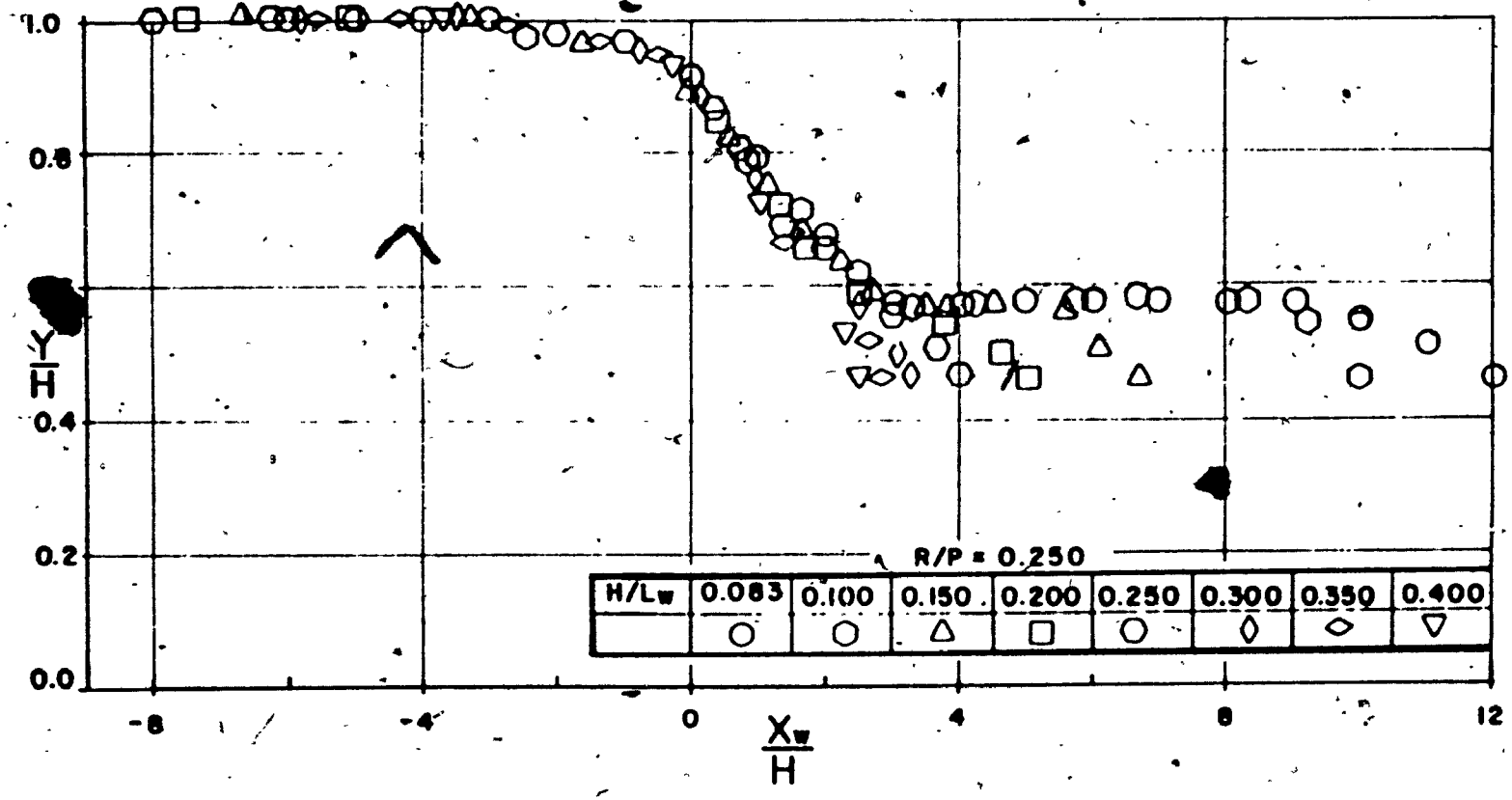

Figure 6.6 Non-dimensional Water Surface Profile for Broad-crested Weir with R/P=0.250

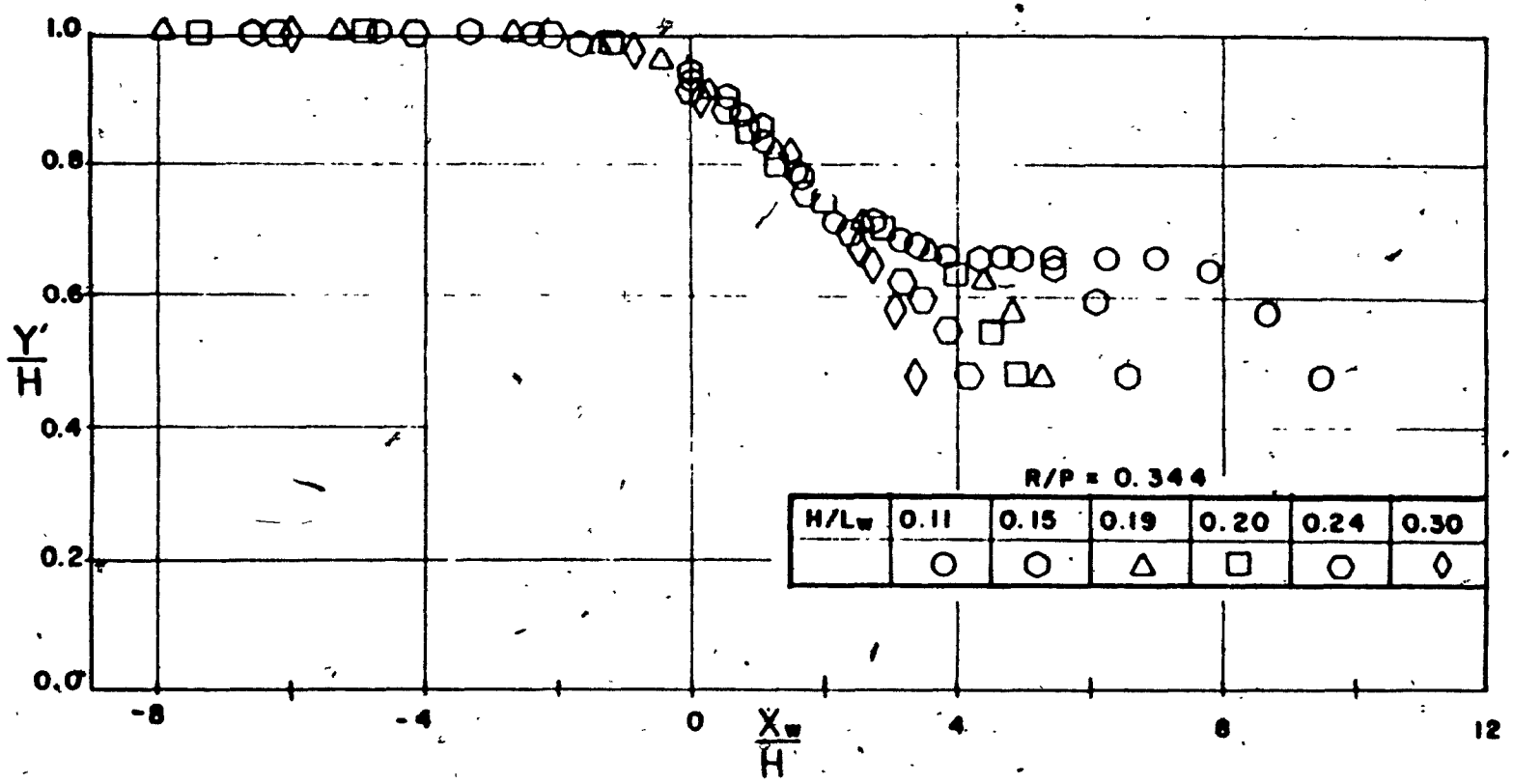

Figure 6.7 Non-dimensional Water Surface Profile for Broad-crested Weir with R/P=0.344

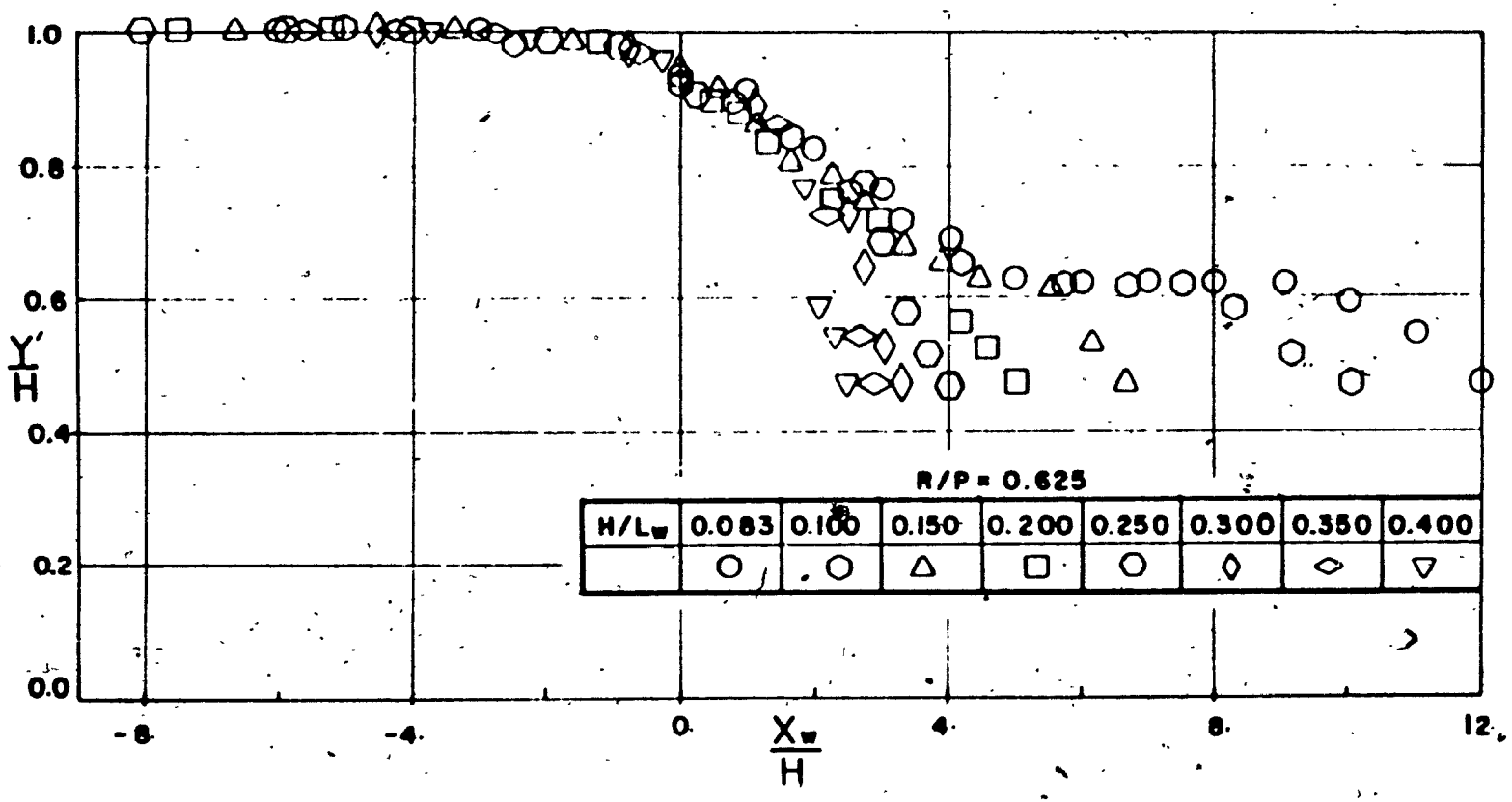

Figure 6.8 Non-dimensional Water Surface Profile for Broad-crested Weir with R/P=0.625

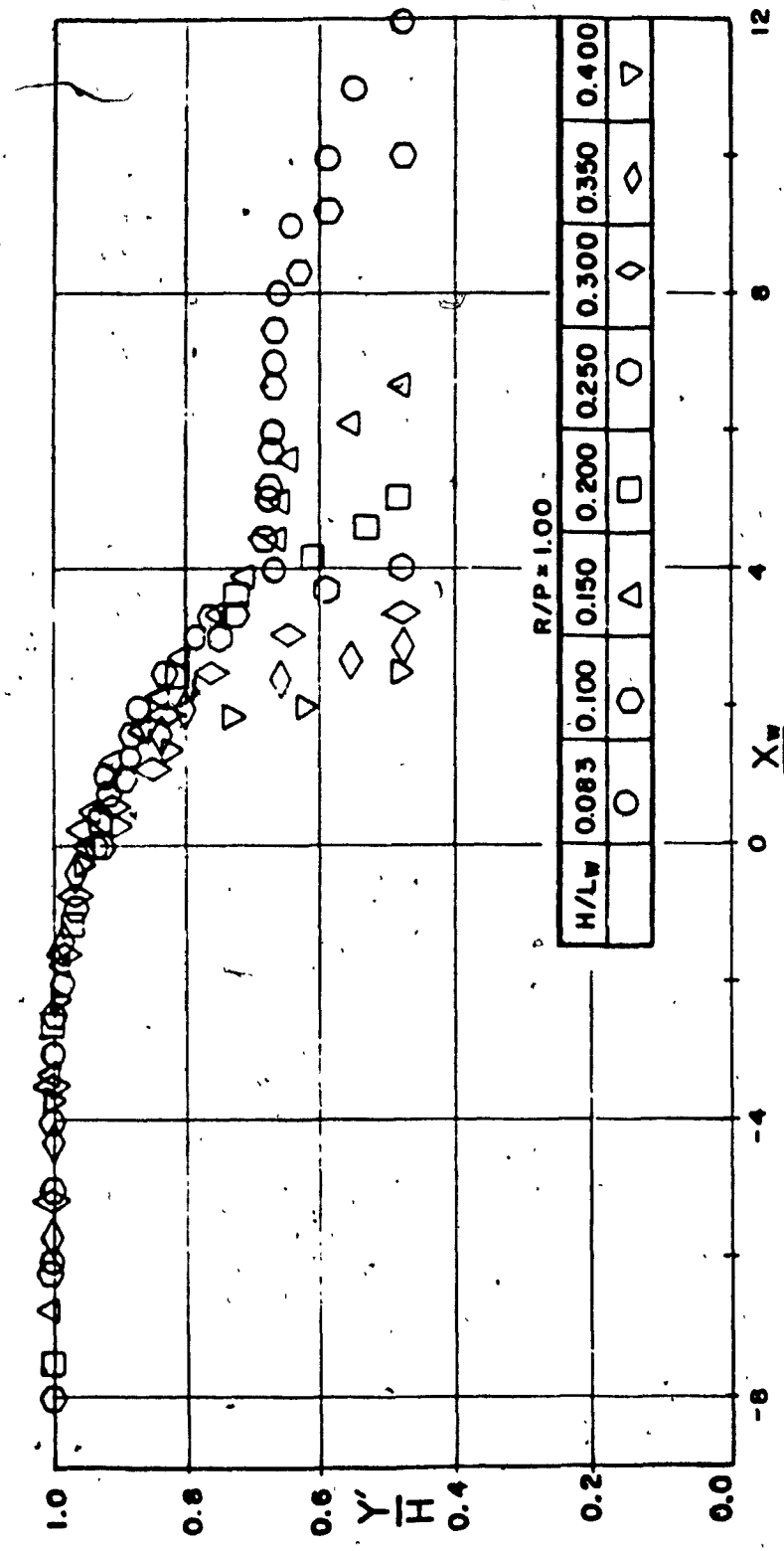

Figure 6.9 Non-dimensional Water Surface Profile for Broad-crested Weir with R/P=1.00

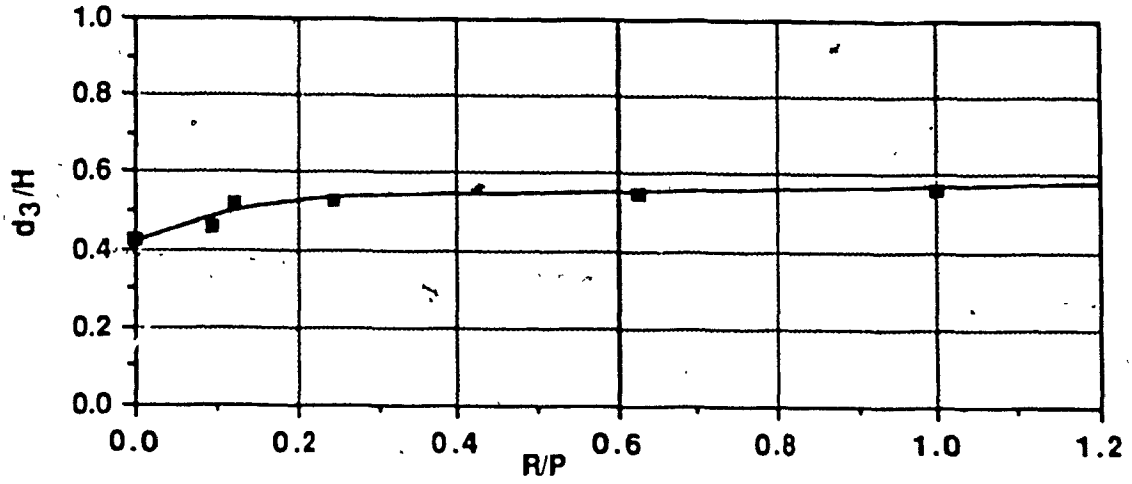

Figure 6.10(a) Variation of d_3 /H with R/P

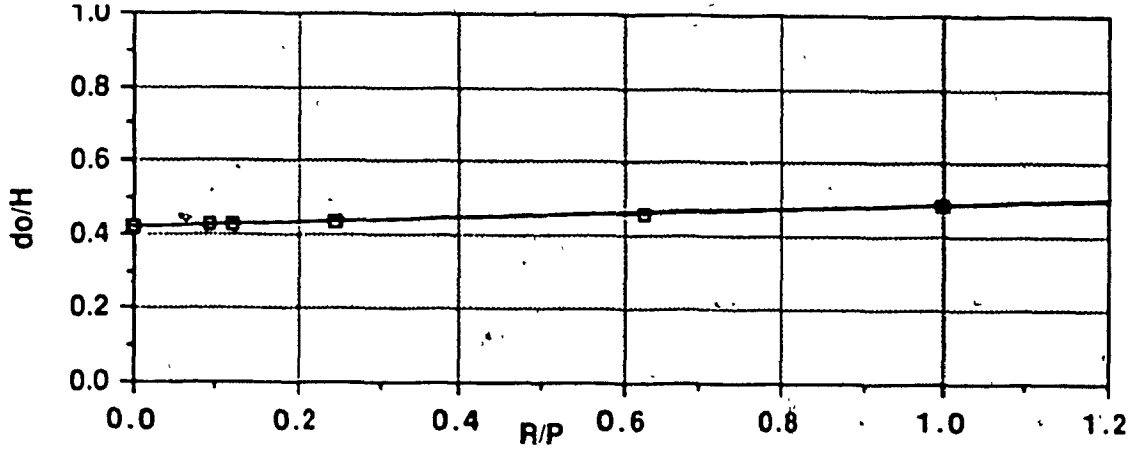

Figure 6.10(b) Variation of do/H with R/P

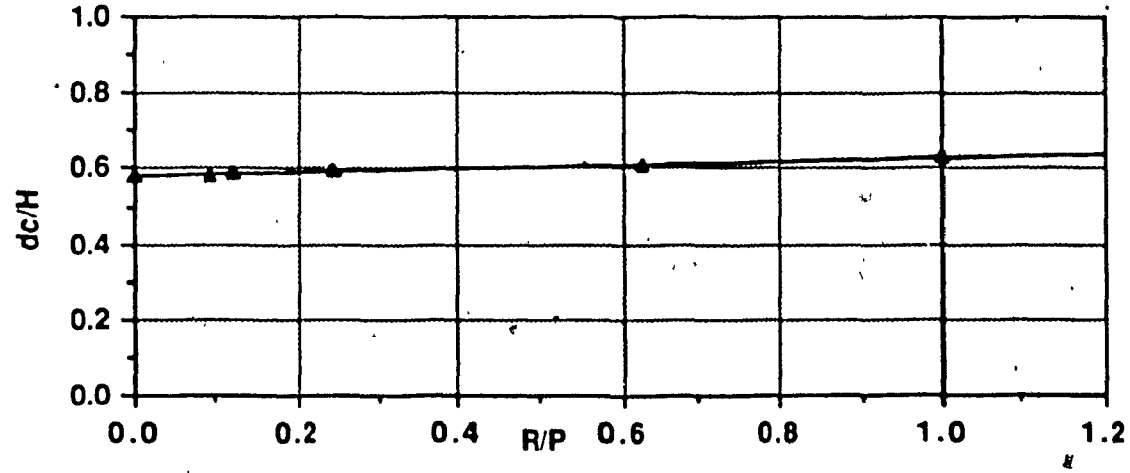

Figure 6.10(c) Variation of dc/H with R/P

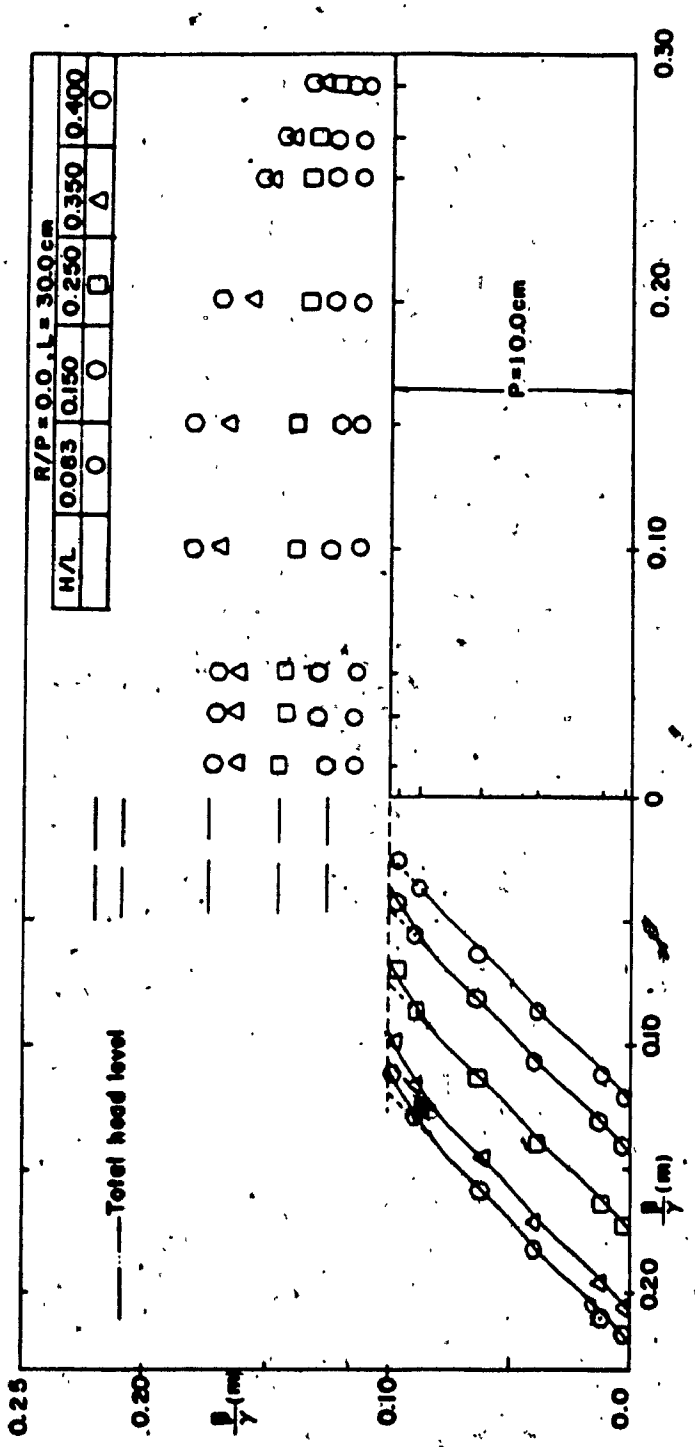

Figure 6.11 Distribution of Static Pressure Head for R / P = 0.0

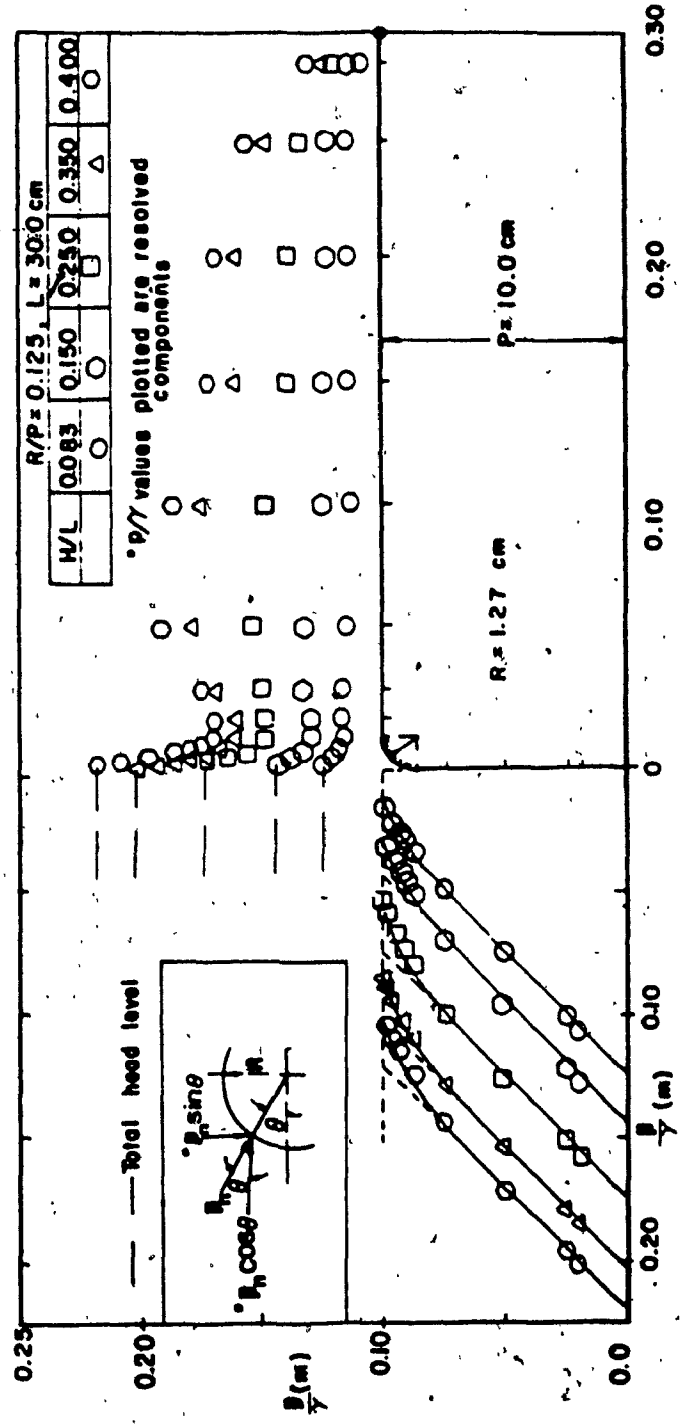

Figure 6.12 Distribution of Static Pressure Head for R / P = 0.125

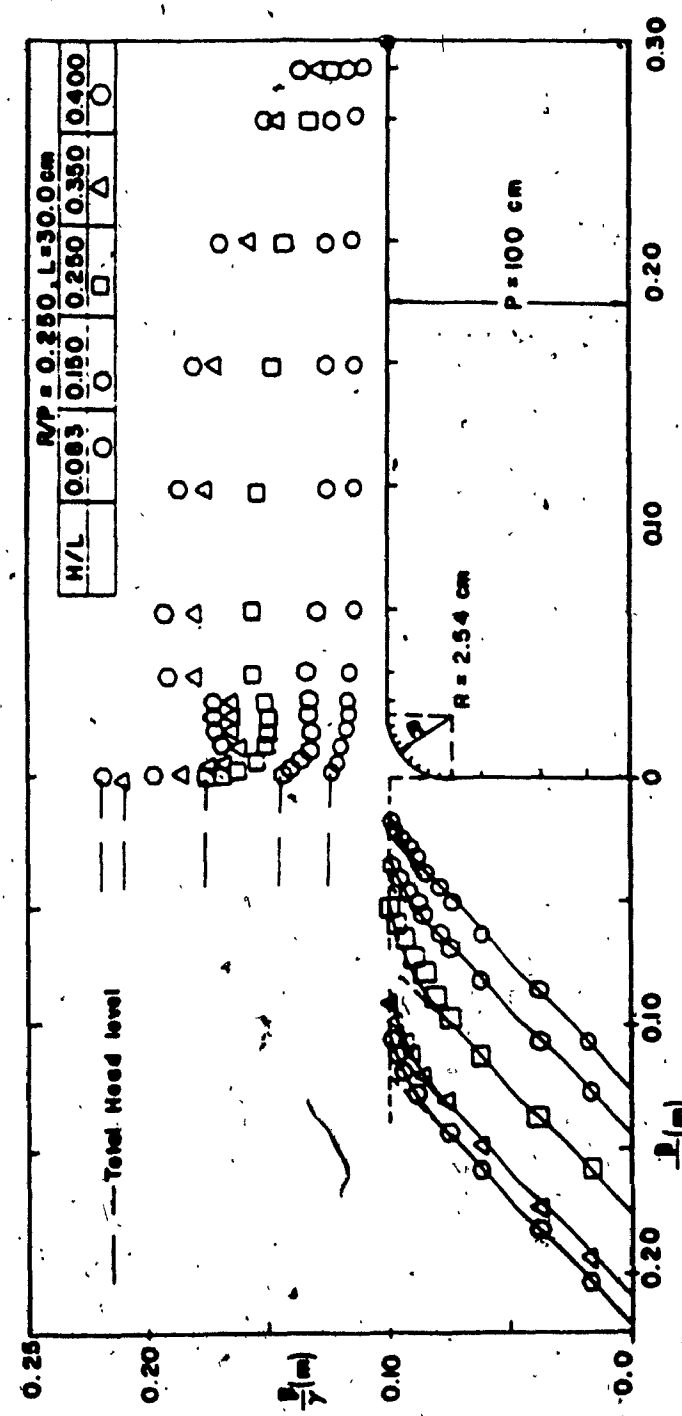

Figure 6.13 Distribution of Static Pressure Head for R / P = 0.250

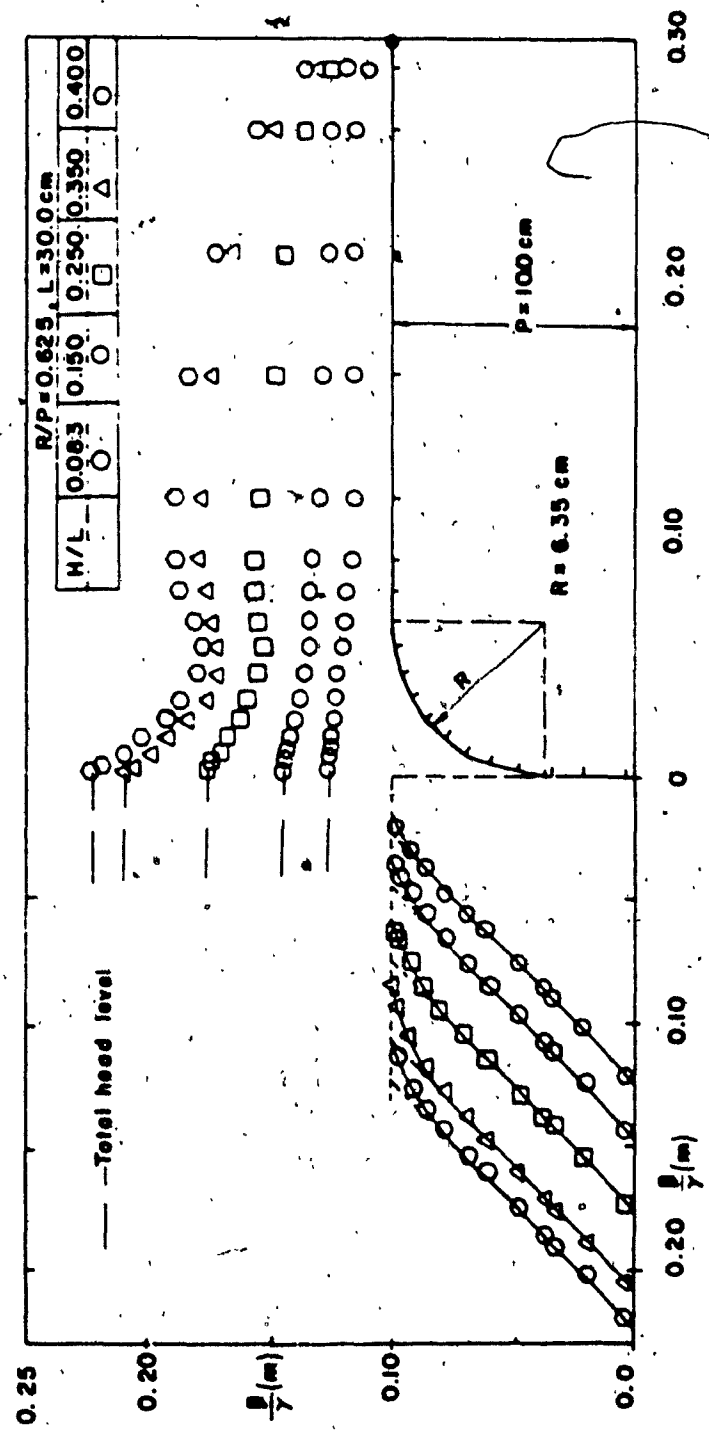

Figure 6.14 Distribution of Static Pressure Head for R/P=0.625

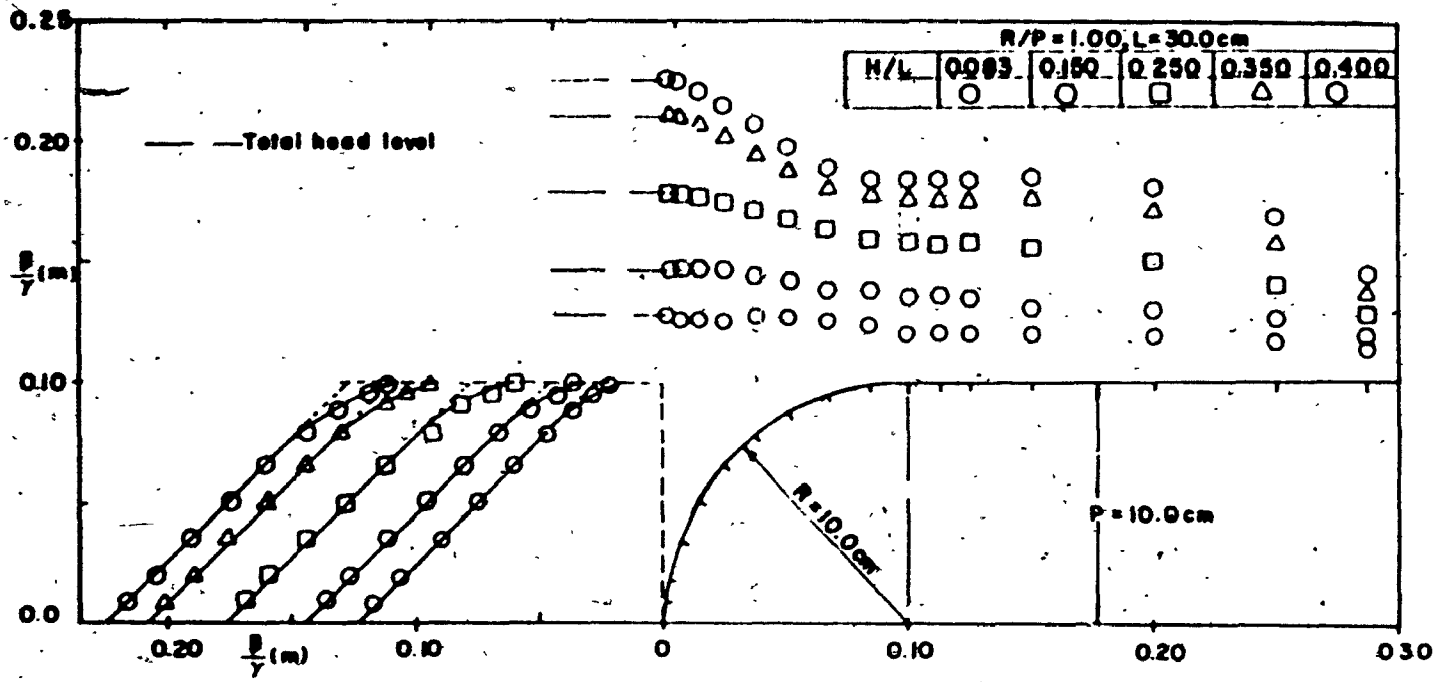

Figure 6-15 Distribution of Static Pressure Head for R / P = 1.00

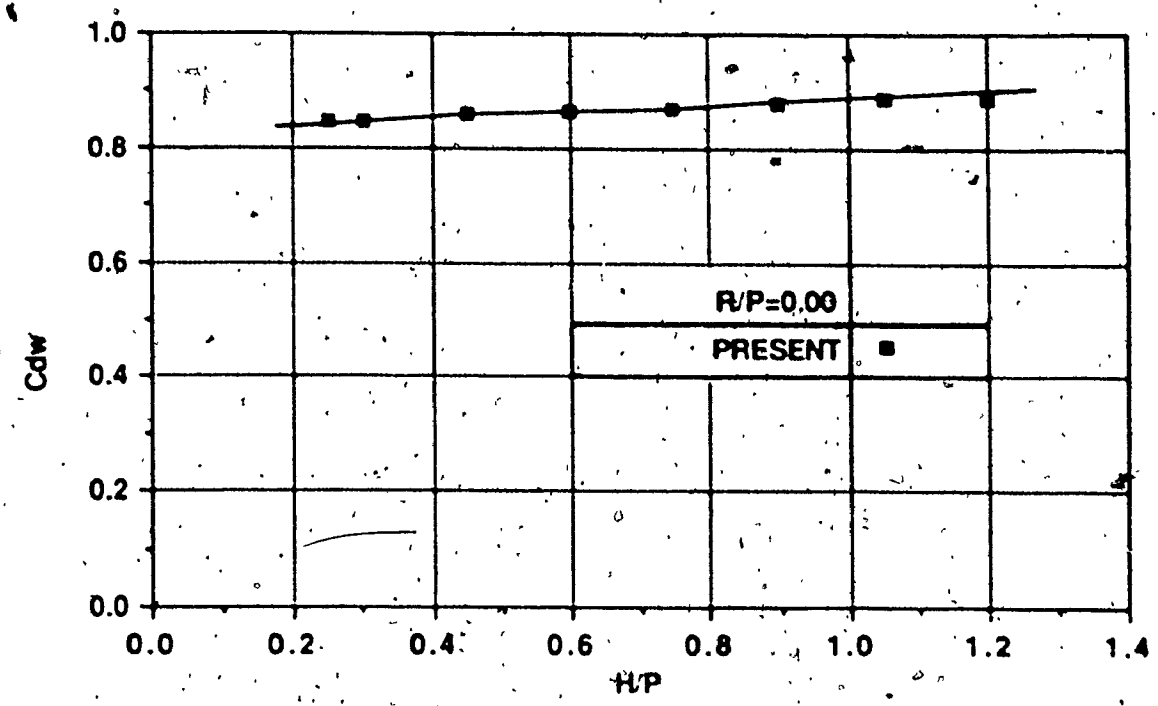

Figure 6.16 Variation of Discharge Coefficient C_{dw} with H/P for R/P=0.00

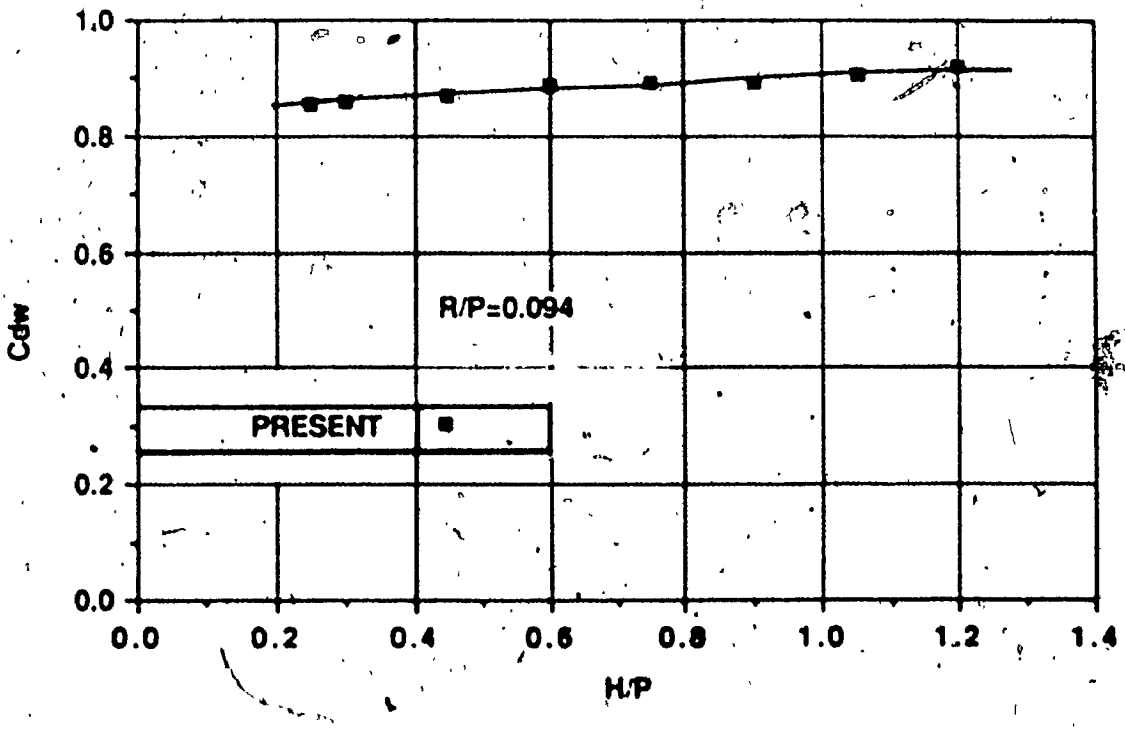

Figure 6.17 Variation of Discharge Coefficient C_{dw} with H/P for R/P=0.094

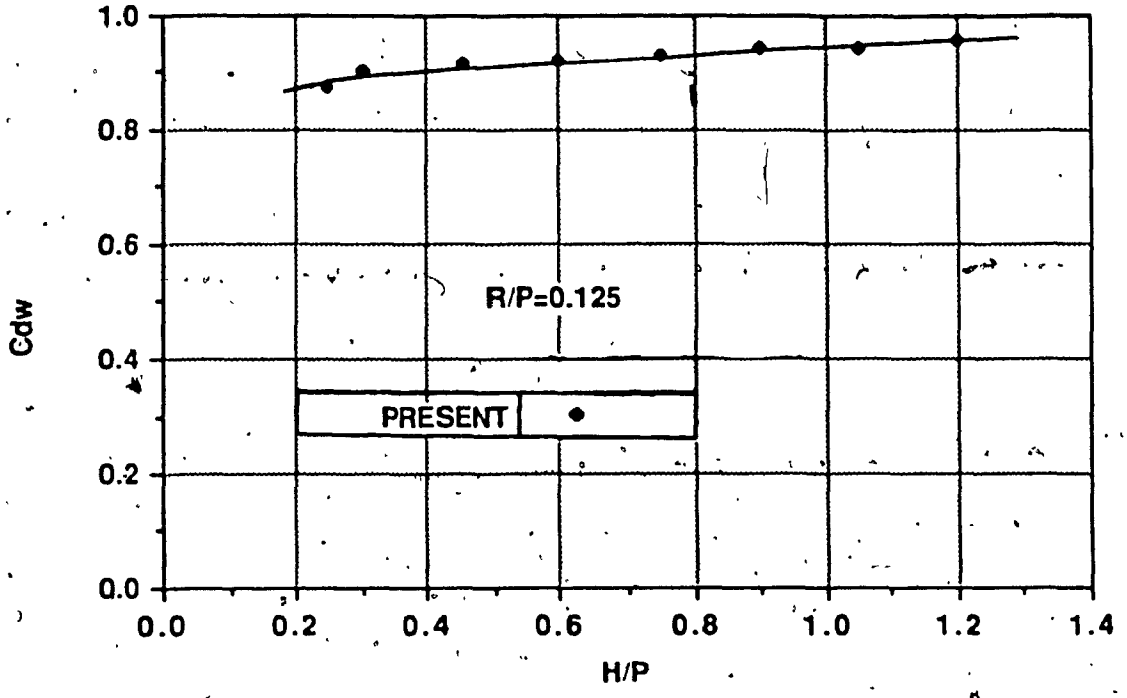

Figure 6.18 Variation of Discharge Coefficient C_{dw} with H/P for R/P=0.125

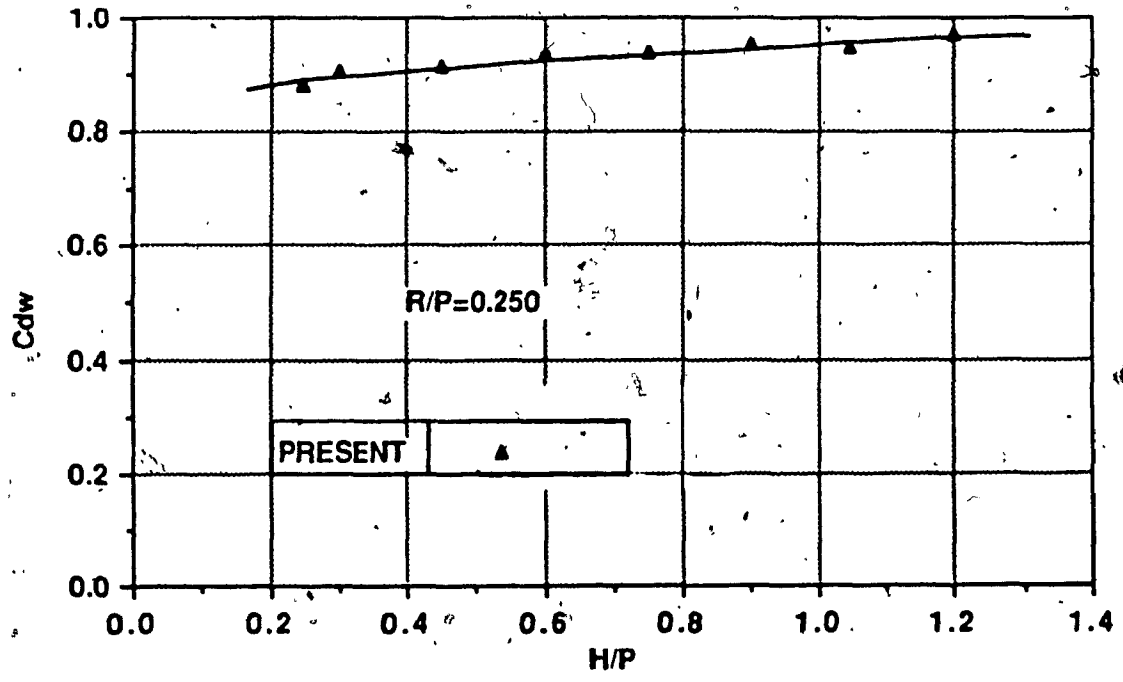

Figure 6.19 Variation of Discharge Coefficient C_{dw} with H/P for R/P=0.250

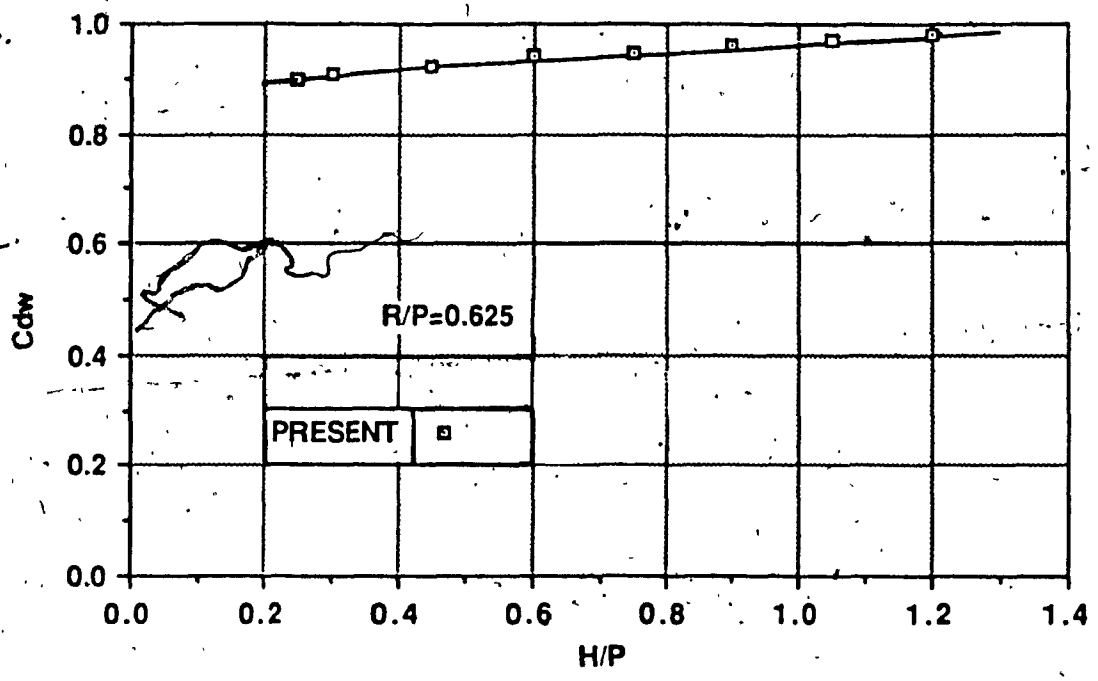

Figure 6.20 Variation of Discharge Coefficient C_{dw} with H/P for R/P=0.625

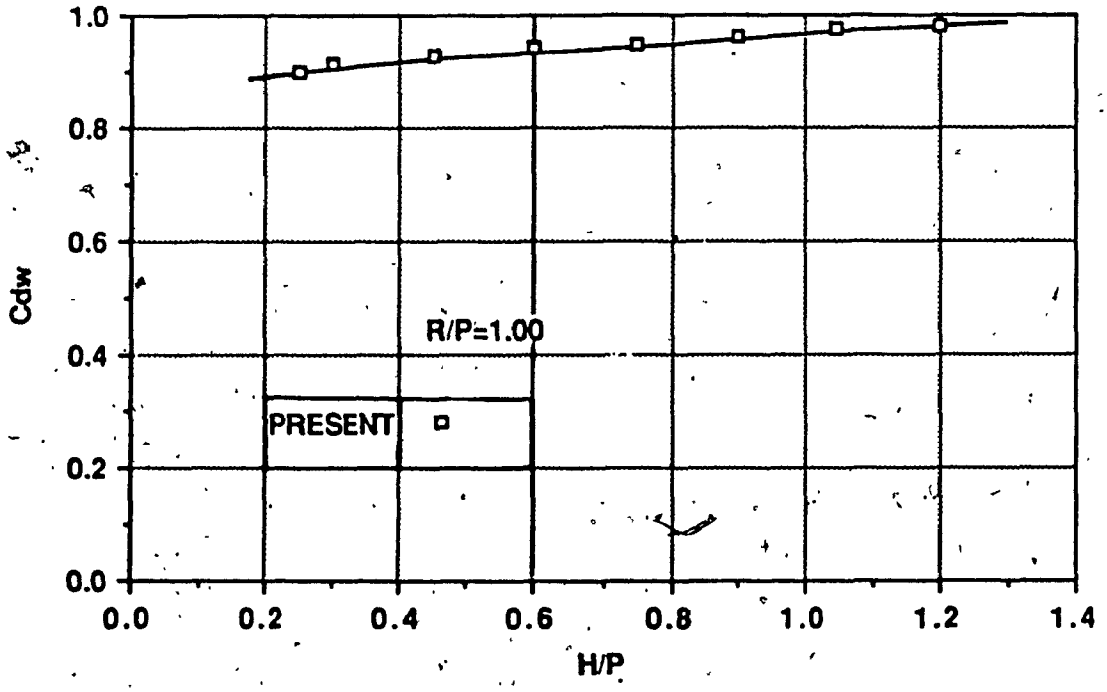

Figure 6.21 Variation of Discharge Coefficient C_{dw} with H/P for R/P=1.00

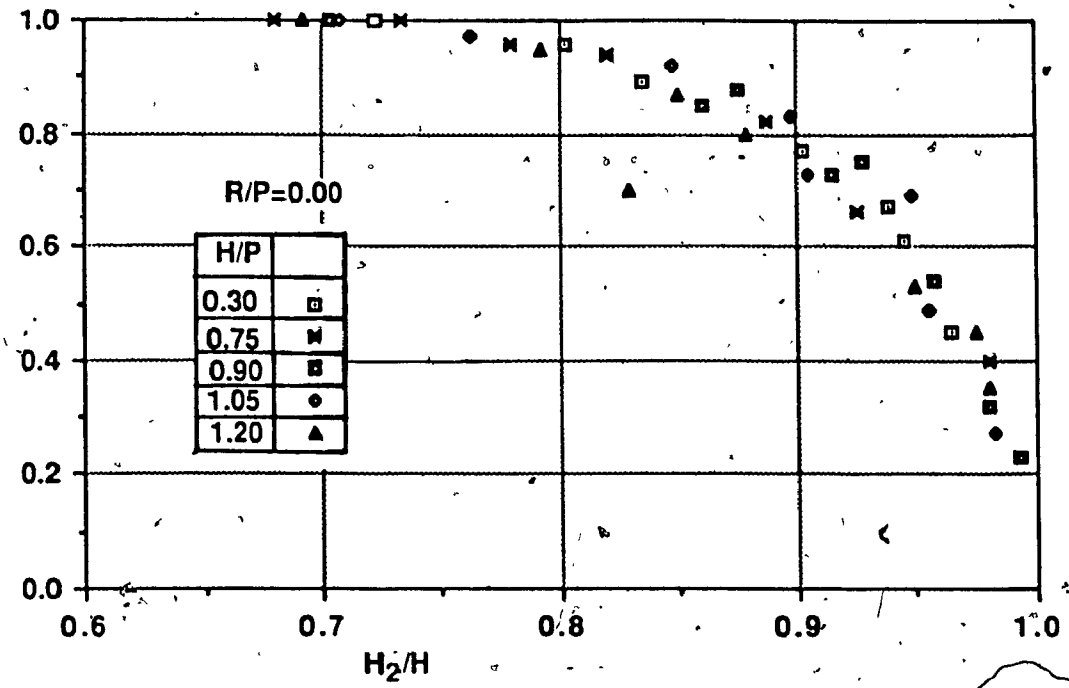

Figure 6.22 Variation of Drowned -flow Reduction factor f with Submergence Ratio for R/P=0.00

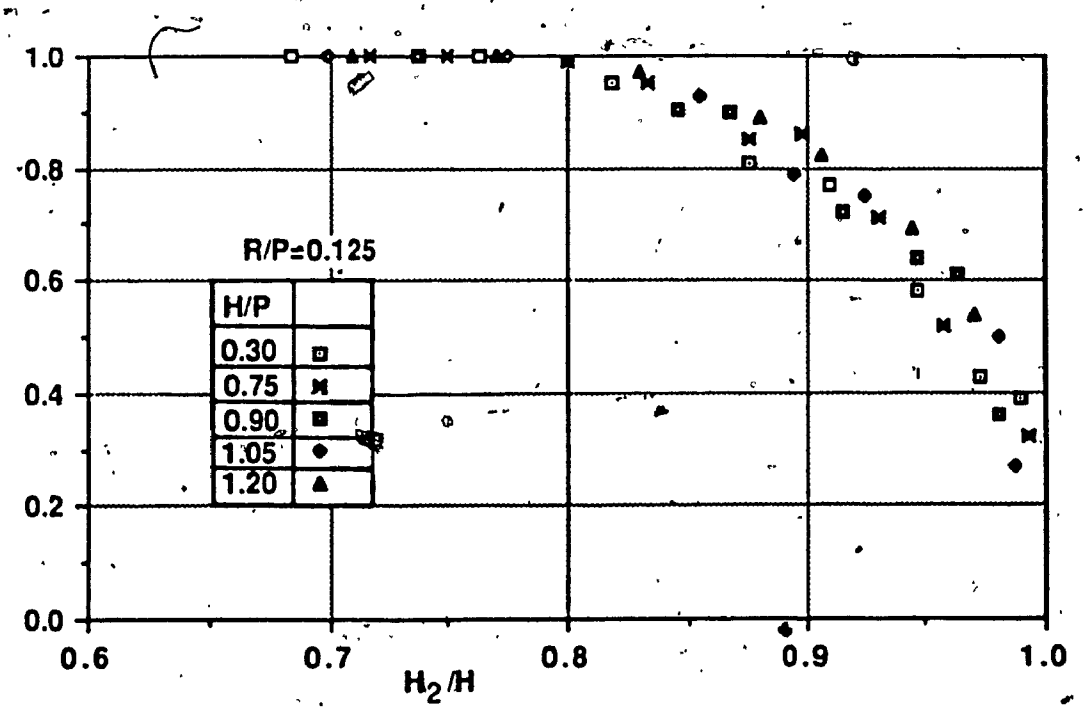

Figure 6.23 Variation of Drowned -flow Reduction factor f with Submergence Ratio for R/P=0.125

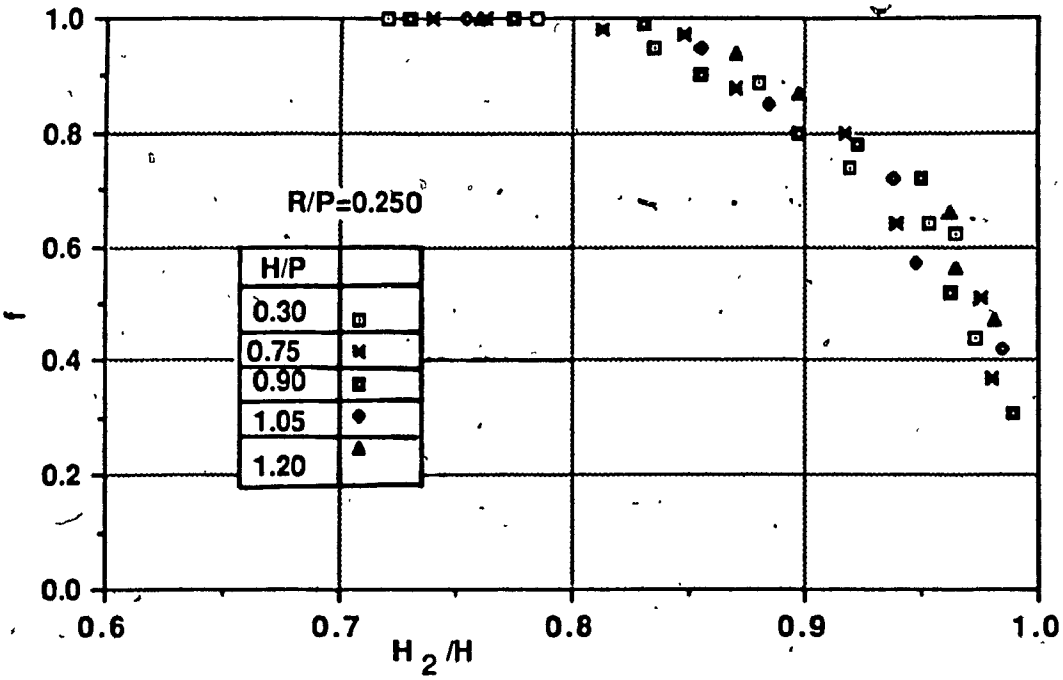

Figure 6.24 Variation of Drowned-flow Reduction factor f with Submergence Ratio for R/P=0.250

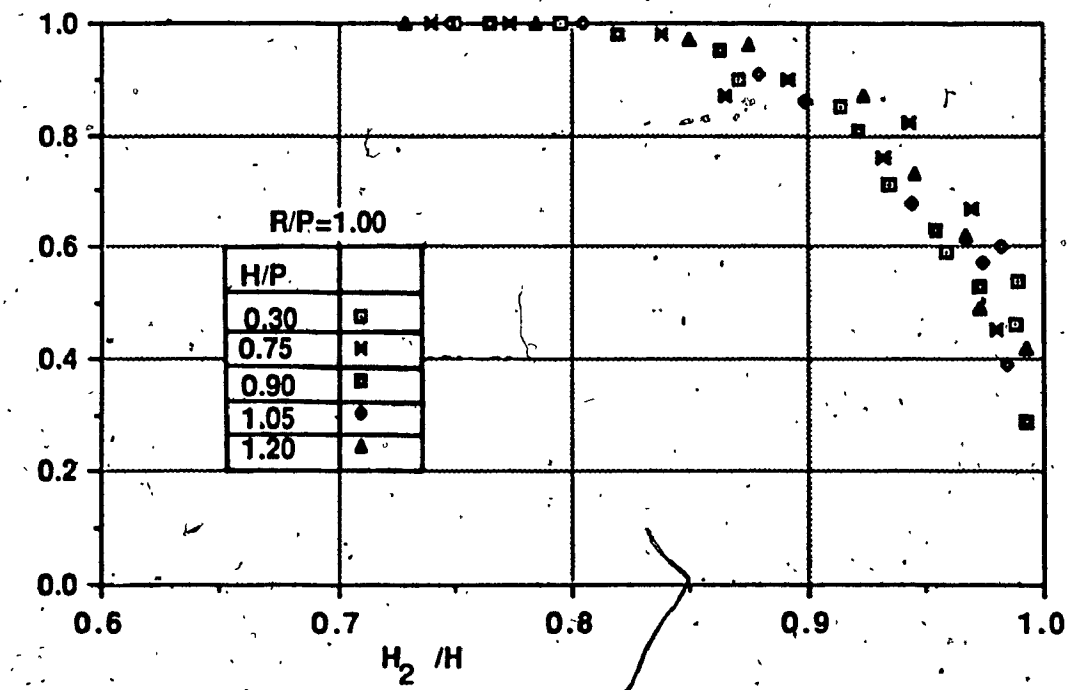

Figure 6.25 Variation of Drowned-flow Reduction factor f with Submergence Ratio for R/P=1.00

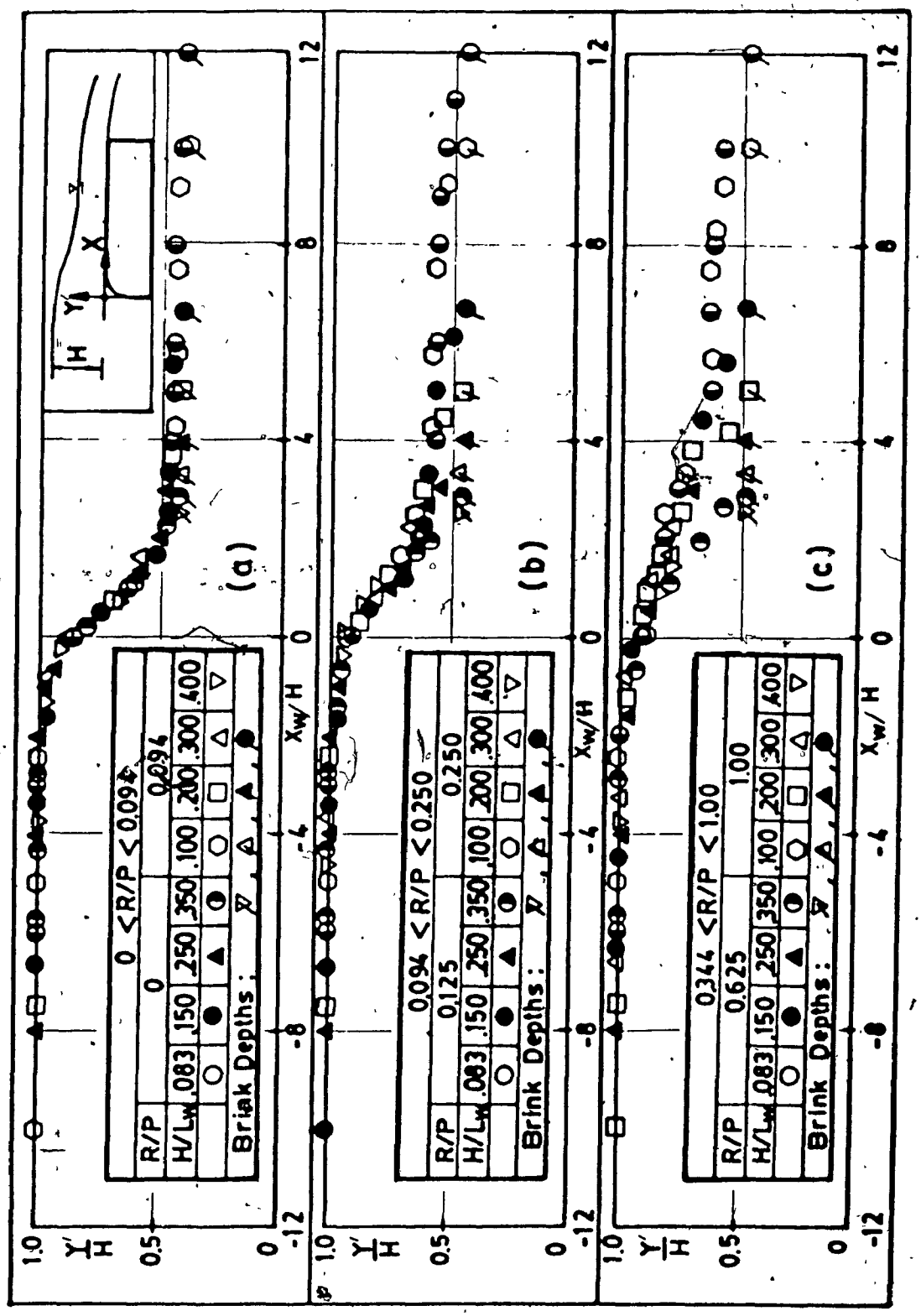

Figure 6.26 Non-dimensional Water Surface Profile

for Broad-crested Weir in the Range 0.0 < R/P < 1.00

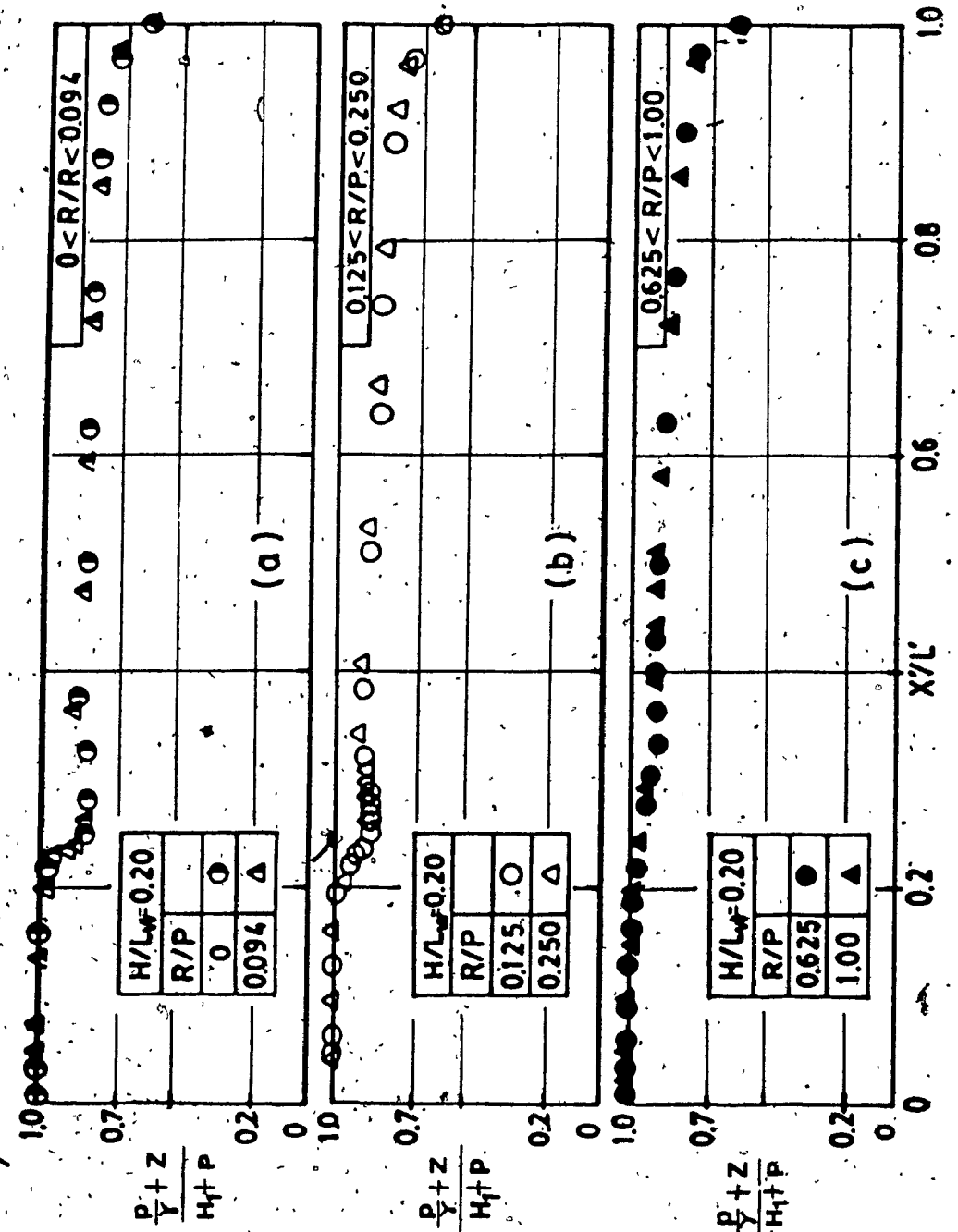

Figure 6.27 Non-dimensional Plot of Static Pressure Profiles for H/P=0.60 (typical)

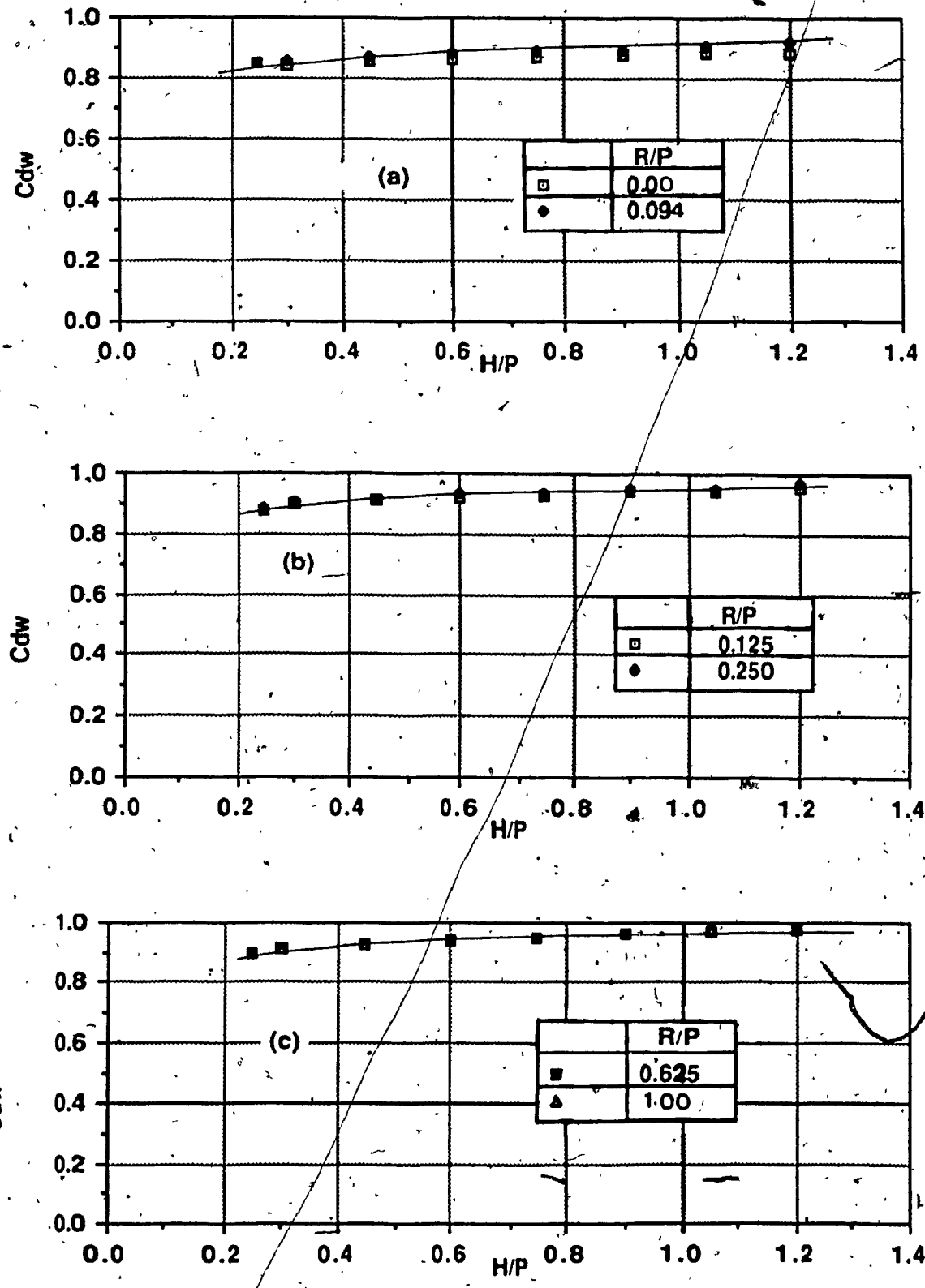

Figure 6.28 Variation of Discharge Coefficient C_{dw} with H/P for (a) 0.0<R/P<0.094; (b) 0.094<R/P<0.250; (c) 0.250<R/P<1.00.

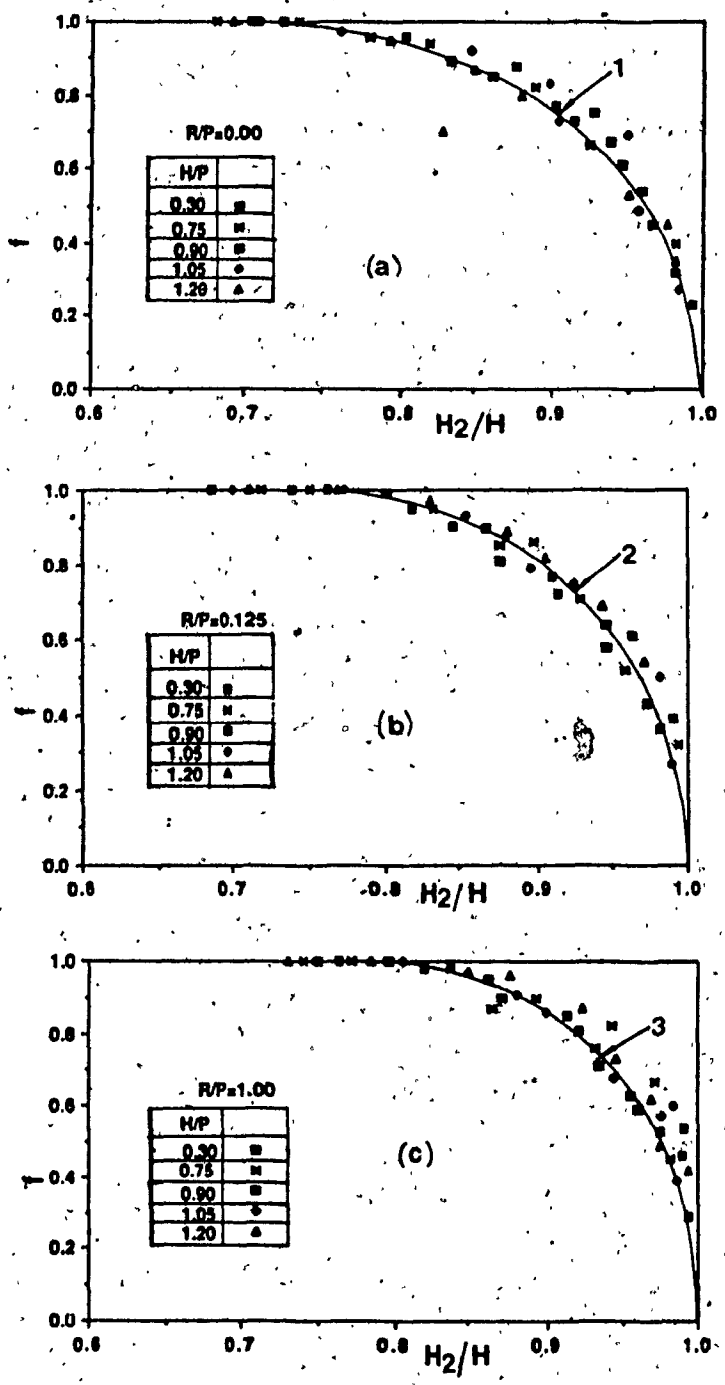

Figure 6.29 Variation of Drowned -flow Reduction factor f with Submergence Ratio for (a) 0.0 < R/P < 0.094; (b) 0.094 < R/P < 0.250; (c) 0.250 < R/P < 1.00.

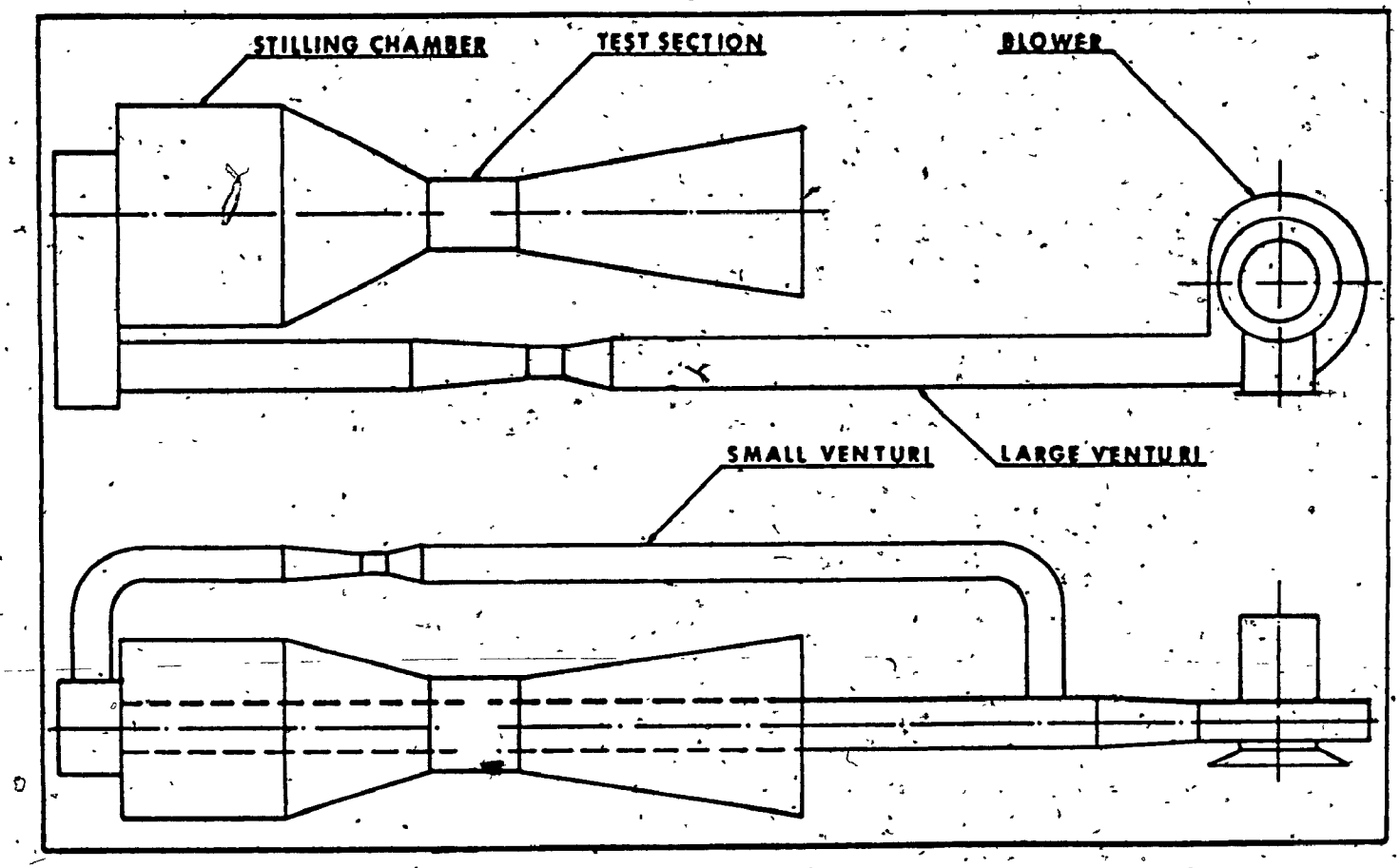

Figure 7.1 Wind Tunnel Set-up

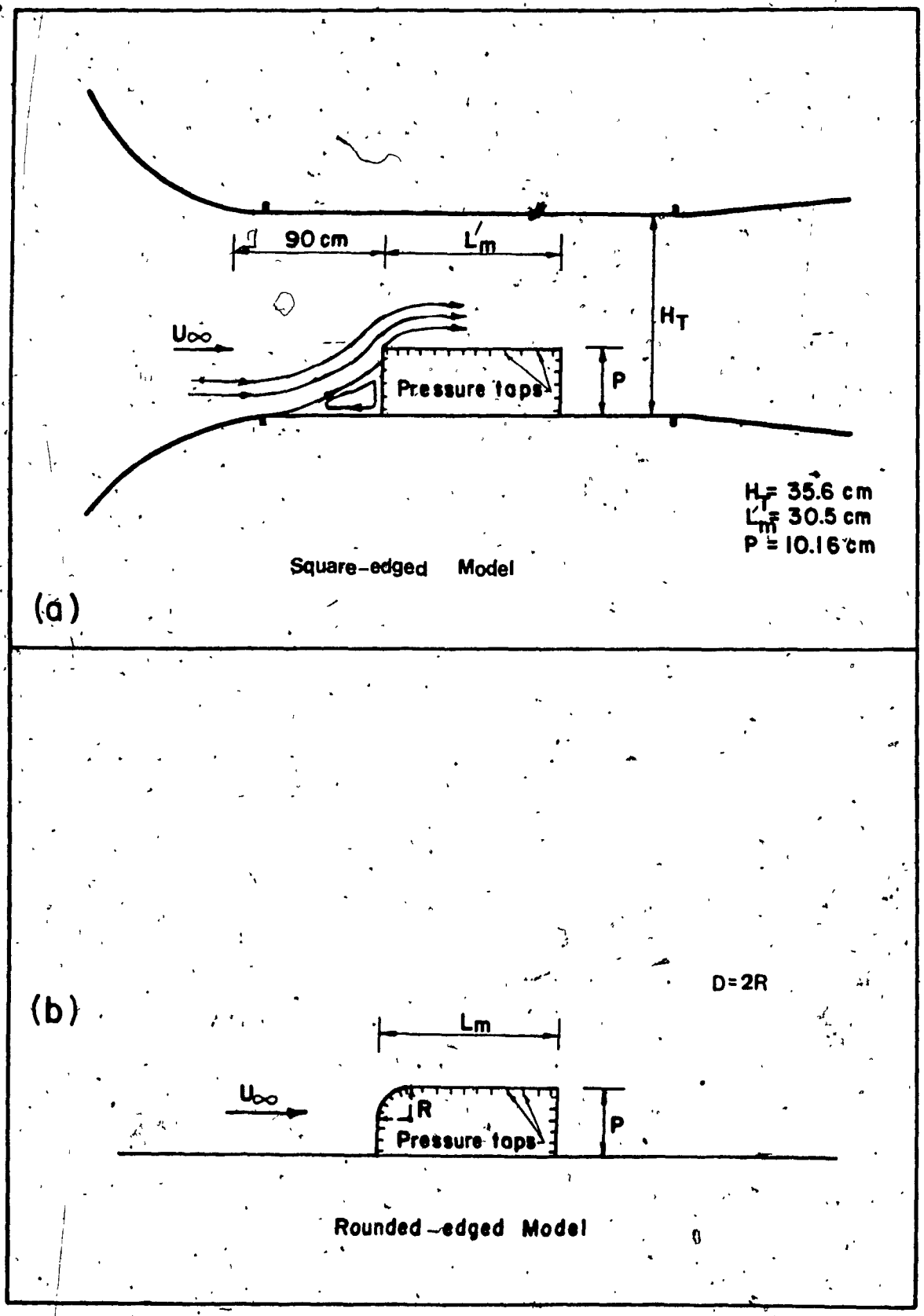

Figure 7.2 Definition Sketch of the Wind Tunnel test section

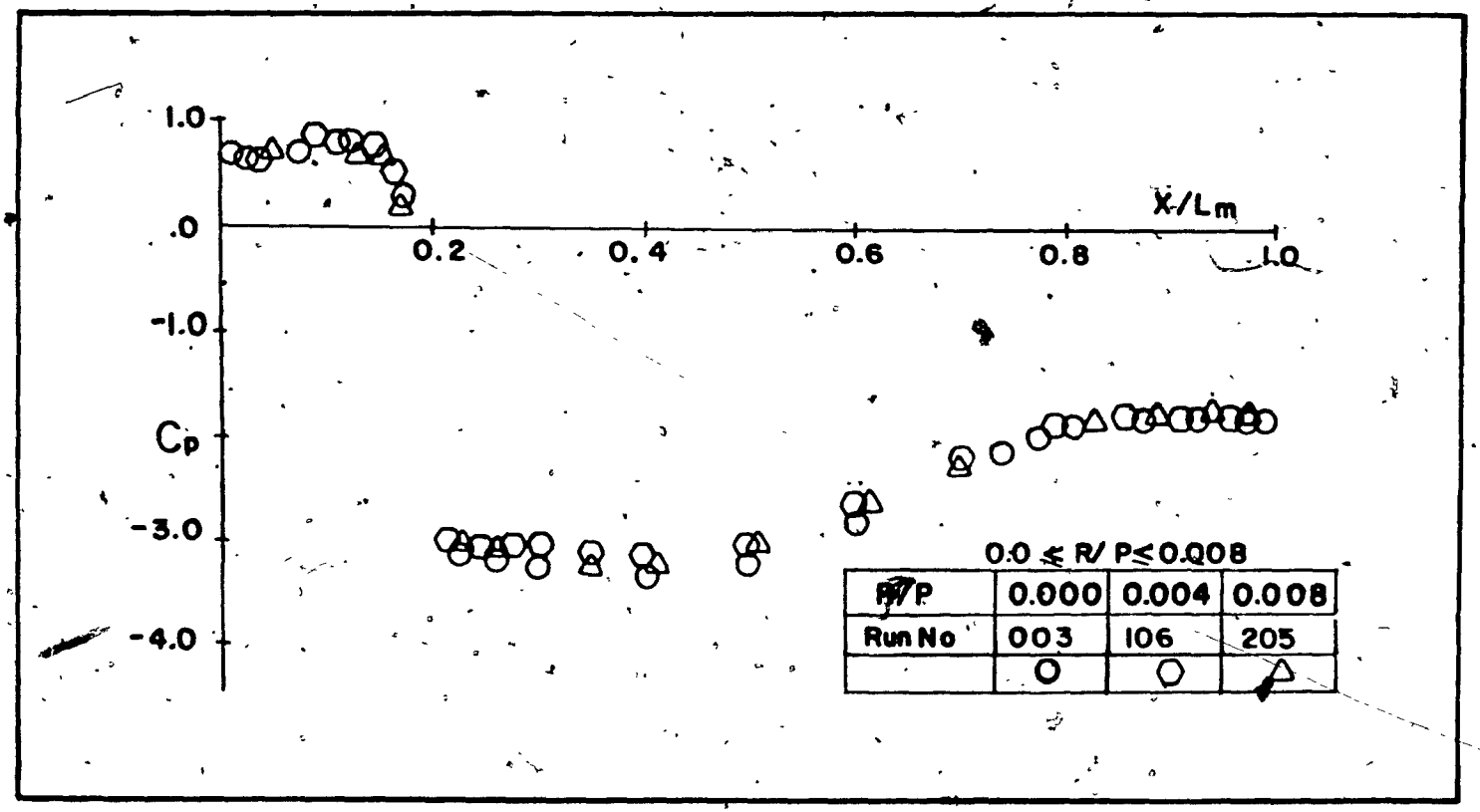

Figure 7.3 Surface Pressure Distributions along Weir model

for 0.0 < R/P < 0.008

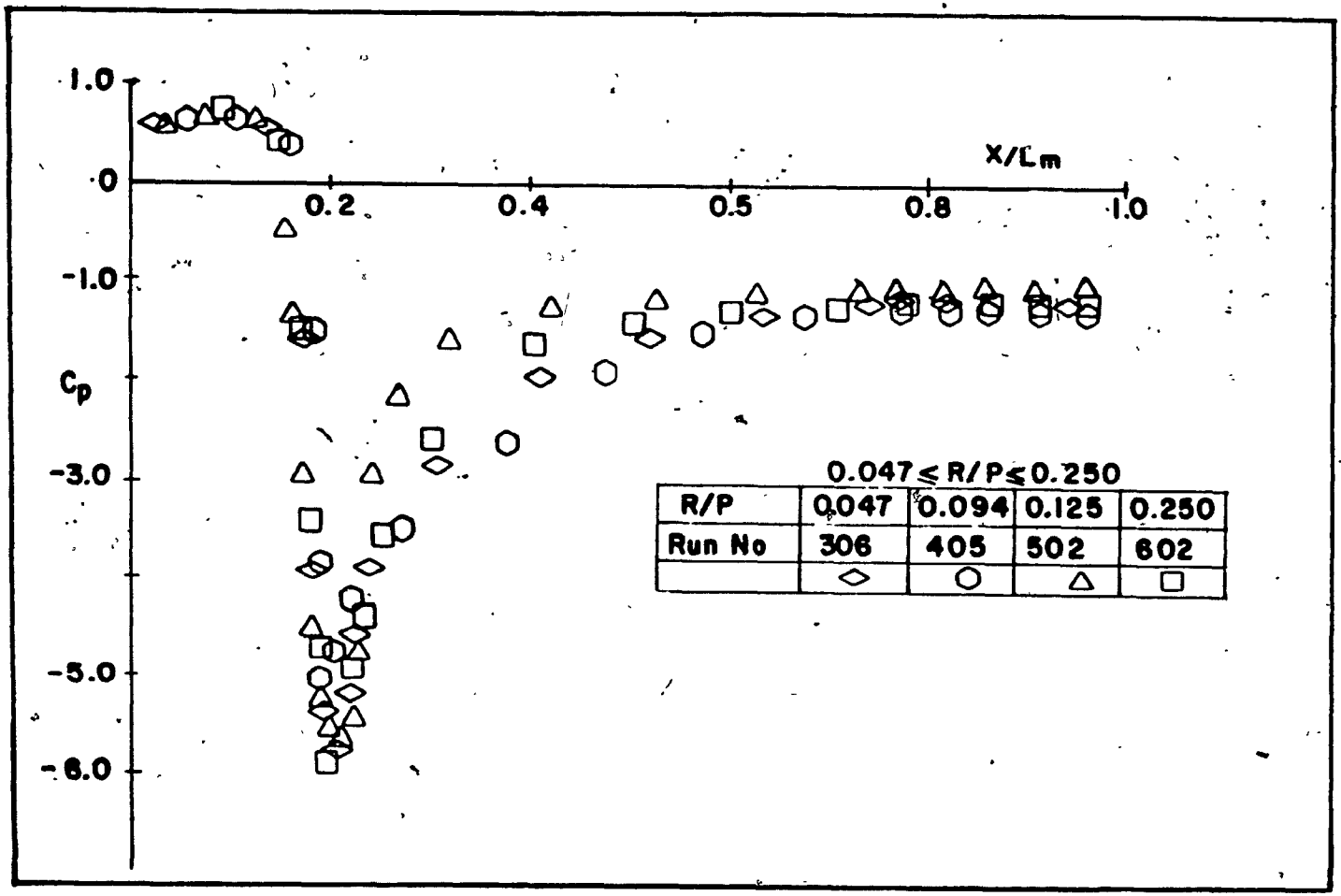

Figure 7.4 Surface Pressure Distributions along Weir model

for $0.047 \leq R/P \leq 0.250$

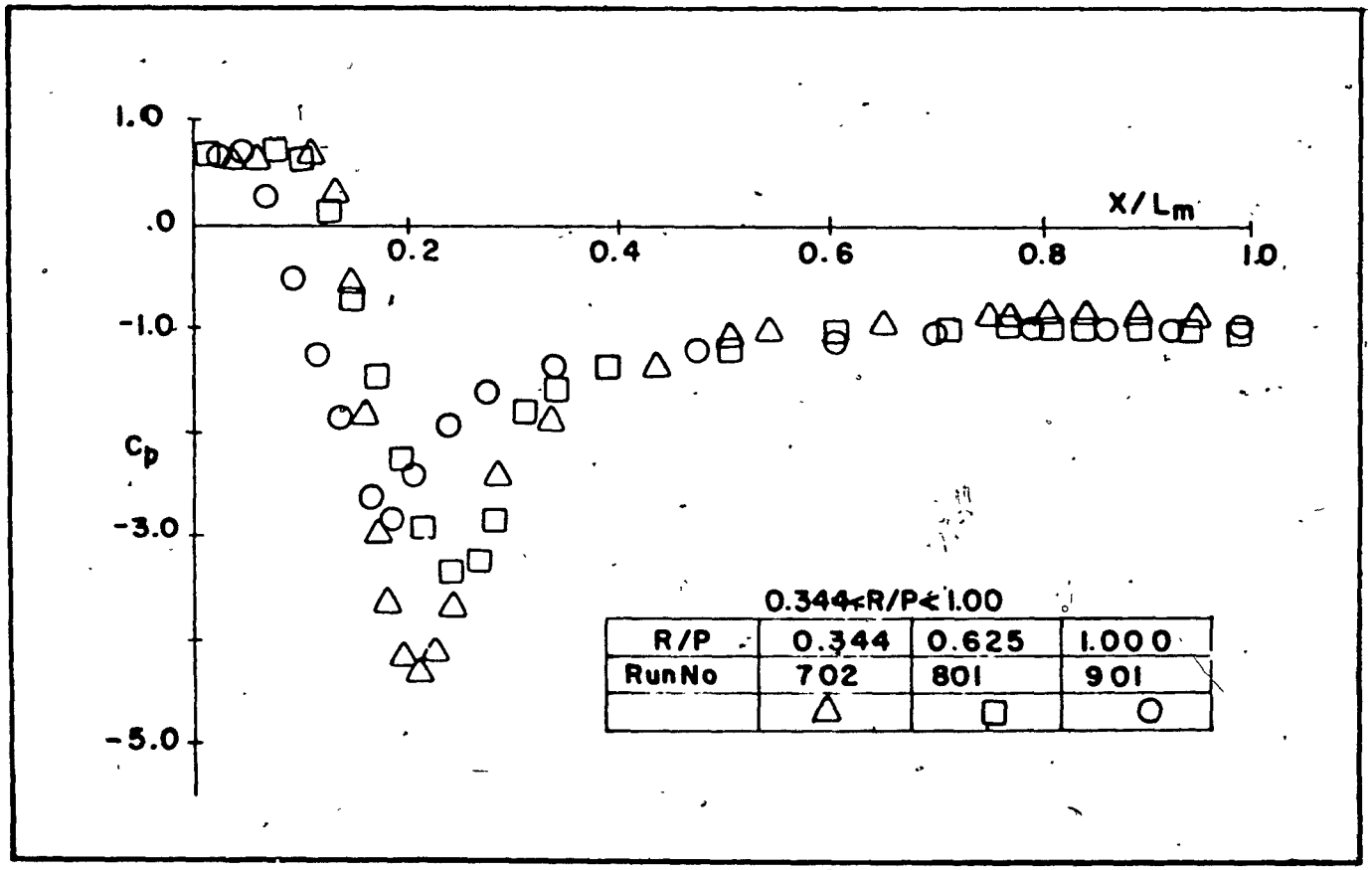

Figure 7.5 Surface Pressure Distribution along Weir model

for 0.344 < R/P < 1.00

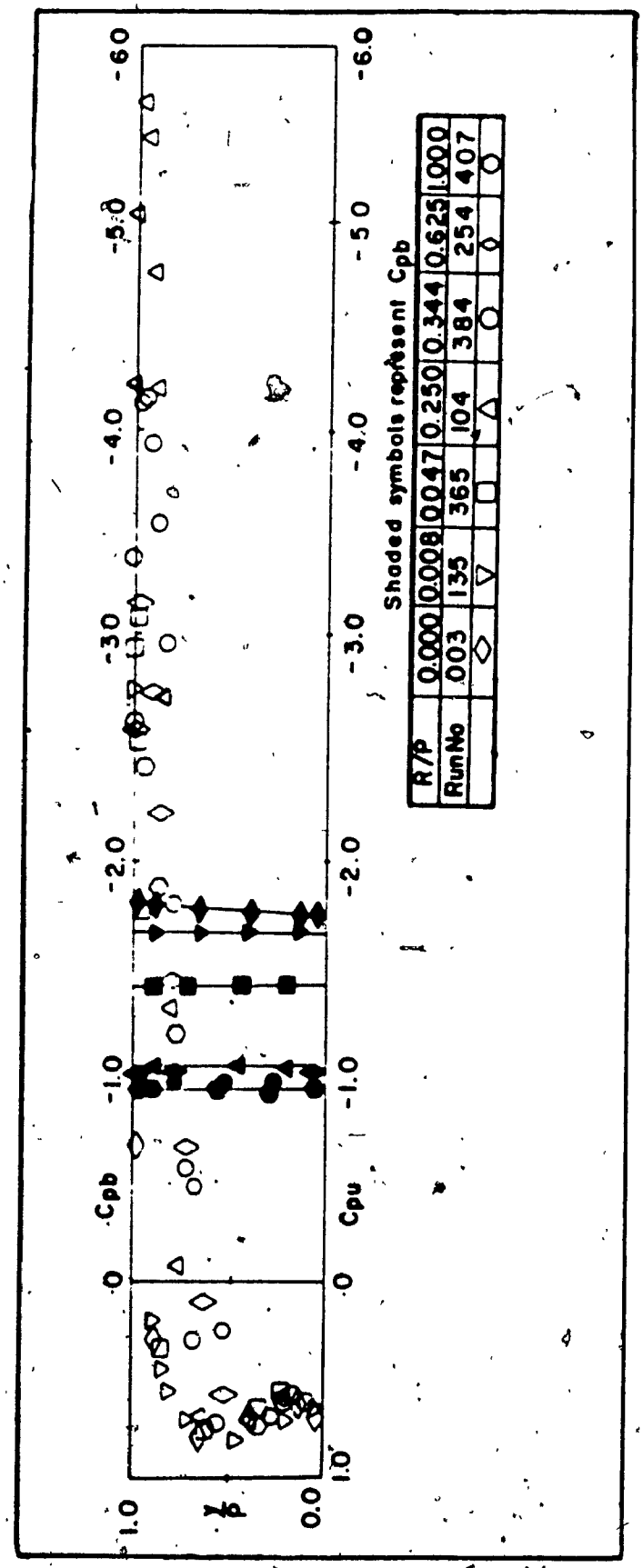

Figure 7.6 Composite Plot of Pressure Coefficients Cpu and Cpb

for the Range 0.0 < R/P < 1.00

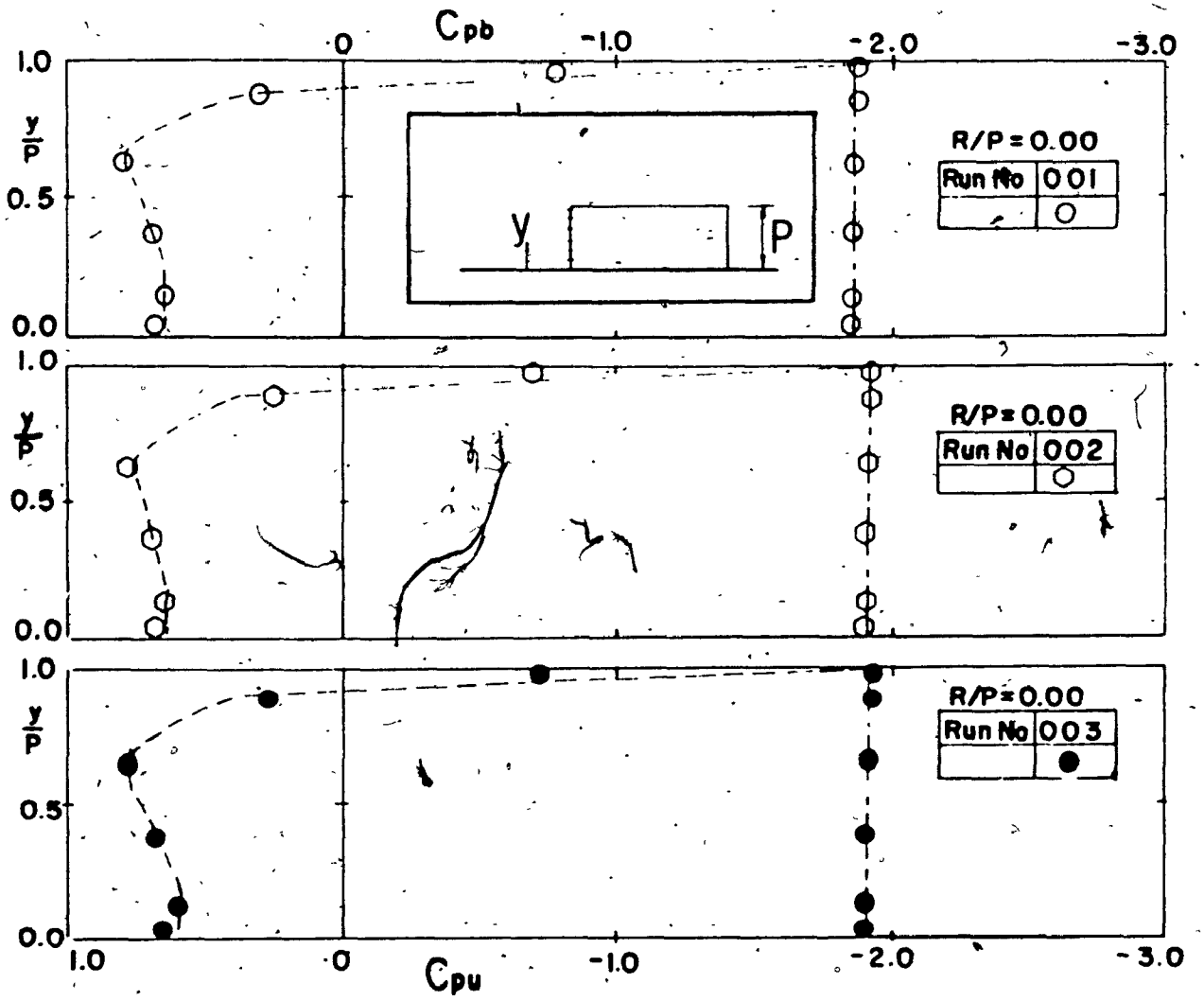

Figure 7.7 Pressure Coefficient on the Front and Rear Surfaces

of model with R/P=0.00

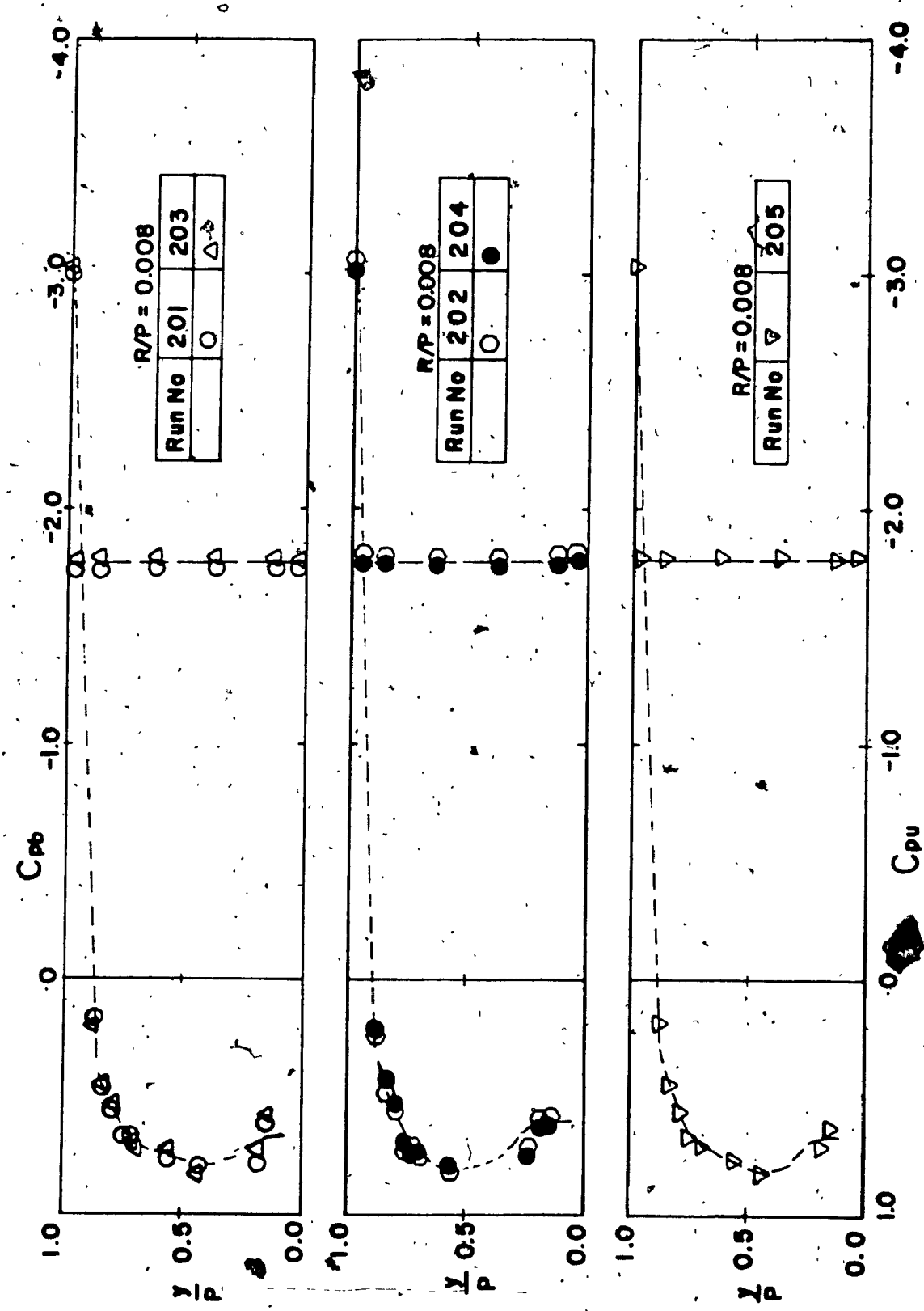

Figure 7.8 Pressure Coefficient on the Front and Rear Surfaces of model with R/P=0.008

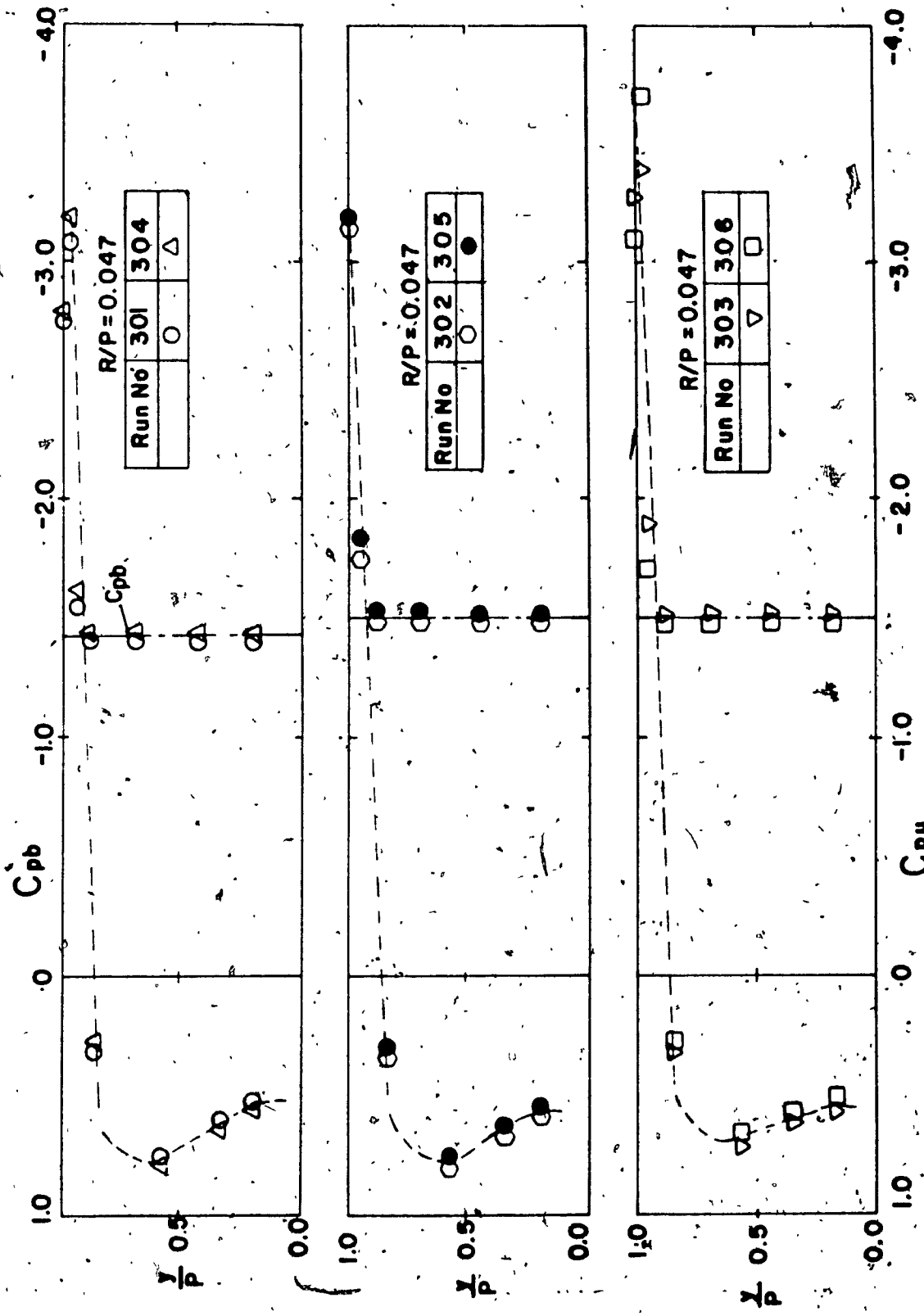

Figure 7.9 Pressure Coefficient on the Front and Rear Surfaces of model with R/P=0.047

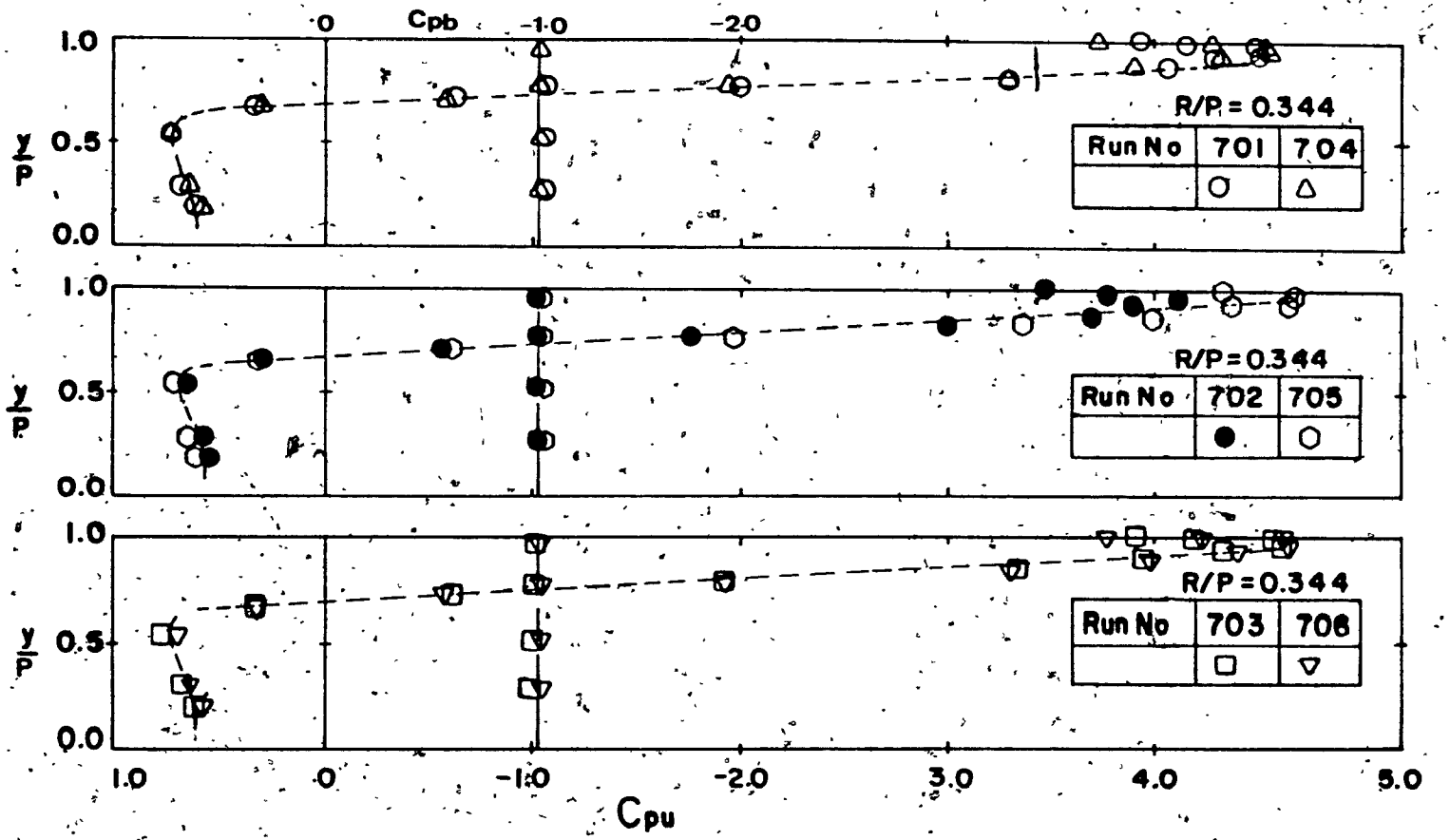

Figure 7.10 Pressure Coefficient on the Front and Rear Surfaces of model with R/P=0.344

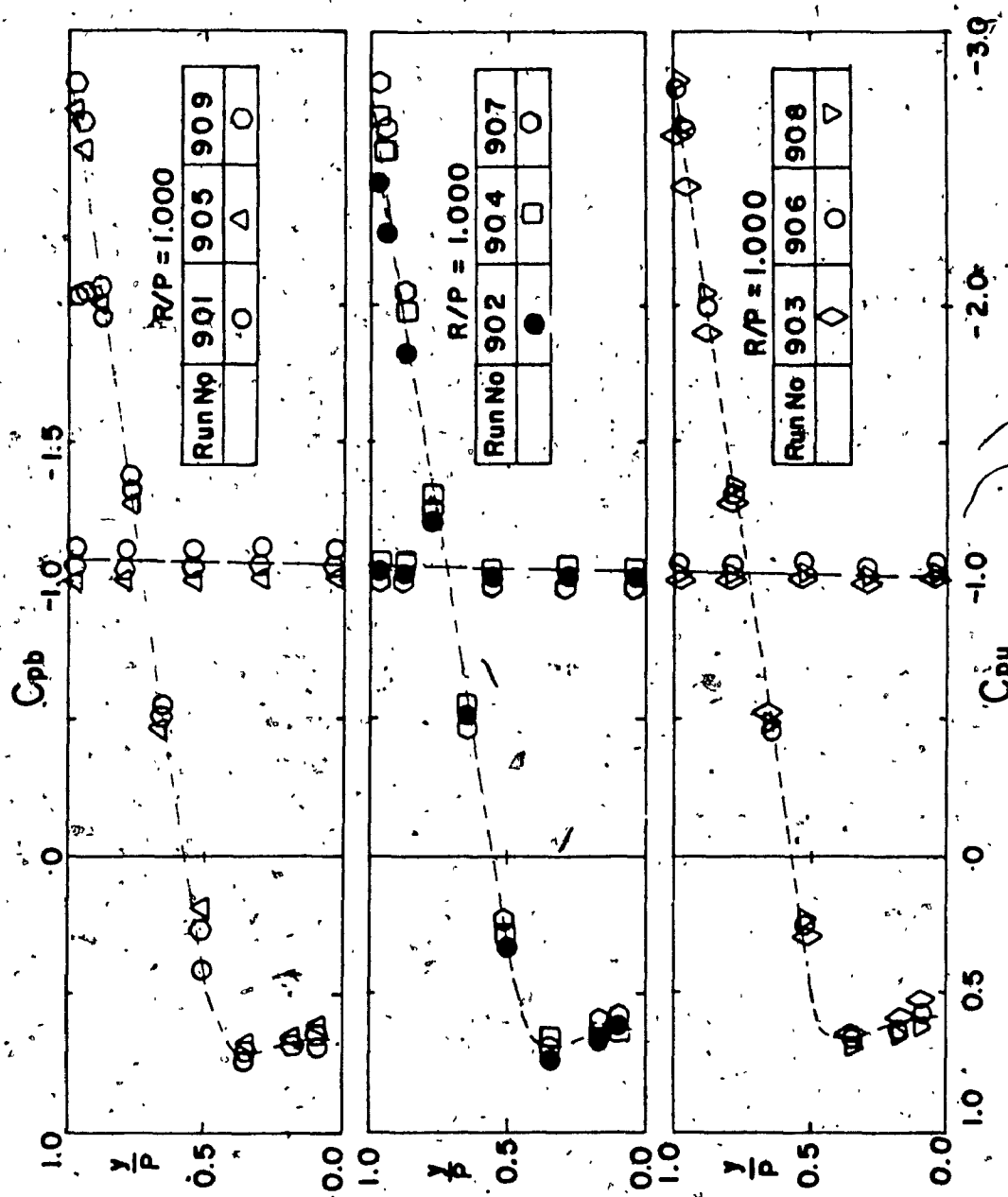

Figure 7.11 Pressure Coefficient on the Front and Rear Surfaces of model with R/P=1.00

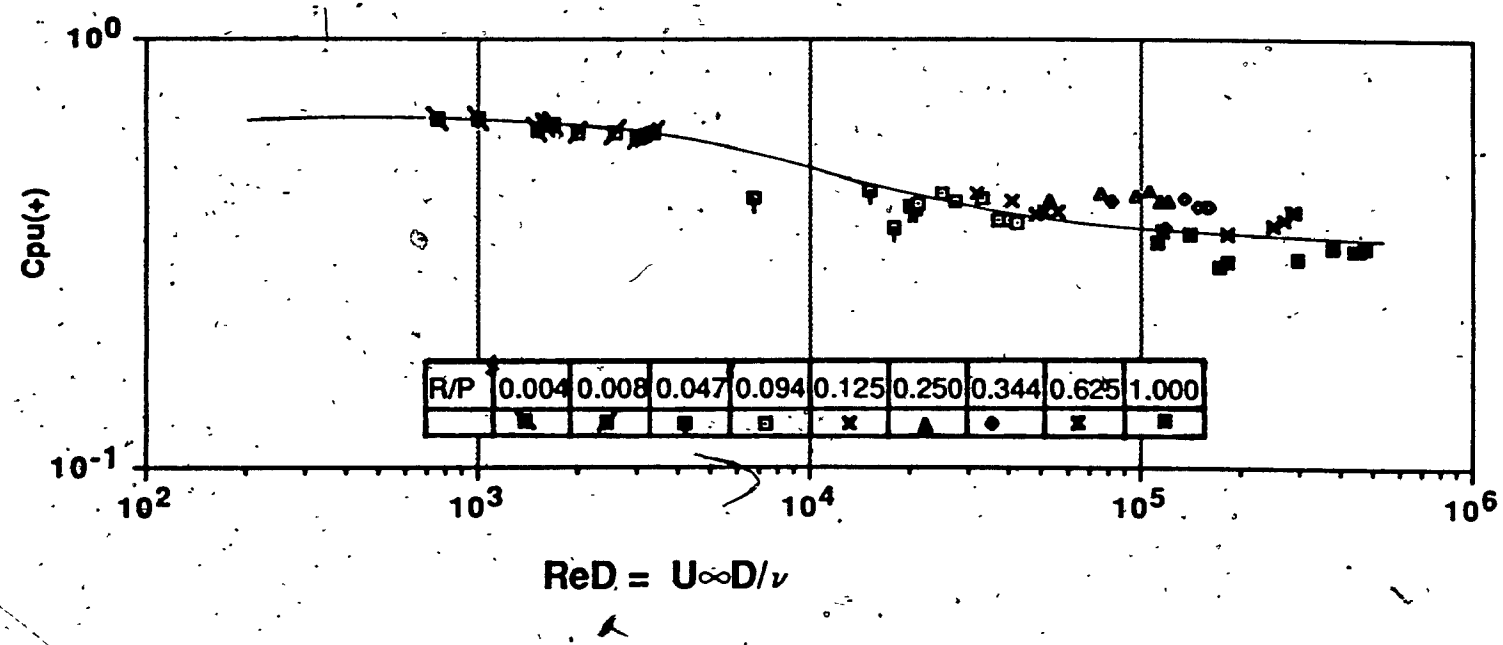

Figure 7.12(a) Variation of Cpu(+) with Reynolds Number ReD

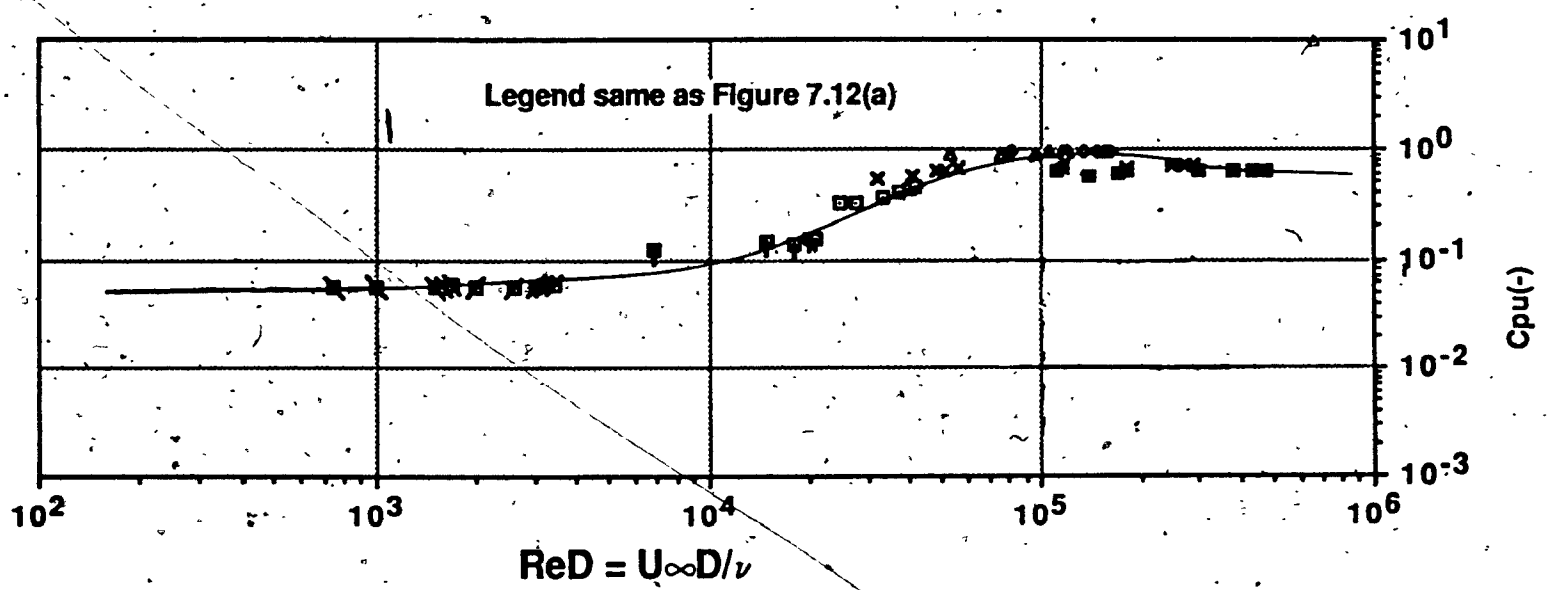

Figure 7.12(b) Variation of Cpu(-) with Reynolds Number ReD

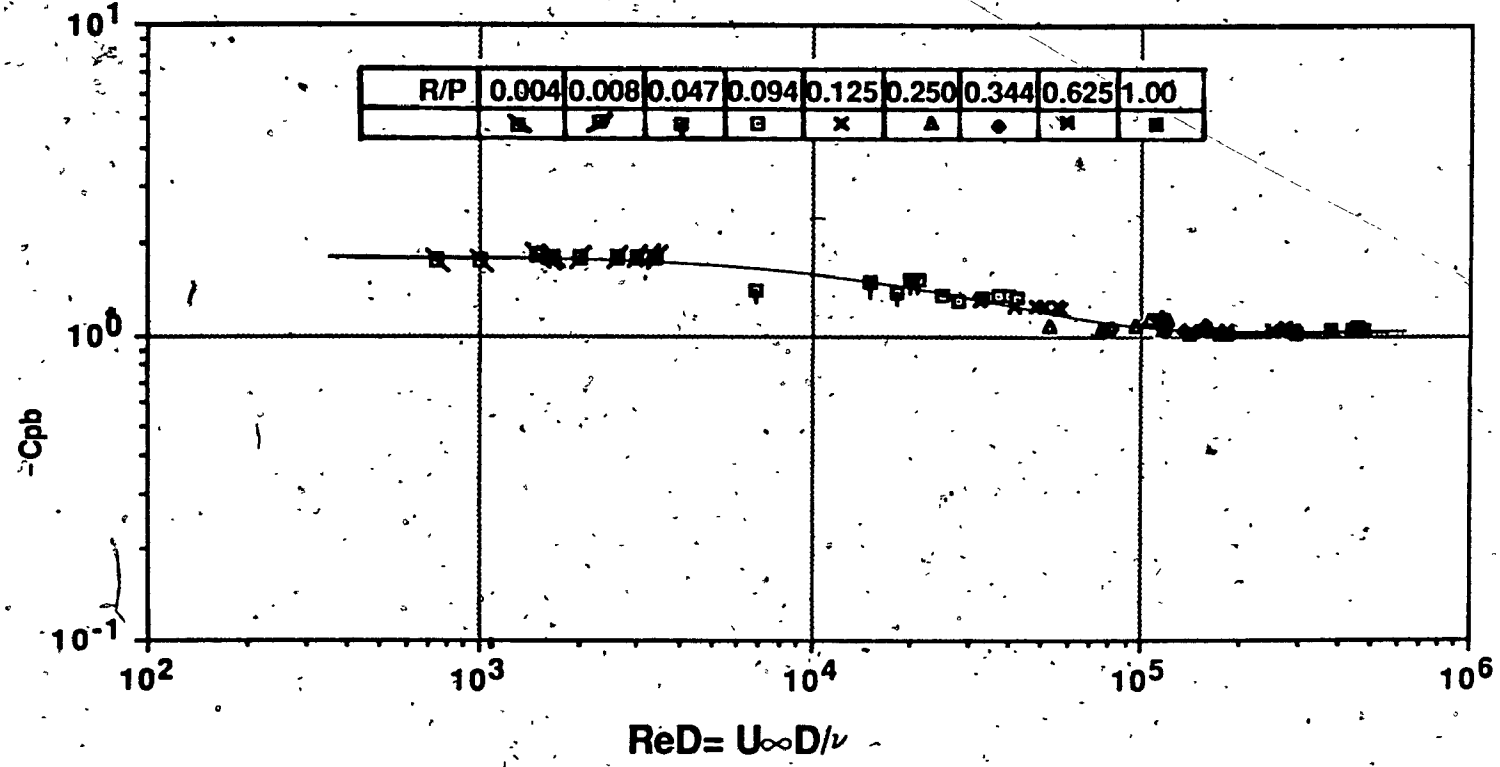

Figure 7.13 Variation of -Cpb with Reynolds Number ReD

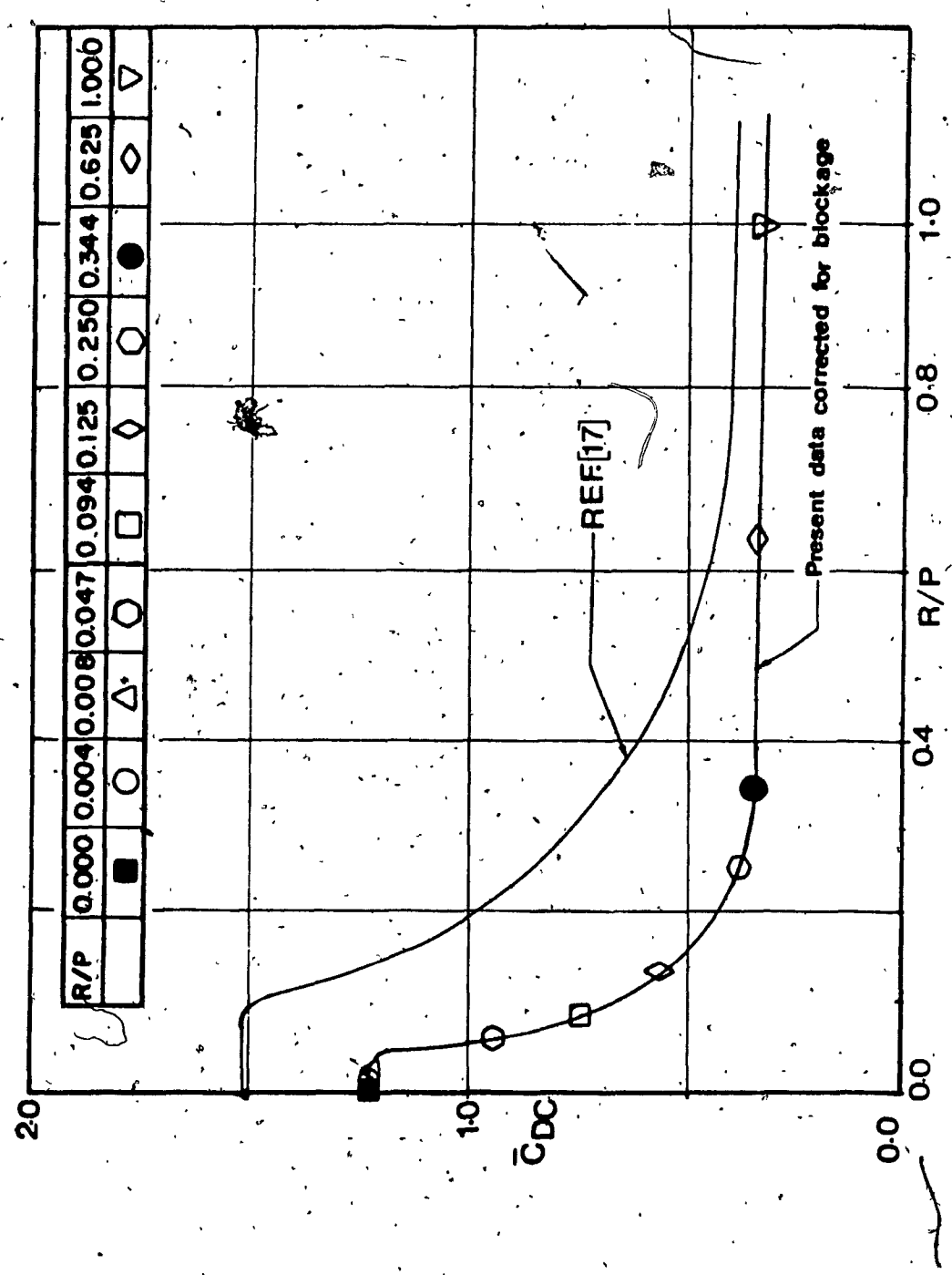

Figure 7.14 Variation of average Form Drag Coefficient $\bar{C}_{DC}$ With R/P

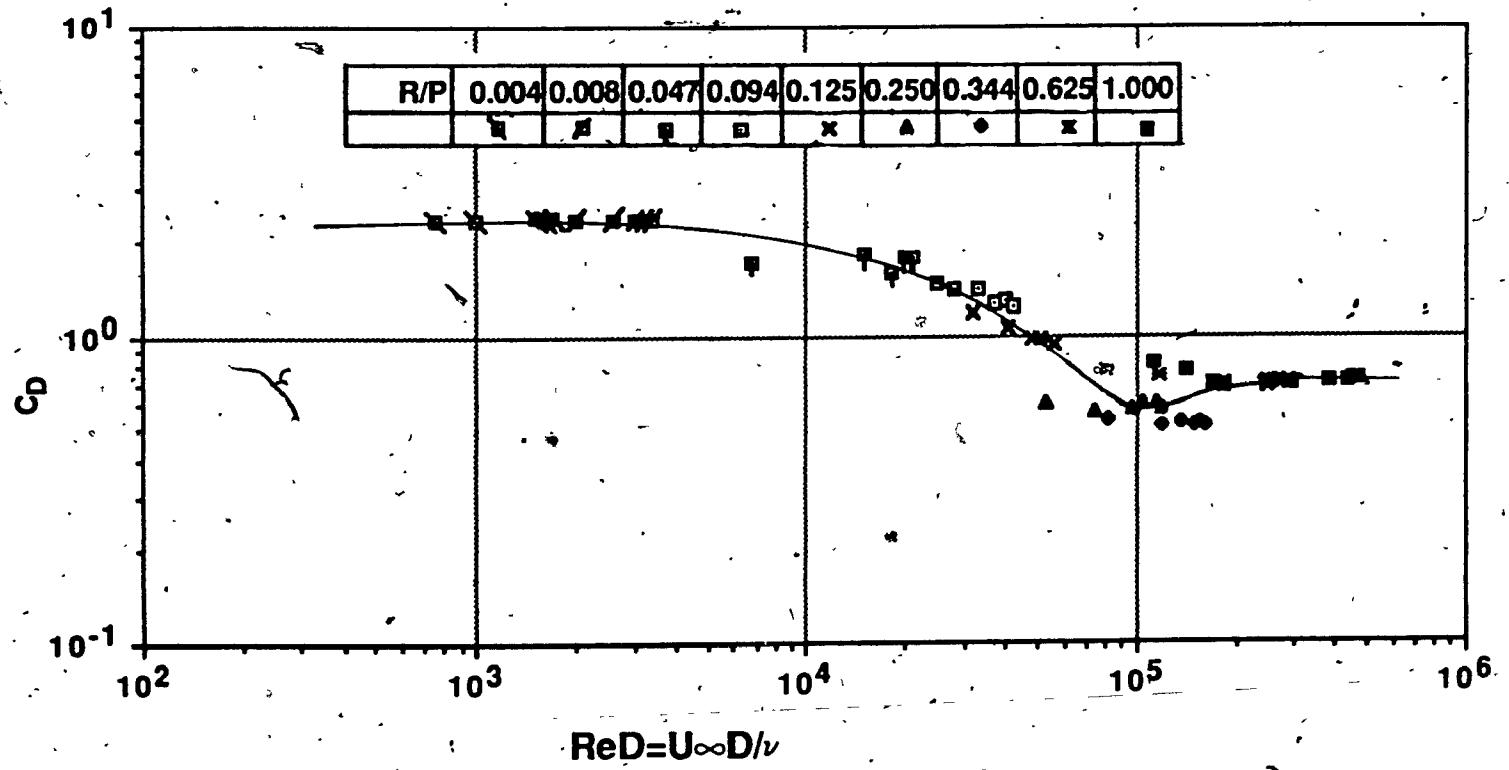

Figure 7.15 Variation of Form Drag Coefficient C_D with ReD

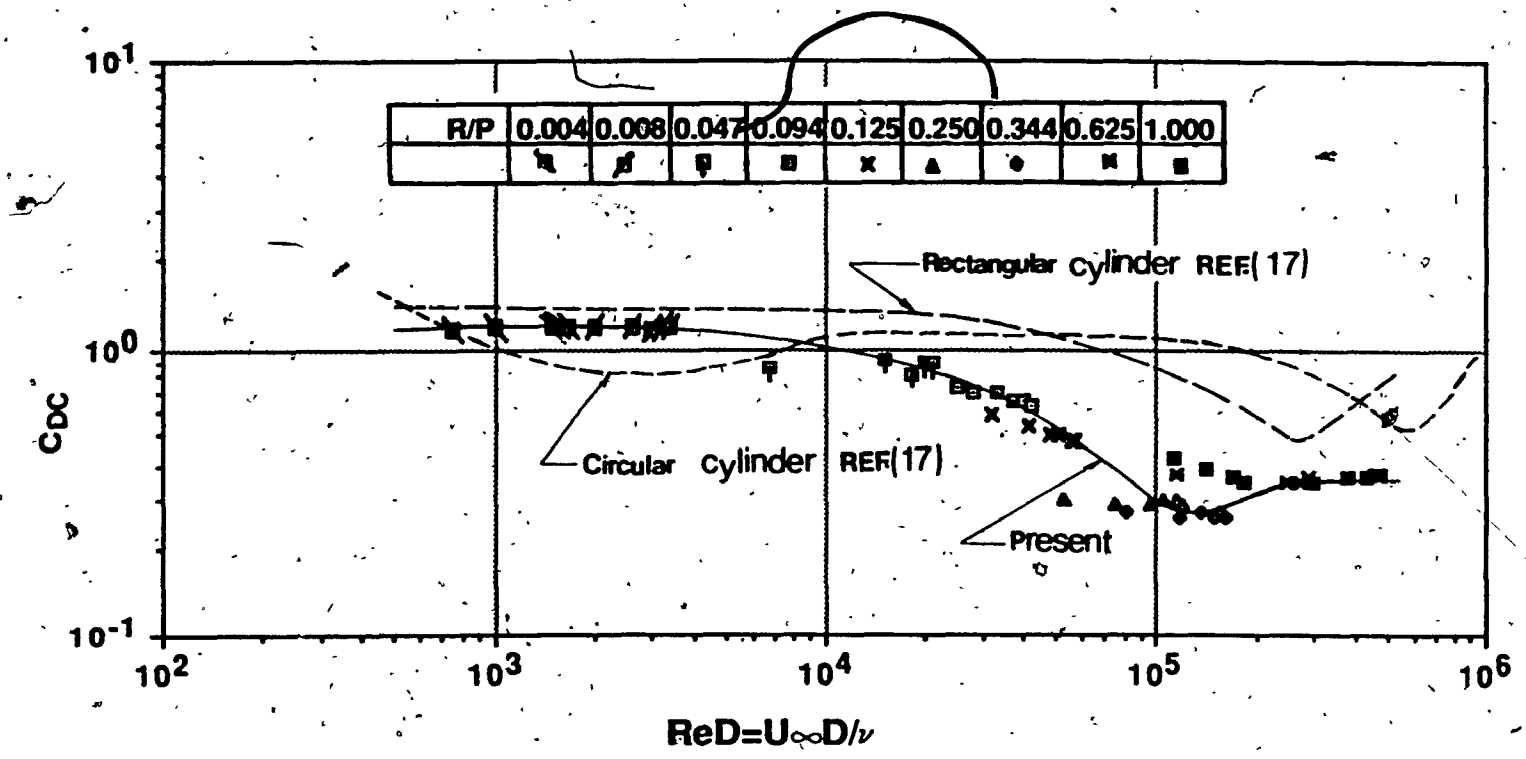

Figure 7.16 Variation of Form Drag Coefficient C_{DC} with ReD

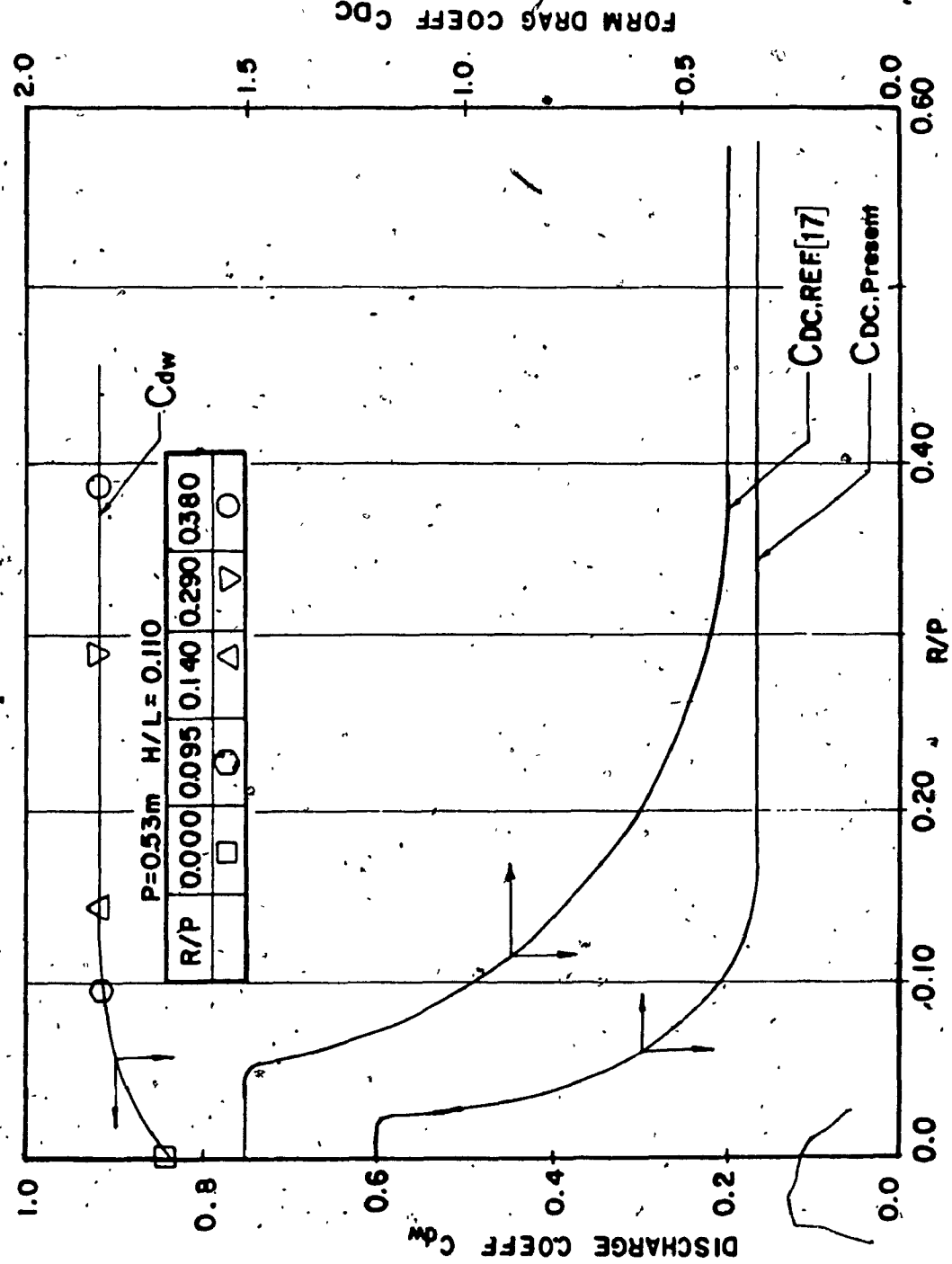

Figure 7.17 Variation of Discharge Coefficient C_{dw} with R/P.

TABLES

TABLE 2.1

SOME TYPICAL STUDIES ON LATERAL WEIRS

INVESTIGATOR AND REFERENCE NUMBER	TYPE OF CHANNEL SECTION CONSIDERED	NATURE OF FLOW IN MAIN CHANNEL	TYPE OF SOLUTION PROPOSED	REMARKS
Coleman and Smith [14]	Rectangular	Supercritical	Empirical	Proposes three empirical equations.
Nimo [47]	Rectangular	Subcritical and Supercritical	Semi-empirical	Theoretical approach based on momentum balance. No equation given for the coefficient of discharge.
DeMarchi [18]	Rectangular	Subcritical and Supercritical	Analytical	Theoretical approach based on constant energy in main channel.
Frazer [22]	Rectangular	Subcritical, critical and supercritical	Analytical	Constant energy with hydraulic jump in the channel reach spanned by the weir.
Allen [3]	Circular (Rectangular weir outlet)	Supercritical	Empirical	Effects of channel slope on discharge. No Equation for coefficient of discharge.
Subramanya and Awasthy [69]	Rectangular	Subcritical and Supercritical	Analytical	With effects of main channel velocity considered, they obtained a relationship between discharge coefficient and Froude number.

TABLE 2.1 (Continued)

SOME TYPICAL STUDIES ON LATERAL WEIRS

INVESTIGATOR AND REFERENCE NUMBER	TYPE OF CHANNEL SECTION CONSIDERED	NATURE OF FLOW IN MAIN CHANNEL	TYPE OF SOLUTION PROPOSED	REMARKS
El-Khashab and Smith [20]	Trapezoidal channel and rectangular weir	Subcritical and Supercritical	Numerical	Presented experimental investigation of velocity-distribution and surface profiles in the vicinity of weir.
Ramamurthy and Carballada [54]	Rectangular	Subcritical	Analytical and Experimental	Proposed a hydrodynamic model for rectangular weirs adopting the two-dimensional lateral outlet model.
Present study	Trapezoidal	Subcritical	Analytical and Experimental	For $0<L/B<1$ expressions are developed based on the two-dimensional lateral outlet model for trapezoidal lateral weir characteristics (namely, discharge discharge coefficient).

TABLE 2.2

RANGE OF GEOMETRIC VARIABLES: Trapezoidal Lateral Weir

Bottom width of main channel, b_o=10.16cm; side slope of main channel Z_1=1.5

Series	Sill height P in mm	Length of Weir at sill level L_s, in mm	Side Slope of Weir Projection Z	L/B
1	0.0	101.6	0.83	1.0
2	50.8	186.2	0,83	1.0
3	101.6	271.0	0.83	1.0
4	0.0	76.2	0.62	0.75
5	50.8	142.0	0.62	0.75
6	101.6	203.2	0.62	0.75
7	0.0	50.8	0.43	0.50
8	50.8	93.2	0.43	0.50
9	101.6	135.4	0.43	0.50

* inclined distance

Table 2.3

Lateral Weir in Trapezoidal Channels: Measurements and Computed Results

b_o = 10.2 cm, S' = 0.0 cm, vertical sill height = S = 0.0 cm, Z_1 = 1.5, Z = 0.83, L/B = 1.00, L_s = 10.2 cm

Run Number	Flow Depth Y_1 (cm)	Discharge Q_1 (l/sec)	Actual Weir Discharge Q_w' (l/sec)	Predicted Weir Discharge Q_w (l/sec) [Eq. 3]	η_o	Actual Mean Discharge Coeff. $\bar{C}_d$	Predicted Mean Discharge Coeff. $\bar{C}_d$	% deviation in $\bar{C}_d$ $\frac{(8)-(7)}{(7)} \times 100\%$
(1)	(2)	(3)	(4)	(5)	(6)	(7)	(8)	(9)
1	7.71	8.75	5.94	6.00	0.391	0.496	0.482	-2.8
2	8.60	10.90	7.36	7.00	0.389	0.501	0.482	-3.8
3	11.61	20.66	13.02	13.00	0.393	0.498	0.477	-4.2
4	6.10	5.04	3.96	4.00	0.364	0.519	0.495	-4.6
5	5.21	3.76	2.83	3.00	0.370	0.491	0.494	+0.6
6	7.32	7.16	5.38	5.00	0.361	0.510	0.495	-2.9
7	8.81	8.21	7.36	8.00	0.290	0.524	0.520	-0.8
8	10.00	14.51	9.91	10.00	0.372	0.515	0.488	-5.2
9	11.10	18.08	11.12	12.00	0.380	0.478	0.483	+1.1
10	11.80	21.14	13.02	14.00	0.389	0.483	0.479	+0.8
11	12.59	24.54	15.00	15.00	0.392	0.488	0.477	-2.3
12	6.19	4.92	3.99	4.00	0.346	0.516	0.502	-2.7
13	6.80	6.20	4.67	5.00	0.361	0.504	0.495	-1.8
14	6.10	4.87	3.99	4.00	0.353	0.528	0.499	-5.5
15	7.19	7.08	5.26	5.00	0.367	0.509	0.493	-3.1
16	9.11	11.66	8.21	8.00	0.373	0.510	0.488	-4.3
17	10.30	15.03	9.91	10.00	0.372	0.487	0.488	+0.2
18	12.19	21.00	13.73	14.00	0.364	0.490	0.490	0.0
19	13.81	21.34	17.55	18.00	0.291	0.524	0.517	-1.3
20	11.70	17.49	13.02	13.00	0.335	0.518	0.502	-3.1

Table 2.3 (Continued)

Lateral Weir in Trapezoidal Channels: Measurements and Computed Results

b_o = 10.2 cm, S' = 5.1 cm, vertical sill height = S = 2.82 cm, Z_1 = 1.5, Z = 0.83, L/B = 1.00, L s = 18.6 cm

Run Number	Flow Depth Y_1 (cm)	Discharge Q_1 (l/sec)	Actual Weir Discharge Q_w (l/sec)	Predicted Weir Discharge Q_t (l/sec)	η_o	Actual Mean Discharge Coeff. $\bar{C}_d$	Predicted Mean Discharge Coeff. $\bar{C}_d$	% deviation in $\bar{C}_d$ $\frac{(8)-(7)}{(7)} \times 100\%$
(1)	(2)	(3)	(4)	(5)	(6)	(7)	(8)	(9)
21	8.20	8.04	5.21	5.00	0.390	0.519	0.489	-5.8
22	7.41	5.66	3.40	4.00	0.354	0.457	0.504	+10.3
23	9.11	8.04	6.23	7.00	0.316	0.511	0.516	+1.0
24	10.61	11.52	9.34	10.00	0.319	0.530	0.514	-3.0
25	11.49	16.41	11.32	12.00	0.370	0.508	0.494	-2.7
26	6.10	2.46	2.26	2.00	0.251	0.564	0.538	-4.6
27	10.61	12.06	9.34	10.00	0.332	0.524	0.509	-2.9
28	8.41	6.31	5.38	5.00	0.300	0.545	0.522	-4.2
29	9.11	7.73	6.51	7.00	0.305	0.538	0.520	-3.3
30	10.00	10.56	8.07	8.00	0.333	0.520	0.510	-1.9
31	6.71	4.81	2.83	3.00	0.376	0.489	0.496	+1.4
32	9.11	9.06	6.51	7.00	0.352	0.518	0.503	-2.9
33	9.82	11.04	7.64	8.00	0.360	0.504	0.500	-0.8
34	8.00	7.92	4.53	5.00	0.404	0.474	0.484	+2.1
35	8.81	19.53	5.94	6.00	0.658	0.352	0.344	-2.3
36	7.32	11.32	3.68	4.00	0.615	0.378	0.375	-0.8
37	5.50	3.68	1.67	2.00	0.446	0.488	0.469	-3.9
38	13.60	25.53	16.70	17.00	0.388	0.502	0.485	-3.4
39	12.71	16.16	13.87	14.00	0.298	0.527	0.520	-1.3
40	4.60	0.85	0.83	0.90	0.182	0.577	0.556	-3.6

Table 2.3 (Continued)

Lateral Weir in Trapezoidal Channels: Measurements and Computed Results

b_o = 10.2 cm, S' = 10.2 cm vertical sill height = S = 5.64 cm, Z_1 = 1.5, Z = 0.83, L/B = 1.00, L_s = 27.1 cm

Run Number	Flow Depth Y_1 (cm)	Discharge Q_1 (l/sec)	Actual Weir Discharge Q'_w (l/sec)	Predicted Weir Discharge Q_t (l /sec)	η_o	Actual Mean Discharge Coeff. $\bar{C}_d$	Predicted Mean Discharge Coeff. $\bar{C}_d$	% deviation in $\bar{C}_d$ $\frac{(8)-(7)}{(7)} \times 100\%$
(1)	(2)	(3)	(4)	(5)	(6)	(7)	(8)	(9)
41	7.80	6.51	1.70	2.00	0.502	0.455	0.445	-2.2
42	10.00	13.58	4.25	5.00	0.502	0.380	0.442	+16.3
43	10.21	16.44	5.38	6.00	0.553	0.420	0.415	-1.2
44	10.91	17.55	6.51	7.00	0.511	0.426	0.437	+2.5
45	7.71	5.66	1.42	2.00	0.466	0.425	0.462	+8.7
46	8.90	9.62	3.11	3.00	0.496	0.444	0.447	+0.7
47	10.09	13.87	4.81	5.00	0.500	0.416	0.443	+6.5
48	11.61	19.24	7.92	9.00	0.485	0.437	0.449	+2.8
49	13.29	15.57	12.45	13.00	0.301	0.541	0.522	-3.5
50	10.91	7.64	6.79	7.00	0.251	0.565	0.538	-4.8
51	8.60	2.83	2.55	3.00	0.183	0.545	0.556	+2.0
52	9.39	4.25	3.96	4.00	0.211	0.575	0.549	-4.5
53	10.58	7.08	5.94	6.00	0.250	0.543	0.538	-0.9
54	11.80	9.34	8.21	9.00	0.249	0.529	0.538	+1.7
55	14.81	21.51	16.98	17.00	0.317	0.541	0.516	-4.6
56	10.21	14.72	5.38	6.00	0.512	0.443	0.437	-1.4
57	9.21	11.60	3.68	4.00	0.530	0.439	0.429	-2.3
58	8.69	9.34	2.83	3.00	0.510	0.438	0.440	+0.5
59	11.40	11.32	7.92	8.00	0.323	0.540	0.515	-4.6
60	9.11	11.32	3.40	4.00	0.533	0.422	0.428	+1.4

Table 2.3 (Continued)

Lateral Weir in Trapezoidal Channels: Measurements and Computed Results

b_o = 10.2 cm, S' = 0.0 cm, vertical sill height = S = 0.0 cm, Z_1 = 1.5, Z = 0.62, L/B = 0.75, L s = 7.6 cm

Run Number	Flow Depth Y_1 (cm)	Discharge Q_1 (l/sec)	Actual Weir Discharge Q_w (l/sec)	Predicted Weir Discharge Q_t (l/sec)	η_o	Actual Mean Discharge Coeff. $\bar{C}_d$	Predicted Mean Discharge Coeff. $\bar{C}_d$	% deviation in $\bar{C}_d$ $\frac{(8)-(7)}{(7)} \times 100\%$
(1)	(2)	(3)	(4)	(5)	(6)	(7)	(8)	(9)
1	6.31	4.81	2.83	3.00	0.330	0.484	0.493	+1.9
2	8.11	8.24	5.66	5.00	0.340	0.605	0.487	-19.5
3	9.30	10.67	6.51	6.00	0.332	0.541	0.489	-9.6
4	10.21	12.91	7.27	7.00	0.331	0.507	0.489	-3.6
5	11.10	16.58	8.49	9.00	0.353	0.493	0.478	-3.0
6	11.31	19.64	8.75	9.00	0.395	0.471	0.458	-2.8
7	12.31	23.49	10.47	11.00	0.394	0.478	0.457	-4.3
8	12.80	25.61	11.32	11.00	0.395	0.477	0.456	-4.4
9	10.21	15.82	7.08	7.00	0.395	0.464	0.459	-1.1
10	11.49	20.74	9.06	9.00	0.401	0.468	0.454	-3.0
11	10.40	16.02	7.36	8.00	0.386	0.470	0.463	-1.5
12	10.21	20.15	8.83	9.00	0.391	0.461	0.459	-0.4
13	12.31	22.95	10.19	11.00	0.387	0.469	0.461	-1.7
14	11.61	25.39	9.00	9.00	0.465	0.426	0.420	-1.4
15	12.50	28.75	10.70	11.00	0.452	0.444	0.427	-3.8
16	4.51	2.30	1.60	2.00	0.306	0.506	0.505	-0.2
17	5.61	4.08	2.24	2.00	0.350	0.465	0.485	+4.3
18	7.32	7.44	3.40	4.00	0.374	0.427	0.472	+10.5
19	9.30	14.12	5.94	6.00	0.422	0.452	0.446	-1.3
20	4.51	2.69	1.66	2.00	0.351	0.506	0.486	-3.9

Table 2.3 (Continued)

Lateral Weir in Trapezoidal Channels: Measurements and Computed Results

b_0 = 10.2 cm, S' = 5.1 cm, vertical sill height = S = 2.82 cm, Z_1 = 1.5, Z = 0.62, L/B = 0.75, L_s = 14.2 cm

Run Number	Flow Depth Y_1 (cm)	Discharge Q_1 (l/sec)	Actual Weir Discharge Q'_w (l/sec)	Predicted Weir Discharge Q_t (l/sec)	η_o	Actual Mean Discharge Coeff. $\bar{C}_d$	Predicted Mean Discharge Coeff. $\bar{C}_d$	% deviation in $\bar{C}_d$ $\frac{(8)-(7)}{(7)} \times 100\%$
(1)	(2)	(3)	(4)	(5)	(6)	(7)	(8)	(9)
21	6.01	1.73	1.56	2.00	0.186	0.557	0.549	-1.4
22	8.29	4.98	3.68	4.00	0.247	0.524	0.529	+0.9
23	10.00	8.01	5.94	6.00	0.258	0.533	0.524	-1.6
24	11.31	11.40	7.92	8.00	0.277	0.527	0.517	-1.9
25	12.20	14.04	9.34	10.00	0.285	0.518	0.513	-0.9
26	13.81	19.75	12.45	13.00	0.301	0.516	0.506	-1.9
27	6.90	2.75	2.41	2.00	0.211	0.569	0.541	-4.9
28	9.21	6.34	4.81	5.00	0.248	0.531	0.528	-0.6
29	10.61	9.45	6.79	7.00	0.266	0.528	0.521	-1.3
30	12.41	14.49	9.62	10.00	0.284	0.515	0.513	-0.4
31	15.00	23.83	15.00	15.00	0.300	0.517	0.505	-2.3
32	6.20	4.75	1.76	2.00	0.434	0.472	0.453	-4.0
33	8.60	10.47	3.96	4.00	0.443	0.436	0.446	+2.3
34	10.91	16.84	7.08	7.00	0.419	0.452	0.455	+0.7
35	12.31	21.93	9.06	10.00	0.415	0.439	0.456	+3.9
36	11.61	13.47	8.21	9.00	0.305	0.503	0.505	+0.3
37	9.69	8.80	5.38	6.00	0.301	0.503	0.508	+1.0
38	8.69	6.82	4.16	4.00	0.299	0.508	0.510	+0.4
39	6.20	2.72	1.59	2.00	0.266	0.491	0.524	+6.7
40	11.80	12.59	8.49	9.00	0.277	0.511	0.516	+1.0

Table 2.3 (Continued)

Lateral Weir in Trapezoidal Channels: Measurements and Computed Results

b_o = 10.2 cm, S' = 10.2 cm, vertical sill height = S = 5.64 cm, Z_1 = 1.5, Z = 0.62, L/B = 0.75, L_s = 20.3 cm

Run Number	Flow Depth Y_1 (cm)	Discharge Q_t (l/sec)	Actual Weir Discharge Q'_w (l/sec)	Predicted Weir Discharge Q_t (l/sec)	η_o	Actual Mean Discharge Coeff. $\bar{C}_d$	Predicted Mean Discharge Coeff. $\bar{C}_d$	% deviation in $\bar{C}_d$ $\frac{(8)-(7)}{(7)} \times 100\%$
(1)	(2)	(3)	(4)	(5)	(6)	(7)	(8)	(9)
41	8.29	4.26	1.68	2.00	0.297	0.528	0.514	-2.6
42	10.00	7.36	3.36	4.00	0.300	0.487	0.512	+5.1
43	11.89	11.26	6.44	7.00	0.290	0.525	0.514	-2.1
44	12.89	14.53	8.12	8.00	0.304	0.514	0.508	-1.2
45	13.59	16.52	9.24	10.00	0.302	0.503	0.509	+1.2
46	14.00	17.86	10.36	11.00	0.304	0.519	0.508	-2.0
47	13.11	16.13	8.62	9.00	0.322	0.514	0.501	-2.5
48	12.50	13.24	7.28	8.00	0.300	0.507	0.510	+0.6
49	11.31	9.30	5.04	6.00	0.276	0.489	0.520	+6.3
50	9.69	6.50	3.08	3.00	0.289	0.503	0.516	+2.6
51	13.02	22.71	8.12	9.00	0.439	0.445	0.448	+0.7
52	10.79	15.23	4.48	5.00	0.468	0.425	0.436	+2.6
53	8.50	7.81	1.68	2.00	0.469	0.404	0.438	+8.4
54	12.10	12.07	6.72	7.00	0.298	0.518	0.511	-1.4
55	13.20	15.51	8.68	9.00	0.305	0.513	0.508	-0.9
56	14.30	19.10	10.81	11.00	0.307	0.509	0.506	-0.6
57	8.81	2.21	1.90	2.00	0.134	0.501	0.563	+12.3
58	11.31	6.50	5.38	6.00	0.196	0.548	0.546	-0.3
59	14.11	14.62	10.64	11.00	0.248	0.544	0.528	-2.9
60	9.39	3.36	2.80	3.00	0.168	0.554	0.554	0.0

Table 2.3 (Continued)

Lateral Weir in Trapezoidal Channels: Measurements and Computed Results

b_o = 10.2 cm, S' = 0.0 cm, vertical sill height = S = 0.0 cm, Z_f = 1.5, Z = 0.43, L/B = 0.50, L_s = 5.1 cm

Run Number	Flow Depth Y_1 (cm)	Discharge Q_1 (l/sec)	Actual Weir Discharge Q_w' (l/sec)	Predicted Weir Discharge Q_t (l/sec)	η_o	Actual Mean Discharge Coeff. $\bar{C}_d$	Predicted Mean Discharge Coeff. $\bar{C}_d$	% deviation in $\bar{C}_d$ $\frac{(8)-(7)}{(7)} \times 100\%$
(1)	(2)	(3)	(4)	(5)	(6)	(7)	(8)	(9)
1	16.49	13.31	12.56	13.00	0.127	0.572	0.557	-2.6
2	15.21	12.65	10.52	11.00	0.145	0.561	0.551	-1.8
3	14.60	17.45	9.62	10.00	0.215	0.534	0.525	-1.7
4	11.89	11.51	6.48	7.00	0.220	0.537	0.524	-2.4
5	10.21	9.30	4.87	5.00	0.245	0.535	0.514	-3.9
6	9.69	10.56	4.23	4.00	0.304	0.489	0.487	-0.4
7	8.60	13.21	3.15	3.00	0.456	0.394	0.407	+3.3
8	5.30	6.25	1.36	1.00	0.537	0.374	0.364	-2.7
9	4.91	3.26	1.18	1.00	0.361	0.454	0.464	+2.2
10	6.19	7.25	1.84	2.00	0.478	0.411	0.398	-3.2
11	10.09	15.84	4.59	5.00	0.402	0.448	0.435	-2.9
12	11.40	19.62	5.83	6.00	0.388	0.456	0.441	-3.2
13	13.20	18.20	7.92	8.00	0.275	0.515	0.499	-3.1
14	16.00	20.20	11.14	12.00	0.204	0.518	0.529	+2.1
15	15.30	17.20	10.62	11.00	0.082	0.573	0.569	-0.7
16	6.71	4.90	2.10	2.00	0.301	0.485	0.492	+1.4
17	11.00	16.60	5.58	6.00	0.359	0.482	0.458	-5.0
18	4.60	2.90	1.09	1.00	0.362	0.468	0.464	-0.9
19	4.91	3.50	1.20	1.00	0.383	0.452	0.453	+0.2
20	5.70	4.18	1.63	2.00	0.347	0.485	0.470	-3.1

Table 2.3 (Continued)

Lateral Weir in Trapezoidal Channels: Measurements and Computed Results

b_o = 10.2 cm, S' = 5.1 cm, vertical sill height = S = 2.82 cm, Z_1 = 1.5, Z = 0.43, L/B = 0.50, L_s = 9.31 cm

Run Number	Flow Depth Y_1 (cm)	Discharge Q_1 (l/sec)	Actual Weir Discharge Q_w (l/sec)	Predicted Weir Discharge Q_t (l/sec)	η_o	Actual Mean Discharge Coeff. $\bar{C}_d$	Predicted Mean Discharge Coeff. $\bar{C}_d$	% deviation in $\bar{C}_d$ $\frac{(8)-(7)}{(7)} \times 100\%$
(1)	(2)	(3)	(4)	(5)	(6)	(7)	(8)	(9)
21	8.90	5.35	2.97	3.00	0.227	0.544	0.527	-3.1
22	9.39	6.05	3.36	3.00	0.227	0.538	0.527	-2.0
23	11.49	9.16	5.04	6.00	0.217	0.504	0.530	+5.1
24	13.41	13.41	7.56	8.00	0.223	0.531	0.526	-0.9
25	14.51	17.00	8.40	9.00	0.235	0.491	0.521	+6.1
26	9.91	10.56	3.64	4.00	0.339	0.474	0.477	+0.6
27	11.40	14.53	5.04	5.00	0.338	0.471	0.476	+1.1
28	12.31	16.94	5.60	6.00	0.332	0.441	0.478	+8.3
29	13.81	21.31	7.84	8.00	0.322	0.479	0.482	+0.6
30	10.61	12.26	4.48	5.00	0.337	0.497	0.477	-4.0
31	9.39	5.91	3.36	3.00	0.222	0.540	0.529	-2.0
32	11.80	8.43	5.58	6.00	0.189	0.561	0.540	-3.7
33	14.11	15.34	8.68	9.00	0.227	0.543	0.525	-3.3
34	14.81	17.86	9.24	10.00	0.236	0.515	0.521	+1.2
35	8.81	4.56	2.88	3.00	0.200	0.551	0.537	-2.5
36	9.91	5.66	3.81	4.00	0.190	0.550	0.540	-1.8
37	12.41	8.57	6.16	7.00	0.172	0.532	0.546	+2.6
38	13.90	11.54	8.40	9.00	0.178	0.558	0.543	-2.7
39	4.30	3.08	0.31	0.32	0.621	0.365	0.324	-11.2
40	7.01	5.15	1.48	2.00	0.365	0.455	0.467	+2.6

Table 2.3 (Continued)

Lateral Weir in Trapezoidal Channels: Measurements and Computed Results

b_o = 10.2 cm, S' =10.2 cm, vertical sill height = S = 5.64 cm, Z_1 = 1.5, Z = 0.43, L/B = 0.50, L_s = 13.5 cm

Run Number	Flow Depth Y_1 (cm)	Discharge Q_1 (l/sec)	Actual Weir Discharge Q_w' (l/sec)	Predicted Weir Discharge Q_t (l/sec)	η_o	Actual Mean Discharge Coeff. $\bar{C}_d$	Predicted Mean Discharge Coeff. $\bar{C}_d$	% deviation in $\bar{C}_d$ $\frac{(8)-(7)}{(7)} \times 100\%$
(1)	(2)	(3)	(4)	(5)	(6)	(7)	(8)	(9)
41	10.52	5.26	2.80	3.00	0.193	0.546	0.541	-0.9
42	10.15	7.98	2.94	3.00	0.273	0.512	0.510	-0.4
43	12.59	12.10	4.90	5.00	0.271	0.509	0.510	+0.2
44	14.17	16.07	7.09	7.00	0.267	0.517	0.511	-1.2
45	15.51	19.82	8.40	9.00	0.265	0.489	0.511	+4.5
46	13.11	19.82	5.60	6.00	0.386	0.472	0.456	-3.4
47	7.71	5.18	0.73	1.00	0.434	0.453	0.436	-3.8
48	9.39	8.90	1.85	2.00	0.409	0.458	0.447	-2.4
49	11.31	13.94	3.36	4.00	0.394	0.441	0.453	+2.7
50	12.31	18.93	4.48	5.00	0.424	0.439	0.436	-0.7
51	13.29	23.35	5.74	6.00	0.428	0.444	0.433	-2.5
52	12.31	18.65	4.48	5.00	0.419	0.441	0.439	-0.5
53	10.91	13.82	3.08	3.00	0.424	0.444	0.437	-1.6
54	15.91	17.22	9.52	10.00	0.218	0.534	0.530	-0.8
55	15.21	15.18	8.12	9.00	0.215	0.514	0.531	+3.3
56	14.00	11.96	6.72	7.00	0.209	0.535	0.534	-0.2
57	12.80	9.18	5.32	5.00	0.201	0.551	0.538	-2.4
58	11.00	5.99	2.98	3.00	0.194	0.496	0.541	+9.1
59	7.89	2.27	0.87	1.00	0.190	0.562	0.543	-3.4
60	9.82	6.50	2.21	2.00	0.282	0.523	0.597	-3.1

TABLE 3.1

RANGE OF GEOMETRIC VARIABLES: Lateral Orifice Tests

Model No.	Sill height S, in mm	Orifice Height a, in mm	S/a	L/B
1	101.6	25.4	4.00	1.00
2	50.8	25.4	2.00	1.00
3	101.6	76.2	1.33	1.00
4	101.6	127.0	0.80	1.00
5	50.8	127.0	0.40	1.00

Table 3.2

Rectangular Lateral Orifices: Measurements and Computed Results

B = 25.4 cm, L = 25.4 cm, S = 10.16 cm, a = 2.54 cm, S/a = 4.0, L/B = 1.0

Run Number	Flow Depth Y_1 (cm)	Discharge Q_1 (l /sec)	Actual Orifice Discharge Q_o (l /sec)	Predicted Orifice Discharge Q_o (l /sec)	Orifice Parameter η_{01}	Actual Discharge Coeff. $\bar{C}_{do}$	Predicted Discharge Coeff. $\bar{C}_{do}$	% deviation in $\bar{C}_{do}$ $\frac{(8) - (7)}{(7)} \times 100\%$
(1)	(2)	(3)	(4)	(5)	(6)	(7)	(8)	(9)
1	12.7	16.60	1.80	1.79	0.592	0.401	0.399	-0.5
2	13.5	19.50	2.40	2.44	0.577	0.446	0.453	+1.6
3	15.2	25.90	3.30	3.33	0.561	0.478	0.482	+0.8
4	17.0	26.30	3.90	3.97	0.467	0.509	0.518	+1.8
5	18.6	26.20	4.40	4.44	0.397	0.530	0.535	+0.9
6	24.4	26.00	5.90	5.88	0.244	0.564	0.562	-0.4
7	26.2	30.00	5.90	6.28	0.247	0.528	0.562	+6.4
8	26.3	14.80	6.00	6.27	0.124	0.549	0.574	+4.6

Table 3.2 (Continued)

Rectangular Lateral Orifices: Measurements and Computed Results

B = 25.4 cm, L = 25.4 cm, S = 5.0 cm, a = 2.5 cm, S/a = 2.0, L/B = 1.0

Run Number	Flow Depth Y_1 (cm)	Discharge Q_1 (l /sec)	Actual Orifice Discharge Q_0 (l /sec)	Predicted Orifice Discharge Q_0 (l /sec)	Orifice Parameter η_{01}	Actual Discharge Coeff. $\bar{C}_{do}$	Predicted Discharge Coeff. $\bar{C}_{do}$	% deviation in $\bar{C}_{do}$ $\frac{(8) - (7)}{(7)} \times 100\%$
(1)	(2)	(3)	(4)	(5)	(6)	(7)	(8)	(9)
9	7.4	5.20	1.70	1.66	0.374	0.513	0.502	-2.1
10	8.8	9.30	2.80	2.67	0.434	0.540	0.515	-4.6
11	11.2	13.00	3.40	3.69	0.383	0.494	0.536	+8.5
12	14.5	16.90	4.70	4.72	0.319	0.548	0.550	+0.3
13	16.3	20.60	5.10	5.21	0.317	0.539	0.551	+2.2
14	24.4	26.80	7.00	6.95	0.216	0.570	0.566	-0.7
15	24.5	34.60	7.10	6.99	0.273	0.567	0.559	-1.4
16	27.0	34.60	7.40	7.44	0.236	0.560	0.564	+0.7
17	28.4	38.00	7.80	7.69	0.239	0.571	0.563	-1.4
18	20.1	27.50	6.00	6.10	0.299	0.545	0.555	+1.8

Table 3.2 (Continued)

Rectangular Lateral Orifices: Measurements and Computed Results

B = 25.4 cm, L = 25.4 cm, S = 10.16 cm, a = 7.62 cm, S/a = 1.33 ; L/B = 1.0

Run Number	Flow Depth Y_1 (cm)	Discharge Q_1 (l /sec)	Actual Orifice Discharge Q_o (l /sec)	Predicted Orifice Discharge Q_o (l /sec)	Orifice Parameter η_{01}	Actual Discharge Coeff. $\bar{C}_{do}$	Predicted Discharge Coeff. $\bar{C}_{do}$	% deviation in $\bar{C}_{do}$ $\frac{(8)-(7)}{(7)} \times 100\%$
(1)	(2)	(3)	(4)	(5)	(6)	(7)	(8)	(9)
19	13.0	13.60	2.00	2.12	0.486	0.429	0.456	+6.3
20	15.3	16.90	5.30	5.17	0.399	0.505	0.492	-2.6
21	16.1	19.50	6.50	6.43	0.405	0.495	0.490	-1.0
22	18.0	22.40	10.00	9.70	0.368	0.525	0.509	-3.0
23	19.3	25.80	11.50	11.45	0.367	0.527	0.524	-0.6
24	20.2	30.00	12.70	12.49	0.385	0.532	0.524	-1.5
25	23.3	41.90	14.90	15.42	0.404	0.508	0.526	+3.5
26	24.9	49.20	15.70	16.74	0.417	0.493	0.525	+6.5
27	12.8	5.40	1.70	1.84	0.227	0.506	0.547	+8.1
28	23.9	52.10	16.00	16.11	0.464	0.508	0.512	+0.8

Table 3.2 (Continued)

Rectangular Lateral Orifices: Measurements and Computed Results

B = 25.4 cm, L = 25.4 cm, S = 10.16 cm, a = 12.7 cm, S/a = 0.80, $\sqrt{B}$ = 1.0

Run Number	Flow Depth Y_1 (cm)	Discharge Q_1 (l/sec)	Actual Orifice Discharge Q_o (l/sec)	Predicted Orifice Discharge Q_o (l/sec)	Orifice Parameter η_{01}	Actual Discharge Coeff. C_{do}	Predicted Discharge Coeff. $\bar{C}_{do}$	% deviation in C_{do} $\frac{(8)-(7)}{(7)} \times 100\%$
(1)	(2)	(3)	(4)	(5)	(6)	(7)	(8)	(9)
29	13.3	15.10	2.50	2.47	0.497	0.455	0.450	-1.1
30	14.4	17.60	3.80	3.89	0.468	0.453	0.464	+2.4
31	15.8	23.00	5.90	6.00	0.480	0.451	0.458	+1.5
32	17.3	26.60	8.80	8.55	0.456	0.483	0.469	-2.9
33	18.6	29.20	11.30	10.97	0.434	0.493	0.478	-3.0
34	19.2	25.50	11.60	12.06	0.366	0.485	0.505	+4.1
35	19.9	24.50	13.30	13.43	0.332	0.512	0.516	+0.8
36	20.4	34.50	15.30	14.70	0.425	0.502	0.482	-4.0
37	21.4	37.90	17.40	16.87	0.426	0.497	0.482	-3.0
38	21.8	42.00	18.40	17.83	0.449	0.487	0.472	-3.0
39	22.5	45.80	20.00	19.49	0.459	0.480	0.468	-2.5
40	22.6	27.00	19.40	19.29	0.289	0.533	0.530	-0.6
41	27.2	52.00	28.40	27.34	0.381	0.546	0.525	-3.9
42	32.1	55.00	33.80	32.81	0.310	0.563	0.546	-3.0
43	32.9	58.00	35.30	33.67	0.312	0.573	0.546	-4.7

Table 3.2 (Continued)

Rectangular Lateral Orifices: Measurements and Computed Results

B = 25.4 cm, L = 25.4 cm, S = 5.08 cm, a = 12.7 cm, S/a = 0.40, L/B = 1.0

Run Number	Flow Depth Y_1 (cm)	Discharge Q_1 (l /sec)	Actual Orifice Discharge Q_o (l /sec)	Predicted Orifice Discharge Q_o (l /sec)	Orifice Parameter η_{01}	Actual Discharge Coeff. $\bar{C}_{do}$	Predicted Discharge Coeff. $\bar{C}_{do}$	% deviation in $\bar{C}_{do}$ $\frac{(8) - (7)}{(7)} \times 100\%$
(1)	(2)	(3)	(4)	(5)	(6)	(7)	(8)	(9)
44	7.3	5.30	1.60	1.56	0.392	0.507	0.495	-2.3
45	8.1	8.30	2.40	2.47	0.460	0.455	0.467	+2.6
46	9.0	11.00	3.60	3.62	0.477	0.457	0.459	+0.4
47	9.8	14.50	4.70	4.77	0.515	0.435	0.442	+1.6
48	10.3	16.70	5.50	5.54	0.531	0.430	0.433	+0.7
49	10.8	17.80	6.20	6.34	0.520	0.429	0.439	+2.3
50	11.1	19.10	6.90	6.84	0.527	0.439	0.436	-0.6
51	12.2	24.40	8.50	8.77	0.552	0.409	0.422	+3.2
52	14.1	24.80	12.60	12.40	0.460	0.475	0.467	-1.7
53	15.4	28.80	15.60	15.15	0.458	0.482	0.468	-2.9
54	23.1	43.70	29.00	28.70	0.368	0.536	0.531	-0.9
55	24.4	46.50	30.60	30.24	0.359	0.541	0.534	-1.3
56	24.9	50.70	31.60	30.92	0.376	0.543	0.531	-2.2

TABLE 4.1

GEOMETRIC VARIABLES: Lateral Weir-Orifice Units

Length of unit, L = 25.4 cm; Width of main channel B = 25.4 cm; L/B = 1.0

Series	Sill height S, in mm	Orifice Height a, in mm	Blocked height b, in mm	S/a	b/a
1	101.6	127.0	127.0	0.80	1.00
2	101.6	76.2	76.2	1.33	1.00
3	101.6	25.4	101.6	4.0	4.00

Table 4.2 a
Lateral Weir-Orifice Units: Measurements and Computed Results

B = 254.0 mm, L = 254.0 mm, S = 101.6 mm, a = 127.0 mm, S/a = 0.80

Run Number	Discharge Q_1 (l/sec)	Actual Q_o (l/sec) (at Y=S+a)	Froude Number F_1	Actual Q_{ro} (y=S+a)	Predicted Q_{ro} [modified Eq. 4.20]	% deviation in Q_{ro} $\frac{(6) - (5)}{(5)} \times 100$
(1)	(2)	(3)	(4)	(5)	(6)	(7)
1	27.8	21.1	0.320	0.760	0.755	-0.7
2	32.6	21.5	0.375	0.660	0.653	-1.1
3	33.3	21.1	0.383	0.635	0.636	+0.2
4	33.6	20.7	0.387	0.615	0.631	+2.6
5	35.2	21.1	0.405	0.600	0.604	+0.7
6	38.3	22.2	0.440	0.580	0.561	-3.3
7	39.5	21.8	0.455	0.550	0.539	-2.0
8	40.0	21.6	0.460	0.540	0.532	-1.5
9	40.4	21.3	0.465	0.527	0.529	+0.4
10	41.3	21.6	0.475	0.523	0.520	-0.6
11	42.6	22.2	0.490	0.520	0.503	-3.3
12	44.4	21.3	0.510	0.480	0.484	+0.8
13	46.1	21.4	0.530	0.465	0.470	+1.1
14	47.0	20.9	0.540	0.445	0.460	+3.4
15	50.9	21.1	0.585	0.415	0.427	+2.9
16	55.4	21.1	0.637	0.380	0.393	+3.4

Table 4.2b
Lateral Weir-Orifice Units: Measurements and Computed Results

B = 254.0 mm, L = 254.0 mm, S = 101.6 mm, a = 76.2 mm, S/a = 1.33

Run Number	Discharge Q_i (l/sec)	Actual Q_o (l/sec) (at Y=S+a)	Froude Number F_1	Actual Q_{ro} (y=S+a)	Predicted Q_{ro} [modified Eq. 4.20]	% deviation in Q_{ro} $\frac{(6)-(5)}{(5)} \times 100$
(1)	(2)	(3)	(4)	(5)	(6)	(7)
17	17.3	9.8	0.290	0.565	0.568	+0.5
18	19.7	10.3	0.331	0.525	0.500	-4.8
19	21.1	9.9	0.354	0.470	0.470	0.0
20	21.7	9.8	0.364	0.453	0.457	+0.8
21	22.4	10.1	0.375	0.450	0.446	-0.9
22	23.1	9.9	0.388	0.430	0.432	+0.5
23	24.9	10.0	0.418	0.400	0.402	+0.5
24	26.6	9.8	0.445	0.370	0.378	+2.2
25	28.1	10.4	0.470	0.369	0.357	-3.3
26	29.8	10.4	0.500	0.350	0.338	-3.4
27	31.8	10.1	0.534	0.316	0.318	+0.6
28	35.2	9.8	0.590	0.277	0.288	+4.0

Table 4.2c
Lateral Weir-Orifice Units: Measurements and Computed Results

B = 254.0 mm, L = 254.0 mm, S = 101.6 mm, a = 25.4 mm, S/a = 4·00

Run Number	Discharge Q_1 (l/sec)	Actual Q_o (l/sec) (at Y=S+a)	Froude Number F_1	Actual Q_{ro} (y=S+a)	Predicted Q_{ro} [modified Eq. 4.20]	% deviation in Q $\frac{(6)-(5)}{(5)} \times 100$
(1)	(2)	(3)	(4)	(5)	(6)	(7)
29	6.9	1.9	0.193	0.280	0.272	-2.9
30	8.1	2.0	0.225	0.250	0.235	-6.0
31	9.9	2.1	0.212	0.274	0.194	-8.5
32	10.2	1.8	0.283	0.180	0.189	+5.0
33	10.8	1.9	0.300	0.179	0.177	-1.1
34	11.7	2.0	0.325	0.170	0.165	-2.9
35	12.6	1.9	0.350	0.150	0.153	+2.0
36	14.8	2.0	0.410	0.135	0.132	-2.2
37	16.4	1.8	0.455	0.112	0.119	+6.3
38	17.7	2.0	0.490	0.115	0.109	-5.2
39	19.8	2.0	0.550	0.100	0.097	-3.0
40	21.6	1.9	0.600	0.090	0.087	-3.3

Table 4.3
Lateral Weir-Orifice Unit: Measurements and Computed Results

B = 254.0 mm, L = 254.0 mm, S = 101.6 mm, a = 127.0 mm, S/a = 0.8, b/a = 1.0

Run Number	Flow depth, Y_u (mm)	Discharge Q_l (l /sec)	Actual Q_{wo} (l /sec)	Froude Number F_l	Actual Q_r	Predicted Q_r [Eq. 4.20]	Flow depth h_3 (mm)	h_3/a	% deviation in Q $\frac{(7) - (6)}{(6)} \times 100$
(1)	(2)	(3)	(4)	(5)	(6)	(7)	(8)	(9)	(10)
1	451.5	77.2	61.9	0.320	0.802	0.793	95.0	0.755	-1.1
2	451.7	90.5	62.6	0.375	0.692	0.686	96.1	0.757	-0.9
3	452.0	92.6	61.7	0.383	0.666	0.668	96.4	0.759	+0.3
4	452.4	93.7	60.3	0.387	0.644	0.661	96.8	0.762	+2.6
5	452.6	98.1	61.6	0.405	0.628	0.632	97.0	0.764	+0.6
6	452.9	106.6	64.7	0.440	0.607	0.588	97.3	0.766	-3.1
7	453.3	110.4	63.4	0.455	0.574	0.563	97.7	0.769	-1.9
8	453.5	111.7	62.9	0.460	0.563	0.555	97.9	0.771	-1.4
9	453.8	113.1	62.2	0.465	0.550	0.550	98.2	0.773	0.0
10	453.9	115.5	62.9	0.475	0.545	0.541	98.3	0.774	-0.7
11	454.0	119.2	64.5	0.490	0.541	0.524	98.4	0.775	-3.1
12	454.1	124.1	61.9	0.510	0.499	0.504	98.5	0.775	+1.0
13	454.1	128.9	62.3	0.530	0.483	0.490	98.5	0.775	+1.4
14	454.2	131.5	60.6	0.540	0.461	0.476	98.6	0.776	+3.3
15	454.4	142.5	61.1	0.585	0.429	0.441	98.8	0.778	+2.8
16	454.9	155.4	60.9	0.637	0.392	0.407	99.3	0.782	+3.8

Table 4.3 (Continued)
Lateral Weir-Orifice Unit: Measurements and Computed Results

B = 254.0 mm, L = 254.0 mm, S = 101.6 mm, a = 76.2 mm, S/a = 1.33, b/a = 1.0

Run Number	Flow depth, Y_u (mm)	Discharge Q_l (l /sec)	Actual Q_{wo} (l /sec)	Froude Number F_1	Actual Q_r	Predicted Q_r [Eq. 4.20]	Flow depth h_3 (mm)	h_3/a	% deviation in Q_r $\frac{(7)-(6)}{(6)} \times 100$
(1)	(2)	(3)	(4)	(5)	(6)	(7)	(8)	(9)	(10)
17	279.0	34.0	21.3	0.290	0.627	0.632	25.0	0.328	+0.8
18	279.2	38.9	22.5	0.331	0.579	0.552	25.2	0.330	-4.7
19	279.4	41.6	21.6	0.354	0.518	0.520	25.4	0.333	+0.4
20	279.9	42.9	21.4	0.364	0.499	0.507	25.9	0.340	+1.6
21	280.8	44.4	22.0	0.375	0.495	0.494	26.8	0.351	-0.2
22	280.9	46.0	21.8	0.388	0.474	0.476	26.9	0.353	+0.4
23	281.0	49.5	21.8	0.418	0.440	0.444	27.0	0.354	+0.9
24	281.3	52.8	21.4	0.445	0.406	0.416	27.3	0.358	+2.5
25	282.2	56.1	22.6	0.470	0.403	0.396	28.2	0.370	-1.7
26	282.6	59.7	22.9	0.500	0.383	0.376	28.6	0.375	-1.8
27	284.0	64.3	22.1	0.534	0.344	0.355	30.0	0.393	+3.2
28	284.3	71.1	21.4	0.590	0.301	0.324	30.3	0.398	+7.6

Table 4.3 (Continued)
Lateral Weir-Orifice Unit: Measurements and Computed Results

B = 254.0 mm, L = 254.0 mm, S = 101.6 mm, a = 25.4 mm, b = 101.6 mm, S/a = 4.0, b/a = 4.0

Run Number	Flow depth, Y_u (mm)	Discharge Q_1 (l/sec)	Actual Q_{wo} (l/sec)	Froude Number F_1	Actual Q_r	Predicted Q_r [Eq. 4.20]	Flow depth h_3 (mm)	h_3/a	% deviation in Q_r $\frac{(7)-(6)}{(6)} \times 100$
(1)	(2)	(3)	(4)	(5)	(6)	(7)	(8)	(9)	(10)
29	245.1	18.6	7.3	0.193	0.394	0.388	16.5	0.650	-1.5
30	245.2	21.7	7.6	0.225	0.348	0.326	16.6	0.655	-6.3
31	245.3	26.5	7.8	0.274	0.296	0.284	16.7	0.659	-4.1
32	245.5	27.4	7.1	0.283	0.258	0.271	16.9	0.665	-5.0
33	246.4	29.2	7.5	0.300	0.255	0.253	17.8	0.700	-0.8
34	246.5	31.6	7.6	0.325	0.240	0.235	17.9	0.705	-2.1
35	246.6	34.1	7.3	0.350	0.213	0.200	18.0	0.708	-6.1
36	247.0	40.0	7.6	0.410	0.189	0.186	18.4	0.725	-1.6
37	247.1	44.4	7.1	0.455	0.160	0.169	18.5	0.728	+5.6
38	247.2	47.9	7.7	0.490	0.160	0.157	18.6	0.730	-1.9
39	247.4	53.9	7.7	0.550	0.142	0.140	18.8	0.740	-1.4
40	247.7	58.8	7.5	0.600	0.128	0.125	19.1	0.750	-2.3

TABLE 5.1
TYPICAL STUDIES ON FLOW OVER SHARP-CRESTED WEIRS

INVESTIGATOR	SUGGESTED EQUATION FOR DISCHARGE COEFFICIENT C_{de}	LIMITATION	REMARKS
Bazin [5]	$C_{de} = \left(0.6075 + \frac{0.0045}{H}\right)\left(1 + 0.55\left(\frac{1}{1+W/H}\right)^2\right)$		Equation holds good for relatively high weirs
Francis [21]	$C_{de} = 0.622\left[\left(1 + \frac{V_0^2}{2gH}\right)^{1.5} - \left(\frac{V_0^2}{2gH}\right)^{1.5}\right]$		
Swiss, S.I.A. [64]	$C_{de} = \left(0.615 + \frac{0.000615}{H+0.0016}\right)\left(1 + 0.5\left(\frac{H/W}{1+H/W}\right)\right)^2$	0.025m<H<0.88m W>0.3m H/W<1.0	Equation does not cover the entire weir range
Institute de Mecanique des Fluides de Toulouse [75]	$C_{de} = \left(0.627 + 0.018\ H_1 / W\right)$	H>0.03m W>0.1m H/W<2.5	Equation expressed in terms of the total head rather than the gauged head
Rehbock [57]	$C_{de} = \left(0.602 + 0.0832\ H/W\right)\left(1 + \frac{0.00125}{H}\right)^{1.5}$	0.03m<H<0.75m W>0.3m H/W<1.0	Effect of fluid property considered

TABLE 5.1 (Continued)
TYPICAL STUDIES ON FLOW OVER SHARP-CRESTED WEIRS

Kindsvater and Carter [38]	$C_{de} = \left(0.602 + 0.075\ H/W\right)\left(B-0.001\right)\left(1 + \frac{0.001}{H}\right)^{1.5}$	H>0.03m B>0.15m W>0.10m H/W<2.0	The effect of fluid property on the channel width is considered.
White [77]	$C_{de} = 0.596\left(1 + 0.153\ H/W\right)\left(1 + \frac{0.001}{H}\right)^{1.5}$	H>0.02m W>0.15m H/W≤2.2	Effect of fluid property considered
Kandaswamy and Rouse [36, 37]	$C_{de} = 0.605 + 0.08\ H/W$ —weir $C_{de} = 1.06\left(1 + W/H\right)^{1.5}$ —sill	0<H/W<10 10<H/W<∞	The proposed equation covers the weir and sill ranges of flow
Present study	Equations (5.20) and (5.26) for both weir and sill ranges	.625≤H/W≤∞	Equations developed covers the entire weir and sill ranges of flow

TABLE 5.2

MAIN VARIABLES: Sharp-Crested Weir Tests

Test Series	Weir Height W, mm	Measured Head H, mm	H/W	Arbitrary Weir Designation
1	101.6	63.5	0.625	
2	101.6	114.3	1.12	
3	50.8	101.6	2.00	
4	25.4	86.4	3.44	
5	25.4	101.6	4.00	→ WEIR RANGE
6	12.7	60.1	4.73	
7	12.7	76.2	6.00	
8	12.7	101.6	8.00	
9	12.7	108.8	8.57	
10	6.4	63.5	10.00	
11	6.4	76.2	12.00	
12	6.4	95.3	15.00	→ SILL RANGE
13	3.2	63.5	20.00	
14	3.2	79.4	25.00	
15	3.2	105.7	33.30	
16	0.0	76.2	∞	→ FREE OVERFALL

TABLE 5.3

Rectangular Sharp-crestd Weir: Measurements and Results

Channel width B = 60.3 cm.

Weir Desig-nation	Weir Height W (cm)	Measured Head H (cm)	Measured Discharge Q_1 (/sec)	H/W	Flow Depth at Section EF Y_o (cm)	Flow Depth at Section KL h_e (cm)	Y_o/H	h_e/H	Actual C_{de} Eq. (5.12)	Predicted C_{de} (Momentum) Eq. (5.20)	Predicted C_{de} (Velocity) Eq. (5.27)
(1)	(2)	(3)	(4)	(5)	(6)	(7)	(8)	(9)	(10)	(11)	(12)
01	25.4	2.5	4.30	0.10	1.3	3.2	0.52	0.69	0.61	0.61	0.68
02	5.1	3.2	6.60	0.63	1.7	2.3	0.54	0.71	0.67	0.65	0.70
03	5.1	5.7	16.80	1.12	3.2	4.2	0.56	0.74	0.71	0.69	0.73
04	2.5	5.0	15.70	2.00	3.1	3.8	0.62	0.77	0.79	0.78	0.79
05	1.3	4.5	14.80	3.44	3.0	3.7	0.67	0.81	0.89	0.88	0.87
06	1.3	5.2	19.70	4.00	3.6	4.3	0.69	0.83	0.92	0.93	0.90
07	1.3	6.1	25.80	4.73	4.4	5.2	0.73	0.85	0.95	0.96	0.95
08	0.6	3.6	13.40	6.00	2.8	3.2	0.78	0.88	1.05	1.10	1.02
09	0.6	4.8	22.00	8.00	4.0	4.5	0.84	0.94	1.17	1.18	1.09
10	0.6	5.1	24.30	8.57	4.3	4.8	0.84	0.94	1.18	1.19	1.10
11	0.3	3.0	11.00	10.00	2.5	2.8	0.85	0.92	1.21	1.19	1.23
12	0.3	3.6	14.20	12.00	3.0	3.3	0.84	0.91	1.21	1.17	1.22
13	0.3	4.5	19.70	15.00	3.7	4.0	0.82	0.89	1.19	1.16	1.18
14	0.3	5.4	25.40	18.00	4.3	4.6	0.80	0.86	1.16	1.14	1.16
15	0.3	6.0	30.00	20.00	4.7	5.1	0.79	0.84	1.14	1.15	1.15
16	0.2	5.0	22.30	25.00	3.9	4.2	0.78	0.83	1.13	1.12	1.13
17	0.2	6.7	34.00	33.33	5.1	5.3	0.76	0.78	1.10	1.10	1.11
18	0.0	7.7	40.7	∞	5.6	5.6	0.73	0.73	1.06	1.07	1.06

TABLE 5.4

Rectangular Sharp-crested Weir: Pressure and Velocity Data

H/W = 0.625; H = 3.2 cm; $U_o = \sqrt{2gH} = 0.792$ m/sec; W = 5.1 cm.

Section KL: h_e = 2.3 cm, h_e/H = 0.714					Section EF: Y_o = 1.3 cm; Y_o/H = 0.540				
y/h_e	p/γ cm	$p/\gamma h_e$	V(h) (m/sec)	$V(h)/U_o$	y/Y_o	$\frac{p}{\gamma}$ cm	$p/\gamma Y_o$	V(y) (m/sec)	$V(y)/U_o$
0.062	0.1	0.056	0.754	0.952	0.095	0.3	0.203	0.73	0.92
0.182	0.5	0.211	0.656	0.828	0.276	0.4	0.290	0.62	0.78
0.302	1.1	0.482	0.484	0.611	0.458	0 4	0.317	0.54	0.68
0.422	1.0	0.444	0.439	0.554	0.640	0.3	0.255	0.49	0.62
0.542	1.0	0.441	0.397	0.501	0.821	0.2	0.160	0.47	0.59
0.662	0.7	0.310	0.373	0.471					
0.782	0.4	0.191	0.372	0.470					
0.902	0.2	0.095	0.356	0.450					

TABLE 5.4 (Continued)

Rectangular Sharp-crested Weir: Pressure and Velocity Data

H/W = 1.12; H = 5.7 cm; U_o = 1.057 m/sec; W = 5.1 cm.

Section KL: h_e = 4.2 cm, h_e/H = 0.736					Section EF: Y_o = 3.2 cm; Y_o/H = 0.560				
y/h_e	p/γ cm	$p/\gamma\, h_e$	V(h) (m/sec)	$V(h)/U_o$	y/Y_o	$\frac{p_e}{\gamma}$ cm	$p/\gamma\, Y_o$	V(y) (m/sec)	$V(y)/U_o$
0.032	0.4	0.090	1.000	0.946	0.043	0.6	0.173	0.98	0.93
0.095	0.8	0.192	0.917	0.868	0.125	0.7	0.225	0.93	0.88
0.157	1.7	0.395	0.767	0.726	0.207	0.8	0.251	0.88	0.84
0.220	2.0	0.476	0.671	0.635	0.289	0.9	0.276	0.85	0.80
0.282	2.1	0.496	0.610	0.577	0.371	1.0	0.302	0.79	0.75
0.344	2.1	0.495	0.560	0.530	0.452	1.0	0.314	0.75	0.71
0.407	1.9	0.473	0.529	0.500	0.534	0.8	0.245	0.74	0.70
0.469	1.8	0.431	0.505	0.478	0.616	0.8	0.244	0.70	0.66
0.531	1.6	0.389	0.486	0.460	0.698	0.7	0.215	0.68	0.64
0.594	1.5	0.368	0.442	0.419	0.780	0.5	0.161	0.66	0.62
0.656	1.4	0.326	0.420	0.398	0.862	0.3	0.106	0.65	0.61
0.719	1.1	0.264	0.420	0.397	0.944	0.2	0.051	0.62	0.59
0.780	0.9	0.222	0.419	0.396					
0.843	0.8	0.180	0.418	0.395					
0.906	0.4	0.100	0.418	0.395					
0.068	0.3	0.065	0.418	0.395					

TABLE 5.4 (Continued)

Rectangular Sharp-crested Weir: Pressure and Velocity Data

H/W = 2.00; H = 5.0 cm; U_o = 0.990 m/sec; W = 2.5 cm.

Section KL: h_e = 3.8 cm, h_e/H = 0.765					Section EF: Y_o = 3.1 cm; Y_o/H = 0.610				
y/h_e	p/γ cm	$p/\gamma h_e$	V(h) (m/sec)	$V(h)/U_o$	y/Y_o	$\frac{p}{\gamma}$ cm	$p/\gamma Y_o$	V(y) (m/sec)	$V(y)/U_o$
0.070	1.7	0.450	0.725	0.732	0.088	0.7	0.210	0.88	0.89
0.205	1.8	0.493	0.608	0.614	0.258	1.0	0.330	0.75	0.76
0.340	1.9	0.490	0.505	0.510	0.427	0.9	0.290	0.69	0.70
0.470	1.7	0.450	0.420	0.424	0.600	0.8	0.254	0.62	0.63
0.610	1.3	0.354	0.396	0.400	0.766	0.5	0.168	0.57	0.58
0.740	0.8	0.210	0.386	0.390	0.936	0.2	0.054	0.55	0.55
0.880	0.3	0.090	0.363	0.367					

TABLE 5.4 (Continued)

Rectangular Sharp-crested Weir: Pressure and Velocity Data

H/W = 3.44; H = 4.5 cm; U_o = 0.940 m/sec; W = 1.30 cm.

Section KL: h_e = 3.7 cm, h_e/H = 0.810					Section EF: Y_o = 3.0 cm; Y_o /H = 0.670				
y/h_e	p/γ cm	$p/\gamma\, h_e$	V(h) (m/sec)	$V(h)/U_o$	y/Y_o	$\frac{p}{\gamma}$ cm	$p/\gamma\, Y_o$	V(y) (m/sec)	$V(y)/U_o$
0.041	0.80	0.212	0.833	0.886	0.050	0.6	0.198	0.88	0.94
0.119	1.1	0.288	0.758	0.806	0.148	0.7	0.228	0.80	0.85
0.198	1.5	0.390	0.661	0.703	0.245	1.0	0.332	0.72	0.77
0.276	1.7	0.440	0.583	0.620	0.342	1.0	0.321	0.68	0.72
0.355	1.6	0.413	0.548	0.583	0.439	0.9	0.303	0.64	0.68
0.434	1.5	0.386	0.510	0.543	0.536	0.8	0.250	0.62	0.66
0.512	1.3	0.333	0.492	0.523	0.633	0.7	0.221	0.58	0.62
0.591	1.1	0.280	0.471	0.501	0.730	0.6	0.187	0.56	0.60
0.669	0.8	0.202	0.471	0.501	0.827	0.5	0.154	0.54	0.57
0.748	0.7	0.175	0.427	0.454	0.924	0.3	0.089	0.53	0.56
0.826	0.2	0.047	0.472	0.502					
0.905	0.2	0.043	0.404	0.430					

TABLE 5.4 (Continued)

Rectangular Sharp-crested Weir: Pressure and Velocity Data

H/W = 4.00; H = 5.2 cm; U_o = 1.00 m/sec; W = 1.3 cm.

Section KL: h_e=4.3 cm, h_e/H = 0.827					Section EF: Y_o = 3.6 cm; Y_o /H = 0.690				
y/h_e	p/γ cm	$p/\gamma h_e$	V(h) (m/sec)	$V(h)/U_o$	y/Y_o	$\frac{p}{\gamma}$ cm	$p/\gamma Y_o$	V(y) (m/sec)	$V(y)/U_o$
0.035	0.9	0.204	0.887	0.887	0.043	0.60	0.170	0.93	0.93
0.103	1.2	0.269	0.818	0.818	0.127	0.8	0.223	0.87	0.87
0.170	1.6	0.379	0.716	0.716	0.210	1.1	0.304	0.79	0.79
0.238	1.8	0.422	0.643	0.643	0.293	1.1	0.302	0.76	0.76
0.305	1.8	0.421	0.600	0.600	0.377	1.1	0.301	0.72	0.72
0.372	1.7	0.398	0.562	0.562	0.460	1.1	0.300	0.67	0.67
0.440	1.6	0.364	0.534	0.534	0.543	1.0	0.271	0.64	0.64
0.508	1.4	0.330	0.505	0.505	0.627	0.9	0.242	0.61	0.61
0.575	1.2	0.284	0.486	0.486	0.710	0.8	0.214	0.60	0.60
0.643	1.0	0.239	0.475	0.475	0.793	0.6	0.158	0.59	0.59
0.710	0.7	0.171	0.466	0.466	0.877	0.4	0.102	0.57	0.57
0.778	0.5	0.104	0.465	0.465	0.960	0.1	0.030	0.55	0.55
0.845	0.3	0.058	0.444	0.444					
0.912	0.1	0.013	0.422	0.422					
0.980	0.1	0.012	0.420	0.420					

TABLE 5.4 (Continued)

Rectangular Sharp-crested Weir: Pressure and Velocity Data

H/W = 4.73; H = 6.1 cm; U_o = 1.094 m/sec; W = 1.3 cm.

Section KL: h_e = 5.2 cm, h_e/H = 0.851					Section EF: Y_o = 4.4 cm; Y_o/H = 0725				
y/h_e	p/γ cm	$p/\gamma h_e$	V(h) (m/sec)	$V(h)/U_o$	y/Y_o	$\frac{p}{\gamma}$ cm	$p/\gamma Y_o$	V(y) (m/sec)	$V(y)/U_o$
0.030	1.20	0.229	0.960	0.877	0.036	0.52	0.118	0.03	0.94
0.087	1.5	0.284	0.895	0.818	0.105	0.9	0.207	0.96	0.88
0.144	2.1	0.395	0.789	0.721	0.174	1.1	0.252	0.92	0.84
0.200	2.2	0.413	0.737	0.674	0.243	1.3	0.296	0.88	0.80
0.258	2.1	0.412	0.695	0.635	0.312	1.4	0.317	0.83	0.76
0.315	2.1	0.411	0.650	0.595	0.381	1.4	0.316	0.79	0.72
0.372	2.0	0.392	0.619	0.566	0.450	1.3	0.292	0.76	0.69
0.429	1.9	0.372	0.586	0.536	0.519	1.2	0.280	0.72	0.66
0.486	1.7	0.334	0.569	0.520	0.588	1.1	0.256	0.70	0.64
0.543	1.5	0.295	0.551	0.504	0.657	1.1	0.241	0.68	0.62
0.600	1.3	0.257	0.533	0.487	0.726	0.9	0.198	0.66	0.60
0.657	1.1	0.219	0.513	0.469	0.794	0.8	0.173	0.63	0.58
0.714	0.9	0.180	0.494	0.452	0.863	0.4	0.090	0.62	0.57
0.771	0.7	0.142	0.474	0.433	0.932	0.2	0.040	0.61	0.56
0.828	0.5	0.095	0.462	0.422					
0.885	0.2	0.047	0.452	0.413					
0.942	0.1	0.008	0.430	0.393					

TABLE 5.4 (Continued)

Rectangular Sharp-crested Weir: Pressure and Velocity Data

H/W = 6.0; H = 3.6 cm; U_o = 0.840 m/sec; W = 0.60 cm.

Section KL: h_e=3.2 cm, h_e/H = 0.883					Section EF: Y_o = 2.8 cm; Y_o /H = 0.780				
y/h_e	p/γ cm	$p/\gamma h_e$	V(h) (m/sec)	$V(h)/U_o$	y/Y_o	$\frac{p}{\gamma}$ cm	$p/\gamma Y_o$	V(y) (m/sec)	$V(y)/U_o$
0.050	0.9	0.267	0.722	0.859	0.061	0.5	0.170	0.77	0.92
0.147	1.2	0.361	0.640	0.762	0.118	0.6	0.207	0.74	0.88
0.224	1.2	0.376	0.588	0.700	0.179	0.7	0.246	0.71	0.84
0.341	1.1	0.356	0.547	0.651	0.296	0.9	0.302	0.65	0.77
0.438	1.0	0.325	0.511	0.609	0.414	0.8	0.300	0.61	0.72
0.535	0.8	0.260	0.493	0.587	0.518	0.7	0.240	0.59	0.70
0.632	0.6	0.194	0.474	0.564	0.649	0.7	0.238	0.53	0.63
0.729	0.4	0.130	0.454	0.540	0.767	0.6	0.198	0.50	0.59
0.826	0.2	0.065	0.433	0.515	0.885	0.3	0.100	0.49	0.58
0.923	0.1	0.015	0.400	0.476					

TABLE 5.4 (Continued)

Rectangular Sharp-crested Weir: Pressure and Velocity Data

H/W = 8.0; H = 4.8 cm; U_o = 0.970 m/sec; W = 0.60 cm.

Section KL: h_e=4.5 cm, h_e/H = 0.935					Section EF: Y_o = 4.0 cm; Y_o/H = 0.835				
y/h_e	p/γ cm	$p/\gamma h_e$	V(h) (m/sec)	$V(h)/U_o$	y/Y_o	$\frac{p}{\gamma}$ cm	$p/\gamma Y_o$	V(y) (m/sec)	$V(y)/U_o$
0.039	0.9	0.206	0.869	0.896	0.046	0.4	0.10	0.92	0.95
0.113	1.7	0.376	0.776	0.779	0.136	0.9	0.217	0.84	0.87
0.189	1.8	0.399	0.704	0.726	0.225	1.1	0.274	0.80	0.82
0.262	1.9	0.422	0.650	0.670	0.314	1.2	0.302	0.75	0.77
0.337	1.7	0.372	0.635	0.655	0.404	1.2	0.300	0.71	0.73
0.486	1.6	0.347	0.557	0.574	0.493	1.2	0.299	0.66	0.68
0.561	1.0	0.220	0.582	0.600	0.671	0.8	0.210	0.62	0.64
0.635	0.8	0.172	0.574	0.592	0.760	0.8	0.207	0.57	0.59
0.710	0.6	0.122	0.558	0.575	0.850	0.5	0.131	0.56	0.58
0.784	0.3	0.072	0.542	0.558	0.939	0.2	0.057	0.55	0.57
0.859	0.1	0.022	0.522	0.539					
0.933	0.1	0.015	0.514	0.530					

TABLE 5.4 (Continued)

Rectangular Sharp-crested Weir: Pressure and Velocity Data

H/W = 8.57; H = 5.1 cm; U_o = 1.00 m/sec; W = 0.6 cm.

Section KL: h_e=4.8 cm, h_e/H = 0.938					Section EF: Y_o = 4.3 cm; Y_o/H = 0.840				
y/h_e	p/γ cm	$p/\gamma h_e$	V(h) (m/sec)	$V(h)/U_o$	y/Y_o	$\frac{p}{\gamma}$ cm	$p/\gamma Y_o$	V(y) (m/sec)	$V(y)/U_o$
0.034	0.7	0.139	0.941	0.941	0.043	0.4	0.092	0.96	0.96
0.100	0.9	0.182	0.902	0.902	0.126	0.9	0.227	0.90	0.90
0.167	1.9	0.398	0.792	0.792	0.208	1.1	0.266	0.87	0.87
0.233	1.9	0.397	0.764	0.764	0.291	1.3	0.292	0.83	0.83
0.299	1.8	0.374	0.746	0.746	0.374	1.3	0.304	0.80	0.80
0.365	1.7	0.351	0.726	0.726	0.456	1.2	0.289	0.78	0.78
0.431	1.5	0.307	0.716	0.716	0.539	1.2	0.280	0.75	0.75
0.498	1.3	0.262	0.706	0.706	0.621	1.2	0.273	0.73	0.73
0.564	1.3	0.261	0.674	0.675	0.704	0.9	0.218	0.72	0.72
0.630	1.3	0.260	0.642	0.642	0.787	0.7	0.162	0.71	0.71
0.696	1.0	0.205	0.637	0.637	0.869	0.5	0.107	0.70	0.70
0.762	0.8	0.160	0.626	0.626	0.952	0.2	0.048	0.69	0.69
0.828	0.4	0.083	0.631	0.631					
0.894	0.2	0.039	0.620	0.626					
0.961	0.1	0.016	0.600	0.600					

TABLE 5.4 (Continued)

Rectangular Sharp-crested Weir: Pressure and Velocity Data

H/W = 10.0; H = 3.0 cm; U_o = 0.767 m/sec; W = 0.3 cm.

Section KL: h_e=2.8 cm, h_e/H = 0.920					Section EF: Y_o = 2.5cm; Y_o /H = 0.845				
y/h_e	p/γ cm	$p/\gamma h_e$	V(h) (m/sec)	$V(h)/U_o$	y/Y_o	$\frac{p}{\gamma}$ cm	$p/\gamma Y_o$	V(y) (m/sec)	$V(y)/U_o$
0.070	0.7	0.238	0.677	0.883	0.083	0.4	0.140	0.71	0.93
0.204	1.1	0.400	0.578	0.753	0.241	0.4	0.175	0.67	0.87
0.338	1.1	0.406	0.525	0.684	0.400	0.5	0.199	0.61	0.80
0.472	1.0	0.350	0.492	0.641	0.559	0.5	0.190	0.57	0.74
0.606	0.8	0.270	0.469	0.611	0.717	0.3	0.137	0.54	0.70
0.740	0.5	0.183	0.447	0.583	0.816	0.2	0.060	0.53	0.69
0.874	0.3	0.094	0.425	0.554					

TABLE 5.4 (Continued)

Rectangular Sharp-crested Weir: Pressure and Velocity Data

H/W = 12.0; H = 3.6 cm; U_0 = 0.840 m/sec; W = 0.3 cm.

Section KL: h_e=3.3 cm, h_e/H = 0.910					Section EF: Y_0 = 3.0cm; Y_0/H = 0.835				
y/h_e	p/γ cm	$p/\gamma h_e$	V(h) (m/sec)	$V(h)/U_0$	y/Y_0	$\frac{p}{\gamma}$ cm	$p/\gamma Y_0$	V(y) (m/sec)	$V(y)/U_0$
0.054	0.8	0.252	0.734	0.874	0.063	0.4	0.136	0.78	0.93
0.157	1.2	0.352	0.655	0.780	0.185	0.5	0.174	0.73	0.87
0.261	1.4	0.418	0.579	0.689	0.307	0.6	0.212	0.68	0.81
0.364	1.3	0.382	0.547	0.651	0.429	0.5	0.171	0.66	0.78
0.468	1.0	0.313	0.529	0.630	0.551	0.5	0.169	0.61	0.73
0.571	0.9	0.261	0.501	0.597	0.673	0.3	0.127	0.58	0.69
0.675	0.7	0.208	0.473	0.563	0.795	0.3	0.085	0.55	0.65
0.779	0.5	0.139	0.454	0.540	0.915	0.1	0.043	0.51	0.71
0.882	0.3	0.069	0.433	0.515					
0.986	0.1	0.018	0.403	0.480					

TABLE 5.4 (Continued)

Rectangular Sharp-crested Weir: Pressure and Velocity Data

H/W = 15.0; H = 4.5 cm; U_o = 0.939 m/sec; W = 0.3 cm.

Section KL: h_e=4.0 cm, h_e/H = 0.890					Section EF: Y_o = 3.7cm; Y_o /H = 0.820				
y/h_e	p/γ cm	$p/\gamma h_e$	V(h) (m/sec)	$V(h)/U_o$	y/Y_o	$\frac{p}{\gamma}$ cm	$p/\gamma Y_o$	V(y) (m/sec)	$V(y)/U_o$
0.042	1.0	0.250	0.824	0.878	0.052	0.4	0.110	0.89	0.95
0.124	1.3	0.330	0.753	0.802	0.150	0.6	0.174	0.84	0.89
0.206	1.5	0.383	0.688	0.733	0.250	0.8	0.205	0.79	0.84
0.287	1.6	0.409	0.632	0.674	0.349	0.8	0.220	0.75	0.80
0.369	1.5	0.381	0.602	0.641	0.448	0.8	0.218	0.71	0.76
0.450	1.3	0.326	0.643	0.685	0.547	0.7	0.200	0.68	0.72
0.532	1.1	0.284	0.563	0.600	0.646	0.7	0.183	0.64	0.68
0.613	0.9	0.230	0.547	0.582	0.745	0.6	0.165	0.60	0.64
0.695	0.8	0.188	0.520	0.554	0.844	0.4	0.095	0.59	0.63
0.777	0.5	0.133	0.502	0.535	0.943	0.2	0.050	0.56	0.60
0.858	0.3	0.079	0.483	0.514					
0.940	0.1	0.024	0.463	0.493					

TABLE 5.4 (Continued)

Rectangular Sharp-crested Weir: Pressure and Velocity Data

H/W = 18.0; H = 5.4 cm; U_o = 1.029 m/sec; W = 0.3 cm.

Section KL: h_e = 4.6 cm; h_e/H = 0.860					Section EF: Y_o = 4.3cm; Y_o/H = 0.80				
y/h_e	p/γ cm	$p/\gamma h_e$	V(h) (m/sec)	$V(h)/U_o$	y/Y_o	$\frac{p}{\gamma}$ cm	$p/\gamma Y_o$	V(y) (m/sec)	$V(y)/U_o$
0.037	1.2	0.265	0.905	0.879	0.043	0.5	0.120	0.98	0.95
0.107	1.4	0.310	0.852	0.828	0.126	0.6	0.146	0.94	0.91
0.178	1.6	0.355	0.795	0.773	0.208	0.9	0.200	0.89	0.86
0.249	1.8	0.400	0.735	0.714	0.309	0.7	0.170	0.86	0.84
0.319	1.9	0.422	0.683	0.664	0.374	0.7	0.169	0.83	0.81
0.390	2.0	0.421	0.641	0.623	0.456	0.7	0.167	0.79	0.77
0.461	1.7	0.374	0.626	0.608	0.539	0.7	0.166	0.76	0.74
0.531	1.6	0.338	0.604	0.587	0.622	0.6	0.151	0.73	0.71
0.602	1.3	0.279	0.596	0.579	0.704	0.5	0.123	0.68	0.66
0.672	1.1	0.231	0.580	0.564	0.787	0.5	0.108	0.67	0.65
0.743	0.9	0.184	0.564	0.548	0.869	0.3	0.066	0.65	0.63
0.814	0.6	0.136	0.547	0.532	0.952	0.2	0.051	0.63	0.61
0.884	0.4	0.089	0.530	0.515					
0.955	0.2	0.042	0.511	0.497					

TABLE 5.4 (Continued)

Rectangular Sharp-crested Weir: Pressure and Velocity Data

H/W = 20.0; H = 6.0 cm; U_o = 1.085 m/sec; W = 0.3 cm.

Section KL: h_e = 5.1 cm, h_e/H = 0.843					Section EF: Y_o = 4.7cm; Y_o/H = 0.790				
y/h_e	p/γ cm	$p/\gamma h_e$	V(h) (m/sec)	$V(h)/U_o$	y/Y_o	$\frac{p}{\gamma}$ cm	$p/\gamma Y_o$	V(y) (m/sec)	$V(y)/U_o$
0.034	0.7	0.137	0.014	0.935	0.040	0.4	0.087	1.04	0.96
0.100	0.8	0.157	0.977	0.900	0.118	0.6	0.136	1.00	0.92
0.164	1.1	0.220	0.919	0.847	0.195	0.8	0.160	0.96	0.88
0.229	1.7	0.326	0.834	0.769	0.275	0.9	0.185	0.92	0.85
0.294	1.9	0.368	0.777	0.716	0.350	1.0	0.209	0.88	0.81
0.359	1.9	0.367	0.740	0.682	0.428	1.0	0.208	0.85	0.78
0.425	1.8	0.345	0.714	0.658	0.505	1.0	0.207	0.81	0.75
0.490	1.8	0.343	0.674	0.621	0.583	0.9	0.193	0.78	0.72
0.555	1.5	0.300	0.660	0.608	0.660	0.8	0.166	0.76	0.70
0.620	1.3	0.256	0.647	0.506	0.738	0.7	0.140	0.74	0.68
0.685	1.1	0.212	0.632	0.582	0.816	0.5	0.112	0.71	0.65
0.750	0.9	0.169	0.616	0.568	0.893	0.3	0.073	0.68	0.63
0.815	0.6	0.124	0.602	1.555	0.943	0.1	0.010	0.67	0.62
0.880	0.4	0.080	0.587	0.541					

TABLE 5.4 (Continued)

Rectangular Sharp-crested Weir: Pressure and Velocity Data

H/W = 25.0; H = 5.0 cm; U_o = 0.990 m/sec; W = 0.2 cm.

Section KL: h_e = 4.2 cm, h_e/H = 0.839					Section EF: Y_o = 3.9cm; Y_o/H = 0.780				
y/h_e	p/γ cm	$p/\gamma h_e$	V(h) (m/sec)	$V(h)/U_o$	y/Y_o	$\frac{p}{\gamma}$ cm	$p/\gamma Y_o$	V(y) (m/sec)	$V(y)/U_o$
0.059	0.5	0.120	0.927	0.937	0.069	0.58	0.149	0.93	0.94
0.171	0.8	0.198	0.856	0.865	0.203	0.75	0.191	0.87	0.88
0.284	1.4	0.326	0.757	0.764	0.336	0.82	0.211	0.82	0.83
0.396	1.4	0.326	0.706	0.713	0.469	0.73	0.186	0.78	0.79
0.509	1.1	0.267	0.679	0.686	0.603	0.72	0.184	0.73	0.74
0.622	0.9	0.210	0.651	0.658	0.736	0.63	0.161	0.69	0.70
0.734	0.6	0.134	0.633	0.639	0.869	0.36	0.093	0.66	0.67
0.847	0.3	0.077	0.602	0.608					
0.960	0.1	0.030	0.564	0.570					

TABLE 5.4 (Continued)

Rectangular Sharp-crested Weir: Pressure and Velocity Data

H/W = 33.3; H = 6.7 cm; U_0 = 1.146 m/sec; W = 0.2 cm.

Section KL: h_e=5.3 cm, h_e/H = 0.784					Section EF: Y_0 = 5.1cm; Y_0 /H = 0.760				
y/h_e	p/γ cm	$p/\gamma h_e$	V(h) (m/sec)	$V(h)/U_0$	y/Y_0	$\frac{p}{\gamma}$ cm	$p/\gamma Y_0$	V(y) (m/sec)	$V(y)/U_0$
0.043	0.5	0.094	1.090	0.952	0.054	0.6	0.117	1.09	0.95
0.127	0.9	0.174	1.020	0.890	0.158	0.8	0.160	1.04	0.91
0.210	1.4	0.255	0.944	0.824	0.263	1.1	0.215	0.99	0.86
0.294	1.3	0.254	0.904	0.789	0.367	1.1	0.212	0.95	0.83
0.377	1.3	0.253	0.862	0.752	0.471	1.0	0.191	0.86	0.75
0.461	1.2	0.223	0.833	0.727	0.575	0.9	0.177	0.81	0.71
0.544	1.0	0.195	0.802	0.700	0.679	0.9	0.175	0.79	0.69
0.628	1.0	0.194	0.754	0.658	0.783	0.7	0.139	0.76	0.66
0.711	0.9	0.165	0.721	0.629	0.888	0.5	0.101	0.72	0.63
0.795	0.6	0.109	0.702	0.613	0.992	0.0	0.006	0.69	0.60
0.878	0.4	0.080	0.667	0.582					
0.962	0.1	0.026	0.646	0.564					

TABLE 6.1

CLASSIFICATION OF FINITE CREST WIDTH WEIRS

RANGE OF H/L_w	DESCRIPTION OF FLOW PATTERN	SKETCH OF FLOW PATTERN	CLASSIFICATION OF WEIR
$H/L_w < 0.08$	The flow over the weir crest is subcritical and the weir cannot be used to determine the discharge. The flow pattern consists of series of standing waves on the weir crest.	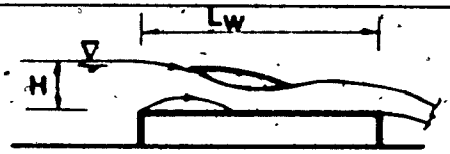	Long-crested
$0.08 \leq H/L_w \leq 0.40$	In this range, the weir can accurately be described as broad-crested since a region of parallel flow exists for a considerable portion of the weir crest.	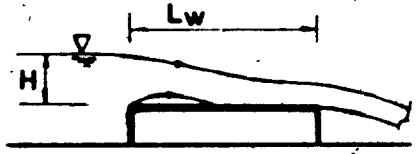	Broad-crested*
$0.4 \leq H/L_w < 1.50$	In this range, the weir can no longer be termed broad-crested but should be classified as narrow-crested. The flow pattern is entirely curvilinear.	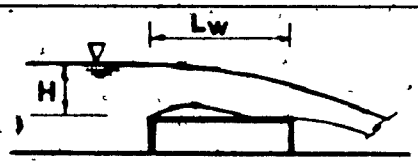	Narrow-crested
$1.5 \leq H/L_w$	In this range, the flow pattern consists of a nappe springing clear off the crest, touching the weir only at the upstream corner. For values of $H/L>3$, the weir is similar to a sharp-crested weir and can be used to estimate flow rates.	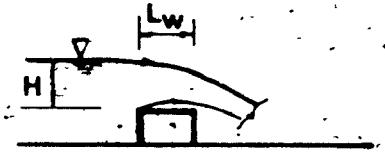	Sharp-crested

*+ Range Considered

TABLE 6.2

RANGE OF VARIABLES: Broad-Crested Weir Tests.

Weir length L_w = 30.0 cm; Weir Height P = 10.16 cm; Channel Width B = 25.4 cm

Series	Radius of Upstream Corner R in cm	R/P	Range of H/L_w	Range of H/P	Range of H/R
1	0.00	0.000	0.083 - 0.400	0.250 - 1.20	-
2	0.95	0.094	0.083 - 0.400	0.250 - 1.20	2.67 - 12.80
3	1.27	0.126	0.083 - 0.400	0.250 - 1.20	2.00 - 9.60
4	2.54	0.250	0.083 - 0.400	0.250 - 1.20	1.00 - 4.80
5	3.49	0.344	0.083 - 0.400	0.250 - 1.20	0.73 - 3.50
6	6.35	0.625	0.083 - 0.400	0.250 - 1.20	0.40 - 1.92
7	10.0	1.000	0.083 - 0.400	0.250 - 1.20	0.25 - 1.20

Table 6.3

Rectangular Broad-Crested Weir: Measurements and Computed Results

B = 25.4 cm, L_w = 30.5 cm, P = 10.16 cm, R = 0.0 cm, R/P = 0.0, L_w/P = 3.0

Run Number	Measured Head H (cm)	Measured Discharge Q_1 (l/sec)	Depth at Parallel Flow d_3 (cm)	H/P	Actual Discharge Coeff. C_{dw}	Predicted Discharge Coeff. C_{dw}	% deviation in C_{dw} $\frac{(7)-(6)}{(6)} \times 100\%$
(1)	(2)	(3)	(4)	(5)	(6)	(7)	(8)
1	2.5	1.45	1.08	0.25	0.847	0.841	-0.7
2	3.1	2.00	1.35	0.30	0.846	0.848	+0.2
3	4.6	3.67	2.00	0.45	0.859	0.858	-0.1
4	6.1	5.63	2.65	0.60	0.863	0.865	+0.2
5	7.6	7.88	3.30	0.75	0.869	0.871	+0.2
6	9.1	10.44	3.98	0.90	0.878	0.882	+0.5
7	10.7	13.46	4.69	1.05	0.888	0.892	+0.4
8	12.2	16.41	5.36	1.20	0.889	0.900	+1.2

Table 6.3

Rectangular Broad-Crested Weir: Measurements and Computed Results

B = 25.4 cm, L_w = 30.5 cm, P = 10.16 cm, R = 0.96 cm, R/P = 0.094, L_w/P = 3.0

Run Number	Measured Head H (cm)	Measured Discharge Q_1 (l /sec)	Depth at Parallel Flow d_3 (cm)	H/P	Actual Discharge Coeff. C_{dw}	Predicted Discharge Coeff. C_{dw}	% deviation in C_{dw} $\frac{(7) - (6)}{(6)} \times 100\%$
(1)	(2)	(3)	(4)	(5)	(6)	(7)	(8)
9	2.5	1.46	1.15	0.25	0.853	0.858	+0.6
10	3.1	2.03	1.43	0.30	0.859	0.864	+0.6
11	4.6	3.71	2.12	0.45	0.868	0.875	+0.8
12	6.1	5.80	2.81	0.60	0.889	0.883	-0.6
13	7.6	8.11	3.50	0.76	0.894	0.890	-0.4
14	9.1	10.63	4.19	0.90	0.894	0.900	+0.7
15	10.7	13.72	4.92	1.05	0.905	0.909	+0.4
16	12.2	16.99	5.61	1.20	0.921	0.917	-0.4

Table 6.3

Rectangular Broad-Crested Weir: Measurements and Computed Results

B = 25.4 cm, L_w = 30.5 cm, P = 10.16 cm, R = 1.27cm, R/P = 0.125, L_w/P = 3.0

Run Number	Measured Head H (cm)	Measured Discharge Q_1 (l/sec)	Depth at Parallel Flow d_3 (cm)	H/P	Actual Discharge Coeff.,C_{dw}	Predicted Discharge Coeff.,C_{dw}	% deviation in C_{dw} $\frac{(7) - (6)}{(6)} \times 100\%$
(1)	(2)	(3)	(4)	(5)	(6)	(7)	(8)
17	2.5	1.50	1.30	0.25	0.876	0.886	+1.1
18	3.1	2.13	1.61	0.30	0.901	0.893	-0.9
19	4.6	3.91	2.39	0.45	0.915	0.907	-0.9
20	6.1	6.00	3.17	0.60	0.920	0.917	-0.3
21	7.6	8.43	3.95	0.75	0.929	0.927	-0.2
22	9.1	11.20	4.73	0.90	0.942	0.939	-0.3
23	10.7	14.31	5.56	1.05	0.944	0.950	+0.6
24	12.2	17.70	6.34	1.20	0.959	0.960	+0.1

Table 6.3

Rectangular Broad-Crested Weir: Measurements and Computed Results

B = 25.4 cm, L_w = 30.5 cm, P = 10.16 cm, R = 2.54 cm, R/P = 0.250, L_w/P = 3.0

Run Number	Measured Head H (cm)	Measured Discharge Q_1 (l/sec)	Depth at Parallel Flow d_3 (cm)	H/P	Actual Discharge Coeff. C_{dw}	Predicted Discharge Coeff. C_{dw}	% deviation in C_{dw} $\frac{(7)-(6)}{(6)} \times 100\%$
(1)	(2)	(3)	(4)	(5)	(6)	(7)	(8)
25	2.5	1.51	1.33	0.25	0.882	0.891	+1.0
26	3.1	2.14	1.64	0.30	0.905	0.897	-0.9
27	4.6	3.90	2.44	0.45	0.913	0.911	-0.2
28	6.1	6.10	3.23	0.60	0.935	0.922	-1.4
29	7.6	8.51	4.03	0.75	0.938	0.932	-0.6
30	9.1	11.31	4.82	0.90	0.952	0.944	-0.8
31	10.7	14.40	5.67	1.05	0.950	0.956	+0.6
32	12.2	17.90	6.47	1.20	0.970	0.967	-0.3

Table 6.3

Rectangular Broad-Crested Weir: Measurements and Computed Results

B = 25.4 cm, L_w = 30.5 cm, P = 10.16 cm, R = 6.4 cm, R/P = 0.625, L_w/P = 3.0

Run Number	Measured Head H (cm)	Measured Discharge Q_i (l/sec)	Depth at Parallel Flow d_3 (cm)	H/P	Actual Discharge Coeff. C_{dw}	Predicted Discharge Coeff. C_{dw}	% deviation in C_{dw} $\frac{(7)-(6)}{(6)} \times 100\%$
(1)	(2)	(3)	(4)	(5)	(6)	(7)	(8)
33	2.5	1.54	1.38	0.25	0.900	0.897	-0.3
34	3.1	2.15	1.71	0.30	0.910	0.904	-0.7
35	4.6	3.95	2.58	0.45	0.925	0.922	-0.3
36	6.1	6.14	3.36	0.60	0.941	0.931	-1.1
37	7.6	8.60	4.18	0.75	0.948	0.941	-0.7
38	9.1	11.42	5.01	0.90	0.961	0.954	-0.7
39	10.7	14.68	5.89	1.05	0.969	0.967	-0.2
40	12.2	18.10	6.71	1.20	0.981	0.978	-0.3

Table 6.3

Rectangular Broad-Crested Weir: Measurements and Computed Results

B = 25.4 cm, L_w = 30.5 cm, P = 10.16 cm, R = 10.2 cm, R/P = 1.00, L_w/P = 3.0

Run Number	Measured Head H (cm)	Measured Discharge Q_1 (l/sec)	Depth at Parallel Flow d_3 (cm)	H/P	Actual Discharge Coeff. C_{dw}	Predicted Discharge Coeff. C_{dw}	% deviation in C_{dw} $\frac{(7) - (6)}{(6)} \times 100\%$
(1)	(2)	(3)	(4)	(5)	(6)	(7)	(8)
41	2.5	1.54	1.40	0.25	0.900	0.899	-0.1
42	3.1	2.16	1.74	0.30	0.915	0.907	-0.9
43	4.6	3.96	2.58	0.45	0.927	0.922	-0.5
44	6.1	6.14	3.42	0.60	0.941	0.934	-0.7
45	7.6	8.60	4.26	0.75	0.948	0.945	-0.3
46	9.1	11.42	5.10	0.90	0.961	0.958	-0.3
47	10.7	14.79	5.99	1.05	0.976	0.971	-0.5
48	12.2	18.12	6.83	1.20	0.982	0.983	+0.1

Table 6.4

Submergence Studies on Rectangular Broad-crested Weir: Measurements and Results

B = 25.4; L_w = 30.5 cm; P = 10.16 cm; L_w/P = 3.00

Run Number	Submerged Flow Discharge, Q_m (l/sec)	Downstream Measured Head, H_2 (cm)	Drowned Flow Reduction, f ($=Q_m/Q$)	Submergence Ratio, S_h ($=H_2/H$)	Other pertinent details
(1)	(2)	(3)	(4)	(5)	(6)
1	2.00	2.24	1.00	0.723	
2	1.92	2.49	0.96	0.803	H = 3.10 cm
3	1.78	2.59	0.89	0.835	Q = 2.00 l /sec
4	1.54	2.80	0.77	0.903	H/P = 0.30
5	1.34	2.91	0.67	0.938	R = 0.00 cm
6	1.22	2.93	0.61	0.945	R/P = 0.00
7	0.90	2.99	0.45	0.965	
8	7.88	5.17	1.00	0.680	H = 7.60 cm
9	7.88	5.57	1.00	0.733	Q = 7.88 l /sec
10	7.57	5.93	0.96	0.780	H/P = 0.75
11	7.41	6.23	0.94	0.820	R = 0.00 cm
12	6.46	6.75	0.82	0.888	R/P = 0.00
13	5.20	7.02	0.66	0.923	
14	3.15	7.45	0.40	0.980	
15	10.44	6.40	1.00	0.703	H = 9.10 cm
16	8.87	7.83	0.85	0.860	Q = 10.44 l /sec
17	9.19	7.96	0.88	0.875	H/P = 0.90
18	7.62	8.33	0.73	0.915	R = 0.00 cm
19	7.83	8.45	0.75	0.928	R/P = 0.00
20	5.64	8.72	0.54	0.958	
21	3.34	8.97	0.32	0.986	
22	2.40	9.04	0.23	0.993	
23	13.46	7.49	1.00	0.708	H = 10.70 cm
24	13.06	8.16	0.97	0.763	Q = 13.46 l /sec
25	12.38	9.07	0.92	0.848	H/P = 1.05
26	11.17	9.61	0.88	0.898	R/P = 0.00

Table 6.4 (Continued)

Submergence Studies on Rectangular Broad-crested Weir: Measurements and Results

B = 25.4; L_w = 30.5 cm; P = 10.16 cm; L_w/P = 3.00

Run Number	Submerged Flow Discharge, Q_m (l/sec)	Downstream Measured Head, H_2 (cm)	Drowned Flow Reduction, f (=Q_m/Q)	Submergence Ratio, S_h (=H_2/H)	Other pertinent details
(1)	(2)	(3)	(4)	(5)	(6)
27	9.83	9.68	0.73	0.905	R/P = 0.00
28	9.29	10.14	0.69	0.948	
29	6.60	10.22	0.49	0.955	
30	3.63	10.52	0.27	0.983	
31	16.41	8.44	1.00	0.692	H = 12.20 cm
32	15.59	9.68	0.95	0.793	Q = 16.41 l/sec
33	11.49	10.11	0.70	0.829	H/P = 1.20
34	14.28	10.37	0.87	0.850	R = 0.00 cm
35	13.13	10.72	0.80	0.879	R/P = 0.00
36	8.70	11.59	0.53	0.950	
37	7.39	11.90	0.45	0.975	
38	5.74	11.96	0.35	0.980	
39	2.13	2.12	1.00	0.685	H = 3.10 cm
40	2.13	2.37	1.00	0.763	Q = 2.13 l/sec
41	2.02	2.54	0.95	0.818	H/P = 0.304
42	1.73	2.71	0.81	0.875	R = 1.27 cm
43	1.64	2.82	0.77	0.910	R/P = 0.125
44	1.24	2.93	0.58	0.946	
45	0.92	3.01	0.43	0.972	
46	0.83	3.07	0.39	0.990	
47	8.43	5.56	1.00	0.718	H = 7.60 cm
48	8.43	5.70	1.00	0.750	Q = 8.43 l/sec
49	8.35	6.08	0.99	0.800	H/P = 0.75
50	8.01	6.63	0.95	0.833	R = 1.27 cm
51	7.17	6.65	0.85	0.875	R/P = 0.125
52	7.25	6.83	0.86	0.898	

Table 6.4 (Continued)

Submergence Studies on Rectangular Broad-crested Weir: Measurements and Results

B = 25.4; L_w = 30.5 cm; P = 10.16 cm; L_w/P = 3.00

Run Number	Submerged Flow Discharge Q_m (l/sec)	Downstream Measured Head H_2 (cm)	Drowned Flow Reduction, f ($=Q_m/Q$)	Submergence Ratio S_h ($=H_2/H$)	Other pertinent details
(1)	(2)	(3)	(4)	(5)	(6)
53	5.99	7.07	0.71	0.930	
54	4.38	7.28	0.52	0.958	R/P = 0.125
55	12.70	7.55	0.32	0.993	
56	11.20	6.71	1.00	0.737	H = 9.10 cm
57	10.19	7.70	0.91	0.846	Q = 11.20 l/sec
58	10.08	7.90	0.90	0.868	H/P = 0.90
59	8.06	8.33	0.72	0.915	R = 1.27 cm
60	7.17	8.61	0.64	0.946	R/P = 0.125
61	6.83	8.74	0.61	0.960	
62	0.36	8.92	0.36	0.980	
63	14.31	7.49	1.00	0.700	H = 10.70 cm
64	14.31	8.29	1.00	0.775	Q = 14.31 l/sec
65	13.31	9.14	0.93	0.855	H/P = 1.05
66	11.30	9.58	0.79	0.895	R = 1.27 cm
67	10.73	9.90	0.75	0.925	R/P = 0.125
68	7.16	10.49	0.50	0.980	
69	17.70	8.66	1.00	0.710	
70	17.70	8.66	1.00	0.710	H = 12.20 cm
71	17.70	9.39	1.00	0.770	Q = 17.70 l/sec
72	17.17	10.13	0.97	0.830	H/P = 1.20
73	15.75	10.74	0.89	0.880	R = 1.27 cm
74	14.51	11.05	0.82	0.906	R/P = 0.125
75	12.21	11.52	0.69	0.944	
76	9.56	11.83	0.54	0.970	

Table 6.4 (Continued)

Submergence Studies on Rectangular Broad-crested Weir: Measurements and Results

B = 25.4; L_w = 30.5 cm; P = 10.16 cm; L_w/P = 3.00

Run Number	Submerged Flow Discharge Q_m (l/sec)	Downstream Measured Head H_2 (cm)	Drowned Flow Reduction, f $(=Q_m/Q)$	Submergence Ratio S_h $(=H_2/H)$	Other pertinent details
(1)	(2)	(3)	(4)	(5)	(6)
77	2.14	2.24	1.00	0.721	H = 3.10 cm
78	2.14	2.43	1.00	0.785	Q = 2.14 l/sec
79	2.03	2.59	0.95	0.835	H/P = 0.30
80	1.91	2.73	0.89	0.880	R = 2.54 cm
81	1.58	2.85	0.74	0.920	R/P = 0.250
82	1.37	2.95	0.64	0.952	
83	1.33	2.99	0.62	0.968	
84	0.94	3.02	0.44	0.973	
85	8.51	5.62	1.00	0.740	H = 7.60 cm
86	8.51	5.84	1.00	0.768	Q = 8.51 l/sec
87	8.34	6.18	0.98	0.813	H/P = 0.75
88	8.25	6.45	0.97	0.848	R = 2.54 cm
89	7.49	6.61	0.88	0.870	R/P = 0.250
90	6.81	6.98	0.80	0.918	
91	5.45	7.14	0.64	0.940	
92	4.34	7.41	0.51	0.975	
93	3.15	7.45	0.37	0.980	
94	11.31	6.64	1.00	0.730	H = 9.10 cm
95	11.31	7.05	1.00	0.775	Q = 11.31 l/sec
96	11.20	7.55	0.99	0.830	H/P = 0.90
97	10.18	7.78	0.90	0.855	R = 2.54 cm
98	9.05	8.17	0.80	0.898	R/P = 0.250
99	8.82	8.40	0.78	0.923	
100	8.14	8.65	0.72	0.950	
101	5.88	8.76	0.52	0.963	
102	3.51	9.01	0.31	0.990	

Table 6.4 (Continued)

Submergence Studies on Rectangular Broad-crested Weir: Measurements and Results

B = 25.4; L_w = 30.5 cm; P = 10.16 cm; L_w/P = 3.00

Run Number	Submerged Flow Discharge Q_m (l/sec)	Downstream Measured Head H_2 (cm)	Drowned Flow Reduction $(=Q_m/Q)$	Submergence Ratio S_h $(=H_2/H)$	Other pertinent details
(1)	(2)	(3)	(4)	(5)	(6)
103	14.40	8.08	1.00	0.755	H = 10.70 cm
104	13.68	9.15	0.95	0.855	Q = 14.40 l/sec
105	12.24	9.47	0.85	0.885	H/P = 1.05
106	10.37	10.04	0.72	0.938	R = 2.54 cm
107	8.21	10.14	0.57	0.948	R/P = 0.250
108	6.05	10.54	0.42	0.985	
109	17.90	9.27	1.00	0.760	H = 12.20
110	16.83	10.6	0.94	0.870	Q = 17.90 l/sec
111	15.57	10.96	0.87	0.898	H/P = 1.20
112	11.81	11.75	0.66	0.963	R = 2.54 cm
113	10.02	11.77	0.56	0.965	R/P = 0.250
114	8.41	11.97	0.47	0.981	
115	2.20	2.33	1.00	0.750	H = 3.10 cm
116	2.20	2.47	1.00	0.795	Q = 2.20 l/sec
117	1.98	2.70	0.90	0.870	H/P = 0.30
118	1.87	2.84	0.85	0.915	R = 10.16 cm
119	1.56	2.90	0.71	0.935	R/P = 1.00
120	1.30	2.98	0.59	0.960	
121	1.01	3.06	0.46	0.988	
122	1.19	3.07	0.54	0.990	
123	8.60	5.62	1.00	0.740	H = 7.60 cm
124	8.60	5.88	1.00	0.773	Q = 8.60 l/sec
125	8.43	6.37	0.98	0.838	H/P = 0.75
126	7.48	6.57	0.87	0.865	R = 10.16 cm
127	7.74	6.79	0.90	0.893	R/P = 1.00
128	6.54	7.09	0.76	0.933	

Table 6.4 (Continued)

Submergence Studies on Rectangular Broad-crested Weir: Measurements and Results

B = 25.4; L_w = 30.5 cm; P = 10.16 cm; L_w/P = 3.00

Run Number	Submerged Flow Discharge Q_m (l/sec)	Downstream Measured Head H_2 (cm)	Drowned Flow Reduction f $(=Q_m/Q)$	Submergence Ratio S_h $(=H_2/H)$	Other pertinent details
(1)	(2)	(3)	(4)	(5)	(6)
129	7.05	7.17	0.82	0.943	
130	5.42	7.26	0.63	0.955	
131	5.76	7.37	0.67	0.970	
132	3.87	7.45	0.45	0.980	
133	11.42	6.96	1.00	0.765	H = 9.10 cm
134	11.19	7.46	0.98	0.82	Q = 11.42 l/sec
135	10.85	7.85	0.95	0.863	H/P = 0.90
136	9.25	8.40	0.81	0.923	R = 10.16 cm
137	7.20	8.69	0.63	0.955	R/P = 1.00
138	6.05	8.85	0.53	0.973	
139	3.31	9.04	0.29	0.993	
140	14.79	8.00	1.00	0.748	H = 10.70 cm
141	14.79	8.61	1.00	0.805	Q = 14.79 l/sec
142	13.46	9.42	0.91	0.880	H/P = 1.05
143	12.72	9.63	0.86	0.900	R = 10.16 cm
144	10.06	10.11	0.68	0.945	R/P = 1.00
145	8.43	10.43	0.57	0.975	
146	8.87	10.52	0.60	0.983	
147	5.77	10.54	0.39	0.986	
148	18.12	8.91	1.00	0.730	H = 12.20 cm
149	18.12	9.58	1.00	0.785	Q = 18.12 l/sec
150	17.58	10.37	0.97	0.850	H/P = 1.20
151	17.40	10.68	0.96	0.875	R = 10.16 cm
152	15.76	11.29	0.87	0.925	R/P = 1.00
153	13.23	11.53	0.73	0.945	
154	11.23	11.81	0.62	0.968	
155	8.88	11.87	0.49	0.973	
156	7.61	12.12	0.42	0.993	

TABLE 7.1

GEOMETRIC PARAMETERS OF SURFACE-MOUNTED MODELS; Wind Tunnel Tests

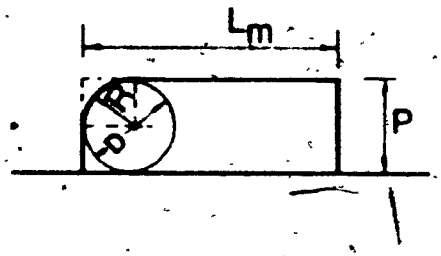

MODEL DESIGNATION	CORNER RADIUS R(cm)	MODEL HEIGHT P(cm)	MODEL LENGTH L_m(cm)	DEGREE OF ROUNDING (R/P)	ASPECT RATIO, L_m/P
00	0.00	10.16	30.48	0.000	3.0
10	0.04	10.16	30.48	0.004	3.0
20	0.08	10.16	30.48	0.008	3.0
30	0.48	10.16	30.48	0.047	3.0
40	0.95	10.16	30.48	0.094	3.0
50	1.27	10.16	30.48	0.125	3.0
60	2.54	10.16	30.48	0.250	3.0
70	3.49	10.16	30.48	0.344	3.0
80	6.35	10.16	30.48	0.625	3.0
90	10.16	10.16	30.48	1.000	3.0

TABLE 7.2

TABULATION OF EXPERIMENTAL DATA:-Wind Tunnel Tests

Model Designation	Corner Radius, R(cm)	Run Number	Velocity U_∞ (m/sec)	R_{eD} ($=U_\infty D/\nu$) x 10^5	R_{eL_w} x 10^5	PRESSURE COEFFICIENT, C_p				DRAG COEFFICIENT	
						C_{pu} +ve	C_{pu} -ve	C_{pu}	C_{pb}	C_D	C_{DC}
1	2	3	4	5	6	7	8	9	10	11	12
00	0.00	001	17.83	–	3.50	0.521	0.059	+0.580	-1.80	2.38	1.20
		002	27.58	–	5.40	0.570	0.055	+0.625	-1.80	2.43	1.22
		003	33.44	–	6.50	0.625	0.055	+0.680	-1.81	2.49	1.25
10	0.04	101	14.70	0.0075	2.87	0.643	0.056	+0.587	1.74	2.33	1.17
		102	22.50	0.010	4.37	0.643	0.056	+0.587	1.76	2.35	1.18
		103	29.40	0.015	5.70	0.615	0.056	+0.559	1.83	2.39	1.20
		104	31.60	0.016	6.10	0.626	0.056	+0.570	1.80	2.37	1.19
		105	33.40	0.0168	6.45	0.627	0.057	+0.570	1.81	2.38	1.20
20	0.08	201	18.20	0.020	3.60	0.605	0.056	+0.549	1.79	2.34	1.18
		202	25.80	0.206	4.98	0.601	0.056	+0.545	1.79	2.34	1.18
		203	29.80	0.030	5.80	0.587	0.056	+0.531	1.80	2.33	1.17
		204	31.70	0.032	6.15	0.593	0.057	+0.536	1.81	2.35	1.18
		205	33.40	0.034	6.50	0.599	0.057	+0.541	1.80	2.34	1.18
30	0.48	301	11.20	0.068	2.17	0.422	0.124	+0.298	1.40	1.69	0.86
		302	25.00	0.150	4.85	0.439	0.142	+0.297	1.49	1.79	0.91
		303	29.70	0.180	5.80	0.358	0.135	+0.222	1.36	1.58	0.80
		304	32.80	0.200	6.40	0.400	0.153	+0.248	1.52	1.77	0.90
		305	33.60	0.206	6.60	0.394	0.154	+0.240	1.53	1.77	0.90
		306	34.20	0.210	6.70	0.406	0.154	+0.252	1.52	1.77	0.90
40	0.95	401	20.40	0.248	3.97	0.431	0.328	+0.103	1.34	1.44	0.73
		402	23.00	0.277	4.44	0.416	0.327	+0.090	1.30	1.39	0.70
		403	27.70	0.331	5.30	0.421	0.369	+0.052	1.33	1.38	0.70
		404	31.00	0.370	5.92	0.371	0.413	-0.042	1.34	1.24	0.65
		405	33.70	0.400	6.40	0.372	0.439	-0.067	1.34	1.28	0.65
		406	34.40	0.419	6.70	0.368	0.456	-0.088	1.31	1.23	0.62

TABLE 7.2 (CONTINUED)
TABULATION OF EXPERIMENTAL DATA: Wind Tunnel Tests

1	2	3	4	5	6	7	8	9	10	11	12
50	1.27	501	19.30	0.320	3.83	0.433	0.547	-0.110	1.28	1.17	0.59
		502	25.10	0.410	4.92	0.412	0.584	-0.172	1.24	1.07	0.54
		503	29.50	0.480	5.80	0.387	0.643	-0.256	1.24	0.98	0.50
		504	31.80	0.510	6.17	0.391	0.658	-0.266	1.23	0.97	0.50
		505	33.70	0.560	6.67	0.392	0.679	-0.287	1.24	0.95	0.48
		506	34.40	0.562	6.74	0.388	0.667	-0.280	1.22	0.94	0.48
60	2.54	601	16.20	0.530	3.20	0.416	0.887	-0.471	1.07	0.60	0.30
		602	23.00	0.750	4.50	0.429	0.906	-0.477	1.04	0.57	0.29
		603	29.50	0.960	5.80	0.426	0.926	-0.502	1.08	0.58	0.29
		604	32.40	1.05	6.30	0.436	0.952	-0.515	1.11	0.60	0.30
		605	35.50	1.15	6.87	0.412	0.960	-0.548	1.14	0.60	0.30
		606	36.70	1.20	7.20	0.414	0.958	-0.544	1.13	0.58	0.29
70	3.49	701	17.70	0.810	3.50	0.414	0.942	-0.528	1.06	0.53	0.27
		702	25.90	1.18	5.13	0.360	0.842	-0.520	1.03	0.51	0.26
		703	30.10	1.35	5.90	0.422	0.939	-0.517	1.04	0.52	0.27
		704	32.90	1.48	6.44	0.402	0.934	-0.532	1.04	0.51	0.26
		705	35.00	1.56	6.79	0.403	0.950	-0.547	1.07	0.52	0.27
		706	35.90	1.60	6.98	0.400	0.937	-0.538	1.04	0.51	0.26
80	6.35	801	13.90	1.16	2.80	0.354	0.667	-0.313	1.05	0.73	0.37
		802	22.10	1.82	4.40	0.345	0.692	-0.348	1.04	0.59	0.35
		803	30.30	2.49	6.00	0.362	0.721	-0.360	1.04	0.68	0.35
		804	33.40	2.72	6.54	0.372	0.728	-0.356	1.05	0.69	0.35
		805	35.00	2.87	6.90	0.388	0.726	-0.338	1.04	0.71	0.36
		806	35.40	2.89	6.93	0.388	0.727	-0.339	1.04	0.70	0.36
90	10.16	901	8.32	1.12	1.67	0.333	0.631	-0.298	1.12	0.82	0.42
		902	10.16	1.40	2.10	0.347	0.585	-0.237	1.01	0.77	0.39
		903	12.80	1.71	2.56	0.294	0.616	-0.322	1.02	0.70	0.36
		904	13.70	1.82	2.73	0.301	0.633	-0.332	1.01	0.68	0.35
		905	22.60	2.96	4.40	0.305	0.629	-0.324	1.01	0.69	0.35
		906	29.00	3.80	5.70	0.324	0.642	-0.317	1.03	0.71	0.36
		907	33.40	4.35	6.50	0.317	0.640	-0.323	1.04	0.71	0.36
		908	35.00	4.56	6.80	0.319	0.647	-0.328	1.05	0.72	0.37
		909	35.90	4.71	7.10	0.322	0.646	-0.324	1.04	0.72	0.37